UNIVERSITAT DE LES ILLES BALEARS
DEPARTAMENT DE FISICA

Programa de Doctorat de Fisica

Theoretical issues in Numerical Relativity simulations

Tesi Doctoral

Daniela Alic

Director: Prof. Carles Bona

2009

El director de tesi Carles Bona Garcia, Catedràtic de Fìsica Teòrica de la Universitat de les Illes Balears, adscrit al Departament de Fìsica, certifica que aquesta tesi doctoral ha estat realitzada pel Sra. Daniela Delia Alic, i perquè quedi constància escrita firma

a Palma 16 de Juny de 2009,

Prof. Carles Bona   Daniela Alic

Acknowledgments

I would like to express my sincere gratitude to my thesis supervisor, Prof. Carles Bona, for his guidance and help throughout these four years.

I would like to thank especially my collaborators Dr. Sascha Husa and Dr. Carlos Palenzuela, for many useful and valuable discussions, comments and suggestions, from which I learned so much during these years, for all their encouragement and support.

I would like to thank Dr. Juan Barranco and Dr. Argelia Bernal for the collaboration in boson star project, providing the initial data for the study of mixed states boson stars. I thank Dr. Cecilia Chirenti, for kindly sharing with us the code for calculating the frequencies of the unstable mixed state boson star configurations. I would also like to thank Frank Ohme for his participation in the gauge instabilities study, providing the Penrose diagrams for the slices. Many thanks to Carles Bona-Casas for his collaboration in the black hole projects.

I thank all the members of the AEI Astrophysical Relativity Division and LSU Physics and Astronomy Department, for creating a such pleasant and stimulating research environment during my research stays in Germany and USA. I thank all my colleagues from the UIB Agencia EFE.

Special thanks to my dear friend Raul Vicente, and to my precious little water turtle Zapatuki.

I am grateful to my family for all their love and support.

Daniela Alic
Palma, June 2009.

Abstract

In this thesis we address several analytical and numerical problems related with the study of general relativistic black holes and boson stars.

The task of solving numerically the Einstein equations ($G_{ab} = \kappa T_{ab}$) has turned out to be a very complex problem. Various reductions to first-order-in-time hyperbolic systems appear in the literature, but there is no general recipe that prescribes the optimal technique for any given situation, which leads to a variety of formulations.

In the first part of this thesis, we present an analytical and numerical comparison between three different formulations of the Einstein equations. A detailed analysis of these systems is performed, marking the weak points and proposing improvements, in the form of constraint adjustments and damping terms.

Black holes are considered to be some of the most interesting astrophysical compact objects. They are vacuum solutions of the Einstein equations. The challenge of dealing with black hole (BH) simulations comes from the fact that they hide a space-time singularity, a point where the attraction becomes so intense that an observer would get trapped and absorbed into it. As a consequence, one of the main problems that needed to be overcome were the steep gradients appearing around the BH apparent horizon, marking the region between the outer nearly inertial wave zone and the highly accelerated behavior of the inner plunging zone. To this purpose, we developed a new centered finite volume (CFV) method based on the flux splitting approach. This algorithm is the first one in the class of finite volume methods which allows third order accuracy by only piece-wise linear reconstruction.

The finite volume methods are commonly used in the numerical study of relativistic astrophysical systems which contain matter sources, in order to deal with shocks or any other type of discontinuities. However, in most cases one does not require the use of limiters and the CFV method can be efficiently used in the form of an adaptive dissipation algorithm, in order to deal with the steep gradients. We present a comparison between our CFV method and the standard finite difference plus dissipation techniques, and show that our method allows longer and more accurate BH evolutions, even at low resolutions.

In this thesis, we discuss the techniques for dealing with the singularity, steep

gradients and apparent horizon location, in the context of a single Schwarzschild BH, in both spherically symmetric and full 3D simulations. Our treatment of the singularity involves scalar field stuffing, which consists in matching a scalar field in the inner region of the BH, such that the metric becomes regular inside the horizon. Additionally, for comparison, we appeal to the puncture technique, which reduces the singularity to a point, while the interior BH region is maintained sufficiently regular for numerical purposes. Even though the singularity is no longer a problem in the initial data, it can become a problem in a finite amount of time, if one does not choose suitable coordinate conditions.

We perform BH evolutions using the '1+log' singularity avoiding slicing, which ensures that the coordinate time rate is slowing down in the strongly collapsing regions, but it keeps flowing at the same rate as proper time in the wave zone. In this context, we develop a geometrical picture of the slicings approaching the stationary state, for situations where the treatment of the singularity involves both scalar field stuffing and the puncture technique. Our 3D numerical results show the first long term simulation of a Schwarzschild BH in normal coordinates, without the need to excise the singularity from the computational domain.

The family of singularity avoiding slicing conditions which are currently used in BH evolutions, have been shown to produce gauge instabilities. We extend this study and show that, contrary to previous claims, these instabilities are not generic for evolved gauge conditions. We follow the behavior of the slicing in evolutions of Schwarzschild spacetime and perform a detailed study of the pathologies which can arise from two models: perturbing the initial slice and perturbing the initial lapse. A comparison with the results available in the literature allows us to identify most instabilities and propose a cure.

Regarding the choice of space coordinate conditions, we developed an alternative to the current prescriptions, based on a generalized Almost Killing Equation (AKE). This condition is expected to adapt the coordinates to the symmetry of the problem under study. The 3-covariant AKE shift can be used in combination with any slicing, without loosing its quasi-stationary properties. Our numerical tests address harmonic and black hole spacetimes.

Our research work extends also to the study of regular spacetimes with matter. We explore boson star configurations as dark matter models and focus on Mixed State Boson Stars (MSBS) configurations constructed in the context of General Relativity. Contrary to previous studies, where bosons populate only the ground state, in our case different excited states are coexisting simultaneously. We performed the first general relativistic study of MSBS configurations, using the Einstein-Klein-Gordon system in spherical symmetry. Following the evolution of MSBS under massless scalar field perturbations, we identify the unstable models and find a criteria of separation between stable and unstable configurations. Our conclusions regarding the long term stability of MSBS configurations, suggest that they can be suitable candidates for dark matter models.

Contents

Part I

Introduction

Chapter 1

Overview

The theory of General Relativity describes gravity as a geometric property of the spacetime. It had a very important impact in modern physics, as it changed our understanding of the notion of time, the geometry of space, the motion of bodies and the propagation of light. Its predictions are fully consistent with the current observations and experiments. Some of the most important results are the prediction of black holes and gravitational waves.

General Relativity is based on the Einstein field equations, which relate the curvature of spacetime with the matter content. In practice, the theory has proven to be very complex, as it relies on a system of ten coupled, nonlinear, partial differential equations in four dimensions. Exact solutions are known only in cases with high symmetry in space (spherical or axial symmetry) or in time (static or stationary solutions). The study of astrophysical relevant systems, has led to the field of Numerical Relativity, which deals with solving the Einstein equations numerically.

Even though Numerical Relativity appeared as an independent field of research in the 1960's, only recently the computational power has allowed extensive numerical studies. A better understanding of the theoretical issues and the development of numerical methods, allowed the study of complex problems, from single stars and black holes, to collisions of compact objects, gravitational collapse and singularity structure.

One of the most important results in the field, has been the ability to predict gravitational radiation signals from binary black hole and neutron star simulations. This progress provides significant support for the new generation of gravitational wave detectors, as accurate gravitational waveform templates for astrophysical sources are crucial in the search strategy. Hybrid-templates are now constructed from analytical post-Newtonian approximations and numerical solutions of the Einstein field equations. Detection of gravitational radiation is expected to soon open a new window to the universe.

Theoretical framework

General Relativity's basic principles imply that Einstein's field equations should ensure causal propagation of the gravitational field. According to the causality principle, two events causally correlated can not happen at the same time, but the cause must precede the effect. Correspondingly, we expect that the partial differential equations which propagate initial data of the Einstein equations, or any other relativistic field theory, exclude instantaneous propagation of physical degrees of freedom, in other words, that they are hyperbolic in a suitable sense. Because of the covariant form of the Einstein equations, the hyperbolicity is not manifested in an immediate sense.

The Einstein field equations ($G_{ab} = \kappa T_{ab}$) can be written as a second order quasi-linear system of partial differential equations. In order to perform numerical time evolutions, the evolution equations are often written as a first-order-in-time system. An important aspect of the work in the field of Numerical Relativity is finding hyperbolic reduction techniques which lead to the most suitable Einstein system. The main idea is to convert the initial value problem (IVP) for Einstein's equations into an IVP for a hyperbolic system of partial differential equations, for which the IVP is well-posed. Various hyperbolic reductions appear in the literature, but there is no general recipe that prescribes the optimal technique for any given situation, which leads to a variety of formulations.

In Numerical Relativity, one commonly uses the 3+1 decomposition of the Einstein system, which leads to evolution and constraint equations, elliptic equations that can be interpreted as first integrals of the basic evolution system. The initial data is specified at some hypersurface of constant time and then evolved into the future by equations of hyperbolic character. When specifying the initial data, the solution is subjected to constraints, which are preserved by the continuum evolution equations, but not by the discretized evolution system.

The usual *free evolution* approach consists in using the constraints just for monitoring the quality of the simulation, with no mechanism for moderating the growth of the constraint violation modes. This approach is not proper, as unstable constraint violation modes can arise due to the non-linear source terms. In order to obtain accurate long term numerical simulations one could take into account adjustments to the formulations of the field equations, in the form of suitable damping terms [1, 2].

The Einstein theory leaves four degrees of freedom undetermined, corresponding to the choice of the coordinate system. In order to complete the evolution system, one needs to specify both the slicing condition, namely an equation for the lapse which provides the foliation of the spacetime in space-like hypersurfaces, and an equation for the shift, which dictates how the spatial coordinates are carried from one slice to the other. An essential problem in the numerical treatment of black hole systems has been finding the most suitable gauge conditions.

Black holes

An important break-through in the field of Numerical Relativity has been solving the binary black hole problem. This success relies on two formulations of the Einstein equations: the generalized harmonic [3–6] and the BSSN system [7,8]. Their approach towards the treatment of the black hole (BH) singularity is different, due to the analytical structure of these systems and the related gauge choice.

The problem of finding a suitable gauge conditions has proven to be one of the main challenges faced by the numerical relativity community. The harmonic implementations usually require the excision technique in order to remove the BH interior from the computational domain, as their slicing condition is only marginally singularity avoiding (the singularity is reached in a finite amount of time). The control of dynamical excision involves serious technical problems, as the collapse region grows and moves across the computational grid, so one needs to repopulate the grid points in a consistent way [6]. An alternative to excision is the *stuffed* BH approach, where the interior region black hole region is covered by a scalar field that eventually collapses [9].

The codes based on the BSSN system use the 'moving puncture' approach, where the interior BH region is maintained sufficiently regular for numerical purposes. They employ a strong singularity avoiding slicing condition, which ensures that the coordinate time rate is slowing down in the strongly collapsing regions, but it keeps flowing at the same rate as proper time in the wave zone. Even in scenarios in which a physical singularity is formed in a finite amount of proper time, one never sees it happen in coordinate (computer) time. This feature is crucial for the puncture technique, as otherwise they could grow by accreting neighboring time lines [10]. A key ingredient in the BSSN simulations is the 'Gamma driver' shift, a gauge condition that dynamically adapts the time lines to the symmetry of the problem, such that the evolution reaches a stationary state. The moving puncture technique can be viewed as an *excision by under-resolution*, as in the limit of infinite resolution the data never becomes stationary [11].

The challenge of dealing with BH simulations comes from the fact that they hide a space-time singularity, a point where the attraction becomes so intense that an observer would get trapped and absorbed into it. As a consequence, one of the main problems that needed to be overcome were the steep gradients appearing around the BH apparent horizon, marking the region between the outer nearly inertial wave zone and the highly accelerated behavior of the inner plunging zone [12]. This behavior can be dealt with by advanced numerical methods, or by adding more resolution in the affected areas, employing Fixed or Adaptive Mesh Refinement. These techniques produce higher resolution subgrids in the dynamical region, while keeping a computationally affordable grid resolution in the outer regions [13–15].

Binary black hole systems are now a major area of research in numerical rel-

ativity, as they are considered one of the most promising sources of gravitational waves. In the last years, important progress has been made starting with the first simulation done by Pretorius [9], followed by the Brownsville and Goddard numerical relativity groups which marked the moving punctures breakthrough [16–19]. The availability of gravitational waves templates opened the way to fruitful collaborations with the data analysis community.

However, this impressive progress marks only a stage of maturity in the otherwise young research field of Numerical Relativity. The geometric picture of the 'moving punctures' evolutions has been only recently understood [11], in the context of a time independent representation of a Schwarzschild black hole using maximal slices. The result was extended to the hyperbolic slicing conditions commonly used in numerical relativity. There are further gauge issues that need to be clarified, related with the behavior of these singularity avoiding slicing conditions and related instabilities. Alternatives to the 'Gamma driver' shift condition are still explored for different 3+1 formulations of the Einstein equations [20], including generalized harmonic formulations [21]. We are still in need of robust numerical codes for non-stationary scenarios, which allow various choices of gauge conditions.

Matter spacetimes

The numerical simulation of black hole spacetimes involve the vacuum Einstein equations. However, most relativistic astrophysical systems contain matter sources and require in addition the theory of fluid dynamics. The simulation of matter spacetimes require special numerical methods, due to the non-linearities in the Euler equations which give rise to propagating discontinuities arising even from smooth initial data. These discontinuities take the form of steep gradients in the variables.

A particularly useful approach to solving non-linear systems of evolution equations is the method of lines (MoL), which decouples the treatment of space and time. It is based on the idea of discretizing first the spatial dimensions, while leaving the time dimension continuous, leading to a semi-discrete system. Then one can solve the resulting system of coupled ordinary differential equations using a time integration method. The standard spatial discretization methods rely on finite difference (FD) algorithms or finite volumes (FV), which reduce to FD plus a special form of numerical dissipation. The development of high resolution shock capturing algorithms which require only the characteristic speeds [22, 23], has significantly increased the efficiency of the codes. The adaptive numerical viscosity terms are also very efficient in dealing with steep gradients that appear in the black hole simulations [24].

Considerable progress has been achieved in the last two years in extracting gravitational wave signals from binary neutron star systems [25–27]. Systematic

studies present the dynamics of the inspiral and merger phases, while last phase reveals a black hole surrounded by a torus [28]. However, questions related, for example, with the mechanism responsible for gamma ray bursts require further investigation. Furthermore, the numerical modeling of astrophysical processes involving highly dynamical magnetic fields, for which resistive effects play an important role, can not be dealt with by ideal magneto-hydro-dynamic (MHD) formulation. The development of numerical techniques that allow a solution to the relativistic resistive MHD equations, opens new possibilities of investigation [29, 30].

An interesting topic in General Relativity is the study of dark matter, which lies at the interface between the fields of observational astrophysics, cosmology and numerical relativity. Scalar field dark matter models, in which the dark matter particle is a spin-0 boson, are becoming a serious candidate. The boson particles can collapse into the same quantum state of the gravitational potential to form a Bose Einstein condensate. One of these Bose Einstein condensate is a compact gravitating object, named boson star.

Boson stars are self-gravitating scalar field objects, for which the gravity attraction balances the dispersive character of the scalar field. Their numerical modeling is more straightforward than for fluid stars, as the evolution of smooth initial data for a scalar field tends to stay smooth, in contrast with hydrodynamical fluid evolutions.

Previous relativistic studies regarding the stability of boson stars, showed that the only stable configurations are made of ground state scalar fields [31]. The associated mass density profiles decay exponentially as $r \to \infty$, making it difficult to fit the flat rotational curves of most galaxies. However, a generalization of boson stars configurations has been proposed [32], which considers a system of bosons formed by particles coexisting in ground and excited states. These Mixed State Boson Star can be seen as a collection of complex scalar fields, one for each state, coupled only through gravity. The different composition of ground and excited states could explain why the galaxy halos have so different masses and sizes, and could allow a more accurate fit of the rotational curves of the stars in galaxies [33].

Some of the major topics in the field of Numerical Relativity are the development and improvement of numerical methods, boundary conditions and gauge choices that allow long and accurate numerical evolutions. The current studies are modeling real astrophysical situations and allow extraction of gravitational wave templates.

1.1   Thesis Organization

This thesis is organized in six parts: introduction in the field of Numerical Relativity, an analytical and numerical comparison to 3+1 formulations of the Einstein

equations, the development of numerical methods employed in relativistic simulations and their application in the numerical study of black holes and boson stars, the choice of gauge conditions for black hole evolutions, concluding remarks and an appendix. The description of the subsequent chapters proceeds as follows:

- The first chapter offers a brief overview on some current topics in the field of Numerical Relativity and sets the conventions that will be used throughout the thesis.

- The second chapter contains general notions of differential geometry, with the purpose of setting the notation and conventions for the basic mathematical objects that are used in this thesis. The basic steps of a 3+1 decomposition of Einstein's field equations and the main ideas of the theory of well-posed evolution systems are briefly pointed out.

- The third chapter deals with 3+1 formulations of the Einstein equations. We present three systems based on the metric (Z3, Z4 and BSSN) and one on the tetrad formalism (Friedrich-Nagy), followed by a brief comparison of the systems at an analytical level.

- The fourth chapter is based on the Apples with Apples Alliance (AwA) tests, the first community effort to produce cross-validation in Numerical Relativity. We are focusing on numerical results obtained with the Kranc implementations of the Z4, BSSN and FN systems. A detailed analysis of the behavior of these systems is performed, marking the weak points and proposing improvements.

- The fifth chapter concerns new techniques currently used in Numerical Relativity in order to solve the discretized Einstein equations. We present a new centered finite volume algorithm based on the flux splitting approach. This algorithm is the first one in the class of finite volume methods which allows third order accuracy by only piece-wise linear reconstruction. In the variant without limiters, the centered finite volume method leads to an adaptive dissipation algorithm, which can be used in combination with the standard finite difference methods.

- The sixth chapter presents numerical evolutions of black hole spacetimes. The techniques for dealing with the singularity, steep gradients and apparent horizon locations are discussed in the context of a single Schwarzschild black hole, in both spherically symmetric and full 3D simulations. We present a comparison between our centered finite volume method and the standard finite difference plus dissipation techniques, when dealing with steep gradients in normal coordinates. We perform evolutions using the '1+log' slicing and develop a geometrical picture of the approach to the stationary state, for both scalar field stuffing and puncture techniques. Our

3D numerical results based on the Z4 system, show the first long term simulation of a Schwarzschild black hole in normal coordinates without excision.

- The seventh chapter is focused on boson stars, as models for dark matter. We present evolutions performed with the Einstein-Klein-Gordon system, using as initial data several complex scalar fields, following the classical approximation. The study is focused on two models. In the first one, we add a massless scalar field perturbation to a model of ground configuration and follow the evolution in order to see the effect of the perturbation on the stability of the configuration. In the second one, we perform the first general relativistic study of Mixed State Boson Stars evolutions. Using perturbations, we identify the unstable models and find a criteria of separation between stable and unstable configurations.

- The eighth chapter refers to time coordinate (lapse) conditions and related instabilities. Our investigation is focused on a singularity avoiding slicing condition currently used in binary black hole evolutions, namely the '1+log' slicing. We follow the behavior of the slicing in evolutions of Schwarzschild spacetime and perform a detailed study of the pathologies which can arise from two models: perturbing the initial slice and perturbing the initial lapse. A comparison with the results available in the literature allows us to identify most instabilities and propose a cure.

- The ninth chapter concentrates on the choice of space coordinate conditions (shift) well suited for black hole evolutions. We develop a generalized Almost Killing Equation (AKE), based on considerations of approximative symmetries in the spacetime. We show that the 3-covariant AKE shift equation can be used in combination with any slicing condition, without loosing its quasi-stationary properties. Our numerical tests address harmonic and black hole spacetimes.

- The tenth chapter contains concluding remarks.

The Appendix presents a summary of numerical methods and the explicit form of Einstein evolution systems employed in this thesis.

1.2 Conventions

Throughout this thesis, we are using the system of *geometric units*, where the speed of light c and Newton's gravitational constant G are set equal to one, so they will be omitted from the formulas. All quantities will be given a dimension of a power of length. In order to recover the standard SI units, one has to multiply the quantity with the corresponding powers of c and G. The conversion factor for a quantity with dimension of time is c (e.g. $t \to ct$), while for a quantity with dimension of mass is G/c^2.

All physical quantities will be measured in meters, for example a meter of time being equal to the time it takes light to travel one meter (around 3×10^{-6} meters). A meter of mass is defined as the mass of a point particle that in Newton's theory has an escape velocity equal to the speed of light at a distance of two meters.

Our unit of length will be the mass of the system. For example in a black hole simulation, the time and distance will be measured in units of M, where M is the mass of the black hole.

The covariant derivative of a quantity Q is noted as: $\nabla_\mu Q$ and the partial derivate: $\partial Q / \partial x^\mu = \partial_\mu Q$.

The following conventions are considered throughout the thesis:

- Lorentzian signature of space-time:

$$(-, +, +, +);$$

- Definition of the Riemann tensor:

$$(\nabla_a \nabla_b - \nabla_b \nabla_a) v_c = R_{abc}{}^d v_d;$$

- The 3D Ricci tensor:

$$R_{ij} = \partial_k \Gamma^k{}_{ij} - \partial_i \Gamma^k{}_{kj} + \Gamma^k{}_{kr} \Gamma^r{}_{ij} - \Gamma^k{}_{ri} \Gamma^r{}_{kj};$$

- The commutator:

$$\nabla_{(a} \nabla_{b)} = \frac{1}{2} (\nabla_b \nabla_a + \nabla_a \nabla_b);$$

- The anti-commutator:

$$\nabla_{[a} \nabla_{b]} = \frac{1}{2} (\nabla_b \nabla_a - \nabla_a \nabla_b);$$

$$\nabla_{[a} \nabla_{|b|} \nabla_{c]} = \frac{1}{2} (\nabla_c \nabla_b \nabla_a - \nabla_a \nabla_b \nabla_c);$$

- The L_2-norm:

$$\|\boldsymbol{u}\| = \sqrt{\sum_m |\boldsymbol{u}_m|^2};$$

Indices notation:

- four dimensional indices (Greek alphabet):

$$\mu, \nu, \tau, \rho, ... = 0, 1, 2, 3;$$

- three dimensional indices (Latin alphabet):

$$a, b, c, d, ... = 1, 2, 3;$$

- three dimensional indices:

$$a', b', c'... = 0, 1, 2;$$

- two dimensional indices:

$$a'', b'', c''... = 1, 2;$$

Einstein's summation rule applies, namely repeated indices are summed over all their possible values.

Chapter 2

General Concepts in Relativity

In this chapter, we briefly present the basic mathematical objects that occur in the geometrical constructions of the theory of General Relativity (just for fixing the notation and nomenclature).

2.1 Geometrical Concepts

In General Relativity the space of physical events is described by a real smooth D-dimensional manifold M_D with local coordinates x^μ, provided with smooth vector fields and linear forms in the local coordinate system, as well as other geometrical objects such as tensors and a connection.

2.1.1 Notions of Local Differential Geometry

Differential geometry is based on the notion of a differential manifold, a continuous and smooth space of n dimensions. A *manifold M* is a space that can be covered by a collection of charts (one-to-one mappings from R^n to M).

The *curve $x^\alpha = x^\alpha(\lambda)$* in terms of a set of coordinates x^α, is defined as a function from a segment of the real line into the manifold. *Vectors* are derivative operators along a given curve. At each point, D linearly independent vectors form a linear space, called the *tangent space* of M_D. One usually chooses as a *coordinate basis* those vectors that are tangent to the coordinate lines.

A *one-form* is a linear, real-valued function of one vector. Also called *covectors*, they form a vector space of the same dimension as the manifold, named the *dual tangent space*. One can introduce two independent fundamental structural objects on a manifold.

The distance ds between two infinitesimally close points on M_D, corresponding to the temporal and spatial distances, is calculated from the the *metric tensor* $g_{\mu\nu}$ as:

$$ds^2 = g_{\mu\nu}dx^\mu dx^\nu.$$

The metric, also known as the first fundamental form, is a symmetric tensor field $g_{\mu\nu} = g_{(\mu\nu)}$ with $D(D+1)/2$ components, called Riemannian if its eigenvalues are positive (negative) definite, and Lorentzian if its signature is $\pm(D-2)$.

I will consider in the following space-times of dimension $D = 4$, with symmetric and Lorentzian metric (signature $sig(g) = 2$). The metric is non-degenerate, namely its components form an invertible matrix $g^{\mu\nu}g_{\nu\tau} = \delta^\mu{}_\tau$.

The metric tensor defines the scalar product between two vectors as

$$g(\vec{v}, \vec{u}) = \vec{v}\,\vec{u} = g_{\mu\nu}v^\mu u^\nu,$$

and a one-to-one mapping between vectors and one-forms:

$$v_\mu = g_{\mu\nu}v^\nu.$$

Two vectors are orthogonal if their scalar product vanishes.

Considering a timelike unit vector $\vec{n}$, the projection operator onto a local tangent space orthogonal to $\vec{n}$ is defined as

$$P_\mu{}^\nu = \delta_\mu{}^\nu + n_\mu n^\nu.$$

The *Lie derivative*,

$$\mathcal{L}_{\vec{v}}\vec{u} = [\vec{v}, \vec{u}],$$

with $[\vec{v}, \vec{u}]^\mu = v^\nu\partial_\nu u^\mu - u^\nu\partial_\nu u^\mu$, can be interpreted as a way to write partial derivatives along the direction of a given vector field, in a way that is independent of the coordinates. If a manifold has a specific symmetry, then the metric is invariant under Lie dragging with respect to a vector field $\vec{\xi}$, called *Killing field*,

$$\mathcal{L}_{\vec{\xi}}g = 0.$$

The second structure that can be introduced is the linear connection, a device for establishing a comparison of vectors in different points of the manifold. This *covariant derivative* operator ∇ must be linear, obey the Leibnitz rule for the derivative of a product and it must reduce to the standard partial derivative for scalar functions. A manifold with only one linear connection is called affine space. A manifold carrying both metric and connection is called metric affine space. A connection for which the metricity condition holds, namely the scalar product of two vectors is preserved under parallel transport

$$\nabla_\rho g_{\mu\nu} = 0,$$

is called metric-compatible.

The Riemannian geometry is a subclass with vanishing torsion of a metric-affine geometry with metric-compatible connection [34]. For any vector fields X^μ, Y^ν, the torsion tensor can be defined as

$$T^\rho{}_{\mu\nu} X^\mu Y^\nu = X^\mu \nabla_\mu Y^\rho - Y^\mu \nabla_\mu X^\rho - [X,Y]^\rho. \tag{2.1}$$

2.1.2 Spacetime Geometry

In the following, I will only consider the case of Riemannian geometry, for which one has two main conditions: the torsion-freeness, $T^\rho{}_{\mu\nu} = 0$, and the condition for the connection to be metric compatible, $\nabla_\rho g_{\mu\nu} = 0$. Then the connection is uniquely defined and it is called the Levi Civita connection,

$$\nabla_\mu g_{\nu\rho} = \partial_\mu g_{\nu\rho} - \Gamma^\alpha{}_{\mu\nu} g_{\alpha\rho} - \Gamma^\alpha{}_{\mu\rho} g_{\nu\alpha} = 0,$$

where $\Gamma^\alpha{}_{\mu\nu}$ is called *Christoffel symbol*. This symbol is symmetric in the last two indices

$$\Gamma^\mu{}_{\nu\rho} = \frac{1}{2} g^{\mu\tau} (\partial_\rho g_{\tau\nu} + \partial_\nu g_{\tau\rho} - \partial_\tau g_{\nu\rho}).$$

The torsion-free condition can be written in terms of the Christoffel symbols as

$$T^\mu{}_{\nu\rho} = \Gamma^\mu{}_{\rho\nu} - \Gamma^\mu{}_{\nu\rho} = 0. \tag{2.2}$$

The *Riemann curvature tensor* arises because the covariant derivative is not commutative, which can be interpreted as the failure of a global notion of parallelism in curved space. This tensor is defined through its action on an arbitrary covector v_μ:

$$(\nabla_\mu \nabla_\nu - \nabla_\nu \nabla_\mu) v_\rho = R_{\mu\nu\rho}{}^\tau v_\tau.$$

The relation leads to the following symmetry $R_{\mu\nu\rho}{}^\tau = -R_{\nu\mu\rho}{}^\tau$. Applying this definition to the metric tensor

$$0 = (\nabla_\mu \nabla_\nu - \nabla_\nu \nabla_\mu) g_{\rho\tau} = R_{\mu\nu\rho}{}^\alpha g_{\alpha\tau} + R_{\mu\nu\tau}{}^\alpha g_{\rho\alpha} = R_{\mu\nu\rho\tau} + R_{\mu\nu\tau\rho},$$

one notes another symmetry $R_{\mu\nu\rho\tau} = -R_{\mu\nu\tau\rho}$.

A relation between the Riemann tensor and the connection can be derived using the torsion-free condition Eq. (2.2),

$$R^\mu{}_{\nu\rho\tau} = \partial_\rho \Gamma^\mu{}_{\tau\nu} - \partial_\tau \Gamma^\mu{}_{\rho\nu} + \Gamma^\mu{}_{\rho\alpha} \Gamma^\alpha{}_{\tau\nu} - \Gamma^\mu{}_{\tau\alpha} \Gamma^\alpha{}_{\rho\nu}. \tag{2.3}$$

Writing the definition of the Riemann tensor in three cases

$$
\begin{aligned}
(\nabla_\mu \nabla_\nu - \nabla_\nu \nabla_\mu) v_\rho &= R_{\mu\nu\rho}{}^\tau v_\tau, \\
(\nabla_\rho \nabla_\mu - \nabla_\mu \nabla_\rho) v_\nu &= R_{\rho\mu\nu}{}^\tau v_\tau, \\
(\nabla_\nu \nabla_\rho - \nabla_\rho \nabla_\nu) v_\mu &= R_{\nu\rho\mu}{}^\tau v_\tau,
\end{aligned}
$$

one obtains

$$\nabla_{[\mu}\nabla_{\nu}v_{\rho]} = -\frac{1}{2}R_{[\mu\nu\rho]}{}^{\tau}v_{\tau},$$

which leads to $R_{[\mu\nu\rho]}{}^{\tau} = 0$. From this relation and the two symmetries of the Riemann tensor, it follows that the tensor also satisfies the symmetry property $R_{\mu\nu\rho\tau} = R_{\rho\tau\mu\nu}$.

Considering the definitions for the Riemann tensor written as

$$2\nabla_{[\mu}\nabla_{\nu]}\nabla_{\rho}v^{\tau} = -R_{\mu\nu\rho}{}^{\beta}\nabla_{\beta}v^{\tau} + R_{\mu\nu\alpha}{}^{\tau}\nabla_{\rho}v^{\alpha},$$
$$2\nabla_{[\mu}\nabla_{\nu}\nabla_{\rho]}v^{\tau} = R_{[\mu\nu|\alpha|}{}^{\tau}\nabla_{\rho]}v^{\alpha}$$

and comparing with

$$2\nabla_{\mu}\nabla_{[\nu}\nabla_{\rho]}v^{\tau} = v^{\alpha}\nabla_{\mu}R_{\nu\rho\alpha}{}^{\tau} + R_{\nu\rho\alpha}{}^{\tau}\nabla_{\mu}v^{\alpha},$$
$$2\nabla_{[\mu}\nabla_{\nu}\nabla_{\rho]}v^{\tau} = \nabla_{[\mu}R_{\nu\rho]\alpha}{}^{\tau}v^{\alpha} + R_{[\nu\rho|\alpha|}{}^{\tau}\nabla_{\mu]}v^{\alpha},$$

we obtain $\nabla_{[\mu}R_{\nu\rho]\alpha}{}^{\tau}v^{\alpha} = 0$. This relation is known as the *Bianchi identity*

$$\nabla_{\mu}R_{\nu\rho\tau\alpha} + \nabla_{\nu}R_{\rho\mu\tau\alpha} + \nabla_{\rho}R_{\mu\nu\tau\alpha} = 0. \tag{2.4}$$

Contracting it with $g^{\mu\tau}g^{\rho\alpha}$ and using the metricity condition, we arrive at

$$\nabla^{\mu}R_{\mu\nu} - \frac{1}{2}\nabla_{\nu}R = 0, \tag{2.5}$$

where the *Ricci curvature tensor* is defined as trace of the Riemann tensor over the second and the forth (or equivalently, the first and the third) indices $R_{\mu\nu} = R_{\mu\rho\nu}{}^{\rho}$. The trace of the Ricci tensor $R = R_{\mu\nu}g^{\mu\nu}$ is the *Ricci scalar curvature*.

2.1.3   The Field Equations

Defining the *Einstein tensor* as

$$G_{\mu\nu} = R_{\mu\nu} - \frac{1}{2}Rg_{\mu\nu}, \tag{2.6}$$

the contracted Bianchi identity leads to

$$\nabla_{\mu}G^{\mu\nu} = 0. \tag{2.7}$$

This is a convenient form of writing the field equations in vacuum.

In cases where matter is considered, one needs to include the conservation laws of energy and momentum in differential form

$$\nabla_{\mu}T^{\mu\nu} = 0, \tag{2.8}$$

where $T_{\mu\nu}$ is the *energy-momentum* tensor, with the following components: T^{00} energy density, T^{0i} momentum density, T^{ij} stress tensor.

The Einstein equations which govern General Relativity, express the relation between the spacetime geometry and the matter content

$$G_{\mu\nu} = \kappa T_{\mu\nu},\qquad(2.9)$$

where the factor $\kappa = 8\pi$ is derived from the Newtonian gravitational limit, calculated in geometric units.

One can picture the Einstein equations as a set of differential equations that one must solve for the spacetime metric, once the energy content of the spacetime is known. Then the resulting deformed geometry will determine the movement of the energy content. In this view, Eq. (2.9) can be equivalently written as

$$R_{\mu\nu} = 8\pi(T_{\mu\nu} - \frac{1}{2}T_\rho{}^\rho g_{\mu\nu}).$$

Allowing for Eq. (2.3), we can express the relation in terms of the connection coefficients

$$\partial_\nu\Gamma^\nu{}_{\mu\rho} - \partial_\mu\Gamma^\nu{}_{\nu\rho} + \Gamma^\tau{}_{\mu\rho}\Gamma^\nu{}_{\nu\tau} - \Gamma^\tau{}_{\nu\rho}\Gamma^\nu{}_{\mu\tau} = 8\pi(T_{\mu\nu} - \frac{1}{2}T_\rho{}^\rho g_{\mu\nu}).\qquad(2.10)$$

The Bianchi identity Eq. (2.5) can also be written as

$$\nabla_0(G^{0\mu} - 8\pi T^{0\mu}) + \nabla_k(G^{k\mu} - 8\pi T^{k\mu}) = 0,$$

where the four Einstein equations

$$G^{0\mu} = 8\pi T^{0\mu},$$

are first integrals of the system, so they get preserved forever provided that the other 6 equations hold true everywhere. This means that only 6 of the 10 Einstein equations are independent, and one can not determine all the metric coefficients. The 4 missing equations correspond to a choice of the coordinate system and they are provided by the *gauge conditions*. This freedom corresponds to the fact that the equations are invariant under general coordinate transformations, namely their physical meaning does not change when we adopt different coordinate systems.

The Einstein equations take only an apparently simple form, as they are a system of coupled non-linear second order partial differential equations, with thousands of terms when expanded in an arbitrary coordinate system. They describe the evolution of the spacetime geometry and the matter content. Einstein's theory describes the way in which the gravitational field propagates in space. Assuming that perturbations propagate as a wave, it predicts the existence of gravitational waves which travel at the speed of light.

2.1.4   Elements of 3+1 Decomposition

The Einstein equations presented in the previous section make no distinction between space and time, as they are written in a 4-covariant form. In order to obtain a more intuitive picture, one can write them as the evolution of the gravitational field in time, starting from a specific initial data. There are several approaches in this direction, namely the 3+1 formulations (which include the harmonic systems), the characteristic and conformal formalisms. I will present in the following the 3+1 approach, which is most commonly used in numerical relativity.

The 3+1 approach consists in foliating the space-time into a one-parameter family of space-like hypersurfaces. The successive hypersurfaces, on which one gives the geometry, are most conveniently described by successive values of a time parameter t. This decomposition is convenient for the systems that one wants to evolve numerically, as the analysis of the dynamics along the evolution can be done directly on the system variables, which have physical meaning.

We choose coordinates adapted to the 3+1 split, that denote the lower (earlier) hypersurface of $\{t = constant\}$ and the upper (later) hypersurface of $\{t + dt = constant\}$. The data set necessary for this construction is:

- the metric of the 3-geometry on the lower hypersurface

$$h_{ij}(t, x, y, z)dx^i dx^j,$$

  that measures the distance between two points in that hypersurface;

- the metric on the upper hypersurface

$$h_{ij}(t + dt, x, y, z)dx^i dx^j;$$

- the lapse of proper time between the lower and the upper hypersurfaces measured by the observers moving along the normal direction to the hypersurfaces

$$d\tau = \alpha(t, x, y, z)dt;$$

- a formula that connects an event on the upper hypersurface with its corresponding event on the lower hypersurface

$$x^i_{upper} = x^i_{lower} - \beta^i(t, x, y, z)dt,$$

  where α is the lapse function and β^i denotes the shift vector.

The lapse and shift account for the gauge conditions. They are not unique and must be specified in a numerical evolution, as α fixes the foliation of the spacetime, and β^i the way in which spatial coordinate system propagates from one hypersurface to the next.

The proper distance between $x^\mu = (t, x^i)$ and $x^\mu + dx^\mu = (t + dt, x^i + dx^i)$ is given by

$$ds^2 = -(\alpha dt)^2 + h_{ij}(dx^i + \beta^i dt)(dx^j + \beta^j dt).$$

More explicitly, writing the general formula for the 4-metric as

$$ds^2 = g_{\mu\nu}dx^\mu dx^\nu,$$

one obtains the following components:

$$g_{00} = (\beta_j\beta^j - \alpha^2), \qquad\qquad g^{00} = -1/\alpha^2,$$
$$g_{0i} = \beta_i, \qquad\qquad g^{0j} = \beta^j/\alpha^2,$$
$$g_{j0} = \beta_j, \qquad\qquad g^{i0} = \beta^i/\alpha^2,$$
$$g_{ij} = h_{ij}, \qquad\qquad g^{ji} = h^{ji} - \beta^i\beta^j/\alpha^2,$$

where $g_{\mu\nu}g^{\nu\tau} = \delta_\mu{}^\tau$.

One can consider a time-like unit vector n_μ normal to the 3-hypersurfaces of $\{t = constant\}$ in the 4-geometry. Performing the decomposition with respect to this vector is convenient, as one can introduce the 3+1 quantities in a way that is independent of the coordinate system. The vector is normalized as $n^\mu n_\mu = -1$.

The hypersurfaces of $\{t = constant\}$ can be locally described by a one-form

$$\Omega_\mu = \nabla_\mu t,$$

normalized as

$$g^{\mu\nu}\Omega_\mu\Omega_\nu = -\frac{1}{\alpha^2}.$$

Then the unit normal to the hypersurface can be written

$$n_\mu = \alpha\Omega_\mu = \alpha\nabla_\mu t.$$

One can consider a future pointing vector field ξ^μ that is not tangent to the spatial hypersurfaces, namely satisfies the condition

$$\xi^\mu\nabla_\mu t = 1.$$

This represents the flow of time through spacetime, as it is the tangent vector to the time lines (lines of constant spatial coordinates). Decomposing it into parts normal and tangential to the 3-hypersurfaces, one finds that the lapse function, the shift vector and the unit normal can be written in terms of the time flow as

$$\alpha = \xi^\mu n_\mu = -(n^\mu\nabla_\mu t)^{-1},$$
$$\beta_\mu = h_{\mu\nu}\xi^\nu,$$
$$n^\mu = -\frac{1}{\alpha}(\xi^\mu - \beta^\mu),$$

where $h_{\mu\nu}$ is the spatial metric.

The lapse, shift and 3-metric determine the components of the unit normal in covariant $n_\mu = (\alpha, 0, 0, 0)$ and contravariant form $n^\mu = (-1/\alpha, \beta^i/\alpha)$.

A useful relation is writing the acceleration in terms of the lapse function as

$$a_\mu = D_\mu ln\alpha. \tag{2.11}$$

This equality is proved in the following

$$
\begin{aligned}
a_\mu &= n^\rho \nabla_\rho n_\mu = \alpha \Omega^\rho \nabla_\rho (\alpha \Omega_\mu) = \alpha \Omega^\rho (\nabla_\rho \alpha) \Omega_\mu + \alpha^2 \nabla^\rho t (\nabla_\rho \nabla_\mu t) \\
&= \alpha \Omega^\rho (\nabla_\rho \alpha) \Omega_\mu + \frac{1}{2} \alpha^2 \nabla_\mu (\nabla_\rho t \nabla^\rho t) = \alpha \Omega^\rho (\nabla_\rho \alpha) \Omega_\mu + \alpha^{-1} \nabla_\mu \alpha
\end{aligned}
$$

and

$$D_\mu \ln \alpha = h^\rho{}_\mu \nabla_\rho \ln \alpha = (\delta^\rho{}_\mu + n^\rho n_\mu)(\alpha^{-1} \nabla_\rho \alpha) = \alpha^{-1} \nabla_\mu \alpha + \alpha \Omega^\rho (\nabla_\rho \alpha) \Omega_\mu.$$

One has now all the ingredients for performing a 3+1 decomposition of various space-time tensors into "spatial" and "temporal" parts. In the following, I will present a summary of the main geometrical objects and the equations used in the 3+1 numerical evolutions of the Einstein equations.

2.2 The 3+1 Form of the Einstein Equations

2.2.1 Basic Geometrical Objects

We consider a 4-dimensional Lorentzian manifold (M, g) and a time-like unit vector field n_μ (with $n^\mu n_\mu = -1$), in respect to which the reduction will be done. Any vector S from the tangential space can be decomposed in parts perpendicular and parallel to n as follows

$$S^\mu = \tilde{S}^\mu - n^\mu S,$$

where by $\tilde{S}^\mu$ we denote the spatial part of the vector, with $\tilde{S}^\mu n_\mu = 0$, and by $S = S^\mu n_\mu$ the temporal part. We will refer to the vectors as "spatial" if they are orthogonal, or "temporal" if they are parallel in respect to n.

The decomposition of the 4-metric gives rise to a spatial metric $h_{\mu\nu}$,

$$g_{\mu\nu} = h_{\mu\nu} - n_\mu n_\nu,$$

where the "$-$" sign follows from the signature $(-, +, +, +)$ on the spacetime. For simplicity reasons, we will restrict the following calculations to normal coordinates ($g_{0i} = 0$) and consider n to be hypersurface orthogonal.

The spatial part of the tensors can be obtained by applying the space projector

$$
\begin{aligned}
h_\mu{}^\nu h_\nu{}^\rho &= h_\mu{}^\rho, \\
h^\mu{}_\rho &= \delta^\mu{}_\rho + n^\mu n_\rho,
\end{aligned}
$$

to every free tensor index. By construction we have $n^\mu h_\mu{}^\nu = 0$.

The decomposition of the derivative of the unit normal described by

$$\nabla_\nu n_\rho = \tilde{D}_\nu n_\rho - n_\nu D n_\rho,$$

defines two derivative operators, that were denoted as $\tilde{D}_\mu = h_\mu{}^\nu \nabla_\nu$ and $D = n^\nu \nabla_\nu$. One can write the natural derivative operator for spatial tensors as

$$
\begin{aligned}
h^\nu{}_\alpha h^\rho{}_\delta \tilde{D}_\mu h_{\nu\rho} = D_\mu h_{\alpha\delta} &= h^\nu{}_\alpha h^\rho{}_\delta h^\tau{}_\mu \nabla_\tau (g_{\nu\rho} + n_\nu n_\rho) = \\
&= h^\nu{}_\alpha h^\rho{}_\delta h^\tau{}_\mu (n_\nu \nabla_\tau n_\rho + n_\rho \nabla_\tau n_\nu) = \\
&= h^\nu{}_\alpha h^\rho{}_\delta (n_\nu K_{\mu\rho} + n_\rho K_{\mu\nu}) = 0,
\end{aligned}
$$

where D_μ is compatible with the spatial metric, so it is the unique derivative operator associated with $h_{\mu\nu}$.

The hypersurface orthogonal part defines the 4-acceleration

$$a_\rho = D n_\rho,$$

while the hypersurface tangential part defines the extrinsic curvature of the 3-geometry

$$K_{\nu\rho} = \tilde{D}_\nu n_\rho, \tag{2.12}$$

which accounts for the change of the normal vector $\vec{n}$, when it is parallel transported from one point of the hypersurface to the other. The concept of extrinsic curvature exists in the context of a 3-geometry embedded as a well-defined slice in a well-defined spacetime and measures the curvature of the slice relative to the enveloping 4-geometry.

The extrinsic curvature, also called the second fundamental form, is a symmetric tensor. This can be proved starting from Frobenius's theorem which states that the necessary and sufficient condition for n_μ to be hypersurface orthogonal is

$$n_{[\mu} \nabla_\nu n_{\rho]} = 0,$$

that projected with $h^{\mu\alpha} h^{\nu\delta}$ leads to

$$
\begin{aligned}
h^{\mu\alpha} h^{\nu\delta} n_\rho \nabla_\mu n_\nu - h^{\mu\alpha} h^{\nu\delta} n_\rho \nabla_\nu n_\mu &= 0, \\
h^{\nu\delta} K^\alpha{}_\nu - h^{\mu\alpha} K^\delta{}_\mu &= 0, \\
K^{\alpha\delta} &= K^{\delta\alpha}.
\end{aligned}
$$

2.2.2 Evolution Equations

Considering the definition of the extrinsic curvature Eq. (2.12), the spatial components of the identity

$$\mathcal{L}_{\vec{n}} g_{\mu\nu} = \nabla_\mu n_\nu + \nabla_\nu n_\mu,$$

allow us to write the second fundamental form as the Lie derivative of the metric in the direction of the unit normal

$$K_{ij} = \frac{1}{2}\mathcal{L}_{\vec{n}}h_{ij}.$$

Then K_{ij} can be interpreted as the variation of the induced metric h_{ij} in the space-time manifold. This provides an evolution equation for the spatial metric

$$\partial_t h_{ij} = -2\alpha K_{ij}. \tag{2.13}$$

An evolution equation for the extrinsic curvature can be obtained from the following projections of the Riemann tensor

$$h_\delta{}^\mu n^\nu h_\gamma{}^\rho R_{\mu\nu\rho}{}^\tau n_\tau = n^\nu h_\delta{}^\mu h_\gamma{}^\rho [(\nabla_\mu\nabla_\nu - \nabla_\nu\nabla_\mu)n_\rho],$$

where the first term in the right side of the equality is computed as

$$\begin{aligned}
n^\nu h_\delta{}^\mu h_\gamma{}^\rho [\nabla_\mu\nabla_\nu n_\rho] &= \\
&= h_\delta{}^\mu h_\gamma{}^\lambda \nabla_\mu [h_\lambda{}^\rho n^\nu \nabla_\nu n_\rho] - h_\delta{}^\mu h_\gamma{}^\lambda [\nabla_\nu n_\rho][\nabla_\mu (n^\nu h_\lambda{}^\rho)] = \\
&= h_\delta{}^\mu h_\gamma{}^\lambda \nabla_\mu a_\lambda - h_\delta{}^\mu h_\gamma{}^\lambda [\nabla_\nu n_\rho][h_\lambda{}^\rho \nabla_\mu n^\nu - n^\nu \nabla_\mu (n_\lambda n^\rho)] = \\
&= D_\delta a_\gamma - K_\delta{}^\alpha K_{\alpha\gamma},
\end{aligned}$$

and the second term leads to

$$\begin{aligned}
n^\nu h_\delta{}^\mu h_\gamma{}^\rho [\nabla_\nu\nabla_\mu n_\rho] &= \\
&= n^\nu h_\delta{}^\chi h_\gamma{}^\lambda \nabla_\nu [h_\chi{}^\mu h_\lambda{}^\rho \nabla_\mu n_\rho] - n^\nu h_\delta{}^\chi h_\gamma{}^\lambda [\nabla_\mu n_\rho][\nabla_\nu (h_\chi{}^\mu h_\lambda{}^\rho)] = \\
&= n^\nu h_\delta{}^\chi h_\gamma{}^\lambda \nabla_\nu K_{\chi\lambda} - n^\nu h_\delta{}^\chi h_\gamma{}^\lambda [\nabla_\mu n_\rho][h_\chi{}^\mu \nabla_\nu (n_\lambda n^\rho) + h_\lambda{}^\rho \nabla_\nu (n_\chi n^\mu)] = \\
&= n^\nu h_\delta{}^\chi h_\gamma{}^\lambda \nabla_\nu K_{\chi\lambda} + a_\gamma a_\delta.
\end{aligned}$$

From the above relations symmetrized, one obtains

$$h_\delta{}^\chi h_\gamma{}^\lambda n^\nu \nabla_\nu K_{\chi\lambda} + D_\delta a_\gamma + K_\delta{}^\alpha K_{\alpha\gamma} = h_\delta{}^\mu n^\nu h_\gamma{}^\rho R_{\mu\nu\rho}{}^\tau n_\tau.$$

Using the Eq. (2.11) in order to replace the acceleration, one finds

$$\partial_t K_{\delta\gamma} = -D_\delta D_\gamma \alpha + \alpha(-K_{\rho\delta}K_\gamma{}^\rho + h_\delta{}^\mu n^\nu h_\gamma{}^\rho R_{\mu\nu\rho}{}^\tau n_\tau). \tag{2.14}$$

2.2.3 Constraint Equations

The intrinsic curvature of the hypersurfaces, given by the spatial Riemann tensor $\mathcal{R}_{\mu\nu\rho}{}^\tau$, describes the internal geometry and depends on the 3-metric. Considering the 4-dimensional Riemann curvature tensor defined through its action on an arbitrary spatial vector S_μ

$$(\nabla_\mu\nabla_\nu - \nabla_\nu\nabla_\mu)S_\rho = R_{\mu\nu\rho}{}^\tau S_\tau,$$

the intrinsic curvature of the three-dimensional hypersurfaces can be defined as

$$(D_\mu D_\nu - D_\nu D_\mu)S_\rho = \mathcal{R}_{\mu\nu\rho}{}^\tau S_\tau.$$

One can calculate the following projection of the 4-Riemann

$$h_\alpha{}^\mu h_\xi{}^\nu h_\gamma{}^\rho R_{\mu\nu\rho}{}^\tau S_\tau = h_\alpha{}^\mu h_\xi{}^\nu h_\gamma{}^\rho (\nabla_\mu \nabla_\nu - \nabla_\nu \nabla_\mu)S_\rho,$$

where the first term in the right side of the equality can be written as

$$
\begin{aligned}
h_\alpha{}^\mu h_\xi{}^\nu h_\gamma{}^\rho \nabla_\mu \nabla_\nu S_\rho & = \\
& = h_\alpha{}^\mu h_\xi{}^\delta h_\gamma{}^\lambda \nabla_\mu (h_\delta{}^\nu h_\lambda{}^\rho \nabla_\nu S_\rho) - h_\alpha{}^\mu h_\xi{}^\delta h_\gamma{}^\lambda (\nabla_\nu S_\rho)[\nabla_\mu (h_\delta{}^\nu h_\lambda{}^\rho)] = \\
& = D_\alpha D_\xi S_\gamma - h_\alpha{}^\mu h_\xi{}^\delta h_\gamma{}^\lambda (\nabla_\nu S_\rho)[h_\lambda{}^\rho \nabla_\mu (n_\delta n^\nu) + h_\delta{}^\nu \nabla_\mu (n_\lambda n^\rho)] = \\
& = D_\alpha D_\xi S_\gamma - K_{\alpha\xi} h_\gamma{}^\rho D S_\rho + K_{\alpha\gamma} K_\xi{}^\rho S_\rho,
\end{aligned}
$$

and a similar calculation for the second term leads to

$$
\begin{aligned}
h_\alpha{}^\mu h_\xi{}^\nu h_\gamma{}^\rho \nabla_\nu \nabla_\mu S_\rho & = \\
& = h_\xi{}^\nu h_\alpha{}^\delta h_\gamma{}^\lambda \nabla_\nu (h_\delta{}^\mu h_\lambda{}^\rho \nabla_\mu S_\rho) - h_\xi{}^\nu h_\alpha{}^\delta h_\gamma{}^\lambda (\nabla_\mu S_\rho)[\nabla_\nu (h_\delta{}^\mu h_\lambda{}^\rho)] = \\
& = D_\xi D_\alpha S_\gamma - h_\xi{}^\nu h_\alpha{}^\delta h_\gamma{}^\lambda (\nabla_\mu S_\rho)[h_\lambda{}^\rho \nabla_\nu (n_\delta n^\mu) + h_\delta{}^\mu \nabla_\nu (n_\lambda n^\rho)] = \\
& = D_\xi D_\alpha S_\gamma - K_{\xi\alpha} h_\gamma{}^\rho D S_\rho + K_{\xi\gamma} K_\alpha{}^\rho S_\rho.
\end{aligned}
$$

So one obtains a first projection of the Riemann tensor

$$h_\alpha{}^\mu h_\xi{}^\nu h_\gamma{}^\rho h_\delta{}^\tau R_{\mu\nu\rho\tau} = \mathcal{R}_{\alpha\xi\gamma\delta} + K_{\alpha\gamma} K_{\xi\delta} - K_{\xi\gamma} K_{\alpha\delta}. \tag{2.15}$$

The evolution equation of the extrinsic curvature Eq. (2.14), can be rewritten using the equation above as

$$\partial_t K_{ij} = -D_i D_j \alpha + \alpha(\mathcal{R}_{ij} + K K_{ij} - 2 K_{ip} K_j{}^p). \tag{2.16}$$

One can consider as a second projection, the equation

$$h_\alpha{}^\mu h_\delta{}^\nu h_\gamma{}^\rho R_{\mu\nu\rho}{}^\tau n_\tau = h_\alpha{}^\mu h_\delta{}^\nu h_\gamma{}^\rho (\nabla_\mu \nabla_\nu - \nabla_\nu \nabla_\mu)n_\rho,$$

where the first term can written as

$$
\begin{aligned}
h_\alpha{}^\mu h_\delta{}^\nu h_\gamma{}^\rho \nabla_\mu \nabla_\nu n_\rho & = \\
& = h_\alpha{}^\mu h_\delta{}^\xi h_\gamma{}^\rho \nabla_\mu (h_\xi{}^\nu \nabla_\nu n_\rho) - h_\alpha{}^\mu h_\delta{}^\xi h_\gamma{}^\rho (\nabla_\nu n_\rho)(\nabla_\mu h_\xi{}^\nu) = \\
& = D_\alpha K_{\delta\gamma} - h_\alpha{}^\mu h_\delta{}^\xi h_\gamma{}^\rho (\nabla_\nu n_\rho)[\nabla_\mu (n_\xi n^\nu)] = \\
& = D_\alpha K_{\delta\gamma} - K_{\alpha\delta} a_\gamma,
\end{aligned}
$$

and a similar calculation for the second term leads to

$$
h_\alpha{}^\mu h_\delta{}^\nu h_\gamma{}^\rho \nabla_\nu \nabla_\mu n_\rho =
$$
$$
= h_\alpha{}^\xi h_\delta{}^\nu h_\gamma{}^\rho \nabla_\nu (h_\xi{}^\mu \nabla_\mu n_\rho) - h_\alpha{}^\xi h_\delta{}^\nu h_\gamma{}^\rho (\nabla_\mu n_\rho)(\nabla_\nu h_\xi{}^\mu) =
$$
$$
= D_\delta K_{\alpha\gamma} - h_\alpha{}^\xi h_\delta{}^\nu h_\gamma{}^\rho (\nabla_\mu n_\rho)[\nabla_\nu (n_\xi n^\mu)] =
$$
$$
= D_\delta K_{\alpha\gamma} - K_{\delta\alpha} a_\gamma .
$$

A second projection for the Riemann tensor is

$$
h_\alpha{}^\mu h_\delta{}^\nu h_\gamma{}^\rho R_{\mu\nu\rho}{}^\tau n_\tau = D_\alpha K_{\delta\gamma} - D_\delta K_{\alpha\gamma} . \tag{2.17}
$$

The Eqs. (2.15) and (2.17) are known as the Gauss-Codazzi equations. We will use them in the following, in order to compute the constraints.

Starting from the Einstein vacuum field equations Eq. (2.9), one can derive the Hamiltonian constraint as

$$
G_{\mu\rho} n^\mu n^\rho = 8\pi T_{\mu\rho} n^\mu n^\rho ,
$$
$$
n^\mu n^\rho \left(R_{\mu\rho} - \frac{1}{2} g_{\mu\rho} R \right) = 8\pi\tau ,
$$
$$
R_{\mu\rho}(n^\mu n^\rho + h^{\mu\rho}) = 16\pi\tau ,
$$
$$
R_{\mu\nu\rho\tau}(h^{\nu\tau} - n^\nu n^\tau)(n^\mu n^\rho + h^{\mu\rho}) = 16\pi\tau ,
$$
$$
h^{\mu\rho} h^{\nu\tau} R_{\mu\nu\rho\tau} = 16\pi\tau .
$$

Calculating double trace of the Gauss equation Eq. (2.15), we obtain

$$
\mathcal{R} + K^2 - K^\alpha{}_\xi K^\xi{}_\alpha = 16\pi\tau . \tag{2.18}
$$

The Momentum constraint can be derived from Eq. (2.9) as

$$
h_\delta{}^\mu G_{\mu\rho} n^\rho = h_\delta{}^\mu T_{\mu\rho} n^\rho ,
$$
$$
h_\delta{}^\mu n^\rho \left(R_{\mu\rho} - \frac{1}{2} g_{\mu\rho} R \right) = 8\pi S_\delta ,
$$
$$
h_\delta{}^\mu n^\rho R_{\mu\rho} = 8\pi S_\delta ,
$$
$$
h_\delta{}^\mu h^{\nu\tau} n^\rho R_{\nu\mu\tau\rho} = 8\pi S_\delta .
$$

Calculating the trace of the Codazzi equation Eq. (2.17), we obtain

$$
D^\alpha K_{\delta\alpha} - D_\delta K = 8\pi S_\delta . \tag{2.19}
$$

The decomposition of the matter terms as a result of splitting the stress energy tensor $T_{\mu\nu}$ into longitudinal and transversal parts, led to the following projections: the energy density,

$$
\tau = T_{\mu\nu} n^\mu n^\nu , \tag{2.20}
$$

the momentum density

$$S_\rho = T^\mu{}_\nu n_\mu h^\nu{}_\rho, \tag{2.21}$$

and the stress energy tensor,

$$S_{\nu\tau} = T_{\mu\nu} h^\mu{}_\rho h^\nu{}_\tau. \tag{2.22}$$

The Hamiltonian and Momentum constraints, Eqs. (2.18) and (2.19) with the matter terms included

$$\mathcal{R} + K^2 - K^p{}_q K^q{}_p - 16\pi\tau = 0, \tag{2.23}$$

$$D_p(K_i{}^p - \delta_i{}^p K) - 8\pi S_i = 0, \tag{2.24}$$

are constraint equations which must be satisfied by the fundamental variables h_{ij}, K_{ij} at all times (on all the slices) [35].

In numerical evolutions, one typically uses only the evolution equations (*free evolution* approach), and the constraints are monitored to assess the accuracy of the numerical solution. The constraints however, play a very important role in the construction of the initial data, as one can not freely specify all the components of the spatial metric and extrinsic curvature as initial conditions. The data must satisfy the constraints, initially and at later times, otherwise one is not solving the Einstein equations. The constraints are also important in the construction of well-posed systems of evolution equations, as described in Section 2.3.

2.2.4   Gauge Degrees of Freedom

The Einstein theory leaves four degrees of freedom undetermined, corresponding to the choice of the coordinate system. In order to obtain a full evolution system, one needs to complete it with equations for the lapse function α and the shift vector β^i. Ideally one should choose gauge conditions which simplify the evolution equations, or make the solution better behaved. There is no clear prescription for the appropriate gauge in general situations, so the choice of gauge will depend on the physical problem under study.

As the Chapters 8,9 are dedicated to various gauge choices and related problems, I will mention here briefly the most common prescriptions.

The most simple gauge choice is known as *geodesic* or *Gauss coordinates*, which translate into $\alpha = 1$, $\beta^i = 0$. It consists in choosing the time coordinate to coincide with the proper time of the Eulerian observers, who will have zero acceleration according to Eq. (2.11) and will follow timelike geodesics. This foliation proves to be unpractical in numerical simulations, as in a non-uniform gravitational field such observers will end up colliding, which amounts to the coordinate system becoming singular (one point has more than one set of coordinates associated to it).

The second natural choice would be to choose a slicing such that the volume elements associated with the Eulerian observers remain constant,

$$\partial_t \sqrt{h} = 0,$$

which according to Eq. (2.13) can be equivalently written as

$$K = \partial_t K = 0.$$

Then the lapse must satisfy an elliptic equation of the type

$$D_p D^p \alpha = \alpha[K_{pq} K^{pq} + 4\pi(\rho + trS)],$$

called *maximal slicing*. This gauge has two important advantages: singularity avoidance, as it does not allow the spatial hypersurfaces to come arbitrarily close to the singularity, and the fact that Eulerian observers will not focus. The big disadvantage of this slicing is that one has to solve an elliptic equation in 3D, which is a very slow computational process. The best option for the moment seem to be the hyperbolic slicing conditions.

Historically, the first prescriptions used were the harmonic coordinates

$$\Box x^\tau = g^{\mu\nu} \nabla_\mu \nabla_\nu x^\tau = 0,$$

which allow the Einstein equations to be written as wave equations for the metric components. This idea stands at the foundation of harmonic formulations of the field equations. Translated in adapted coordinates, the condition reads

$$\Gamma^\tau = g^{\mu\nu} \Gamma^\tau{}_{\mu\nu} = 0. \tag{2.25}$$

In 3+1 language, the $\tau = 0$ component leads to a *harmonic slicing*

$$(\partial_t - \mathcal{L}_\beta)\alpha = -\alpha^2 K, \tag{2.26}$$

while the $\tau = i$ component provides a prescription for the *harmonic shift*

$$(\partial_t - \mathcal{L}_\beta)\beta^i = -\alpha^2(h^{ip}\partial_p \ln \alpha + h^{pq}\Gamma^i{}_{pq}). \tag{2.27}$$

The *Bona-Masso* family of slicing conditions can be viewed as a generalization of the harmonic slicing, for which the lapse has to satisfy

$$(\partial_t - \mathcal{L}_\beta)\alpha = -\alpha^2 f(\alpha)K, \tag{2.28}$$

with $f(\alpha)$ positive. The case $f = 1$ corresponds to the harmonic slicing, and $f = 2/\alpha$ is called '1+log' slicing. This foliation is the most common choice in current numerical relativity simulations, as it ensures singularity avoidance and it has been found to be very robust in black hole simulations.

The most simple choice for the shift vector are the *normal coordinates*, namely

$$\beta^i = 0. \tag{2.29}$$

Even though taking the shift equal to zero works well in many cases, there are prescriptions for how to choose a more convenient shift vector in specific situations. For example, evolving black hole spacetimes with vanishing shift causes the black hole horizon to grow rapidly in coordinate space, such that soon all the computational domain will be inside the black hole. For long term evolutions, it is convenient to have an outward pointing shift vector, that will prevent the time lines from falling into the black hole. Also for systems with angular momentum (rotating neutron stars or black holes), the dragging of inertial frames can be severe and one needs a shift in order to avoid large shears in the spatial metric.

One of the first proposals, by Smar and York, has been the *minimal strain* shift condition. This gauge minimizes a global measure of the change in the volume elements associated with the time lines. An even better option seemed to be using the shift in order to minimize only the changes in the shape of the volume elements, independently of their size, which led to the *minimal distortion* shift condition. However, as these conditions lead to three coupled elliptic equations, they have not been extensively used in numerical simulations.

The minimal distortion equation can also be written as

$$\partial_j(\partial_t \tilde{h}^{ij}) = 0,$$

where $\tilde{h}_{ij}$ is the conformal metric. Then the condition is equivalent to

$$\partial_t \tilde{\Gamma}^i = 0,$$

where $\tilde{\Gamma}^i = -\partial_j \tilde{h}^{ij}$ are the conformal connection functions. This choice is called *Gamma freezing*, as it freezes three of the independent degrees of freedom. The above condition is not 3-covariant, as starting from the same geometry but with different spatial coordinates (for example spherical coordinates), one will get a different evolution of the shift vector.

In practice, one prefers to evolve hyperbolic equations. The *Gamma driver* is a hyperbolic version of the Gamma freezing shift [36, 37],

$$\partial_0^2 \beta^i = F \partial_0 \tilde{\Gamma}^i, \tag{2.30}$$

where $\partial_0 = (\partial_t - \mathcal{L}_\beta)$. It is used in combination with a damping term $-\eta \partial_0 \beta^i$ in order to avoid strong oscillations in the shift. This gauge choice, with $F = \frac{3}{4}$, has been found extremely robust and well-behaved in binary black hole simulations with puncture initial data performed with the BSSN formulation of the Einstein equations, as it controls both the slice stretching and the shear due to the rotation of the hole [11, 38].

2.3 Well-Posed Evolution Problems

2.3.1 Well-Posed Systems

Einstein's equations $G_{\mu\nu} = 8\pi T_{\mu\nu}$ contain second derivatives of the metric and are classified in the category of quasilinear hyperbolic partial differential equations. They can be written in the form

$$\boldsymbol{A}^{\mu\nu}\partial_\mu\partial_\nu\boldsymbol{w} = \boldsymbol{S}(\boldsymbol{w},\partial\boldsymbol{w}).$$

A reduction to a hyperbolic system of first order differential equations can be obtained by extending the set of evolution variables, such that it includes first derivatives $\boldsymbol{u} = \{\boldsymbol{w}, \partial_\nu\boldsymbol{w}\}$. Then the system takes the form

$$\hat{\boldsymbol{A}}^\mu\partial_\mu\boldsymbol{u} = \hat{\boldsymbol{S}}(\boldsymbol{u}),$$

where $\hat{\boldsymbol{A}}^\mu = \hat{\boldsymbol{A}}^\mu(\boldsymbol{w})$ and $\hat{\boldsymbol{S}}$ does not depend on derivatives of $\boldsymbol{u}$.

In Numerical Relativity one formulates the evolution of a physical system

$$\partial_t\boldsymbol{u} = \boldsymbol{A}^i\partial_i\boldsymbol{u} + \boldsymbol{S}(\boldsymbol{u}),$$

as an initial value problem (IVP), also called Cauchy problem. This means that given proper initial and boundary conditions $\boldsymbol{u}(t = 0, x)$, the equations must predict the future evolution of the system $\boldsymbol{u}(t, x)$.

As presented in the previous subsections, one writes the Einstein equations as a Cauchy problem by splitting the roles of space and time. This leads to a non-unique system of evolution equations, as one can arbitrarily add them multiples of the constraints. It changes the nature of the free evolution problem, but the physical solutions (the ones satisfying the constraints) remain the same.

In the physical theory of relativity, changing the initial conditions should only change the outcome by an amount that can be controlled by making the change in the initial conditions smaller. This crucial property, which ensures that the formulation is well behaved in numerical simulations, depends on the *well-posedness* of its system of partial differential equations.

The definition of well-posedness for a system requires that a solution exists, is unique and it depends continuously on the initial data. If the ratio between a chosen discrete norm at time t and its initial value

$$\frac{\|\boldsymbol{u}(t,x)\|}{\|\boldsymbol{u}(0,x)\|} \leq Ke^{\alpha t}$$

is bounded by some constants α and K, which are independent of the initial data, then the system is well-posed in respect to that norm [39]. For first order hyperbolic systems the L_2-norm is usually used [40].

2.3.2 Strongly Hyperbolic Systems

An important property of the hyperbolic systems of evolution equations used in Numerical Relativity, is the fact that they have a finite past domain of dependence (finite propagation speed of the signals) in agreement with the causality principle.

A hyperbolic system can be shown to be well-posed under very general conditions. Is has been proven that a system with source terms $\boldsymbol{S}(\boldsymbol{u})$ linear in the variables $\boldsymbol{u}$ is well-posed, if the system without the sources is well-posed [39]. In the case of the Einstein equations, the sources contain terms which are quadratic in the variables, so the hyperbolicity of the principal part is a necessary, but not sufficient condition for well-posedness.

Applying a reduction to first order, the field evolution equations can be brought in the form

$$\partial_t \boldsymbol{u} + \boldsymbol{A}^i \partial_i \boldsymbol{u} + \boldsymbol{S}(\boldsymbol{u}) = 0.$$

The system is said to be *strongly hyperbolic* if the matrix $\boldsymbol{M} = \boldsymbol{A}^i n_i$ is diagonalizable, namely it has a complete set of linearly independent eigenvectors, and real eigenvalues for each direction n^i. For this class of systems, one can construct energy estimates that bound the solution at later times, such that the growth of the errors can not be more than linear.

If all the eigenvalues are real but the matrix does not have a complete set of eigenvectors, the system is called *weakly hyperbolic*. These systems allow exponentially growing modes and are not well suited for numerical simulations.

Analyzing the matrix $\boldsymbol{M}$, one can find a positive Hermitian $\boldsymbol{H}(n)$ such that

$$\boldsymbol{H}(n)\boldsymbol{M} - \boldsymbol{M}\boldsymbol{H}(n) = 0,$$

for $k^{-1}\boldsymbol{I} \leq \boldsymbol{H}(n) \leq k\boldsymbol{I}$ (k constant), $(\forall)n_i$ with $|n_i| = 1$. $\boldsymbol{H}(n)$ is called symmetrizer. If the operator $\boldsymbol{H}$ does not depend on the direction n_i, then the system is called *symmetric hyperbolic*. The condition reduces then to $\boldsymbol{M}$ being symmetric for any direction, so $\boldsymbol{A}^i$ is symmetric with respect to $\boldsymbol{H}$. Energy estimates can be used to prove well-posedness of the initial boundary value problem (IBVP) for this type of systems.

First order systems of equations can be conveniently written in a Flux Conservative form. This means that the *principal part*, the terms containing the highest order derivatives, can be arranged as

$$\partial_t \boldsymbol{u} + \partial_i \boldsymbol{F}^i = ...,$$

where the flux terms $\boldsymbol{F}^i = \boldsymbol{A}^i \boldsymbol{u}$ depend only on the fields and the source terms on the right-hand-side do not contain derivatives. The systems in this form are also called *balance laws*, as the change of the fields in a volume element can be viewed as a balance between the fluxes entering or leaving through the element boundary and the sources.

The Einstein equations, written as a system of balance laws, can be viewed like a standard system in Fluid Dynamics, with the principal part terms describing transport and the remaining ones acting as sources. The field equations can be physically interpreted as follows: the stress-energy tensor describes sources of non-gravitational nature and the quadratic metric terms describe the action of the gravitational field itself, acting as its own source. One of the main advantages of using a first order flux conservative formulation of the field equations is the fact that one can apply the numerical algorithms developed in the field of Computational Fluid Dynamics.

2.3.3   Boundary Conditions

The problem of choosing proper boundary conditions extends beyond Numerical Relativity. At an analytical level, the IBVP is not well understood for General Relativity. Given Cauchy data on a spacelike hypersurface, and boundary data on a timelike hypersurface, the problem is to determine the solution in the appropriate domain of dependence.

In Numerical Relativity, due to limited computational power, artificial timelike boundaries are used for restricting the calculations to finite grids. The procedure can be described as cutting the piece of space-time that one wants to study and evolve it as a separate system, complemented by initial and boundary conditions in order for a solution to exist and be unique [40]. A strongly hyperbolic evolution system is a necessary and sufficient condition for the Cauchy problem to be well-posed, while a symmetric hyperbolic system allows one to formulate a well-posed IBVP.

In the 3+1 formalism, the well-posed Cauchy problem for the system of evolution equations can become ill-posed if the boundary conditions (IBVP) are not properly chosen [3, 41]. The boundary is not intrinsically imposed by the nature of the geometry, but it is 'put in by hand'. The main conditions that the boundaries have to satisfy, are that the full IBVP remains well-posed, the boundaries are consistent with the constraints and with the physical information flux (e.g. no incoming radiation).

The current development of mesh refinement techniques allows setting the boundaries sufficiently far away, so they remain for a while disconnected from the inner dynamical region. This approach however, is computationally expensive. A similar effect can be obtained by choosing coordinates which transform a finite grid distance into an arbitrarily large spatial distance (*fish-eye* technique) [42, 43]. As long as one is not using elliptic equations, for example elliptic gauge conditions or constrained evolution, the boundary effects can not propagate at infinite speed and affect all the computational domain. So one can ignore the dissipative (or other type of unphysical) effects that the boundary might produce. In general, this is not a safe procedure, as the waves traveling outwards become less resolved in

the computational grid, so they can get backscattered and can produce instabilities and unphysical solutions.

Some of the most common types of boundary conditions are radiative, maximally dissipative and constraint preserving. The *radiative boundaries*, commonly used for the BSSN variables, are based on the assumptions that the spacetime is asymptotically flat, the source of gravitational field is localized in a small region, such that there is a spherical front of gravitational waves at the boundary, and the shift is small, such that its effect on the characteristic speed can be ignored [36].

Maximally dissipative boundary conditions require the characteristic decomposition of the system, as they are applied on the incoming and outgoing modes (eigenvectors) [44]. This method has been extended to the nonlinear IBVP with boundaries containing characteristics, such as occurs in symmetric hyperbolic formulations of General Relativity [45, 46]. Friedrich and Nagy applied the maximally dissipative boundaries in order to develop the first proof of a well-posed IBVP for Einstein's equations [47]. Their formulation of the field equations is quite different from the ADM based systems implemented in the current codes, and it is not apparent how to extend this work to other formalisms. The general principles can be carried over, provided that formulation is written in a symmetric hyperbolic form. Recently it has been applied to the IBVP of a harmonic formulation in order to show that it is well-posed [48].

Constraint preserving boundaries seem to be the most accurate choice. They impose conditions on the eigenfields and the subsidiary system. There are very few codes which have these boundaries implemented [49, 50] and variants are still under development.

Part II

Formulations of the Einstein Equations

Chapter 3

Einstein Evolution Systems

This chapter concerns formulations of the Einstein equations based on the 3+1 decomposition. These formulations take advantage of the fact that the constraints are first integrals of the system and allow for a *free evolution* approach. This means that if one enforces the constraints on the initial data and initial boundary data, then the constraints are guaranteed to be preserved during the evolution (at a continuum level). In numerical simulations however, as they are not enforced by the evolution algorithm, the constraints are not preserved due to discretization errors and limited resolution. This 'unconstrained' evolution introduces a discrimination in the formalism, that breaks the general covariance of the Einstein equations.

In the 3+1 formulations, the field equations of General Relativity are written as a Cauchy problem (Section 2.2). The form of the 3+1 evolution equations, as presented in the previous chapter, is not unique. One can add them constraints in order to obtain various forms of the evolution system. The resulting formulations have the same physical solutions, but they can have different mathematical properties. This freedom of modifying the 3+1 evolution equations led to a large number of alternative systems. The only ones suited, from the numerical behavior point, are the well-posed strongly hyperbolic or symmetric hyperbolic formulations, as they ensure numerical stability (Section 2.3).

In the following, we will present three systems based on the metric (Z3, Z4 and BSSN) and one on the tetrad formalism (Friedrich-Nagy). This brief overview offers a comparison of the systems at an analytical level, which is necessary in order to understand the different behavior of the systems when subjected even to simple numerical tests, like the standard Numerical Relativity testbeds presented in Chapter 4.

3.1 The 3+1 Metric based Systems

The ADM based systems use the 3+1 decomposition and consider the metric and extrinsic curvature as basic evolution variables. They derive from the standard ADM (Arnowitt, Deser, Misner) [51] equations rewritten by York.

The ADM system contains evolution equations for the basic dynamical fields: the spatial metric h_{ij} Eq. (2.13) and the extrinsic curvature K_{ij} Eq. (2.16),

$$
\begin{aligned}
(\partial_t - \mathcal{L}_\beta)h_{ij} &= -2\alpha K_{ij}, \\
(\partial_t - \mathcal{L}_\beta)K_{ij} &= -\nabla_i\nabla_j\alpha + \alpha[\mathcal{R}_{ij} - K_{ij}^2 + KK_{ij} + \\
&\quad + 8\pi(-S_{ij} + \frac{h_{ij}}{2}(trS - \tau))],
\end{aligned}
$$

plus the momentum and energy constraints Eqs. (2.24) and (2.23),

$$
\begin{aligned}
\nabla_p(K_i{}^p - \delta_i{}^p K) - 8\pi S_i &= 0, \\
\mathcal{R} + K^2 - tr(K^2) - 16\pi\tau &= 0.
\end{aligned}
$$

An important concept used by York when rewriting the ADM system, is the well-posedness of the evolution system of the constraints, which guarantees that if the constraints are satisfied initially, they will remain satisfied during the evolution. Despite this feature, the resulting main evolution system of Einstein equations written in ADM form is weakly hyperbolic (even though all the eigenvalues are real, there is not a complete set of eigenvectors), so it can not be used to construct robust numerical evolutions.

3.1.1 The Z Systems

3.1.1.a The Z4 system

The Z systems, developed by Bona et al. [52], use the full Einstein equations, by inclosing the constraints into the dynamical system in a covariant way. The constraints become evolution equations for some extra variables.

The Z4 system is based on an extension of the solution space of the original Einstein field equations by introducing an extra vector Z_μ,

$$
R_{\mu\nu} + \nabla_\mu Z_\nu + \nabla_\nu Z_\mu = 8\pi(T_{\mu\nu} - \frac{1}{2}Tg_{\mu\nu}), \tag{3.1}
$$

so the new set of basic fields is $(g_{\mu\nu}, Z_\mu)$. The solutions of the original Einstein equations can be recovered when Z_μ is a Killing vector. In the generic case, the Killing equation has only the trivial solution

$$
Z_\mu = 0. \tag{3.2}
$$

The Z variables can be interpreted as a measure of the constraint violation in numerical simulations.

The divergence of Eq. (3.1), the conservation laws of the Einstein tensor Eq. (2.7) and stress energy tensor Eq. (2.8), lead to an equation for the Z_μ vector

$$\Box Z_\mu + R_{\mu\nu} Z^\mu = 0. \tag{3.3}$$

This relation represents the subsidiary system, namely the evolution system of the constraints. In order to preserve it during the evolution, one needs to impose at the initial slice both the vanishing of Z_μ and its first time derivative. This implies that the set of initial data for the true Einstein equations must satisfy the energy and momentum constraints, and additionally a zero initial value for the four-vector Z_μ.

The full system can be obtained from Eq. (3.1), written in 3+1 form:

$$
\begin{aligned}
(\partial_t - \mathcal{L}_\beta) K_{ij} &= -\nabla_i \nabla_j \alpha + \alpha[\mathcal{R}_{ij} + \nabla_i Z_j + \nabla_j Z_i - 2K_{ij}^2 + \\
&\quad + (K - 2\theta)K_{ij} + 8\pi(-S_{ij} + \frac{h_{ij}}{2}(trS - \tau))], \quad (3.4) \\
(\partial_t - \mathcal{L}_\beta)\theta &= \frac{\alpha}{2}[\mathcal{R} + 2\nabla_k Z^k + (K - 2\theta)K - tr(K^2) - \\
&\quad -2Z^k \frac{\nabla_k \alpha}{\alpha} - 16\pi\tau], \quad (3.5) \\
(\partial_t - \mathcal{L}_\beta)Z_i &= \alpha[\nabla_j(K_i{}^j - \delta_i{}^j K) + \partial_i \theta - 2K_i{}^j Z_j - \theta\frac{\nabla_i \alpha}{\alpha} - \\
&\quad -8\pi S_i], \quad (3.6)
\end{aligned}
$$

where θ is the projection of Z_μ along the unit normal (defined in Section 2.1.4),

$$\theta = n_\mu Z^\mu = \alpha Z^0.$$

The Z4 system consists of 10 evolution equations (3.4) - (3.6), the only constraints being Eq. (3.2), so the whole set of field equations is used during evolution.

The standard 3+1 decomposition leads to a system of mixed order, as it contains both first and second order space derivatives. We perform a reduction to first order in space, by defining the derivative of the lapse, shift and metric as independent evolution variables,

$$
\begin{aligned}
A_i &= \frac{1}{\alpha}\partial_i \alpha, \quad (3.7) \\
B_i{}^j &= \partial_i \beta^j, \quad (3.8) \\
D_{ijk} &= \frac{1}{2}\partial_i h_{jk}. \quad (3.9)
\end{aligned}
$$

The resulting first order in space system will describe the same physical dynamics as the second order one.

The system is completed by suitable evolution equations for the lapse and shift. At this point we prefer to keep the gauge choice open and define the evolution of the metric components in a general way,

$$\partial_t \alpha = -\alpha^2 Q, \tag{3.10}$$

$$\partial_t \beta^i = -\alpha Q^i, \tag{3.11}$$

$$\partial_t h_{ij} = -2\alpha Q_{ij}, \tag{3.12}$$

where Q and Q^i can be a combination of other dynamical fields, or evolution variables themselves, and

$$Q_{ij} = K_{ij} - \frac{1}{2\alpha}(B_{ij} + B_{ji}) - \frac{1}{\alpha}\beta^p D_{pij},$$

is just a shorthand for the right hand side of Eq. (2.13).

3.1.1.b The Z3 system

The Z3 system can be obtained from the Z4 by a mechanism called *symmetry breaking*. One considers the following recombination

$$\tilde{K}_{ij} \rightarrow K_{ij} + \frac{n}{2}\theta h_{ij},$$

which leads to a similar system, but expressed in a different basis of dynamical fields. Then enforcing the algebraic constraint $\theta = 0$ and suppressing θ as a dynamical quantity, one obtains a one-parameter family of non-equivalent extended systems, that will contain only the three components Z_i of the 4-vector Z_μ as supplementary quantities.

The Z3 family of systems can be written as:

$$
\begin{aligned}
(\partial_t - \mathcal{L}_\beta)h_{ij} &= -2\alpha K_{ij}, \\
(\partial_t - \mathcal{L}_\beta)K_{ij} &= -\nabla_i\nabla_j\alpha + \alpha[\mathcal{R}_{ij} + \nabla_i Z_j + \nabla_j Z_i - 2K_{ij}^2 + KK_{ij} + \\
&\quad + 8\pi(-S_{ij} + \frac{h_{ij}}{2}(trS - \tau))] - \frac{n}{4}\alpha h_{ij}[\mathcal{R} + 2\nabla_k Z^k + \\
&\quad + K^2 - tr(K^2) - 2Z^k\frac{\nabla_k\alpha}{\alpha} - 16\pi\tau], \\
(\partial_t - \mathcal{L}_\beta)Z_i &= \alpha[\nabla_j(K_i{}^j - \delta_i{}^j K) - 2K_i{}^j Z_j - 8\pi S_i].
\end{aligned}
$$

The symmetry of the Z4 system is broken in this transition, as the equivalent of the energy constraint θ, is no longer part of the evolution system. Different

values of the n parameter will lead to different systems from the family of the Z3 evolution systems [53].

In order to complete the system, one has to specify gauge conditions. We keep the gauge choice open for now, as it is not the main focus of this chapter, mentioning that the Eqs. (3.10) - (3.12) can be used in combination with any of the Z systems.

3.1.1.c Ordering Constraints

In order to bring the Z systems into a fully first order form, we introduced as additional evolution variables the spatial derivatives of the lapse, shift and metric, Eqs. (3.7) - (3.9). We provide evolution equations, by applying a time derivative to their definitions and then commuting the space and time derivatives,

$$\partial_t A_i \quad + \quad \partial_p[\delta_i{}^p \alpha Q] = 0, \tag{3.13}$$

$$\partial_t B_i{}^j \quad + \quad \partial_p[\delta_i{}^p \alpha Q^j] = 0, \tag{3.14}$$

$$\partial_t D_{kij} \quad + \quad \partial_p[\delta_k{}^p \alpha Q_{ij}] = 0. \tag{3.15}$$

The original definitions become now a set of first order constraints,

$$\mathcal{A}_i \quad = \quad A_i - \partial_i \ln \alpha = 0, \tag{3.16}$$

$$\mathcal{B}_i{}^j \quad = \quad B_i{}^j - \partial_i \beta^j = 0, \tag{3.17}$$

$$\mathcal{D}_{ijk} \quad = \quad D_{ijk} - \frac{1}{2}\partial_i h_{jk} = 0. \tag{3.18}$$

The ordering of the second derivatives introduces an additional set of constraints,

$$\mathcal{C}_{ij} \quad = \quad \partial_i \mathcal{A}_j - \partial_j \mathcal{A}_i = \partial_i A_j - \partial_j A_i = 0, \tag{3.19}$$

$$\mathcal{C}_{ij}{}^k \quad = \quad \partial_i \mathcal{B}_j{}^k - \partial_j \mathcal{B}_i{}^k = \partial_i B_j{}^k - \partial_j B_i{}^k = 0, \tag{3.20}$$

$$\mathcal{C}_{ijkl} \quad = \quad \partial_i \mathcal{D}_{jkl} - \partial_j \mathcal{D}_{ikl} = \partial_i D_{jkl} - \partial_j D_{ikl} = 0. \tag{3.21}$$

One can notice that in the Eqs. (3.13) - (3.15), the transversal components of the first order derivative variables have zero characteristic speeds, namely their characteristic lines will be the time lines. This can lead to a degeneracy problem in black hole evolutions, as the system becomes weakly hyperbolic. The characteristic cone of the second order system is the light cone, with $(-\beta_n \pm \alpha)$ characteristic speed, and the time lines can cross the light cone. In order to avoid this, one can

use the ordering constraints Eq. (3.20) and rewrite the equations as

$$\partial_t A_i \quad + \quad \partial_p[-\beta^p A_i + \delta_i{}^p(\alpha Q + \beta^q A_q)] =$$
$$= \quad B_i{}^p A_p - tr B A_i, \tag{3.22}$$
$$\partial_t B_i{}^j \quad + \quad \partial_p[-\beta^p B_i{}^j + \delta_i{}^p(\alpha Q^j + \beta^q B_q{}^j)] =$$
$$= \quad B_i{}^p B_p{}^j - tr B B_i{}^j, \tag{3.23}$$
$$\partial_t D_{kij} \quad + \quad \partial_p[-\beta^p D_{kij} + \delta_k{}^p(\alpha Q_{ij} + \beta^q D_{qij})] =$$
$$= \quad B_k{}^p D_{pij} - tr B D_{kij}. \tag{3.24}$$

The characteristic lines of the transversal derivative components are now the normal lines, with $(-\beta^n)$ characteristic speed, so the characteristic crossing is avoided. This ordering adjustment, currently used also by first order harmonic formulations, turned out to be very important in long term simulations with dynamical shift (Chapter 9).

3.1.1.d Damping terms

The use of constraint-violation damping terms is another important ingredient for long term black hole simulations. In hyperbolic formulations, the error associated with constraint violation grows at a bounded rate. However, this can still be very fast in numerical simulations and these growing modes can produce instabilities. Recent studies [1] show that by adding suitable lower-order terms to the Z4 formulation, all constraint violation modes except for constant modes, can be damped. The same prescription can be applied to the harmonic formulations of the Einstein equations, as their constraint evolution system is similar.

The energy and momentum constraint violations can be damped using terms described in [1]. For the first order constraints, we can introduce in Eqs. (3.22) - (3.24) damping terms of the type

$$-\eta_A \mathcal{A}_i \qquad\qquad \text{evolution of A}, \tag{3.25}$$
$$-\eta_B \mathcal{B}_i{}^j \qquad\qquad \text{evolution of B}, \tag{3.26}$$
$$-\eta_D \mathcal{D}_{kij} \qquad\qquad \text{evolution of D}. \tag{3.27}$$

The η damping parameter can be chosen in the range $0 < \eta << \frac{1}{\Delta t}$ in order to ensure numerical stability, as larger values would lead to a stiff system.

The use of this type of damping terms is justified by an analysis of the subsidiary system. Considering the time derivative of Eq. (3.16), taking into account the definition Eq. (3.22) and the constraints Eqs. (3.17), (3.19), we obtain the propagation of the first order constraint of A_i,

$$\partial_t \mathcal{A}_k - \beta^p(\partial_p \mathcal{A}_k - \partial_k \mathcal{A}_p) = \mathcal{B}_k{}^p A_p - \mathcal{B}_p{}^p A_k.$$

The normal and transverse components of the system above, in respect to any spatial direction n can be written as

$$\partial_t \mathcal{A}_n + \beta^\perp(\partial_n \mathcal{A}_\perp) = 0,$$
$$\partial_t \mathcal{A}_\perp - \beta^n(\partial_n \mathcal{A}_\perp) = 0.$$

The eigenvalues are $(0, -\beta^n)$, which means that the system is weakly hyperbolic for any space direction orthogonal to the shift vector. This should not affect the stability of the system, but it may lead to linearly growing first order constraint violations which affect the accuracy of long term simulations.

These considerations justify the use of the damping terms (3.25) - (3.27), which will have an exponential damping effect in the subsidiary system.

3.1.1.e   Ordering ambiguities

The shift ordering constraint Eq. (3.20) can be used for adjusting the first-order evolution equation of the Z_i vector,

$$(\partial_t - \mathcal{L}_\beta)Z_i = \alpha[\nabla_j(K_i{}^j - \delta_i{}^j K) + \partial_i\theta - 2K_i{}^j Z_j - \theta\frac{\nabla_i\alpha}{\alpha} - 8\pi S_i] -$$
$$- \mu(\partial_p B_i{}^p - \partial_i B_p{}^p).$$

The ordering constraints Eq. (3.21) appear in the two forms of the three-dimensional Ricci tensor, namely the standard Ricci decomposition,

$$R_{ij} = \partial_p\Gamma^p{}_{ij} - \partial_i\Gamma^p{}_{pj} + \Gamma^p{}_{pq}\Gamma^q{}_{ij} - \Gamma^q{}_{pi}\Gamma^p{}_{qj},$$

and the DeDonder decomposition,

$$R_{ij} = -\partial_p D^p{}_{ij} + \partial_{(i}\Gamma_{j)p}{}^p - 2D_p{}^{pq}D_{qij} + 4D^{pq}{}_i D_{pqj} - \Gamma_{ipq}\Gamma_j{}^{pq} - \Gamma_{pij}\Gamma^{pq}{}_q.$$

Any combination of the two definitions can be used in the principal part of the evolution equation for the extrinsic curvature Eq. (2.16). We introduce an ordering parameter ξ, where $\xi = 1$ corresponds to the Ricci decomposition and $\xi = -1$ to the DeDonder one.

The values of ξ and μ are free for the Z4 system, as they do not affect the principal part of the system, or the form of the subsidiary system. There are though some special choices, like $\xi = 0$ which ensures that the first order version of the system contains only symmetric combinations of second derivatives of the space metric. It is also worth mentioning that the choice $\mu = 1/2$, $\xi = -1$ allows an equivalence between the first order version of the generalized harmonic formulation and the Z4 system [1].

The numerical simulations presented in this thesis, were performed using the values $\xi = -1$ and $\mu = 1$ for the Z4 system, even though we tested also other

combinations that lead to long-term stability. The choice of the μ parameter is fixed in the case of the Z3 system, as $\mu = 1$ is the only value which ensures strong hyperbolicity.

3.1.2 The BSSN System

The BSSN (Baumgarte, Shapiro, Shibata, Nakamura) system [7,8] is currently one of the most popular formulations of the Einstein equations, used in numerical simulations both with and without matter. Also called the 'conformal Γ formulation', the BSSN is based on the ADM equations in 3+1 form. The particularities of this system are the fact that it introduces a new evolved field (the contracted Christoffel symbols Γ^i), a conformal decomposition and adds constraints to the evolution equations.

The BSSN considers a conformal rescaling of the metric

$$\tilde{h}_{ij} = \psi^{-4} h_{ij},$$

where ψ is the conformal factor, chosen is such a way that the conformal metric has unit determinant $det h = 1$. Then the evolution equation for the determinant of the metric leads to an evolution equation for the conformal factor, taken that the relation $\psi^4 = h^{1/3}$ remains satisfied during the evolution.

One evolves in practice the logarithm of the conformal factor

$$\phi = \ln \psi = \ln h / 12.$$

Then the conformal metric can be written as

$$\tilde{h}_{ij} = e^{-4\phi} h_{ij},$$

and the evolution equation for the natural logarithm of the conformal factor takes the form

$$\partial_t \phi = -\frac{1}{6}(\alpha \, K - \partial_p \beta^p) + \beta^p \partial_p \phi.$$

The extrinsic curvature is split into trace and trace-free parts

$$A_{ij} = K_{ij} - \frac{1}{3} h_{ij} K,$$

and one applies a conformal rescaling to the traceless part

$$\tilde{A}_{ij} = e^{-4\phi} A_{ij}.$$

Due to numerical stability reasons, the constraint $tr\tilde{A} = 0$ is directly imposed during the evolution.

The Christoffel symbols of the conformal metric

$$\tilde{\Gamma}^i = \tilde{h}^{pq}\tilde{\Gamma}^i{}_{pq} = -\partial_p \tilde{h}^{ip}, \tag{3.28}$$

are introduced as auxiliary variables. Their evolution can be derived from the definition above and the evolution equation for the metric as

$$(\partial_t - \mathcal{L}_\beta)\tilde{\Gamma}^i = \tilde{h}^{pq}\partial_p\partial_q\beta^i + \frac{1}{3}\tilde{h}^{ip}\partial_p\partial_q\beta^q - 2(\alpha\partial_p\tilde{A}^{ip} + \tilde{A}^{ip}\partial_p\alpha). \tag{3.29}$$

However, this form is known to lead to unstable evolutions. One fixes the problem by using the momentum constraint

$$\partial_p \tilde{A}^{ip} = -\tilde{\Gamma}^i{}_{pq}\tilde{A}^{pq} - 6\tilde{A}^{ip}\partial_p\phi + \frac{2}{3}\tilde{h}^{ip}\partial_p K + 8\pi\tilde{S}^i,$$

in order to replace the divergence of $\tilde{A}^{ij}$ in the Eq. (3.29).

The system of evolution equations can be obtained from the ADM equations applying the modifications mentioned above, namely

$$
\begin{aligned}
(\partial_t - \mathcal{L}_\beta)\tilde{h}_{ij} &= -2\alpha\tilde{A}_{ij}, \\
(\partial_t - \mathcal{L}_\beta)\phi &= -\frac{1}{6}\alpha\, K, \\
(\partial_t - \mathcal{L}_\beta)\tilde{A}_{ij} &= e^{-4\phi}\{-D_iD_j\alpha + \alpha\mathcal{R}_{ij} + 4\pi\alpha[h_{ij}(trS - \rho) - 2S_{ij}]\}^{TF} + \\
&\quad + \alpha(K\tilde{A}_{ij} - 2\tilde{A}_{ip}\tilde{A}^p{}_j), \\
(\partial_t - \mathcal{L}_\beta)K &= -D_pD^p\alpha + \alpha(\tilde{A}_{ij}\tilde{A}^{ij} + \frac{1}{3}K^2) + 4\pi\alpha(\rho + trS), \\
(\partial_t - \mathcal{L}_\beta)\tilde{\Gamma}^i &= \tilde{h}^{pq}\partial_p\partial_q\beta^i + \frac{1}{3}\tilde{h}^{ip}\partial_p\partial_q\beta^q - 2\tilde{A}^{ip}\partial_p\alpha + \\
&\quad + 2\alpha(\tilde{\Gamma}^i{}_{pq}\tilde{A}^{pq} + 6\tilde{A}^{ip}\partial_p\phi - \frac{2}{3}\tilde{h}^{ip}\partial_p K - 8\pi\tilde{S}^i),
\end{aligned}
$$

where TF denotes the trace-free part of the expression.

This form of the system is successfully used in numerical simulations. One of the key ingredients of BSSN is the use of the momentum constraint to modify the dynamical system. Some additional modifications, related with the way the constraints are treated during the numerical evolution, appear in different implementations and consist in:

- ensuring that the conformal metric has unit determinant

$$\tilde{h}_{ij} \rightarrow \frac{\tilde{h}_{ij}}{det\tilde{h}^{1/3}},$$

- ensuring that the trace-free part of the extrinsic curvature remains trace-free

$$\tilde{A}_{ij} \to \tilde{A}_{ij} - \frac{1}{3}\tilde{A}_{pq}\tilde{h}^p{}_i\tilde{h}^q{}_j,$$

- dividing $\tilde{A}_{ij}$ by the same factor used to remove the $det\tilde{h}_{ij}$

$$\tilde{A}_{ij} \to \frac{\tilde{A}_{ij}}{det\tilde{h}^{1/3}}.$$

Another modification adopted by some groups consists in replacing $\partial_p h^{ip}$ with the corresponding Γ^i, only if the expression appears under a derivative. These specific choices lead to a family of BSSN formulations, with different 'flavors' of the numerical implementation.

3.2 The 3+1 Tetrad based Systems

There are also alternative formulations of the Einstein equations, which are not based on the ADM system. I will present in this section a particular system based on the frame formalism, in which the 3+1 decomposition is performed with respect to the components of an orthonormal tetrad. The basic evolution variables are the tetrad components $(e_i)^\mu$, the four dimensional connection coefficients $\gamma_i{}^j{}_k$ and the electric E_{ij} and magnetic B_{ij} components of the Weyl tensor.

3.2.1 Notions of Frame Formalism

3.2.1.a The Tetrad

The metric tensor g_μ may be defined indirectly, through D vectors forming an orthonormal D-leg $(b^\nu)_\mu$. Then the spacetime metric can be written using the one-forms $b^\nu = (b^\nu)_\mu dx^\mu$ as

$$g_{\mu\nu} = \eta_{\rho\tau}(b^\rho)_\mu(b^\tau)_\nu.$$

The frame indices, counting the number of "legs" spanning the cotangent space at each point, are moved with the Minkowski metric.

In the case of tetrad-theories ($D = 4$) described by the concept of fiber bundle, the $(b^\nu)_\mu$ are considered to be the basic geometrical variables satisfying the field equations (not the metric). The fiber at each point of the manifold contains all orthonormal tetrads related to each other by transformations of the Lorentz group.

The basis is defined as $(e_\rho)^\mu(b^\tau)_\mu = \delta_\rho{}^\tau$ and $(e_\rho)^\mu(b^\rho)_\nu = h^\mu{}_\nu$. Then the 4-metric can be represented in terms of the frame $(e_\rho)^\mu$ as follows

$$g^{\mu\nu} = \eta^{\rho\tau}(e_\rho)^\mu(e_\tau)^\nu,$$

$$g(e_\mu, e_\nu) = \eta_{\mu\nu} = diag(-1, 1, 1, 1).$$

The functions $(e_\rho)^\mu = e_\rho(x^\mu)$ are the coefficients of the frame in a chosen coordinate system.

The 4-dimensional connection-coefficients in this frame $\gamma_\mu{}^\nu{}_\tau$ are defined as

$$\gamma_\tau{}^\rho{}_\xi = (b^\rho)_\nu (e_\tau)^\mu \nabla_\mu (e_\xi)^\nu.$$

The fact that the connection is metric ($\nabla_\mu g_{\nu\rho} = 0$) is expressed through the antisymmetry of the connection-coefficients in their last two indices.

The torsion-free condition translated into

$$(b^\tau)_\nu (e_\rho)^\mu \partial_\mu (e_\alpha)^\nu - (b^\tau)_\nu (e_\alpha)^\mu \partial_\mu (e_\rho)^\nu + \gamma_{\rho\alpha}{}^\tau - \gamma_{\alpha\rho}{}^\tau = 0,$$

provides a constraint equation for the spatial vectors of the tetrad

$$(b^k)_\xi (e_j)^\delta \partial_\delta (e_i)^\xi - (b^k)_\xi (e_i)^\delta \partial_\delta (e_j)^\xi - \Gamma_{ij}{}^k + \Gamma_{ji}{}^k = 0.$$

The projections of the 4-dimensional connection-coefficients are calculated as

$$a^j = \gamma_0{}^j{}_0 = (b^j)_\mu (e_0)^\rho \nabla_\rho (e_0)^\mu,$$

$$\chi_i{}^j = \gamma_i{}^j{}_0 = (b^j)_\mu (e_i)^\rho \nabla_\rho (e_0)^\mu,$$

$$\Lambda^j{}_i = \gamma_0{}^j{}_i = (b^j)_\mu (e_0)^\rho \nabla_\rho (e_i)^\mu,$$

$$\Gamma_k{}^j{}_i = \gamma_k{}^j{}_i = (b^j)_\mu (e_k)^\rho \nabla_\rho (e_i)^\mu,$$

where both $\Lambda^j{}_i$ and $\Gamma_k{}^j{}_i$ are spatial and antisymmetric in their last two indices. The components of a^j (3), $\chi_i{}^j$ (9), $\Lambda^j{}_i$ (3) and $\Gamma_k{}^j{}_i$ (9), account for the 24 connection coefficients of the four-dimensional connection ∇ in respect to the chosen tetrad.

The Einstein vacuum field equations imply the equality between the Riemann and the Weyl tensor

$$R_{\mu\nu\rho\tau} = C_{\mu\nu\rho\tau}.$$

The Weyl tensor can be decomposed

$$
\begin{aligned}
C_{\mu\nu\rho\tau} = {}& -(e_0)_\mu (e_0)_\tau E_{\nu\rho} + (e_0)_\nu (e_0)_\tau E_{\mu\rho} + (e_0)_\mu (e_0)_\rho E_{\nu\tau} - (e_0)_\nu (e_0)_\rho E_{\mu\tau} \\
& - \epsilon_{\mu\nu\xi} E^{\xi\delta} \epsilon_{\delta\rho\tau} - (e_0)_\mu B_\nu{}^\xi \epsilon_{\xi\rho\tau} + (e_0)_\nu B_\mu{}^\xi \epsilon_{\xi\rho\tau} + \epsilon_{\mu\nu}{}^\xi B_{\xi\rho} (e_0)_\tau - \\
& - \epsilon_{\mu\nu}{}^\xi B_{\xi\tau} (e_0)_\rho,
\end{aligned}
$$

in terms of its electric part

$$E_{\nu\tau} = C_{\mu\nu\rho\tau} (e_0)^\mu (e_0)^\rho,$$

and magnetic part

$$B_{\mu\alpha} = \frac{1}{2} C_{\mu\nu\rho\tau} (e_0)^\nu \epsilon^{\rho\tau}{}_{\alpha\xi} (e_0)^\xi.$$

Both $E_{\mu\nu}$ and $B_{\mu\nu}$ are symmetric and trace-free.

3.2.1.b   Gauge choice

We present in the following a particular way of adapting the tetrad to the geometry and a gauge prescription that can be used in order to simplify the system. These gauge choices are just an example, that we adopt here in order to make the comparison with the 3+1 metric formalism more intuitive.

One can consider the standard 3+1 decomposition presented in Chapter 2 and choose $(e_0)^\mu$ to be the equivalent of n^μ, namely the unit vector field orthogonal to the spatial hypersurfaces. Then one extends e_0 to an orthonormal basis $\{(e_0)^\mu, (e_i)^\mu\}$, with $(e_i)^\mu(e_0)_\mu = 0$ and the 'spatial' components of the tetrad can not have components in the 'zero' direction

$$(e_i)^0 = 0.$$

The χ_{ij} connection coefficient becomes a symmetric two tensor, the equivalent of the extrinsic curvature K_{ij} in the metric formalism.

Assuming that the frame is Fermi propagated in the direction of e_0, one can write the law of transport for a non-rotating tetrad of basis vectors (e_μ) carried by an accelerated observer as

$$\nabla_{e_0}(e_i)^c = ((e_0)^c a^p - (e_0)^p a^c)(e_i)_p.$$

This leads to the simplification $\Lambda^j{}_i = 0$. Furthermore one can choose a time slicing determined by a wave equation

$$f^0(t, x^\mu) = -\nabla_\mu \nabla^\mu t.$$

Then the evolution equation for the lapse takes the form

$$\partial_t \alpha = \beta^k (e_k)^p \partial_p \alpha + K_p{}^p \alpha^2 - f^0 \alpha^3.$$

3.2.1.c   Evolution and Constraints for the Connection Coefficients

One can replace the a connection coefficient with $A_i = \alpha a_i$. Then using the definition of the acceleration in respect to the lapse function, we find the following constraint

$$(e_i)^p \partial_p \alpha - A_i = 0,$$

and evolution equation

$$
\begin{aligned}
\partial_t A_j &= -(\alpha^3)(e_j)^p \partial_p f^0 + (\alpha^2)(e_k)^p \partial_p K_j{}^k + \beta^k (e_k)^p \partial_p A_j + 2K_p{}^p \alpha A_j - \\
&\quad -3f^0(\alpha^2)A_j - \alpha A_p K_j{}^p + \alpha^2 K_p{}^q \Gamma_{qj}{}^p - \alpha^2 K_{pj} \Gamma_q{}^{pq}.
\end{aligned}
$$

The standard evolutions and constraints of the metric formalism find correspondent in to the following projections of the Riemann tensor:

- $h_\lambda{}^\mu h_\alpha{}^\nu h_\xi{}^\rho R_{\mu\nu\rho}{}^\tau (e_0)_\tau \to$ the Momentum constraint,

$$(e_j)^p \partial_p K_{ik} - (e_k)^p \partial_p K_{ij} + B_i{}^p \epsilon_{pjk} +$$
$$+ K_{pk} \Gamma_{ji}{}^p + K_{pi} \Gamma_{jk}{}^p - K_{pj} \Gamma_{ki}{}^p - K_{pi} \Gamma_{kj}{}^p = 0;$$

- $(e_0)^\mu h_\xi{}^\nu h_\alpha{}^\rho R_{\mu\nu\rho}{}^\tau (e_0)_\tau \to$ the evolution equation for the extrinsic curvature,

$$\begin{aligned} \partial_t K_{ij} &= \beta^k (e_k)^p \partial_p K_{ij} + (1/2)(e_j)^p \partial_p A_i + (1/2)(e_i)^p \partial_p A_j - \\ &\quad - \alpha E_{ij} - \alpha K_{pj} K_i{}^p + (1/2) A_p \Gamma_{ij}{}^p + (1/2) A_p \Gamma_{ji}{}^p; \end{aligned}$$

- $h_\lambda{}^\mu h_\xi{}^\nu h_\tau{}^\rho R_{\mu\nu\rho}{}^\tau (b^i)_\tau \to$ the Hamiltonian constraint,

$$(e_l)^p \partial_p \Gamma_{kj}{}^i - (e_k)^p \partial_p \Gamma_{lj}{}^i + K_{jl} K_k{}^i - K_{jk} K_l{}^i +$$
$$+ E_l{}^i \delta_{jk} - E_k{}^i \delta_{jl} - E_{jl} \delta_k{}^i + E_{jk} \delta_l{}^i -$$
$$- \Gamma_{pj}{}^i \Gamma_{kl}{}^p - \Gamma_{kj}{}^p \Gamma_{lp}{}^i + \Gamma_{kp}{}^i \Gamma_{lj}{}^p + \Gamma_{pj}{}^i \Gamma_{lk}{}^p = 0;$$

- $(e_0)^\mu h_\xi{}^\nu h_\tau{}^\rho R_{\mu\nu\rho}{}^\tau (b^i)_\tau \to$ the evolution equation for the connection coefficients,

$$\partial_t \Gamma_{jk}{}^i = \beta^l (e_l)^p \partial_p \Gamma_{jk}{}^i - \alpha K_j{}^p \Gamma_{pk}{}^i + A^i K_{jk} - A_k K_j{}^i - \alpha B_{pj} \epsilon_k{}^{pi}.$$

The evolution of the spatial vectors of the frame can be written as a Lie derivative in the direction of the time-flow acting on e_i, which translates into

$$\partial_t (e_j)^a = -(e_k)^a (e_j)^p \partial_p \beta^k - (e_k)^a \beta^q \Gamma_{qj}{}^k + (e_k)^a \beta^q \Gamma_{jq}{}^k - \alpha (e_k)^a K_j{}^k,$$

3.2.1.d Evolution and Constraints for the Weyl tensor

The contracted Bianchi identity

$$\nabla^\mu C_{\mu\nu\rho\tau} = 0.$$

provides evolution and constraint equations for E and B applying the following procedure:

- Projecting with $(e_0)^\tau h^\nu{}_i h^\rho{}_j$ and the symmetrizing in the (i,j) indices $\to$ evolution equation for E,

$$\begin{aligned} \partial_t E_{ij} &= (\alpha/2)\epsilon^k{}_j{}^q (e_k)^p \partial_p B_{qi} + (\alpha/2)\epsilon^k{}_i{}^q (e_k)^p \partial_p B_{qj} + \\ &\quad + \beta^k (e_k)^p \partial_p E_{ij} - 2K_p{}^p \alpha E_{ij} - A^p B_j{}^q \epsilon_{pqi} - A^p B_i{}^q \epsilon_{pqj} + \\ &\quad + (3/2)\alpha E_{pj} K_i{}^p + (3/2)\alpha E_{pi} K_j{}^p - \alpha E_{pq} K^{pq} \delta_{ij} + \\ &\quad + (\alpha/2) B_{pj} \epsilon_{qi}{}^r \Gamma^q{}_r{}^p + (\alpha/2) B_{pi} \epsilon_{qj}{}^r \Gamma^q{}_r{}^p + \\ &\quad + (\alpha/2) B_{pq} \epsilon_{rj}{}^p \Gamma^r{}_i{}^q + (\alpha/2) B_{pq} \epsilon_{ri}{}^p \Gamma^r{}_j{}^q; \end{aligned}$$

- Multiplying with $\epsilon^{\alpha\rho\tau}h^\nu{}_j h_{\alpha i}$ and symmetrizing in the (i,j) indices $\rightarrow$ evolution equation for B,

$$
\begin{aligned}
\partial_t B_{ij} &= (\alpha/2)\epsilon^k{}_{qj}(e_k)^p\partial_p E_i{}^q + (\alpha/2)\epsilon^k{}_{qi}(e_k)^p\partial_p E_j{}^q + \\
&\quad + \beta^k(e_k)^p\partial_p B_{ij} - 2K_p{}^p\alpha B_{ij} + A^p E_j{}^q\epsilon_{pqi} + A^p E_i{}^q\epsilon_{pqj} + \\
&\quad + (3/2)\alpha B_j{}^p K_{pi} + (3/2)\alpha B_i{}^p K_{pj} - \alpha B_p{}^q K_q{}^p\delta_{ij} + \\
&\quad + (\alpha/2)E^{pq}\epsilon_{qrj}\Gamma^r{}_{pi} + (\alpha/2)E^{pq}\epsilon_{qri}\Gamma^r{}_{pj} + \\
&\quad + (\alpha/2)E_j{}^p\epsilon_{qri}\Gamma^r{}_p{}^q + (\alpha/2)E_i{}^p\epsilon_{qrj}\Gamma^r{}_p{}^q;
\end{aligned}
$$

- Contracting with $(e_0)^\tau(e_0)^\nu h^\rho{}_i \rightarrow$ constraint equation for E,

$$
(e_k)^p\partial_p E^k{}_i + E_{pi}\Gamma^q{}_q{}^p + E_{pq}\Gamma^q{}_i{}^p - B_p{}^q\epsilon_{qri}K^{pr} = 0;
$$

- Contracting with $(e_0)^\nu\epsilon^{i\rho\tau} \rightarrow$ constraint equation for B,

$$
(e_k)^p\partial_p B^{ki} - B_p{}^q\Gamma^p{}_q{}^i + B_p{}^i\Gamma^q{}_q{}^p + E_{pq}\epsilon^{pri}K_r{}^q = 0.
$$

Using the projection and orthogonality rules in respect to e_0 and the definitions for the connection-coefficients, one obtains a system of 38 evolution equations in component form, for the lapse (1), spatial derivative of the lapse (3), spatial vectors of the tetrad (9), extrinsic curvature (6), connection-coefficients (9), the electric (5) and magnetic (5) components of the Weyl tensor, and related constraints. The system above, although it has a very simple algebraic structure compared to that of many other reduced systems in tetrad formalism, offers all the information about the four-dimensional metric given in terms of the frame coefficients, the four-dimensional connection, the Weyl tensor, the geometry of the slices and their embedding.

3.2.2 The FN System

The Friedrich-Nagy system is a frame based first order formulation of the Einstein equations, that has been shown to yield a well-posed initial boundary value problem. The system is based on the 3+1 tetrad decomposition, where the time-like unit vector field e_0, in respect to which the decomposition is performed, is extended to an orthonormal frame $((e_0)^\mu, (e_i)^\mu)$. The metric $g_{\mu\nu}$ and all the other fields are represented in terms of the frame e_ν.

The FN formulation is based on the Einstein vacuum equations (translated into: the curvature of the connection is the Weyl curvature), the contracted Bianchi identity and the torsion-free condition for the connection. Performing a hyperbolic reduction, similar to the one presented in Section 3.2.1, one obtains a representation

of the Einstein equations in the form of a symmetric hyperbolic system of evolution equations. Moreover one chooses an *adapted gauge*, motivated by the choice of maximally dissipative boundary conditions.

One assumes a boundary at $\{z = constant\}$ and foliates the interior domain by time-like hypersurfaces T_c given by $\{z = constant\}$. The tetrad will be adapted to this foliation such that e_3 is orthogonal to T_c, which implies

$$(e_{i'})^3 = 0,$$

and $e_3{}^3 > 0$. As e_3 is chosen to be the unit normal, the extrinsic curvature $\gamma_{i'}{}^3{}_{j'}$ on T_c has to be a symmetric tensor

$$\Gamma_{i''}{}^3{}_{j''} - \Gamma_{j''}{}^3{}_{i''} = 0,$$
$$\Lambda^3{}_{j''} - \chi_{j''}{}^3 = 0.$$

The mean extrinsic curvature of T_c is prescribed as a function of the coordinates and used to eliminate the connection coefficient $\gamma_0{}^3{}_0$ from the equations

$$a^3 = \Gamma_1{}^3{}_1 + \Gamma_2{}^3{}_2 + f.$$

The variation of e_0 within T_c is prescribed by the functions $F^{i''}$, according to $D_{e_0} e_0 = F^{i''} e_{i''}$. This fixes the connection coefficients $\gamma_0{}^{i''}{}_0$ as

$$a^{i''} = F^{i''}.$$

The condition for the frame vectors $e_{i''}$ to be Fermi transported with respect to the induced connection on T_c translates into $\gamma_0{}^{i''}{}_{j''} = 0$, namely

$$\Lambda^{i''}{}_{j''} = 0.$$

The tetrad vector e_0 represents the time-flow

$$(e_0)^\mu = e_0(x^\mu) = \delta_0{}^\mu.$$

The resulting system (see Appendix 9.8 for the full system) takes the form

$$\mathbf{A}^0 \partial_t \mathbf{u} + \mathbf{A}^i \partial_i \mathbf{u} + \mathbf{B}(\mathbf{u}, F) = 0,$$

where $F = (f, F^A, \partial_\mu f, \partial_\mu F^A)$ represents the gauge source functions and their derivatives. The matrices $\mathbf{A}^0, \mathbf{A}^i$ are symmetric and depend on the coordinate components of the frame.

As shown by Friedrich and Nagy [47], the FN evolution equations form a symmetric hyperbolic system, with derivatives transversal to the boundary contained only in the Weyl subsystem, to which we can impose maximally dissipative boundary conditions. The IBVP for the evolution system is well-posed, which

means that if one chooses initial data on the hypersurface S, that satisfies the constraints, and solves the symmetric hyperbolic system of evolution equations, with maximally dissipative boundary conditions, one obtains a unique solution of the Einstein equation that depends continuously on the initial data. Moreover, the symmetric hyperbolic subsidiary system leads to a unique solution, therefore the constraints will be satisfied at all times if they are satisfied initially.

3.3 Discussion

We presented an overview of various formulations of the Einstein equations used in Numerical Relativity. Our choice of systems includes three metric based formulations: the Z3, the Z4 (first order in space) and the BSSN (second order in space), and a tetrad based formulation, the FN (first order in space). The apparently small differences in their analytical structure, will translate into obvious differences when subjected to numerical tests, as we will see in the following chapters.

We found that the Z3 system provides an approach that is especially well suited for numerical evolutions in spherical symmetry, as it allows stable long term black hole evolutions in normal coordinates (Chapter 6). The system can be easily brought into a spherically symmetric form, without the complications present in the BSSN, as it does not use a conformal decomposition.

An equivalence between the BSSN and the Z3 system (with $n = 4/3$), can be obtained if one considers the following transformation

$$\tilde{\Gamma}_i = -\tilde{h}_{ip}\partial_q\tilde{h}^{pq} + 2Z^i,$$

which is consistent with the definition of $\tilde{\Gamma}^i$ Eq. (3.28) for the physical solutions ($Z_i = 0$).

The BSSN is currently the most used formulation in binary black hole evolutions. Despite this success, questions regarding the properties and behavior of this formulations are raised by the poor results obtained in standard numerical relativity tests (Chapter 4).

Even though the Z3 represents an improvement over the standard ADM system, as it introduces the momentum constraint as extra dynamical field into the evolution formalism, general covariance is still broken for this system. In this respect, the Z4 is superior, as it incorporates also the energy constraint in the evolution system, through a covariant four-vector Z_μ. The 'zero' vector Z_μ should vanish for the true Einstein solutions, the only constraints are algebraic, and the full set of field equations is used during the evolution.

However, monitoring the Z_μ vector in numerical evolutions, we noticed that it deviates from the initial zero value. Due to truncation errors, the resulting numerical code will actually deal with the extended set of Einstein solutions. This the

price one generally has to pay for performing an unconstrained evolution. But the advantage that the Z systems offer, over other 3+1 metric systems like the BSSN, is controlling the growth of these constraint violations. The Z4 proved to be very robust for long term 3D black hole simulations in normal coordinates (Chapter 6).

A different style of 3+1 formulation is the FN system, a first order in space and time tetrad based formalism. However, there are some common points between the FN and the ADM based metric systems, as the structure of the FN implies a free evolution approach and it uses the technique of adding constraints to evolution equations in order to obtain a symmetric hyperbolic formulation. The main advantage of the FN system relies in the fact that the IBVP for the evolution system has been proven to be well-posed. Even though it performs well in the standard numerical tests (Chapter 4), this system is not currently used in production runs. One of the reasons could be the fact that this formulation is valid only the vacuum case, where $R_{\mu\nu\rho\tau} = C_{\mu\nu\rho\tau}$. Extensions of the FN system which include matter terms have not yet been explored.

Chapter 4

Standard Testbeds for Numerical Relativity

The Apples with Apples Alliance (AwA) has been the first community effort to produce a project for cross-validation of Numerical Relativity codes. The results, published in 2003 and 2008, follow two projects of code comparison, realized with a broad participation of the community. The data was gathered and organized in a CVS repository for checking in test results and via the web pages of AwA (http://www.ApplesWithApples.org).

This pioneering work had a double success. First, it offered an objective view over the status of the formulations and implementations used in Numerical Relativity, impulsing improvements on an analytical level, like constraint damping algorithms, and the development of numerical methods. Second, it opened the way for new large scale collaborations, like the current comparison projects for gravitational wave templates.

In this chapter, we present a review of the AwA tests and the main results that followed. We focus on numerical simulations performed with the formulations presented in Chapter 3, namely the Kranc implementation of the Z4, BSSN and FN systems [54], [55], [56].

4.1   Overview of Numerical Tests

As presented in Chapter 3, the decomposition of the Einstein equations does not lead to a unique formulation of the evolution system. Most formalisms currently used in Numerical Relativity (NR) simulations are based on the free evolution approach.

The problem of choosing the best suited formalism for numerical evolutions proved to be a complicated task. A fair comparison between different formulations, had to concentrate on the behavior of the systems of evolution equations in

an identical numerical set-up, in order to minimize the difference coming from various choices of gauge, boundaries and numerical methods.

The first effort of providing a practical collection of standard tests for NR was proposed in [57]. After analyzing the results of these tests, a second round of comparison has been proposed in [55], using the original testbeds with revised specifications and an additional test.

The purpose of the AwA tests was to give a comparison between various formulations in a standard setting. In order to make the tests computationally affordable to all the NR groups, they were limited to vacuum spacetimes and periodic boundaries.

The criteria proposed for code comparison were:

- *Stability* implies that the growth of the errors should be less than exponential;

- *Accuracy* which depends on the analytic formulation, for example on the treatment of the constraints;

- *Robustness* requires that a code should behave well in a variety of spacetimes, using different gauges;

- *Efficiency* is related to the computational costs of a specific implementation;

- *Degree of mathematical understanding* consists in the possibility to mathematically prove certain features of the evolution systems, like well-posedness.

The standard tests proposed by the AwA community focus mainly on stability, accuracy and robustness.

The tests address a broad range of formulations. The output variables are chosen such that they offer inside about the characteristic behavior of the specific system and allow a comparison with other codes solving the same problem. The time a code runs before crash is not an accepted criteria, unless it is accompanied by an indication of how accurate the code still reproduces the intended physics.

4.2　Implementation and Results

The four tests chosen for code comparison in the initial round were: the Robust Stability, the Gauge Wave, the Linearized Wave and the Gowdy Wave.

The Robust Stability test uses random constraint violating initial data in the linearized regime, which simulates machine error. The noise is added as perturbations around Minkowski space and it proved to be very efficient in revealing unstable modes.

The Gauge Wave testbed is based on an exact wave-like solution, constructed as a nonlinear gauge transformation of the Minkowski spacetime. Nonlinear effects and nontrivial geometry can trigger continuum instabilities in the equations.

The Linearized Wave test proposes as initial data a solution to the linearized Einstein equations. It has physical importance, as it can be used to check the amplitude and phase errors of a gravitational wave as it propagates on the 3-torus.

The Polarized Gowdy testbeds are non-linear wave tests based on exact solutions describing an expanding universe containing plain polarized gravitational waves. The test is carried both in the expanding and collapsing time directions.

In the second round of tests, an additional shifted version of the Gauge Wave test has been included, in which a non-vanishing shift is used to complete the four original tests with periodic boundary conditions.

The initial data is specified by providing the 4-metric of the space-time, or the Cauchy data (3-metric and extrinsic curvature) and the choice of gauge. The physical domain is a cube and the evolution is performed in a specific direction (x, y, z) or diagonal, so the 3D simulations reduce to 1D or 2D runs. All tests use periodic boundary conditions, equivalent to an evolution on a compact spatial manifold with the topology of a 3-torus in the absence of boundaries.

The time evolution algorithms are a third order Runge Kutta integrator or a second order iterative Crank-Nicholson method. The spatial discretization is performed using finite difference algorithms plus Kreiss Oliger dissipation. The simulation domain is a cube of side d, equal to one wavelength, set up to extend an equal distance in the positive and negative directions of each axis. The resolution along a given direction is $dx = d/n$, where n is the number of points. For the tests with one-dimensional features, one considers a minimum number of points in the trivial directions. The size of the time step is given in terms of the grid size, such that the Courant limit is satisfied. A final time for the tests is chosen as $T = 1000$ crossing times (CT), i.e. $2 \times 10^5 \rho$ time steps, where $\rho = 1$ is the lowest resolution and $\rho = 4$ the highest. The standard output is set to every 10 CT and the output quantities have physical or numerical motivations.

One considers for the gauge evolution a harmonic slicing Eq. (2.26) and normal coordinates Eq. (2.29), in all the tests beside the Shifted Gauge Wave, where the evolution of the shift is given by the harmonic condition Eq. (2.27).

4.2.1   The Linear Wave Testbed

In the Linear Wave Test specifications, the initial spatial metric and extrinsic curvature are given by a transverse, trace-free perturbation with components

$$ds^2 = -dt^2 + dx^2 + (1 + H)\, dy^2 + (1 - H)\, dz^2, \tag{4.1}$$

where

$$H = A \sin\left(\frac{2\pi(x - t)}{d}\right). \tag{4.2}$$

It describes a linearized plane wave traveling in the x-direction.
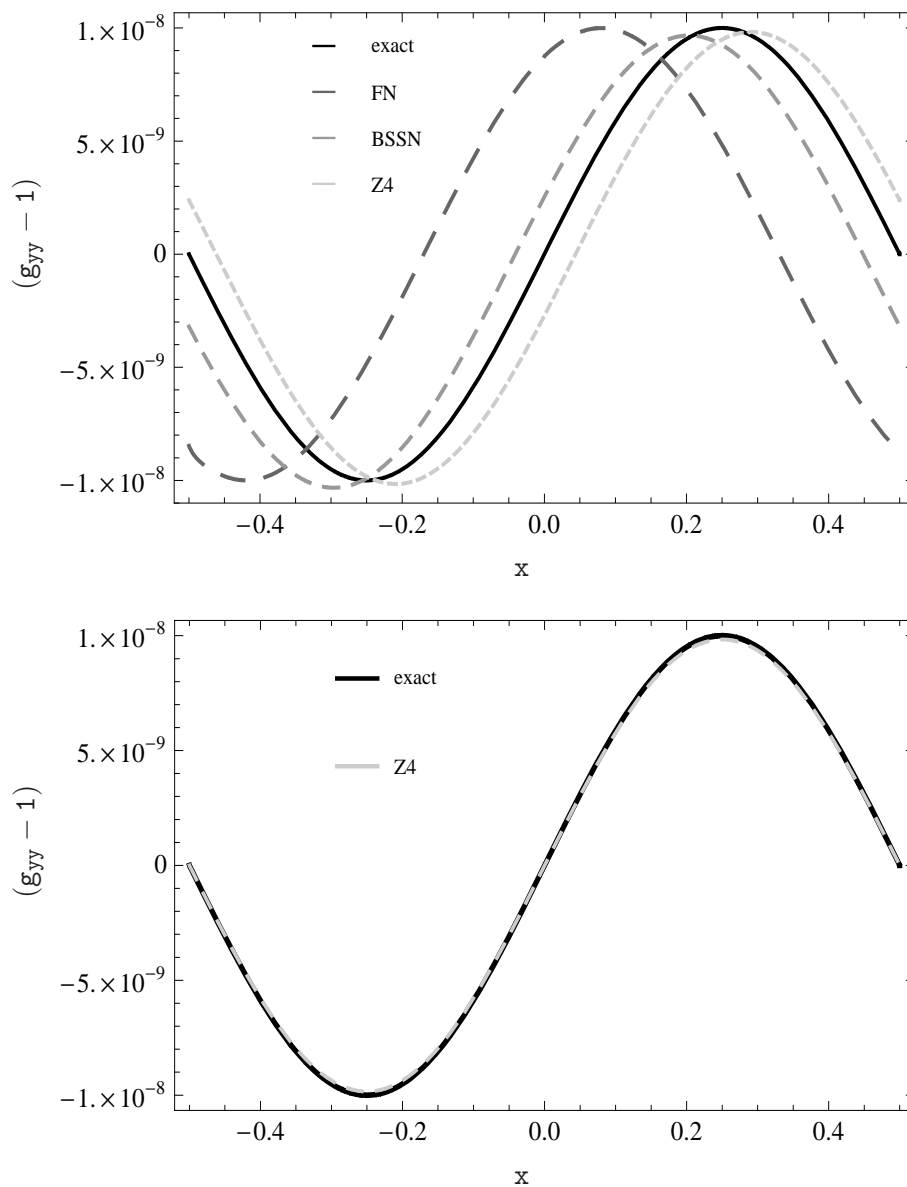
Figure 4.1. Illustration of the g_{yy} variable on the x-axis, in a 1D Linear Wave test with amplitude $A = 0.1$ and resolution $\rho = 4$, at $time = 1000$ CT when the simulation was stopped. Upper panel: Performance of the codes using 2nd order finite differencing. The plots correspond to the analytic solution (black continuous), FN (dark-grey long-dashed), BSSN (medium-grey medium-dashed), Z4 (light-grey short-dashed). Lower panel: Performance of the Z4 code using 4th order finite differencing plus 3rd order dissipation. The plots correspond to the analytic solution (black continuous) and Z4 (grey dashed).
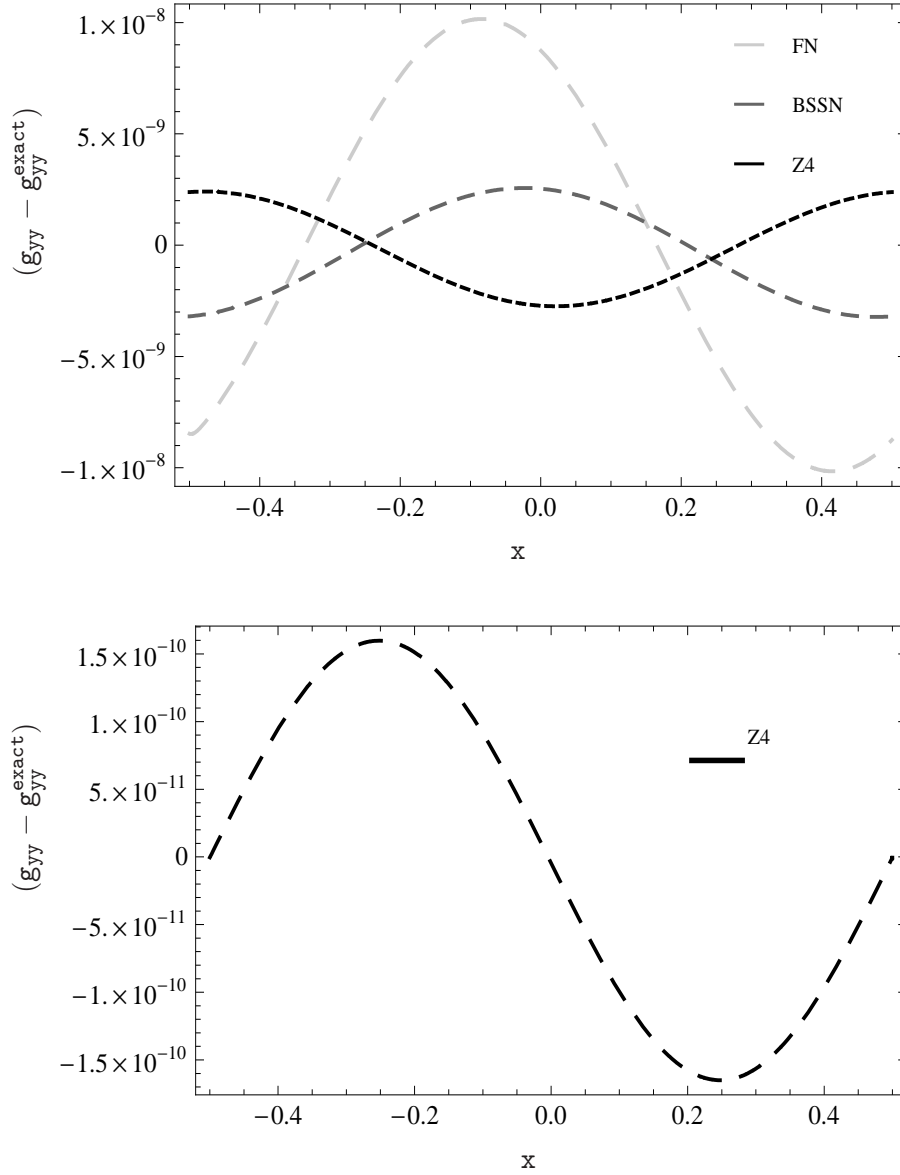
Figure 4.2. Illustration of the error in g_{yy} variable on the x-axis, in a 1D Linear Wave test with amplitude $A = 0.1$ and resolution $\rho = 4$, at $time = 1000$ CT, when the simulation was stopped. Upper panel: Performance of the codes using 2nd order finite differencing. The plots correspond to the FN (light-grey long-dashed), BSSN (medium-grey medium-dashed), Z4 (black short-dashed). Lower panel: Performance of the Z4 code using 4th order finite differencing plus 3rd order dissipation.

The nontrivial components of extrinsic curvature are

$$K_{yy} = -\frac{1}{2}\partial_t H, \quad K_{zz} = \frac{1}{2}\partial_t H. \tag{4.3}$$

The test is performed with amplitude $A = 10^{-8}$, so that quadratic terms are of the order of numerical round-off.

The Linearized Wave test checks the ability of a code to propagate a linearized gravitational wave, which is a necessary attribute for reliable wave extraction. One is interested in the accuracy of the code when propagating the amplitude and phase of the wave.

4.2.1.a   Numerical Results and Comparison

The harmonic codes (*Abigel_harm* and *HarmNaive*) show the best behavior in wave tests [55]. They provide a benchmark for the accuracy that can be obtained with a specific resolution. An interesting result is that a weakly hyperbolic implementation of the generalized harmonic system (*HarmNaive*), does not introduce large errors in this test. This illustrates that linearized tests are not efficient in pointing instabilities related with weakly hyperbolic systems, as the polynomial modes grow only secularly in time. The Linear Wave Test should be viewed as a double check for stability, as it can reveal whether excessive dissipation was used in the Robust Stability Test in order to obtain long term performance.

In Fig. (4.1) one can see a comparison of the 1D wave profiles after 1000 CT, plotted with the exact wave for reference. The numerical results show a good match in the amplitude, but they all suffer a phase delay. This kind of error, specific to the simulations using a 2nd order in space algorithm, can be decreased by employing higher order finite differencing, as exemplified in Fig. (4.2) for the Z4 system.

The Z4, BSSN and FN systems show a good accuracy for the amplitude of the wave, but the FN shows much larger errors for the phase. There are no signs of rapidly growing Hamiltonian constraint violations, which indicate that the implementations are stable.

4.2.2   The Gauge Wave Testbed

The Gauge Wave test is based on the 4-metric

$$ds^2 = (1 - H)(-dt^2 + dx^2) + dy^2 + dz^2, \tag{4.4}$$

where H is given by Eq. (4.2), obtained from the Minkowski metric $ds^2 = -d\hat{t}^2 + d\hat{x}^2 + d\hat{y}^2 + d\hat{z}^2$ by a nonlinear gauge transformation of the type

$$
\begin{aligned}
\hat{t} &= t - \tfrac{Ad}{4\pi} \cos\left(\tfrac{2\pi(x-t)}{d}\right), \\
\hat{x} &= x + \tfrac{Ad}{4\pi} \cos\left(\tfrac{2\pi(x-t)}{d}\right), \\
\hat{y} &= y, \\
\hat{z} &= z.
\end{aligned}
$$

This describes a sinusoidal gauge wave of amplitude A, propagating along the x-axis. The extrinsic curvature, calculated as $K_{ij} = -\frac{1}{2\alpha}\mathcal{L}_t h_{ij}$ is given by

$$
\begin{aligned}
K_{xx} &= \frac{\partial_t H}{2\sqrt{1-H}} = -\frac{\pi A}{d}\frac{\cos\left(\frac{2\pi(x-t)}{d}\right)}{\sqrt{1 - A\sin\left(\frac{2\pi(x-t)}{d}\right)}}, \\
K_{ij} &= 0 \qquad \text{otherwise.} \tag{4.5}
\end{aligned}
$$

The original test specified the amplitudes $A = 0.01$ and $A = 0.1$. Later, a higher amplitude $A = 0.5$ was proposed in order to test the non-linear regime. The time coordinate t in the metric is harmonic and the gauge speed is the speed of light.

The test contains several sources of growing errors coming from the solutions of the continuum problem [2]. One complication comes from the related flat metric

$$
ds^2 = e^{\lambda t}(1 - H)(-dt^2 + dx^2) + dy^2 + dz^2,
$$

which obeys the harmonic coordinate conditions for any λ. Even though the initial data for the Gauge Wave test implies $\lambda = 0$, the numerical errors excite this instability and lead to an exponential growth in the amplitude of the wave. So $H \to e^{\lambda t}H$ represents a harmonic gauge instability of the Minkowski space with periodic boundary conditions. Other instabilities depend on the particular formulation. The discretization schemes can also introduce instabilities in the form of high frequency modes, which in the case of well-posed systems can be cured by artificial dissipation.

4.2.2.a   Numerical Results and Comparison

As in the case of the Linear Wave test, the harmonic codes show the best behavior. The reason could be the analytical structure of these systems, which use the harmonic coordinates to transform the Hamiltonian constraint into an evolution equation. A comparison between the flux conservative (FC) (*Abigel_harm*) and the non-FC (*HarmNaive*) forms of the harmonic system, leads to the conclusion that the exponential modes of the form $e^{\lambda t}H$ are suppressed in the FC implementation [55]. The main source of errors is the phase error, which converges to zero.
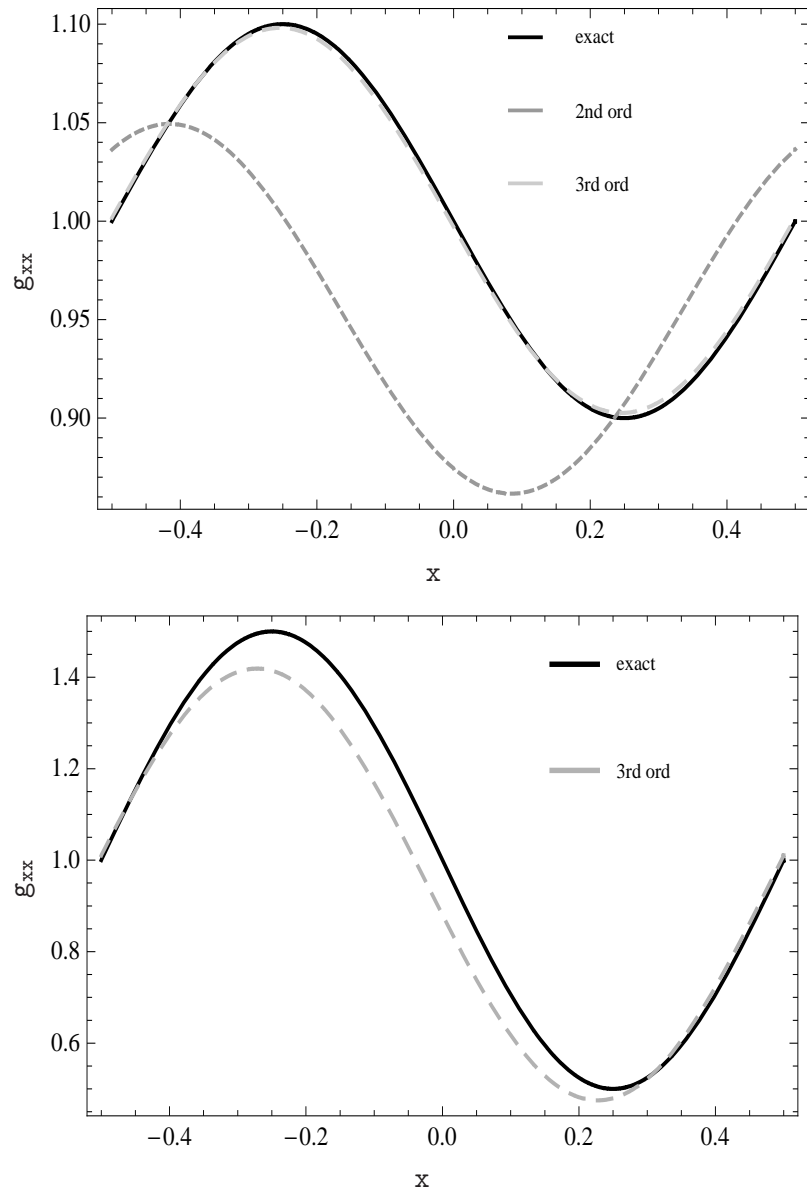
Figure 4.3. Illustration of the Z4 g_{xx} variable on the x-axis, in a 1D Gauge Wave test with amplitudes $A = 0.1$ (upper panel) and $A = 0.5$ (lower panel), for resolution $\rho = 4$. The continuous plot corresponds to the analytic solution, the short-dashed plot to 2nd order finite differencing and the long-dashed plot to 4th order finite differencing plus 3rd order dissipation, at $time = 1000$ CT when the simulation was stopped.
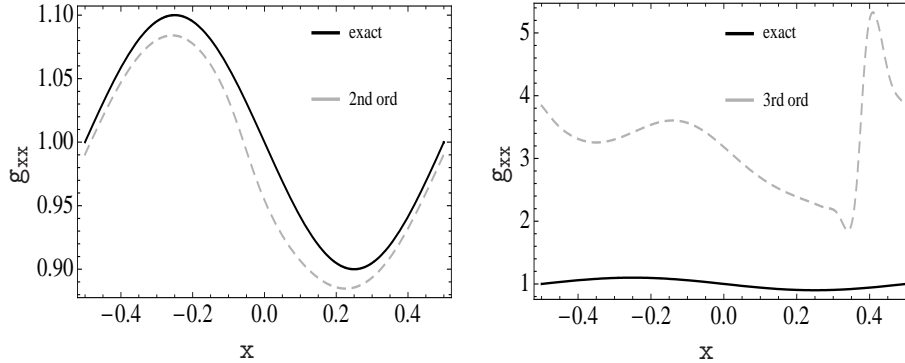
Figure 4.4. Illustration of the KrancBSSN g_{xx} variable on the x-axis, in a 1D Gauge Wave test with amplitude $A = 0.1$ and resolution $\rho = 4$. The continuous plot corresponds to the analytic solution, the dashed one to 2nd order finite differencing at $time = 20$ CT (left panel) and 4th order finite differencing plus 3rd order dissipation, at $time = 80$ CT (right panel).

The Gauge Wave results of the Z4 system are as remarkable as the FC version of the generalized harmonic codes (*Abigail_harm*). The left panel in Fig. (4.3) shows the case of medium amplitude $A = 0.1$. One can notice the significant dissipation and dispersion errors when using a second order finite differencing method. The problems diminish when passing to a third order method, which gets rid of the dispersion error and only a very small amount of numerical dissipation is visible. The right panel in Fig. (4.3) shows the large amplitude case $A = 0.5$, well inside the non-linear regime. The only errors that we could notice, were a small amplitude damping in the wave profile and a small decrease in the mean value of the lapse.

The Z4 exhibits the best behavior when compared with other systems in the same class, like versions of the BSSN, NOR [58], or KST [59] systems. Recent KST results with the Gauge Wave initial data $A = 0.5$, show a phase shift due to cumulative dispersion errors after 500 crossing times, and a growing amplitude mode [60], comparable with the one reported for harmonic systems which do not have a flux conservative form.

The KrancBSSN implementation shows a rapid growth of the Hamiltonian constraint violation. One can observe in Fig. (4.4) the behavior of the wave profile for the g_{xx} component of the metric. The runs were performed with 2nd and 4th order finite difference methods, plus KO dissipation in order to damp the high frequency modes. The use of higher order discretization schemes led to longer evolutions, but it could not prevent the crash.

Actually none of the BSSN implementations showed satisfactory behavior in this test. Analyzing results obtained with other BSSN implementations, one can conclude that this test is a clear example of a case where running 1000 crossing
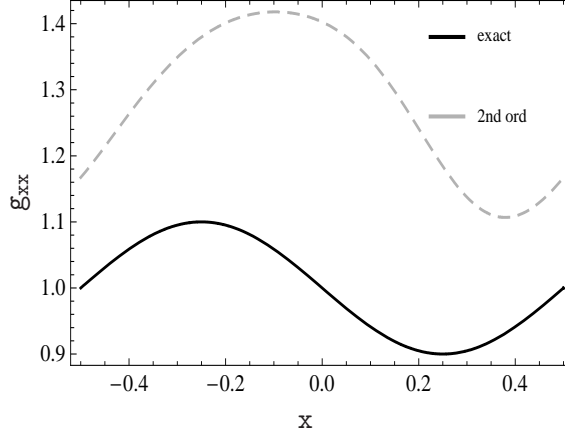
Figure 4.5. Illustration of the FN g_{xx} variable on the x-axis, in a 1D Gauge Wave test with amplitude $A = 0.1$, resolution $\rho = 4$. The continuous plo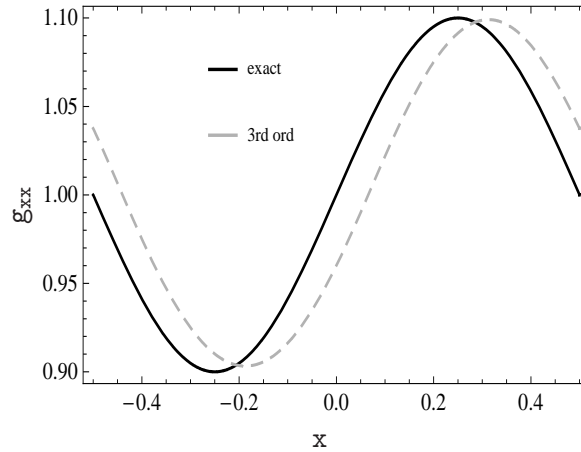t corresponds to the analytic solution and the dashed one to 2nd order finite differencing, at $time = 1000$ CT when the simulation was stopped.

times, with an apparent stable evolution, does not mean that the implementation actually passed the test. The results should be accompanied by a comparison with the exact solution, or plots of the error in the wave form, as presented in [55]. The problem with the BSSN in this test seems to be mainly the $e^{\lambda t}H$ instability, related with the choice of harmonic gauge, and the failure to control the growth of the constraint violations in the BSSN formulation.

Besides the generalized harmonic and the Z4 flux conservative implementations, the FN was the only other code that was able to run the full test up to 1000 crossing times, with the medium $A = 0.1$ amplitude. However, one can notice in Fig. (4.5) the long-wavelength growth due to the $e^{\lambda t}H$ instability of the wave amplitude.

4.2.3 The Shifted Gauge Wave Testbed

The shifted gauge wave can be obtained from the Minkowski metric $ds^2 = -d\hat{t}^2 + d\hat{x}^2 + d\hat{y}^2 + d\hat{z}^2$ using a harmonic coordinate transformation of the type

$$
\begin{aligned}
\hat{t} &= t - \frac{Ad}{4\pi}\cos\left(\frac{2\pi(x-t)}{d}\right), \\
\hat{x} &= x - \frac{Ad}{4\pi}\cos\left(\frac{2\pi(x-t)}{d}\right), \\
\hat{y} &= y, \\
\hat{z} &= z.
\end{aligned}
$$

This leads to the following Kerr-Schild metric

$$ds^2 = -(1 - H)dt^2 + (1 + H)dx^2 - 2H \, dx \, dt + dy^2 + dz^2,$$

where $\beta = -\frac{H}{1+H}$, $\alpha = \frac{1}{\sqrt{1+H}}$, and H is given by Eq. (4.2). The extrinsic curvature is calculated as

$$
\begin{aligned}
K_{xx} &= \frac{\partial_t H}{2\sqrt{1 + H}}, \\
K_{ij} &= 0 \qquad \text{otherwise.}
\end{aligned}
\tag{4.6}
$$

This metric describes a shifted gauge wave propagating along the x-axis. The test is run in a harmonic gauge with amplitude $A = 0.1$ in 1D form.

The Shifted Gauge Wave test identifies two types of instabilities. One is similar to the gauge wave case and arises from the λ-parameter family of vacuum metrics, which reduces to the shifted gauge wave for $\lambda = 0$,

$$ds_\lambda^2 = e^{\lambda t}(-dt^2 + dx^2) + dy^2 + dz^2 + Hk_\alpha k_\beta dx^\alpha dx^\beta,$$

where $k_\alpha = \partial_\alpha(x - t) = (-1, 1, 0, 0)$. This metric has a harmonic driving term $\Gamma^\alpha = -\lambda H k^\alpha$. A gauge satisfying this condition is expected to excite instabilities.

Another type of instability is specific to implementations based on a standard reduction of the Einstein equations to harmonic form, where the metric

$$d\hat{s}_\lambda^2 = -dt^2 + dx^2 + dy^2 + dz^2 + \left(H - 1 + e^{\lambda \hat{t}} \right) k_\alpha k_\beta dx^\alpha dx^\beta, \tag{4.7}$$

satisfies the reduced harmonic equations, but violates the harmonic constraints, as $\Gamma^\mu = \lambda e^{\lambda \hat{t}} k^\mu$. Ref. [2] offers a detailed discussion of these instabilities and a way of constructing constraint adjustments for harmonic formulations. These damping terms proved to be very efficient when tested with the *Abigail_harm* implementation, as the growing modes were suppressed in long term evolutions.

In the standard harmonic formulations, the Einstein equations are satisfied only indirectly, through the harmonic conditions $\Gamma^\mu = 0$. Errors in Γ^μ, of the form described above, are expected to excite instabilities. This is also the case for the Z4 formalism, as the equivalence with the harmonic systems can be translated into $Z^\mu = -\Gamma^\mu/2$.

4.2.3.a   Numerical Results and Comparison

As in the Gauge Wave test, the KrancBSSN results are not satisfactory. One can see in Fig. (4.6) results of the Hamiltonian constraint violation for an amplitude $A = 0.1$. The code shows second order convergence only for a few crossing times. An instability develops that crashes the code rather quickly. The other BSSN implementations show similar problems.
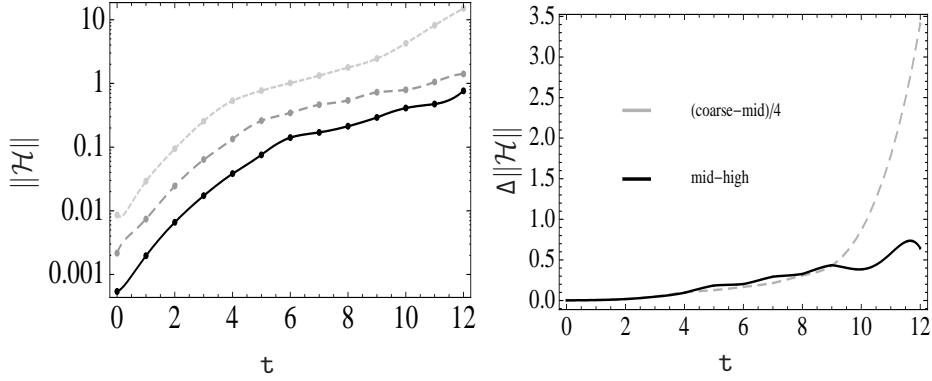
Figure 4.6. Illustration of the BSSN performance in a 1D Shifted Gauge Wave test with amplitude $A = 0.1$ and 2nd order finite differencing plus 3rd order dissipation. Left Panel: The L_2-norm of the Hamiltonian constraint on a logarithmic scale plotted as a function of time, for resolutions $\rho = 1$ (light-grey short-dashed), $\rho = 2$ (dark-grey long-dashed), $\rho = 4$ (black continuous). Right Panel: Convergence test in the L_2-norm of the Hamiltonian constraint plotted as a function of time for resolutions $\rho = 1, 2, 4$. Second order convergence is lost after a few crossing times.

The Z4 results are good, but not so satisfactory as for the Gauge Wave Test. We were able to pass the test performing runs until 1000 crossing times, in the case of medium amplitude $A = 0.1$, high resolution $\rho = 4$ and fourth order finite differencing, plus third order dissipation. One can see in Fig. (4.7) the behavior of

Figure 4.7. Illustration of the Z4 g_{xx} variable on the x-axis, in a 1D Shifted Gauge Wave test with amplitude $A = 0.1$, resolution $\rho = 4$. The continuous plot corresponds to the analytic solution and the dashed one to 4th order finite differencing plus 3rd order dissipation, at $time = 1000$ CT when the simulation was stopped.

the wave profile for the g_{xx} component of the metric, which has a higher dispersion error than in similar runs with the Gauge Waves test.

In the case $A = 0.5$, one can notice the presence of strong violations in the momentum and energy constraints (Z_i, θ variables) and instabilities similar to the ones reported by the harmonic systems. The time at which the code crashes grows with resolution and the implementation exhibits a convergent behavior.

4.2.4 Other Tests

The Robust Stability (RS) test was designed to detect unstable evolution algorithms. It was a crucial test in the first AwA paper, in a context where the theory of well-posedness existed only for fully first order systems. The development of a well-posedness theory for first order in time, second order in space formulations of the Einstein equations, offers now solid ground for numerical stability criteria. As the test involves just the principal part of the evolution system, it can be used to detect weakly hyperbolic systems. In the case of well-posed continuum formulations, the RS test can give a 'pass' or 'fail' result for the numerical algorithm.

In practice, one tests the numerical stability in the linear constant coefficient regime. Perturbations around Minkowski space are generated with random numbers applied at each grid point, to every variable. The idea behind the RS test is: if a code that can not stably evolve such random noise, at machine precision ($\pm 10^{-10}$), will not be able to evolve smooth initial data. All three systems considered here for comparison passed this test.

The Gowdy Wave test uses as initial data an exact solution for an expanding vacuum universe containing a polarized gravitational wave propagating around a 3-torus T^3. The metric has the form

$$ds^2 = t^{-1/2} e^{\lambda/2}(-dt^2 + dz^2) + t(e^P dx^2 + e^{-P} dy^2), \qquad (4.8)$$

where $P(t, z)$ and $\lambda(t, z)$ depend periodically on z and the time coordinate t increases as the universe expands, with a cosmological type singularity at $t = 0$. Detailed specifications can be found in the second AwA paper, and were designed so that neither very large nor very small numbers enter in the initial data.

The Gowdy test is run in both future and past time directions, as analytical studies [61] and numerical experiments [62] indicate that the sign of the extrinsic curvature may have important consequences for constraint violation. The subsidiary system governing constraint propagation can lead to departure from the constraint hypersurface. A negative value of K (the expanding case) tends to damp constraint violation whereas a positive value (the collapsing case) can trigger constraint violating instabilities.

A comparison of the specific three systems considered above is not possible for this test. The results obtained with the KrancBSSN code show an unsatisfactory performance, while for the FN system are completely missing, as it is non-trivial

to specify the initial data in terms of the tetrad. One can see [55] the for results obtained with other systems.

4.3   Discussion

In a time when the binary black hole problem is solved in Numerical Relativity and the community supplies waveforms for gravitational wave detectors, one can ask what is point of this code comparison and if one can still extract useful information out of it. The first round of AwA tests were designed to exhibit code instability and inaccuracy. Even though there are codes which can evolve binary black holes without signs of instabilities, the same implementations have difficulties or even fail with some of the testbeds presented above. The theoretical understanding of what works in numerical relativity is still an open problem.

The continuous development of numerical methods in parallel with formulations of the continuum problem, the construction of physically relevant initial data and the analysis of the physics behind the results, are current investigation tasks. The lack of comparison with the experiment, make the problems even more difficult.

This first round of tests was a good start for establishing methods of code verification. The tests were conceived such that they provide useful and relevant results, but they are in the same time easy to implement and cheap in terms for computational time and resources. The analysis of the output led to an improvement of the tests and to a better understanding of the systems. New benchmarks have been established for the performance of the codes in the wave tests. Deficiencies were revealed for various implementations.

The Robust Stability test is a pass/fail test, which was passed by all three well-posed implementations considered above. The Linear Wave test provided a good comparison of the amplitude and phase errors in the wave profiles. All the formulations showed a satisfactory behavior, which could be further improved by employing higher order numerical methods. The Gauge Wave test was a check for the capacity of the formulations to suppress the long wavelength nonlinear instabilities arising from the analytical problem and the Shifted Gauge wave provides a full comparison of formulations, when shift is involved.

The BSSN implementations showed unsatisfactory results for the last two tests. This problem is most likely related with the fail to control the Hamiltonian constraint violation and maybe to the fact that system is not written is flux conservative form.

The Z4 formalism shows good results, comparable with the generalized harmonic formulations. This success could be explained by the analytical form of the Z4 system, which transforms the constraints into evolution equations for the extra Z variables, allowing for a mechanism to control the errors. The equivalence with

the harmonic systems $Z^\mu = -\Gamma^\mu/2$ suggests that similar constraint adjustments could be used to improve performance in the Shifted Gauge Wave high amplitude case. The use of a flux conservative version of the system seems to be another important ingredient for long term stable evolutions.

The analytical structure of the subsidiary system in the FN formulation allows the preservation of the constraints in long term simulations. This explains the positive results obtained in the wave tests. However, one can notice the long-wavelength growth due to an instability in the wave amplitude, which is typically excited by non-flux conservative formulations.

These results have already led to code improvements, stimulating the development of numerical methods and the use of higher order finite difference schemes. The wave tests show that a numerical algorithm with minimum third order accuracy should be used, in order to avoid large phase errors. A flux conservative form of the system proved to be an important ingredient, especially in cases where the shift is evolved. The need to carry out these tests with a variety of formulations has led to the development of symbolic code generation (Kranc [63, 64]).

The next generation of code comparison already addresses black hole problems. Even though there are only two formalisms (BSSN and generalized harmonic) currently used in order to numerically generate wave-forms, a comparison in the performance of different implementations is still an interesting subject. The guidelines of the future Numerical Relativity effort for code comparison and improvement started with the Samurai project [65], focused on comparing binary-black-hole waveforms, and continued with the NINJA (Numerical Injection Analysis) project [18]. Produced in collaboration with the data analysis community, NINJA is the first study of the sensitivity of existing gravitational wave search algorithms, using gravitational waveforms from binary black hole coalescence produced by ten numerical relativity groups. This work provides a foundation for future analysis and extended projects.

Part III

Numerical Methods and Applications

Chapter 5

Numerical Aspects

Fundamental field theories are most commonly formulated using tensor fields. Mathematically, the fields are continuous functions of space and time and their dynamics is studied using partial differential equations (PDE). An exact solution to these PDE's is known only for some idealized cases, so numerical approximations are required in order to solve the equations in general cases.

In this chapter, we present the basic ideas behind the numerical techniques used in Numerical Relativity, focusing on the Centered Finite Volume method developed in the Palma Relativity group [23].

5.1 Standard Numerical Recipes

From all the currently known methods for spatial discretization, the Numerical Relativity community focuses on the use of finite differencing (FD), finite volumes (FV) and spectral methods. Spectral methods expand the solution as a linear combination of some base functions and then solve for the coefficients of this expansion. FD and FV methods are based on the idea of discretizing the spacetime using different strategies, as the FV replaces the continuum with a set of discrete points which form a grid, while the FV split the domain of dependence of the functions into elementary cells.

5.1.1 Space discretization and Time integration

The most popular approach to solving non-linear systems of evolution equations is the method of lines (MoL), which decouples the treatment of space and time. It is based on the idea of discretizing first the spatial dimensions, while leaving the time dimension continuous, leading to a semi-discrete system. Then one can solve the resulting system of coupled ordinary differential equations using a time integration method. Some of the most common choices are the iterative Crank-Nicholson (ICN) and the third and fourth order Runge Kutta (RK) methods (Appendix 9.4).

Spatial discretization methods rely on finite difference algorithms or finite volumes, which reduce to FD plus some type of numerical dissipation. The even order methods (2nd, 4th, 6th order finite differencing) show mainly dispersion effects, while the odd order methods (1st, 3rd, 5th order dissipation algorithms) have as dominant error dissipative effects [39].

The FD numerical methods may become unstable when applied to solving steep profiles, for example a step function. This translates into high frequency oscillations. As these modes are already unresolved and furthermore accumulate truncation error, they can eventually lead to code crash. In order to solve this problem, one adds numerical dissipative terms to the finite difference operators, which act as filters, by damping the modes with wavelength similar and higher than the grid spacing. The standard way of adding dissipation is the Kreiss Oliger (KO) dissipation algorithm (Appendix 9.5.2).

A special form of numerical dissipation is the numerical viscosity used to deal with steep profiles in hydrodynamical simulations. The non-linearities in the Euler equations give rise to propagating discontinuities that arise even from smooth initial data, for example shocks, which are associated with the crossing of the characteristic lines. These discontinuities take the form of steep gradients in the variables. The dissipation will smooth out the shock into a few grid cells, so that it can be solved numerically.

The standard KO dissipation is not the best suited choice when dealing with steep gradients, which sometimes occur even in vacuum relativistic cases, as a dissipation method with constant coefficients will affect the numerical solution everywhere. One needs an adaptive viscosity term, that becomes larger in regions with steep profiles and minimal in the other regions. Special algorithms have been developed to deal with these problems.

High resolution shock capturing (HRSC) algorithms are a class of numerical methods specifically constructed to deal with discontinuous solutions in fluid dynamics. High order FV schemes of this type are designed to model piecewise continuous solutions, which can contain shock waves or any other kind of discontinuity that can be dynamically generated by the nonlinearities of the principal part of the equations.

We will consider in the following analysis strongly hyperbolic systems of the type

$$\partial_t \boldsymbol{u} + \partial_i \boldsymbol{F}^i = 0,$$

where the flux takes the form $\boldsymbol{F}^i = \boldsymbol{F}^i(\boldsymbol{u})$. The success of Shock-Capturing methods for these systems can be granted in the 1D case, if for the space direction n_i one can write

$$n_i \boldsymbol{A}^i = n_i \frac{\partial \boldsymbol{F}^i}{\partial \boldsymbol{u}},$$

and the characteristic matrix $\boldsymbol{M} = \boldsymbol{A}^i n_i$ has real eigenvalues and a complete set of

eigenvectors. This argument is not true in the multidimensional case, where every axis has its own characteristic matrix. As these matrices do not commute, there is no common base of eigenvectors that can be used. Strategies that try to mimic the 1D case are currently used in relativistic hydrodynamic codes.

5.1.2 Convergence and Stability

An important concept when dealing with approximate solutions is convergence. A numerical solution is only an approximation to the real solution. One needs to have an estimate of the error in the numerical calculation, in order to know how close the result is to the correct solution.

The error can be computed through a convergence test. This consists in performing the calculation for three resolutions $(dx_1, dx_2 = 2dx_1, dx_4 = 4dx_1)$ and computing the relative errors between the solutions. The global convergence factor as a function of time, can be computed using the L_2 norms of the difference between the solutions as

$$c(t) = \frac{\|u_{dx_1} - u_{dx_2}\|}{\|u_{dx_2} - u_{dx_4}\|}.$$

A local convergence factor can also be obtained by the same procedure, using the difference between the solutions (without taking the L_2 norm). One expects a factor of 2^n for an order n convergent scheme. Once the convergence factor is determined, one can perform a Richardson extrapolation in order to improve the rate of convergence [66].

Another important concept is stability, which implies that the solution should remain bounded after a finite time. Stability is the discrete version of the definition of well-posedness. As presented in Chapter 2, strongly hyperbolic systems are a subclass of hyperbolic systems for which the initial-value problem is well-posed in the L_2 norm, defined as

$$\|\boldsymbol{u}^n\| = \sqrt{\Delta x \sum_{k}^{m} |\boldsymbol{u}_k^n|^2}$$

where Δx is the space discretization step, $\boldsymbol{u}_k^n$ is the variable at time n, grid point k, and m is total number of points. A system of discretized equations is stable, if the norm of the numerical solution at a finite time is bounded by the norm at $t = 0$.

A property of finite difference schemes is the Lax equivalence theorem, which states that given a well-posed initial value problem and a consistent FD approximation, convergence to the exact solution is ensured by stability. The stability of the FD scheme can be checked by performing a Von Newman analysis, which verifies that no spatial Fourier components in the system are growing exponentially

with respect to time. One finds a condition which states that the numerical domain of dependence must be larger than the physical domain of dependence. This translates into the Courant-Friedrich-Lewy condition (CFL),

$$max|\lambda|\Delta t \leq \Delta x, \tag{5.1}$$

where λ is the maximum eigenvalue of the characteristic matrix.

5.2 Centered Finite Volume Methods

The numerical study of the evolution of relativistic flows is a topic of great interest in Astrophysics and Numerical Relativity (NR). The field of NR has recently undergone an extraordinary progress after the development of robust codes able to simulate real astrophysical scenarios, like stellar core collapse, collision of compact objects and accretion onto compact objects.

The traditional approach in the numerical simulation of complex classical flows are the HRSC. They are based on solutions of the local Riemann problem (initial value problem with discontinuous initial data). HRSC have a reputation of being computationally expensive, as they make explicit use of the characteristic decomposition of the set of dynamical fields. They are commonly used only in the evolution of matter fields in order to deal with shocks.

In the last years, simpler numerical schemes have been proposed, based on centered finite volume (CFV) methods. These offer a more practical choice, as they require only the values of the propagation speeds. Some complications still arise if one tries to obtain more than second order space accuracy, as the reconstruction process becomes computationally expensive.

These advanced methods have been developed for the field of Computational Fluid Dynamics, but they can be adapted also to vacuum NR simulations when dealing with steep gradients that mimic discontinuities [67]. Einstein's vacuum equations are quasilinear; it means that discontinuities can not spontaneously generate from smooth initial data. But this does not hold at a discrete level. If one deals with steep gradient solutions, the jump between neighbor points can mimic a discontinuous solution, leading to spurious oscillations that can crash the code.

We focused on developing a finite volume method that can be successfully applied to both vacuum and matter general relativistic simulations, with limited computational resources. Our CFV algorithm deals with piecewise continuous solutions, arising in fluid dynamics, and with steep gradients, in black holes evolutions. The method allows for third order space accuracy by using just piecewise linear reconstruction. The proposed FV scheme come as an alternative to the finite differencing plus dissipation methods and can be interpreted as an *adaptive viscosity* generalization of the FD algorithms.

5.2.1 Flux Formulae

The Einstein field equations can be expressed as a system of balance laws,

$$\partial_t \boldsymbol{u} + \partial_i \boldsymbol{F}^i = \boldsymbol{S}.$$

This flux conservative form is well suited for FV discretization. The FV differs from the FD approach, through the fact that one evolves the average of the dynamical fields in some elementary cells, instead of evolving just point values. For simplicity reasons, the one-dimensional case will be presented in the following.
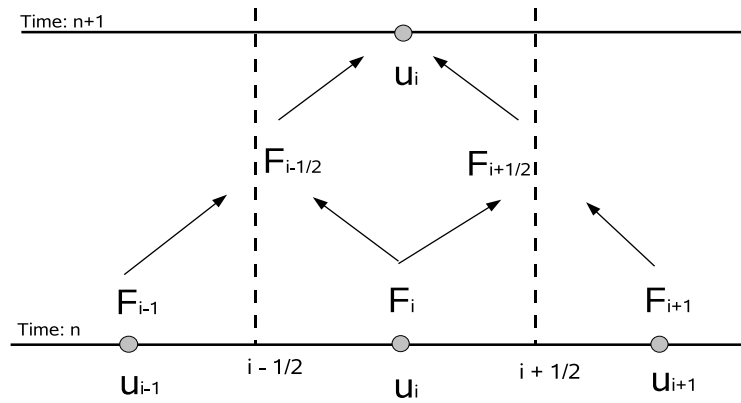
Figure 5.1. Schematic representation of a grid structure with elementary cells. The flux F_i in each grid point i is computed from the variables u_i. The flux $F_{i+1/2}$ at an interface $(i+1/2)$ can be calculated using the fluxes F_i, F_{i+1}. Then the value of a variable u_i in the next time step will be computed from the values of the fluxes $F_{i-1/2}, F_{i+1/2}$ at the neighboring interfaces.

Considering a regular finite difference grid, the elementary cell can be chosen as the interval $(x_{i-\frac{1}{2}}, x_{i+\frac{1}{2}})$ centered in the grid point x_i. The dynamical fields can be modeled as piecewise linear functions in every elementary cell, so that the average values in the cells coincide with the value in the grid point enclosed in the corresponding cell. The first order accurate FV discretization can be written as

$$\boldsymbol{u}_i^{n+1} = \boldsymbol{u}_i^n - \frac{\Delta t}{\Delta x}[\boldsymbol{F}^x_{i+\frac{1}{2}} - \boldsymbol{F}^x_{i-\frac{1}{2}}] + \boldsymbol{S}_i \Delta t, \tag{5.2}$$

where $\boldsymbol{u}_i^n$ are the fields at time n, in the grid point i, and $\boldsymbol{F}^x$ are the corresponding fluxes in the x direction, calculated at the interfaces of the cell centered in the grid point i, Fig. (5.1).

One can recover the standard second order FD method from this algorithm, by choosing a simple average for the flux

$$\boldsymbol{F}_{i+\frac{1}{2}} = \frac{1}{2}(\boldsymbol{F}_i + \boldsymbol{F}_{i+1}). \tag{5.3}$$

These FD methods can not deal with steep gradients and in general develop high-frequency noise that leads to instabilities. For that reason, FD is used in combination with numerical dissipation, that suppresses the spurious high frequency modes. The standard dissipation algorithms are not suited for dealing with discontinuities.

An alternative to the FD approximation of hyperbolic conservation laws designed to deal with discontinuous solutions, is based on the idea of solving the Riemann problem at each cell interface. One example is the Godunov method, a linear monotonicity preserving FV approximation which is only first order accurate. In order to obtain higher order schemes, one had to construct non-linear numerical methods, based on the concepts of slopes and limiters.
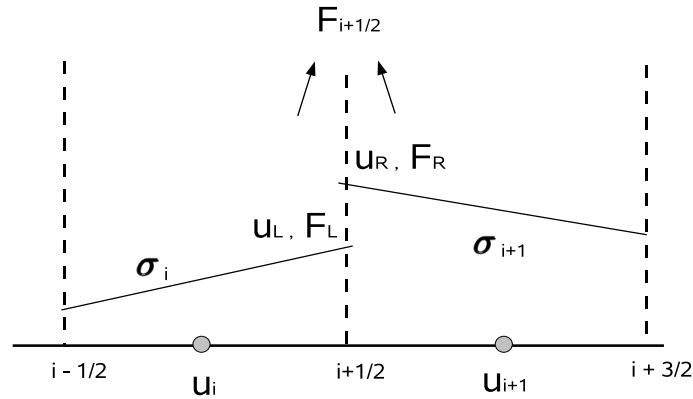
Figure 5.2. Schematic representation of the information computed at an interface. The left prediction u_L, of a variable u at the interface $(i + 1/2)$, can be calculated using the variable u_i in the grid point i and its slope σ_i in the elementary cell $(i - 1/2, i + 1/2)$. The right prediction u_R, of a variable u at the interface $(i + 1/2)$, can be calculated using the variable u_{i+1} in the grid point $(i + 1)$ and its slope σ_{i+1} in the elementary cell $(i - 1/2, i + 1/2)$. The left F_L and right F_R fluxes at the interface are computed from the corresponding u_L, u_R variables. Then the final flux $F_{i+1/2}$ at the interface is obtained from F_L, F_R.

Instead of using Eq. (5.3), one can find a more general prescription for the flux, of the form

$$\boldsymbol{F}_{i+\frac{1}{2}} = f(\boldsymbol{u}_L, \boldsymbol{u}_R), \tag{5.4}$$

where $\boldsymbol{u}_L$ and $\boldsymbol{u}_R$ are the left, respectively right, predictions of the dynamical field at the chosen interface Fig. (5.2),

$$\boldsymbol{u}_L = \boldsymbol{u}_i + \frac{1}{2}\sigma_i \Delta x, \qquad (5.5)$$

$$\boldsymbol{u}_R = \boldsymbol{u}_{i+1} - \frac{1}{2}\sigma_{i+1} \Delta x. \qquad (5.6)$$

They are calculated in respect to the slope σ of the chosen field in the corresponding cell Fig. (5.3). Following this idea, simple alternatives to HRSC schemes have been proposed, for example the HLLE method, which require just the characteristic speeds, not the full characteristic decomposition.
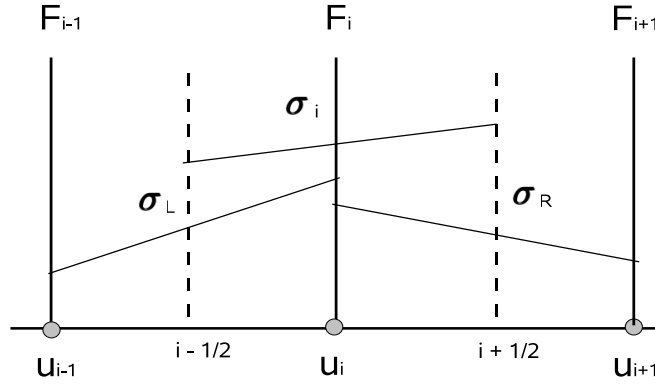
Figure 5.3. Schematic representation of the slopes. The slope σ_i of a variable or flux in an elementary cell $(i - 1/2, i + 1/2)$, can be calculated using the corresponding left σ_L and right σ_R slopes. The σ_L, σ_R can be computed from the values of the variables or fluxes in the neighboring grid points.

An overview of flux formulas [22] can be enclosed in the following general form:

$$\boldsymbol{f}(\boldsymbol{u}^L, \boldsymbol{u}^R) = \frac{1}{2}((I + \tilde{I}^L)\boldsymbol{F}^L + (I - \tilde{I}^R)\boldsymbol{F}^R + (Q^L\boldsymbol{u}^L - Q^R\boldsymbol{u}^R)), \qquad (5.7)$$

where $\boldsymbol{F}^{L,R}$ are the fluxes evaluated at the states $\boldsymbol{u}^{L,R}$ and I is the unit matrix. The terms $Q^{L,R}$ are referred in the literature as *numerical viscosity matrix*.

The matrices $\tilde{I}^{L,R}$ and $\tilde{Q}^{L,R}$ can be expressed as

$$\tilde{I}^{L,R} = \sum_{p=1}^{d} b_p l_p^{L,R} r_p^{L,R},$$

$$\tilde{Q}^{L,R} = \sum_{p=1}^{d} c_p l_p^{L,R} r_p^{L,R},$$

where l_p and r_p are the left, respectively right eigenvectors, and d is the dimension of the problem. For different flux formulae, the coefficients b_p and c_p depend on the eigenvalues λ_p as follows:

	b_p	c_p
$HLLE:$	$\dfrac{\psi_+ + \psi_-}{\psi_+ - \psi_-},$	$\dfrac{1}{2}(\psi_+ - \psi_-),$
$Roe:$	$0,$	$\mid \lambda_p(\tilde{\boldsymbol{u}}) \mid,$
$Marquina:$	$\beta_p,$	$\alpha_p(1 - \beta_p^2),$
$MarquinaFF:$	$0,$	$\alpha_p,$

where λ_+ and λ_- are the minimum and the maximum of λ_p and

$$\psi_+ = max(0, \lambda_+^R, \lambda_+^L),$$
$$\psi_- = min(0, \lambda_-^R, \lambda_-^L),$$
$$\alpha_p = max(\mid \lambda_p^L \mid, \mid \lambda_p^R \mid),$$
$$\beta_p = \frac{1}{2}(sgn(\lambda_p^L), sgn(\lambda_p^R)).$$

The HLLE algorithm is the most simple case, as the coefficients b_p and c_p are independent of p. Then taking into account the orthonormality relations between the right and the left eigenvectors

$$\sum_{p=1}^{d} l_p r_p = I,$$

the matrices $\tilde{I}^{L,R}$ and $\tilde{Q}^{L,R}$ are just the unit matrix multiplied by the corresponding factors. The HLLE flux formula requires only the values of the maximum and minimum propagation speeds, while the Roe and Marquina algorithms need the full decomposition, namely the left and the right eigenvectors [22].

Even simpler alternatives has been proposed, like the local Lax-Friedrichs (LLF) flux formula

$$\boldsymbol{f}(\boldsymbol{u}_L, \boldsymbol{u}_R) = \frac{1}{2}[\boldsymbol{F}_L + \boldsymbol{F}_R + c(\boldsymbol{u}_L - \boldsymbol{u}_R)], \qquad (5.8)$$

where c depends on the characteristic speeds at the interface

$$c = max(\lambda_L, \lambda_R),$$

and λ is the absolute value of the highest characteristic speed.

A comparison with the centered FD methods leads to the conclusion that the supplementary terms play the role of a numerical dissipation. It is worth noticing that the values of the dissipation coefficients are prescribed by the numerical algorithms, in contrast with the FD case where they are arbitrary parameters.

5.2.2 Flux Splitting Approach
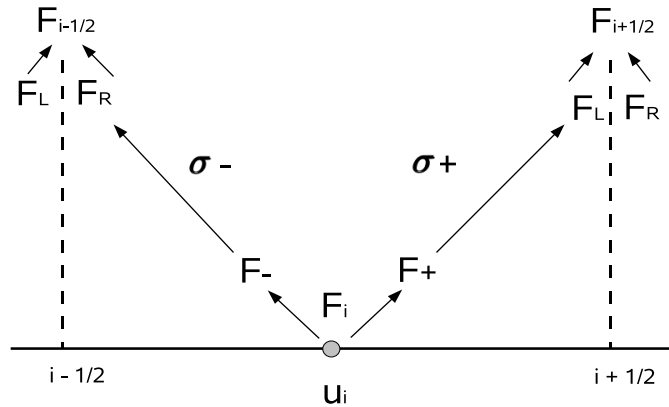
Figure 5.4. Schematic representation of the flux splitting approach. The flux in a grid point F_i is split in two components: F^+ and F^-. The F^- leads to a flux prediction F_R, at the right side of the interface $(i - 1/2)$, using its slope σ_- in the elementary cell $(i - 1/2, i + 1/2)$. The F^+ leads to a flux prediction F_L, at the left side of the interface $(i + 1/2)$, using its slope σ_+ in the elementary cell $(i - 1/2, i + 1/2)$. Then the left and right predictions of the fluxes F_L, F_R allow the calculation of the fluxes $F_{i-1/2}, F_{i+1/2}$ at each interface.

In the flux formula Eq. (5.4) the information from the two sides of the interface is combined in order to obtain a prediction of the flux at every interface. We consider a different approach, in which the information is computed at the grid

nodes, by selecting the components of the flux that will propagate in each direction. This method is known as the *flux splitting approach*.

In view of this method, one can write the flux at a grid point as two simple components

$$\boldsymbol{F}_i^+ = \boldsymbol{F}_i + \lambda_i \boldsymbol{u}_i, \qquad (5.9)$$

$$\boldsymbol{F}_i^- = \boldsymbol{F}_i - \lambda_i \boldsymbol{u}_i, \qquad (5.10)$$

where λ_i is the maximum eigenvalue computed in the i grid point. Then one can reconstruct the flux at each neighbor interface by combining the one-sided predictions

$$\boldsymbol{F}_{i+\frac{1}{2}} = \frac{1}{2}(\boldsymbol{F}_L + \boldsymbol{F}_R). \qquad (5.11)$$

This method can be expressed as a modification of the LLF formula Eq. (5.8), where the predictions from a grid point i towards the left, respectively right interfaces are given by

$$\boldsymbol{f}(\boldsymbol{u}_L, \boldsymbol{u}_R) = \frac{1}{2}[\boldsymbol{F}_L + \boldsymbol{F}_R + \lambda_L \boldsymbol{u}_L - \lambda_R \boldsymbol{u}_R], \qquad (5.12)$$

and the left and the right fluxes can be written according to Eqs. (5.5) - (5.6) as

$$\boldsymbol{F}_L = \boldsymbol{F}_i^+ + \frac{1}{2}\sigma_i^+ \Delta x, \qquad (5.13)$$

$$\boldsymbol{F}_R = \boldsymbol{F}_{i+1}^- - \frac{1}{2}\sigma_{i+1}^- \Delta x. \qquad (5.14)$$

The main difference is that in the flux splitting approach there is a clear separation of the information coming from the left or right side of the interface. The information for the F_i^+ propagates forward, as the one for the F_{i+1}^- backwards in respect to the $(i + \frac{1}{2})$ interface, Fig. (5.4). This offers a clear vision of the information flux in the numerical algorithm.

There is still the problem of computing the slopes for the reconstruction of each flux component. A linear piecewise reconstruction results generically into a second order accurate algorithm [68], as given by the centered slope

$$\sigma^C = \frac{1}{2\Delta x}(\boldsymbol{u}_{i+1} - \boldsymbol{u}_{i-1}). \qquad (5.15)$$

A more general second order algorithm can be obtained by using any average of the left and right slopes

$$\sigma^L = (\boldsymbol{u}_i - \boldsymbol{u}_{i-1})/\Delta x,$$

$$\sigma^R = (\boldsymbol{u}_{i+1} - \boldsymbol{u}_i)/\Delta x.$$

For some applications, second order accuracy is not enough, as the leading third order error is of dispersion type, affecting the numerical propagation speeds. As we saw in Chapter 4, the results of the standard numerical tests are significantly improved when passing from second order FD to fourth order FD algorithms, combined with third order accurate dissipation, where the result is a third order accurate algorithm. In the standard FV approach, third-order accuracy can be obtained by replacing the piecewise linear reconstruction with a piecewise parabolic one (PPM). This increases the complexity of the algorithm and the computational cost of the resulting implementation.

We use a simpler alternative, which takes advantage of the flux splitting approach Eqs. (5.9) - (5.10), and consider the resulting components $\boldsymbol{F}^+$ and $\boldsymbol{F}^-$ as independent dynamical fields, each one with its own slope, namely

$$\sigma_i^L = (\boldsymbol{F}_i^\pm - \boldsymbol{F}_{i-1}^\pm)/\Delta x, \qquad (5.16)$$

$$\sigma_i^R = (\boldsymbol{F}_{i+1}^\pm - \boldsymbol{F}_i^\pm)/\Delta x. \qquad (5.17)$$

One can recover the second order accuracy by a combination

$$\sigma_i^+ = \frac{1}{2}\sigma_i^L + \frac{1}{2}\sigma_i^R, \qquad (5.18)$$

$$\sigma_i^- = \frac{1}{2}\sigma_i^L + \frac{1}{2}\sigma_i^R, \qquad (5.19)$$

but the surprising result is the slope choice

$$\sigma_i^+ = \frac{1}{3}\sigma_i^L + \frac{2}{3}\sigma_i^R, \qquad (5.20)$$

$$\sigma_i^- = \frac{2}{3}\sigma_i^L + \frac{1}{3}\sigma_i^R, \qquad (5.21)$$

that leads to a third order accurate algorithm (see the Appendix 9.5.3 for detailed calculations). The choice of the coefficients is unique, any other combination leads to second order accuracy.

Inserting the choice of slopes Eqs. (5.18) - (5.19) or Eqs. (5.20) - (5.21), into the general slopes Eqs. (5.16) - (5.17), one can calculate the left and right prediction Eqs. (5.13) - (5.14) and eventually the flux at the interface Eq. (5.11). We can obtain this way third order accuracy by a piecewise linear reconstruction. This result is a particularity of the flux splitting approach. The piecewise prefix comes from the slope limiters that can be incorporated in order to deal with shocks or other discontinuities.

This CFV algorithm [23] written in a simple form Eq. (5.2), can be easily extended to the 3D case:

$$\boldsymbol{u}_{ijk}^{n+1} = \boldsymbol{u}_{ijk}^n - \frac{\Delta t}{\Delta x}[\boldsymbol{F}_{i+\frac{1}{2}}^x - \boldsymbol{F}_{i-\frac{1}{2}}^x] - \frac{\Delta t}{\Delta y}[\boldsymbol{F}_{j+\frac{1}{2}}^y - \boldsymbol{F}_{j-\frac{1}{2}}^y] -$$

$$-\frac{\Delta t}{\Delta z}[\boldsymbol{F}_{k+\frac{1}{2}}^z - \boldsymbol{F}_{k-\frac{1}{2}}^z] + \boldsymbol{S}_{ijk}\,\Delta t.$$

One can view the 3D structure as a superposition of the 1D algorithm along every space direction. The stability and monotonicity analysis presented in the following subsection can also be generalized for the 3D case.

5.2.3 Adaptive Dissipation

One can notice that setting to zero the λ terms in Eqs. (5.9), (5.10), and using the choice of slopes Eqs. (5.20), (5.21), the resulting algorithm is the standard fourth order accurate FD method. The extra λ terms downgrade the space accuracy to third order, the same effect that Kreiss Oliger dissipation terms have on the FD scheme. These terms would be the correspondent of the *numerical viscosity matrix* from the HLLE formula Eq. (5.7).

The CFV derivative operator for the choice of slopes Eqs. (5.20), (5.21) can be written in this simple form:

$$D_x(\boldsymbol{F}_i) = \frac{1}{12\Delta x}[-\boldsymbol{F}_{i+2} + 8\boldsymbol{F}_{i+1} - 8\boldsymbol{F}_{i-1} + \boldsymbol{F}_{i-2}] + Dis(\boldsymbol{F}_i),$$

where the first part of the formula is just the centered fourth order FD algorithm. The second part is a new dissipation term [24],

$$Dis_x(\boldsymbol{F}_i) = \frac{1}{12\Delta x}[\lambda_{i+2}\boldsymbol{u}_{i+2} - 4\lambda_{i+1}\boldsymbol{u}_{i+1} + 6\lambda_i\boldsymbol{u}_i - 4\lambda_{i-1}\boldsymbol{u}_{i-1} + \lambda_{i-2}\boldsymbol{u}_{i-2}],$$

which can be viewed as a generalization of the third order Kreiss Oliger dissipation algorithm.

The standard second order FD algorithm can be recovered by setting to zero both the slopes and the λ terms in Eqs. (5.9), (5.10), and it would be equivalent to Eq. (5.3). The choice of slopes Eqs. (5.18), (5.19) leads to a derivative operator equivalent to the standard second order FD, plus a dissipation term of the type mentioned above.

This dissipation algorithm can be extended to the 3D case:

$$\begin{aligned}
Dis_x(\boldsymbol{F}_{i,j,k}^x) &= \frac{1}{12\Delta x}[\lambda_{i+2,j,k}^x\,\boldsymbol{u}_{i+2,j,k} - 4\lambda_{i+1,j,k}^x\,\boldsymbol{u}_{i+1,j,k} + \\
&\quad + 6\lambda_{i,j,k}^x\,\boldsymbol{u}_{i,j,k}^x - 4\lambda_{i-1,j,k}^x\,\boldsymbol{u}_{i-1,j,k}^x + \lambda_{i-2,j,k}^x\,\boldsymbol{u}_{i-2,j,k}^x],
\end{aligned}$$

where λ^x is the maximum characteristic speed along the x axis, and analogous formulae hold for the y and z axes.

Our CFV algorithm can be interpreted as an *adaptive viscosity* modification of centered FD algorithms plus KO dissipation, offering a generalization of the standard dissipation terms. As far as the slope limiters are not required, the CFV method is just a centered FD plus a local dissipation term, which is automatically adapted to the requirements of the numerical simulations.

This generalization procedure can be applied to Kreiss Oliger dissipation operators, used in combination with FD methods, in order to obtain higher order schemes.

5.2.4 Stability and Monotonicity

We consider the Einstein equations in the form of a strongly hyperbolic system. Then we have a complete set of eigenvectors and for each direction and we can express the system as a set of simple advection equations for the characteristic variables. In order to check the stability properties of our CFV algorithm described in the previous subsections, it will be sufficient to consider a single advection equation with a generic speed v. The corresponding flux can be written

$$F(\boldsymbol{u}) = v\,\boldsymbol{u}.$$

In a first order accurate approximation obtained with zero slopes, the corresponding discretization will be given by replacing Eq. (5.11) in the general form Eq. (5.2). The result is the linear three point algorithm:

$$\boldsymbol{u}_i^{n+1} = \boldsymbol{u}_i^n + \frac{\Delta t}{\Delta x}\left\{\frac{1}{2}(\lambda_{i+1} - v_{i+1})\boldsymbol{u}_{i+1}^n + \frac{1}{2}(\lambda_{i-1} + v_{i-1})\boldsymbol{u}_{i-1}^n - \lambda_i\boldsymbol{u}_i^n\right\}.$$

$$(5.22)$$

As λ_i is the absolute value of the maximum characteristic speed calculated in every grid point, one can see that all the coefficients are positive if the Courant stability condition Eq. (5.1) is satisfied. A more restrictive condition is necessary in the 3D case, as we must consider all the spatial directions.

In the general case, the positivity the coefficients in the resulting CFV algorithm, requires an extra factor in the Courant condition

$$\lambda\frac{\Delta t}{\Delta x} \leq \frac{1}{2}.$$

$$(5.23)$$

At this point we take into account that we have considered just the elementary step in the time evolution algorithm. The stability and monotonicity limits for the time step will depend on the choice of the full evolution algorithm.

The positivity of all the coefficients ensure that the algorithm is monotonicity preserving, no spurious numerical oscillations can appear, which implies stability. The converse argument is not true, the stability of the algorithm does not ensure monotonicity. The FD algorithms loose this property, as we can clearly see by setting λ to zero in Eq. (5.22).

However, the monotonicity properties of the piecewise constant reconstruction are not ensured in the piecewise linear case, as problems can arise in the steep gradient regions. This could happen when the series of left $\{u^L\}$ or right $\{u^R\}$ interface predictions show spurious peaks which were not present in the original function. In the case of the centered slope Eq. (5.15), one can show that this will occur only if the left and right slopes differ by a factor of three or more. This would be the real meaning of *steep gradient* in the centered slope case.

A way of preventing oscillations could be by enforcing that both left and right predictions are in the interval limited by the left, respectively right point values. This is equivalent of limited slopes

$$\sigma^{lim} = minmod(2\sigma^L, \sigma, 2\sigma^R), \tag{5.24}$$

where σ is the slope in a given cell. The limiters are constructed in such a way, as to guarantee that the total variation of the numerical solution never increases. The combined CFV plus limiter schemes are called *total variation diminishing* (TVD), as they do not allow spurious oscillations.

The TVD methods become only first order accurate near an extrema due to the limiters. There exist other limiter methods that are essentially non oscillatory (ENO) and allow for the variation to grow as long as it is bounded by an exponential. These methods are called total variation stable.

5.3   Discussion

We presented some of standard techniques currently used in Numerical Relativity in order to solve the discretized Einstein equations. One commonly employs the Method of Lines, where the spatial derivatives are provided by FD or FV methods and the time integration is performed using Runge Kutta methods.

The main topic of this chapter refers to FV methods, in particular the CFV algorithm developed by the Palma group. This algorithm is the first one in the class of FV methods which allows third order accuracy by only piece-wise linear reconstruction. It leads also to a generalized dissipation algorithm, which can be successfully used in combination with FD methods.

This CVF algorithm used in combination with positive-coefficients RK methods, for example the third order RK (Appendix 9.4), ensures that the monotonicity properties of the basic evolution step will be preserved by the resulting strong stability preserving algorithm (SSP). This nice property has though a disadvantage, namely it imposes a limit on the Δt in order to preserve monotonicity Eq. (5.23). In contrast, when one uses the FD methods for space discretization, the basic time scheme is limited only by stability, not monotonicity. Moreover, the RK with non-positive coefficients (for example the fourth order RK) used in combination with the FD algorithms allows larger time steps.

The stability issues presented in this chapter, based on monotonicity results, are valid only when applied to flux conservative systems. This is not entirely our case, as the systems used in Numerical Relativity contain also source terms. These terms do not belong to the principal part, so the positivity of the flux terms ensure some form of stability. Nevertheless, the analogy with Fluid Dynamics is only approximative and the use of slope limiters is a risk, as we could be removing

from the flux part some features that are needed in order to compensate the source part.

Our experience with the vacuum Einstein equations, based on numerical tests, shows that more robust simulations are obtained when the limiters are switched off and that the numerical dissipation built in the proposed CFV method [23] is sufficient to control the high frequency modes and deal with steep gradients. Alternatively, one can use the adaptive dissipation algorithm variant [24], in combination with the standard FD methods.

Chapter 6

Black Hole Simulations

The study of black holes (BH) played for a long time a central role in Numerical Relativity. This particular types of spacetime are the simplest models of gravitating bodies in General Relativity, as they represent vacuum solutions of the Einstein equations. However, the numerical evolution of BH spacetimes implies complications associated with the presence of horizons, singularities and non-trivial topologies.

Black holes form starting from regular initial data, as they represent the final state of the gravitational collapse of compact objects, like supernova core collapse or neutron stars collisions. A problem of special interest in General Relativity is that of binary black hole systems, which are considered to be one of the most powerful sources of gravitational waves.

In this chapter, we consider different issues related with the numerical evolution of black hole spacetimes. The techniques for dealing with the BH singularity, steep gradients formed in normal coordinates, and horizon location, are presented in the context of a single black hole.

This chapter consists of two parts. The first part concerns the evolution of a Schwarzschild BH in spherical symmetry. We study the approach to the stationary state using the '1+log' slicing and the wormhole puncture technique for dealing with the BH singularity. The central finite volume (CFV) methods presented in Chapter 5 are employed for dealing with the steep gradients which arise in a BH evolution with zero shift. We perform a comparison between our CFV scheme and the standard finite difference (FD) method plus Kreiss Oliger (KO) dissipation, and study the behavior in time of the convergence factor across the numerical grid, inside and outside the apparent horizon.

The second part extends our study to a 3D Schwarzschild BH evolution. We consider two approaches for dealing with the BH singularity, namely the puncture technique and scalar field stuffing, and provide numerical evidence that they have a similar approach to the stationary state, in the context of normal coordinates and '1+log' slicing. We prove the efficiency of our CFV method and generalized

dissipation algorithm in 3D simulations.

6.1 Black Hole in Spherical Symmetry

In this section we address problems related the evolution of a Schwarzschild black hole in spherical symmetry.

In spherically symmetric spacetimes the equations of motion are greatly simplified and the number of variables that must be evolved is significantly reduced. Therefore it is relatively easy to study numerically the system, compared to three dimensional simulations. Using high resolution is not a restriction, even without employing complications related with mesh refinement (reflections arising from refinement boundaries, interpolation between meshes). At the same time, of all the symmetries that could be imposed to reduce the field equations to a set of partial differential equations in one space dimension and time, spherical symmetry is clearly the most appropriate for the study of isolated, gravitationally compact objects.

6.1.1 Puncture Initial Data

The initial data for the typical puncture simulation is a black hole with a wormhole topology Fig. (6.2). As we follow the coordinates toward one of the black holes, we do not reach the black hole's singularity but instead pass through a wormhole to another exterior space and find another asymptotically flat region.

We consider such a puncture data in the form of the Schwarzschild metric in isotropic coordinates, where the line element takes the form

$$ds^2 = -\left(\frac{1 - M/(2r)}{1 + M/(2r)}\right)^2 dt^2 + \left(1 + \frac{M}{2r}\right)^4 \left(dr^2 + r^2 d\Omega^2\right), \qquad (6.1)$$

and $d\Omega^2 = d\theta^2 + (\sin\theta)^2 d\phi^2$. The isotropic radial coordinate r is related to the Schwarzschild radial coordinate (area radius) by $R = \sqrt{g_{\theta\theta}}$.

One can notice that $R \to \infty$ for both large and small r, so the isotropic coordinate r does not reach the physical singularity at $R = 0$. There is a minimum of $R = 2M$ at $r = M/2$. The two spaces are connected by a wormhole with a throat at $R = 2M$. The point $r = 0$, which represents the second asymptotically flat end is referred to as the puncture.

Applying a coordinate transformation of the type

$$r = \frac{M}{2} \exp(\eta),$$

one can obtain the form

$$ds^2 = -(\tanh\eta)^2 dt^2 + 4M^2(\cosh\eta/2)^4 (d\eta^2 + d\Omega^2). \qquad (6.2)$$
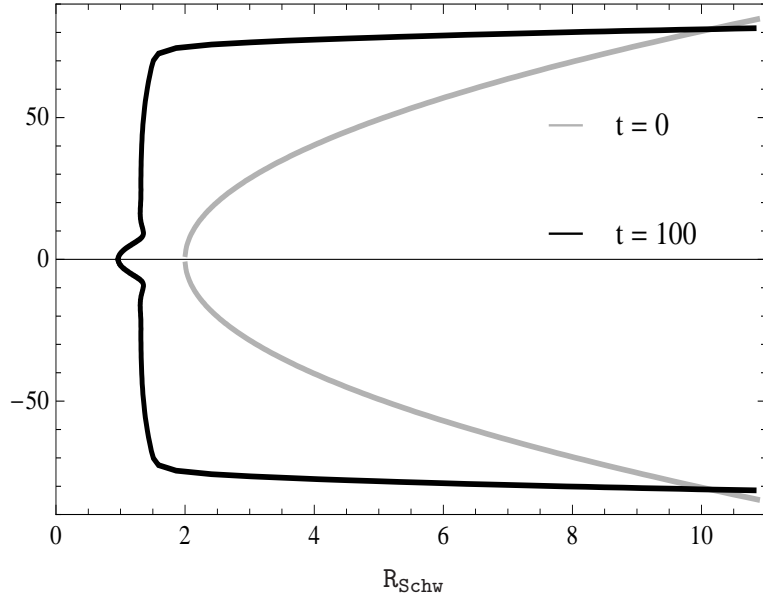
Figure 6.1. Vertical section through an embedding diagram of a two-dimensional slice ($t = const., \theta = \pi/2$) of the Schwarzschild solution. The grey plot corresponds to the diagram at $time = 0$, rescaled by a factor of 10, and the black one, at $time = 100M$. A wormhole connects the two asymptotically flat ends. Notice how the throat of the wormhole stretches in time forming a cylinder with radius $R \approx 1.3M$.

This choice aids in pushing the outer boundaries far from the (dynamical) region of interest, as an evenly spaced grid in η corresponds to a geometrically increasing spacing in r,

$$dr = r d\eta.$$

In these logarithmic coordinates the minimal surface is located at $\eta = 0$.

This type of initial data can be viewed as a wormhole connecting two asymptotically flat regions, where the isometry of the two sides of the wormhole is expressed by the reflection symmetry

$$\eta \leftrightarrow -\eta$$

Fig. (6.1). Numerical simulations can thus be restricted to positive values of η and one can use the reflection property in order to set proper inner boundary conditions at the throat.

A very useful gauge-independent quantity in spherically symmetric spacetimes is the mass aspect function, which approaches the ADM mass as $r \to \infty$. It can be computed in Schwarzschild coordinates (T, R), where the metric has a form

$$ds^2 = -\left(1 - \frac{2M}{R}\right) dT^2 + \left(1 - \frac{2M}{R}\right)^{-1} dR^2 + R^2 d\Omega^2,$$
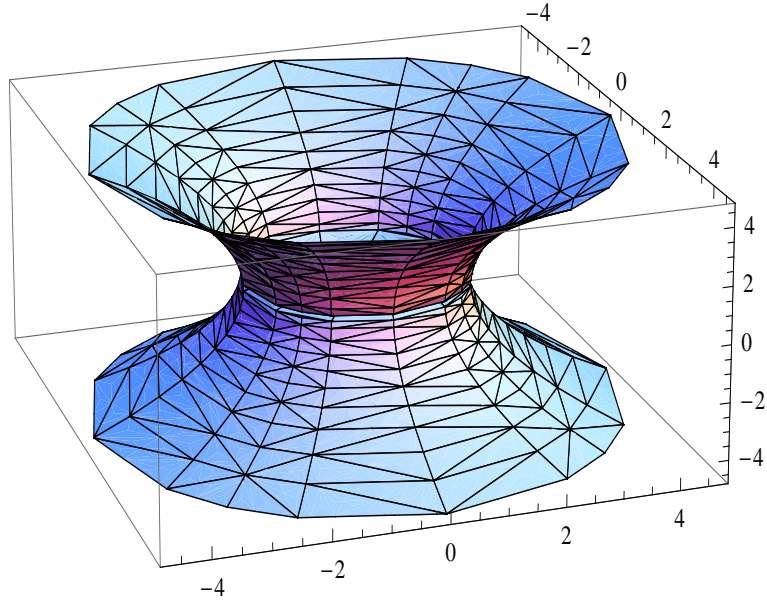
Figure 6.2. Embedding diagram of a two-dimensional slice ($t = 0, \theta = \pi/2$) of the Schwarzschild solution. The distance to the rotation axis is R. A wormhole with the throat at $R = 2M$ connects the two asymptotically flat ends.
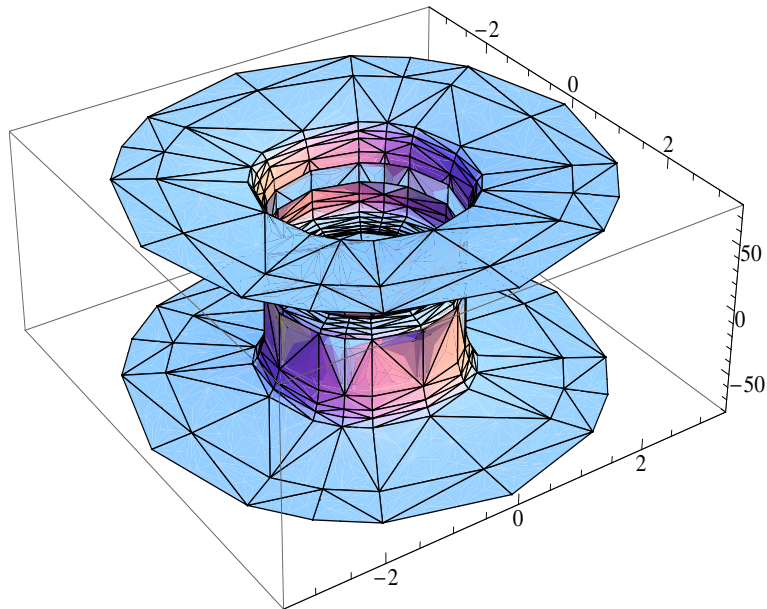
Figure 6.3. Embedding diagram of a two-dimensional slice ($t = 100, \theta = \pi/2$) of the Schwarzschild solution. The distance to the rotation axis is R. The throat of the wormhole stretches, forming a cylinder with radius $R \approx 1.3M$.

and the constant M is the ADM mass of the system. Considering as geometrical invariant the square of the gradient of the areal radius,

$$\nabla_a R \nabla^a R = g^{ab} \nabla_a R \nabla_b R = g^{RR} \nabla_R R \nabla_R R = 1 - \frac{2M}{R},$$

the mass can be defined,

$$M = \frac{R}{2}(1 - g^{ab} \partial_a R \partial_b R).$$

In our coordinates it can be calculated as

$$M(t,\eta) = \frac{\sqrt{g_{\theta\theta}}}{2}\{1 + g_{\theta\theta}[(K_\theta{}^\theta)^2 - g^{\eta\eta}(D_{\eta\theta}{}^\theta)^2]\}, \tag{6.3}$$

where $D_{\eta\theta}{}^\theta = \frac{1}{2}\partial_\eta g_\theta{}^\theta$. The mass aspect function provides the mass inside a sphere of radius r at a fixed time t. It must be constant for a Schwarzschild spacetime in any coordinate system, so it can be very useful in checking the accuracy of the numerical simulations.

One can track the position of the apparent horizon using its definition, namely a two-surface where outgoing light rays have zero expansion,

$$\nabla_p \tilde{n}^p + K_{pq}\tilde{n}^p\tilde{n}^q - K = 0. \tag{6.4}$$

$\tilde{n}$ is the outgoing unit normal, normalized as $\tilde{n}^k \tilde{n}_k = 1$ and

$$\tilde{n}_k = \frac{n_k}{\sqrt{n_i n_j g^{ij}}},$$

with $n_k = x_p \delta_k{}^p$. In spherical symmetry, a simple calculation leads to $\tilde{n}^k = \sqrt{g^{\eta\eta}}\delta_\eta{}^k$. Then the location of the minimal surface can be calculated in this case as the area where

$$f(\eta,t) = 2(\sqrt{g^{\eta\eta}}D_{\eta\theta}{}^\theta - K_\theta{}^\theta) = 0. \tag{6.5}$$

6.1.2 Numerical Specifications and Gauge Choice

We perform numerical simulations with the Z3 system in spherical symmetry (see Appendix 9.6.1 for the complete set of evolution equations). The free parameter that couples the energy constraint in the evolution equation for the extrinsic curvature is $n = 1$ (see Chapter 3). Similar results can be obtained with other values, for example $n = 4/3$, which leads to a system equivalent to a first order in space variant of the BSSN, without the conformal decomposition.

The time evolution is performed with a third order Runge Kutta algorithm (Appendix 9.4). We use for spatial discretization both finite difference plus Kreiss-Oliger dissipation, and central volume methods (Appendix 9.5). The Courant factor is $C = 0.5$.

Our evolution domain extends to $\eta = 10M$ ($r \approx 11000M$). The treatment of the boundaries is settled through a simple and standard *ghost point* technique. In this approach, one populates the missing points at the boundary by copying the time variation of the nearest neighbor, for every evolution variable.

The physical singularity associated with the black holes is not present in the initial data, as our coordinates stop at the throat ($\eta = 0$ corresponds to $r = M/2$), but it will be rapidly approached during the evolution, unless we choose a singularity avoiding condition. We choose as gauge conditions a slicing from the Bona-Masso family Eq. (2.28) with $f = 2/\alpha$, and normal coordinates Eq. (2.29). The initial value of the lapse is $\alpha = 1$.

6.1.3   Numerical Results and Comparison

The wormhole Fig. (6.2), can be pictured in an embedding diagram of a two-dimensional slice ($time = const., \theta = \pi/2$) of the Schwarzschild solution Fig. (6.1). Initially, the throat is located at $R = 2M$.

We evolve the initial data using a foliation of the type,

$$\partial_t \alpha = -2\alpha K.$$

This can be viewed as an asymptotically maximal slicing condition, as it leads to a time independent geometry that is maximally sliced (for $K = 0$ the lapse does not evolve). During the evolution, the slices go the stationary '1+log' solution. The throat stretches into an infinitely long cylinder with radius $R = 1.31241M$, connecting the two asymptotically flat ends. The behavior illustrated in Fig. (6.3) is in agreement with the one described in [69] for the wormhole geometry.

Performing long term simulations (up to 1000M) in this setting is a challenging task, as the numerical methods have to deal with the steep profile of the lapse function. Fig. (6.4) presents the lapse computed with our second and third order CFV methods. The use of a higher order method leads to a steeper profile, the same effect which appears by increasing the resolution, as the numerical solution approaches the exact one.

A comparison between the CFV methods and the FD plus KO dissipation, leads to the conclusion that the FD methods can not deal with steep gradients for longer times. Even though the code does not crash, the FD plots in Fig. (6.4) show that the numerical solution at 1000M has developed very large errors.

The lowest resolution used for our CFV method, that allows us to reach $1000M$ in this 1D BH simulations, is $dx = 0.1$. This is almost double than the minimum resolution required by the FD methods in the same test. Even though the simulation is performed in a low resolution grid, the profiles look smooth without the use of slope limiters.

Studying the propagation speed profiles in Fig. (6.5), one can notice that the maximum gauge speed decreases with time, as the lapse goes to zero in the interior
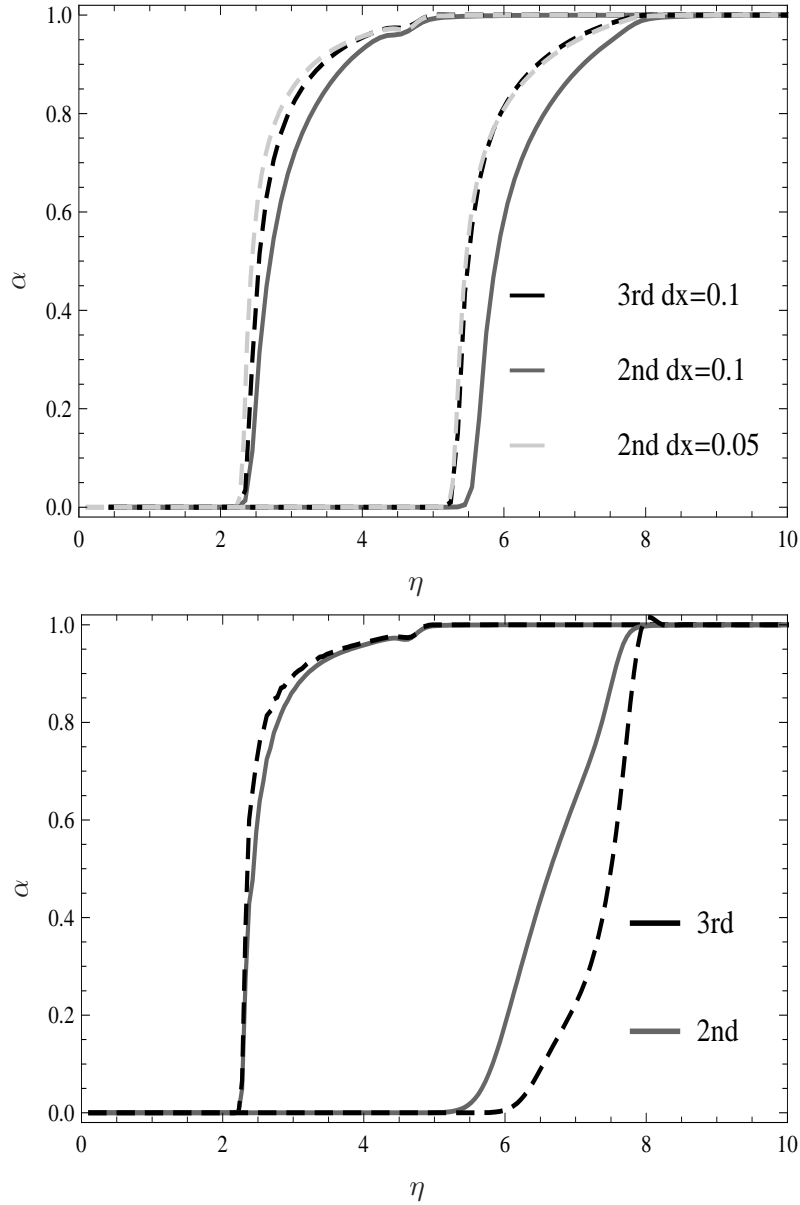
Figure 6.4. Illustration of the Z3 lapse as a function of the η coordinate, for a Schwarzschild black hole simulation in spherical symmetry. The plots represent the collapse of the lapse at $time = 50M$ and $time = 1000M$. Upper Panel: The lapse function is computed in simulations using the 2nd order CFV method, resolution $dx = 0.1$ (continuous grey plot) and $dx = 0.05$ (dashed grey plot), and the 3rd order CFV method, resolution $dx = 0.1$ (dashed black plot). Lower panel: The lapse function is computed in simulations using the 2nd order FD method (grey plot) and the 4th order FD method plus 3rd order dissipation (black plot). Both simulations were performed in a resolution $dx = 0.05$, using 3rd order Kreiss Oliger dissipation with $\sigma = 0.02$.
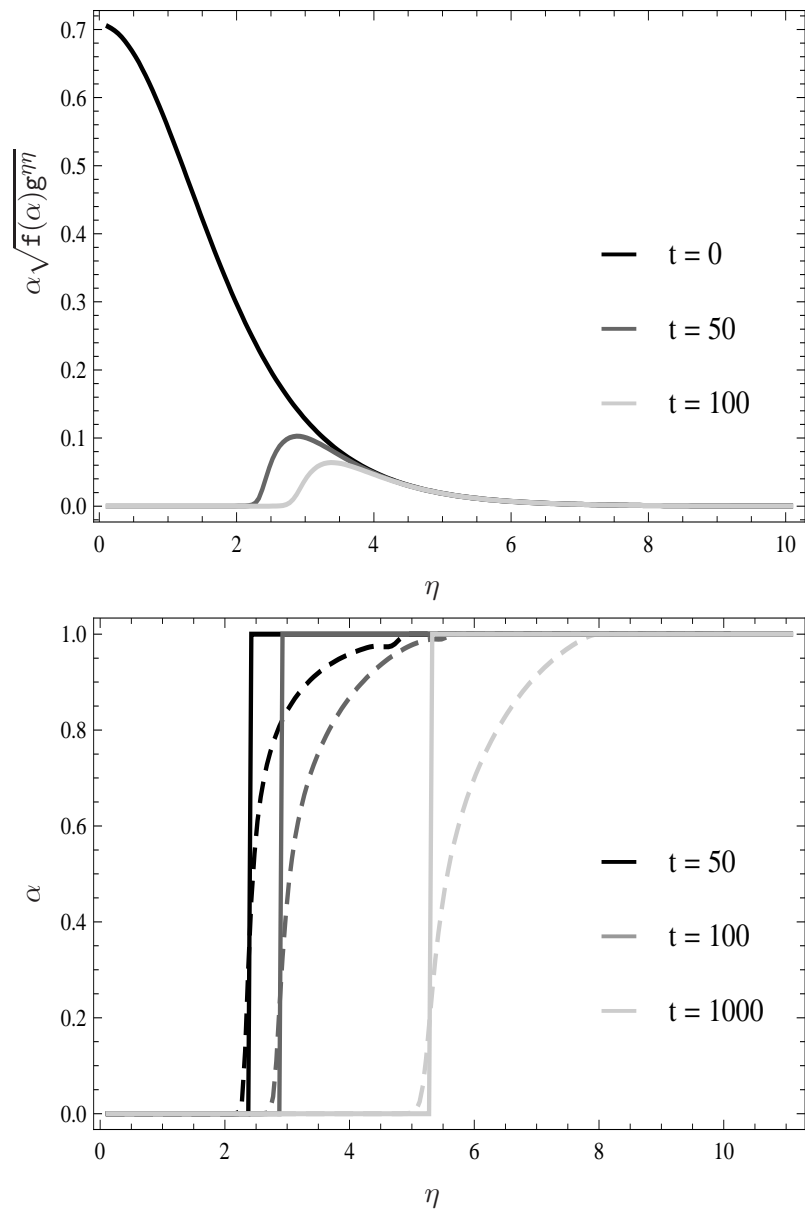
Figure 6.5. Upper panel: Illustration of the maximum gauge speed $\alpha\sqrt{f(\alpha)g^{\eta\eta}}$ as a function of the η coordinate, in a Schwarzschild black hole evolution using the '1+log' slicing. The profiles are presented at $time = 0$ (black plot), $time = 50$M (dark-grey plot) and $time = 100$M (light-grey plot). Lower panel: Illustration of the lapse function and apparent horizon as a function of the η coordinate, in a Schwarzschild black hole evolution using the '1+log' slicing. The dashed plots represent the collapse front of the lapse and the vertical lines the position of the apparent horizon, at $time = 50$M (black plots), $time = 100$M (dark-grey plots), $time = 1000$M (light-grey plots).

of the black hole. This feature appears because of our choice of radial coordinate. A consequence is the fact that the Courant condition becomes less restrictive and it allows for bigger time steps. However, we prefer to maintain the initial time step, in order to have an extra safety factor.

6.1.4 Convergence and Error
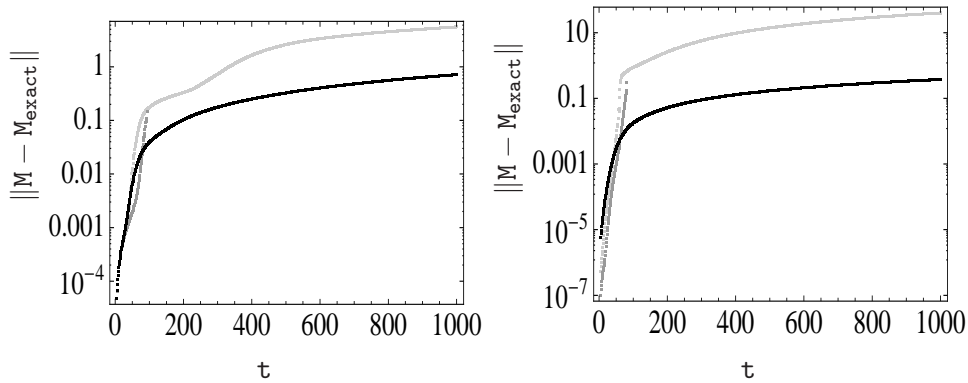
Figure 6.6. Illustration of the L_2-norm of the error in the mass, plotted on a logarithmic scale as a function of time. Left panel: The dark-grey plot correspond to a simulations using the 2nd order FD algorithm without dissipation, which crashes around $time = 100$M. The light-grey plot corresponds to the 2nd order FD method plus 3rd order Kreiss Oliger dissipation and the black plot to the 2nd order CFV method. Right panel: The dark-grey plot corresponds to a simulation using the 4th order FD algorithm without dissipation, which has the smallest errors, but crashes around $time = 80$M. The light-grey plot corresponds to the 4th order FD method plus 3rd order accurate Kreiss Oliger dissipation, and the black plot to the 3rd order CFV method.

We monitor the behavior of the error in the mass, by plotting the L_2-norm of the difference between the computed and the exact mass as a function of time Fig. (6.6). One can notice that the smallest errors correspond to the standard second order FD algorithm. However, this simulation crashes around $time = 100$M, after developing high frequency noise. In long runs, up to $time = 1000$M, the second order CFV method shows significantly smaller errors than the second order FD algorithm plus third order Kreiss Oliger dissipation. A correct comparison can be performed, as all three schemes are second order convergent Fig. (6.7).

We perform a similar comparison between the L_2-norms of the mass error function obtained with the 3rd order CFV algorithm and the 4th order FD method, both with and without 3rd order Kreiss Oliger dissipation. The lowest errors correspond to the standard 4th order FD method, which later develops high frequency oscillations and crashes around $time = 80$M. The 3rd order CFV algorithm leads to accurate long term simulations, as we can observe in Fig. (6.6).
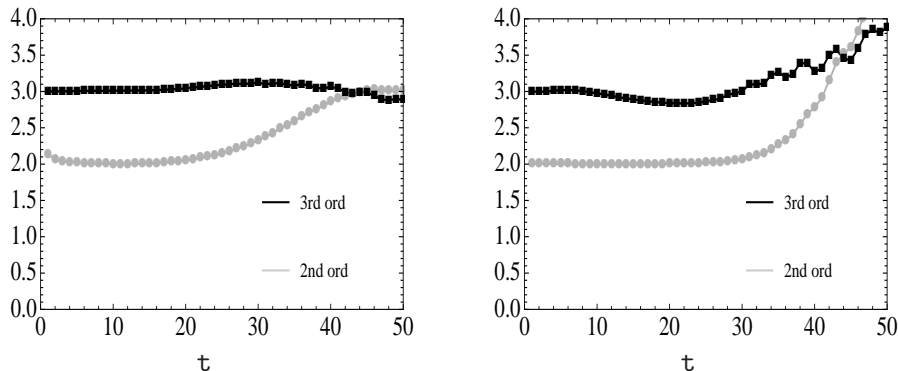
Figure 6.7. Illustration of the convergence factor in the mass, as a function of time. The convergence factor is calculated using the L_2-norms of the differences between the masses at three resolutions $dx = 0.05, 0.025, 0.0125$. Left panel: The convergence plots correspond to simulations using the 2nd order (grey dots) and the 3rd order CFV methods (black dots). Right panel: The convergence plots correspond to simulations using the 2nd order FD method (grey dots) and the 4th order FD method plus 3rd order Kreiss Oliger dissipation (black dots).

As the leading error order in the 4th order FD plus 3rd order KO scheme is given by the dissipation terms, one could in principal lower the viscosity coefficient in order to obtain more accurate results. However this coefficient can be modified only in certain stability limits depending on the specific simulation. In our case, lowering more the viscosity coefficient would result in the appearance of high frequency noise, which leads to premature code crashing. This error comparison does not depend on the resolution, as both schemes show third order accuracy, proven by the convergence tests in Fig. (6.7).

The need to employ dissipation could be avoided by increasing the grid resolution in order to solve the steep profile of the collapse front. This way, one can obtain long evolutions depending on the available computational power. However, this is not an option in 3D, where we require a more efficient management of the computational resources. Then we are forced to appeal to dissipation, either the one intrinsically built in the CFV methods, or the artificial one that is currently used in combination with the FD methods.

The effect of the dissipation is damping the sharp features specific to the high frequency noise. One can get away with solving the collapse front in a limited resolution, but the price to pay is more numerical error. The adaptive viscosity built in the CFV method provides a compromise between accuracy and computational efficiency.

The convergence plots are presented early in the evolution (until $time = 50M$), as at later times large errors develop the inner zones, for both CFV and FD simulations. The reason is not the failure of the algorithm, but it is rather a consequence
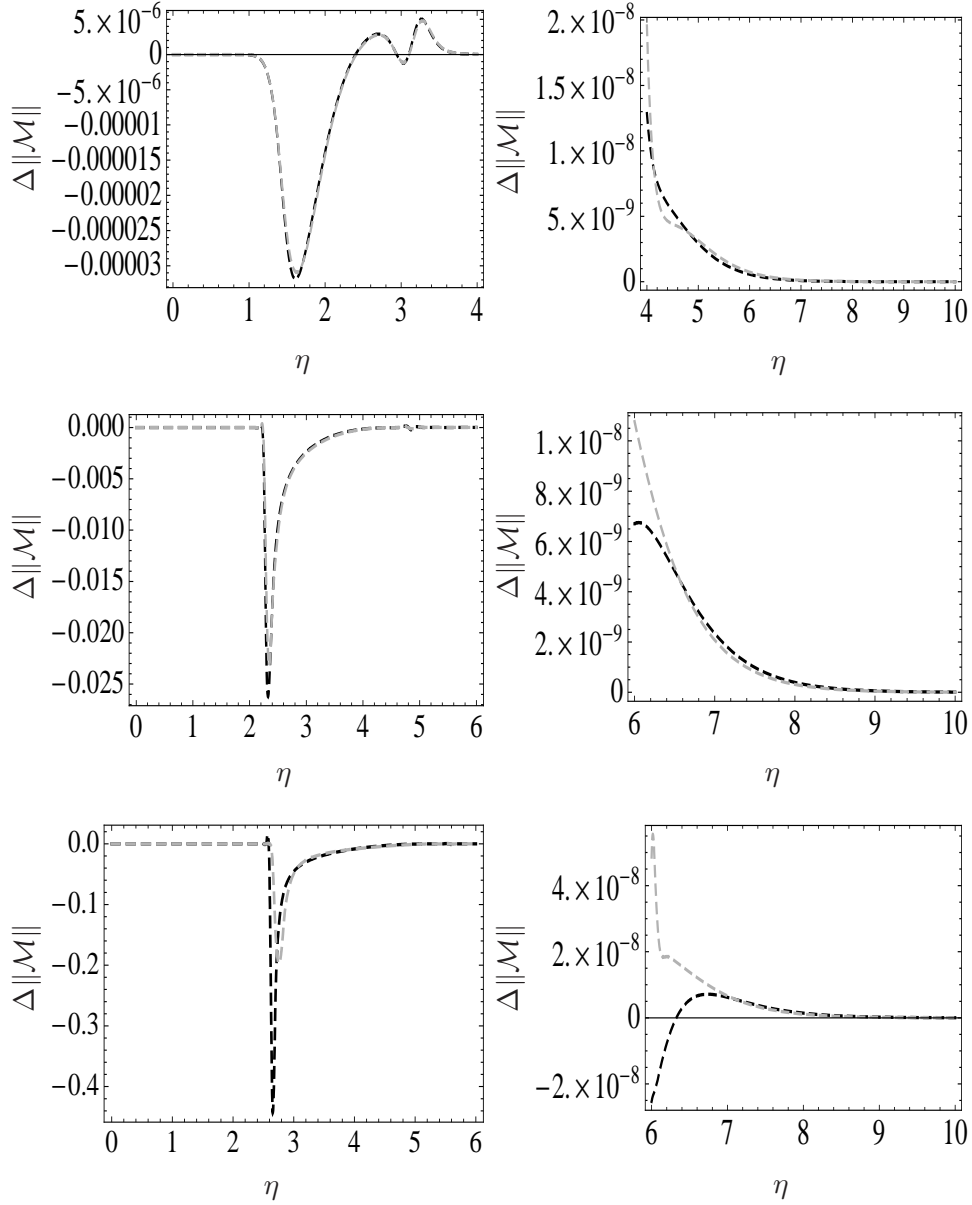
Figure 6.8. Illustration of the local convergence factor in the Mass, as a function of the η coordinate, in a simulation using the 3rd order CFV method. The grey plots correspond to the difference between the middle $dx = 0.025$ and high resolutions $dx = 0.0125$, while the black plots represent the rescaled difference between the coarse $dx = 0.05$ and middle resolutions $dx = 0.025$. Upper panels ($time = 10M$): A convergence factor of 3 is obtained in the interior BH region where the dissipation terms are active (left panel), and a factor of 4 in the outer region where the dissipation parameter is close to zero (right panel). Middle panels ($time = 50M$): The convergence factor starts downgrading to a value of 2.7 in the regions close to the apparent horizon (left panel), while keeping a value of 4 in the outer region (right panel). Lower panels ($time = 100M$): The convergence factor drops to a value of 1.6 in the regions close to the apparent horizon (left panel), while keeping a value of 4 in the outer region (right panel).

of the large errors in a highly nonlinear context. Further investigation indicates a downgrade of convergence around the collapse front, while the outer region keeps the proper convergence rate Fig. (6.8). Convergence is lost both inside the apparent horizon (AH) and in the outer points close to the AH. Using the '1+log' singularity avoiding slicing, the collapse front of the lapse function coincides with the position of the AH, Fig. (6.5). So the downgrade of the convergence factor at the location of the AH can be seen as an effect of the numerical method dealing with steep gradients.

The outer boundary also shows a fluctuation in the convergence order, but this problem remains localized in few boundary points and does not extend throughout the domain. As the physically relevant part of the spacetime is the outer region, this partial loss of convergence is not considered problematic. A similar behavior appears when using the FD plus KO dissipation [12], and it indicates that the wave extraction zone should be located away both from the outer boundary and the collapse front.

6.1.5   Discussion

The numerical tests presented in this section show that our CFV algorithm performs well even at low resolutions ($dx = 0.1$), which is an advantage that the other standard FD methods can not offer. However, at low resolutions the performance of the system depends on the way the system is written. More explicit, if one uses the system with all indices covariant, the results obtained are quite different than the ones obtained with the same system, but written with mixed indices. In 1D simulations, one always has enough computational resources to improve resolution and show the equivalence of the two approaches. This is not the case in 3D, at least not in single grid numerical simulations.

Performing a comparison between different numerical techniques currently used, we showed that our CFV numerical method allows for longer and more accurate evolutions. The 1D spherically symmetric case provides just the initial step in setting up numerical methods suitable to address the evolution of the full Einstein equations [23, 54].

We stress the idea that these CFV methods are useful in evolving smooth solutions of quasi-linear strongly hyperbolic systems, as the full non-linear Einstein equations in vacuum when written in flux conservative form. Although the main motivation of this work is to present techniques for the numerical simulation of the Einstein equations, the methods presented could be applied to any system of this form.

Moreover, in vacuum cases, one can use the CFV method in the form of FD plus the adaptive dissipation algorithm (presented in Section 5.2.3). As long as one does not require the use of limiters, the two approaches are equivalent and can be applied even to systems implemented in a non flux-conservative form.

6.2   Black Hole in 3D

One of the most important problems when dealing with black holes spacetimes
is the presence of singularities, where the geometric quantities become infinite.
The physical singularity can be dealt with by using different techniques like ex-
cision, puncture and stuffing. Excision consists in cutting out a region inside the
black hole apparent horizon, in a consistent way. As this is a rather numerically
than analytically challenging task, we will focus in the following on the other two
approaches.

In the puncture approach, one of the asymptotically flat regions is compact-
ified, so that its spatial infinity is transformed into a single point. The puncture
data is smooth everywhere, except the metric factor, which diverges near the sin-
gularity. However, if one prefers to deal with non-singular initial data, one can
use the stuffing technique and replace the vacuum interior of the black hole by a
singularity-free matter solution.

In this section I will present an analytical and numerical comparison between
the two approaches, in the context of a 3D Schwarzschild black hole evolution in
normal coordinates.

We perform numerical simulations using the Z4 system, with the adjustments
presented in Subsection 3.1.1, which turned out to be crucial for long-term sta-
bility. Our gauge choice is a singularity avoiding slicing condition and normal
coordinates, namely

$$
\begin{aligned}
\partial_t \alpha &= \alpha^2 f(\alpha)\,(K - m\theta), \\
\partial_t \beta^i &= 0.
\end{aligned}
$$

We choose a value of $m = 2$, as the evolution equation for the combination $(K - 2\theta)$ corresponds to the BSSN evolution equation for K. The gauge parameter is set
to $f = 2/\alpha$, the most common choice in BH simulations with the BSSN system,
due to its strong singularity avoidance properties. The behavior of the system with
various choices of gauge is discussed in detail in the Chapters 8 and 9.

6.2.1   Scalar Field Stuffing

6.2.1.a   Initial Data

We consider as initial data the standard wormhole puncture metric Eq. (6.1), for
which the interior region is isometric to the exterior one. Then the spatial part of
the line element in isotropic coordinates can be written as

$$
dl^2 = \psi^4 \delta_{ij} dx^i dx^j, \tag{6.6}
$$

where $\psi = 1 + \frac{M}{2r}$, M is the mass and $r = \sqrt{x^2 + y^2 + z^2}$. The Schwarzschild
radial coordinate R is related with the isotropic radial coordinate by $R = \psi^2 r$. The
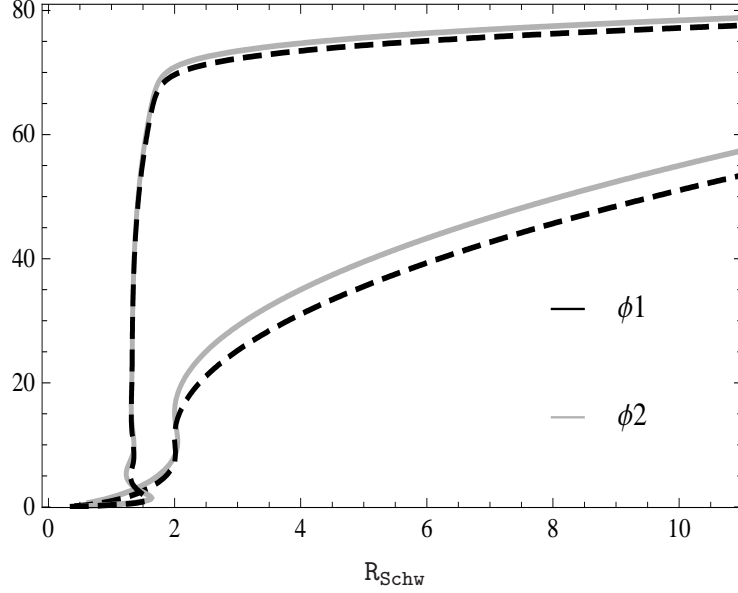
Figure 6.9.   Vertical section through an embedding diagram of a two-dimensional slice ($t = const., \theta = \pi/2$) of the Schwarzschild solution with scalar field stuffing. The black dashed plots correspond to a scalar field given by Eq. (6.15), and the grey continuous plots to Eq. (6.19). The plots are presented at $time = 0$, rescaled by a factor of 5, and $time = 100M$. Notice the smooth matching in the initial data at the throat $R = 2M$. The second asymptotically flat end has been replaced by a singularity-free matter solution. At later times a cylinder with radius $R \approx 1.3M$ forms and the behavior is similar to the one presented in Fig. (6.1).

value $r = M/2$ marks the location of the apparent horizon and $r = 0$ is the image of space infinity.

Our numerical test are based on the 'wormhole' type of puncture data for black hole evolutions, where the singularity in the conformal factor is $\psi \sim 1/r$. The typical choice in current black hole evolutions is the 'trumpet' data, where the singularity is milder $\psi \sim 1/\sqrt{r}$ [69]. However, most of our simulations are following the *stuffed black hole* approach [70], where we match a scalar field in the interior BH region, such that the metric becomes regular inside the horizon Fig. (6.12). The procedure is described in the following.

6.2.1.b   Matter Terms

The stress-energy tensor associated to the 'stuffed' scalar field can be written as

$$T_{\mu\nu} = \phi_\mu \phi_\nu - \frac{g_{\mu\nu}}{2}(g^{\tau\rho}\phi_\tau \phi_\rho), \tag{6.7}$$
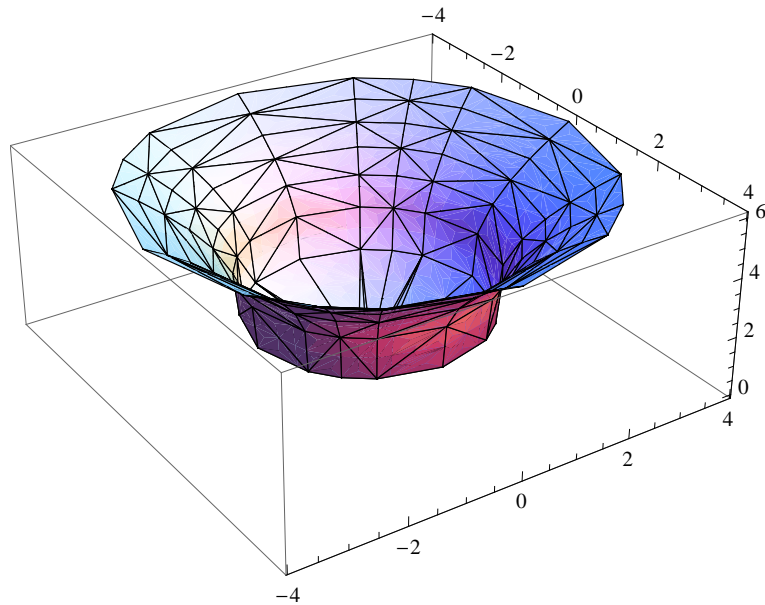
Figure 6.10. Embedding diagram of a two-dimensional slice ($t = 0, \theta = \pi/2$) of the Schwarzschild solution with scalar field stuffing. The location of the throat is at $R = 2M$ and the distance to the rotation axis is R. The second asymptotically flat end, present in Fig. (6.2), has been replaced by a singularity-free matter solution.
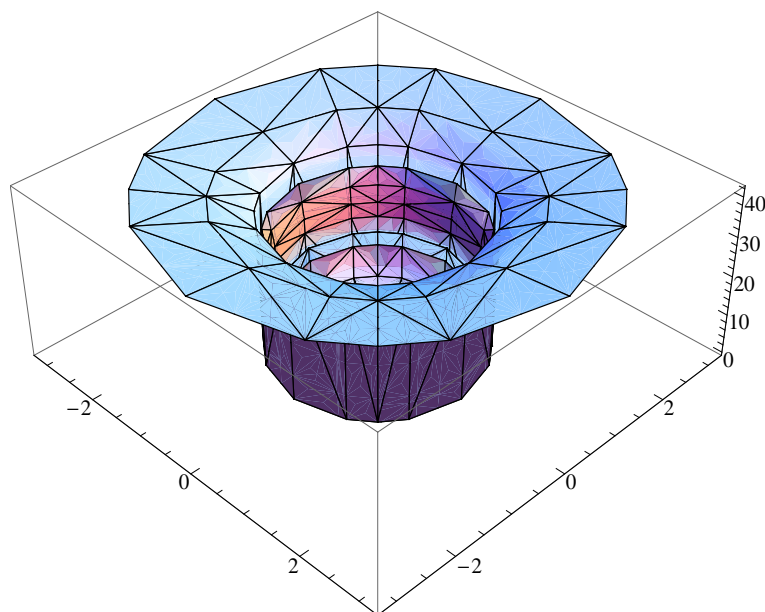
Figure 6.11. Embedding diagram of a two-dimensional slice ($t = 100, \theta = \pi/2$) of the Schwarzschild solution with scalar field stuffing. An infinitely long cylinder with radius $R \approx 1.3M$ forms and the behavior is similar to the one presented in Fig. (6.3).

where $\phi_\mu = \partial_\mu \phi$. The scalar field can be decomposed in spatial and normal components as follows

$$\phi_i = \partial_i \phi, \qquad \phi_n = n^\mu \phi_\mu = -\frac{1}{\alpha}(\phi_t - \beta^p \phi_p).$$

Performing a 3+1 decomposition of Eq. (6.7), and using the definitions Eqs. (2.20) - (2.22), we obtain the components of $T_{\mu\nu}$ in terms of the scalar field:

$$
\begin{aligned}
\tau &= \frac{1}{2}(\phi_n{}^2 + \phi^p \phi_p + \frac{\beta^p}{\alpha}\phi_p \phi_n), \\
S_i &= \phi_n \phi_i, \\
S_{ij} &= \phi_i \phi_j + \frac{1}{2}g_{ij}(\phi_n{}^2 - \phi^p \phi_p - \frac{\beta^p}{2\alpha}\phi_n \phi_p).
\end{aligned}
$$

These matter terms enter in the sources of the Einstein field equations (2.10).

6.2.1.c   Scalar Field Evolution Equations

An evolution equation for the scalar field is given by the stress-energy tensor conservation Eq. (2.8). This leads to a scalar wave equation for ϕ,

$$\Box \phi = \frac{1}{\sqrt{g}}\partial_\mu[\sqrt{g}g^{\mu\nu}\phi_\nu] = 0. \tag{6.8}$$

where g is the determinant of the spacetime metric.

A first order version of the flux conservative evolution equations can be obtained by considering the first derivatives $\phi_i = \partial_i \phi$ and $\phi_t = \partial_t \phi$ as independent quantities,

$$
\begin{aligned}
\partial_t \phi_i &+ \partial_i[-\phi_t] = 0, \\
\partial_t F_\phi &+ \partial_p[\sqrt{g}(g^{pq}\phi_q - \frac{\beta^p}{\alpha^2}\phi_t)] = 0,
\end{aligned}
\tag{6.9}
$$

where $F_\phi = -\frac{\sqrt{g}}{\alpha^2}(\phi_t - \beta^p \phi_p)$. The principal part of the matter evolution system is fully decoupled from that of the field equations.

6.2.1.d   Matching Technique

The initial data must satisfy the energy and momentum constraints Eqs. (3.5, 3.6), where θ and Z_i are set to zero. In the time symmetric case $K_{ij} = 0$, the constraints translate into

$$
\begin{aligned}
\mathcal{R} &= 16\pi\tau, \tag{6.10} \\
0 &= \phi_n \phi_i. \tag{6.11}
\end{aligned}
$$
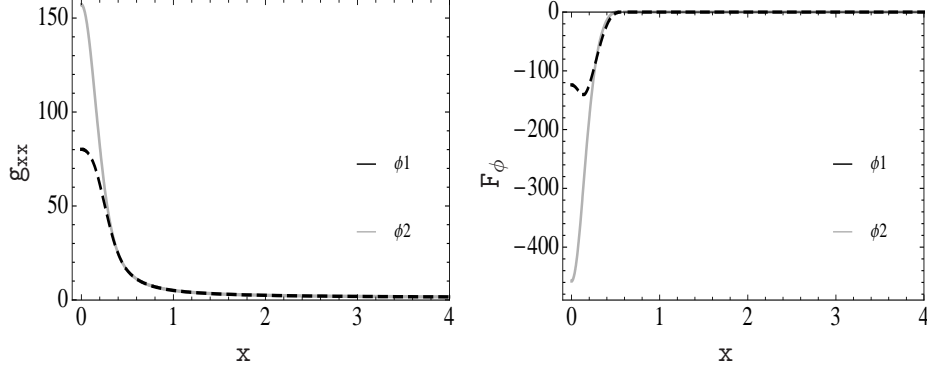
Figure 6.12. Illustration of the initial data for a Schwarzschild black hole in isotropic coordinates. The black dashed curves correspond to a scalar field matching given by Eq. (6.15) and the grey continuous ones, by Eq. (6.19). Left panel: The metric component g_{xx} on the x-axis. Note the smooth matching in the Schwarzschild metric between the interior region, which contains the scalar field, and the exterior region. The matching point is $r = M/2$, respectively $x = 0.5$ in this figure. Right panel: The scalar field variable F_ϕ on the x-axis.

The momentum constraint Eq. (6.11) can be satisfied by considering ϕ_i to be zero everywhere on the initial time slice, while the energy constraint leads to a condition for the time component of scalar field.

In order to calculate the energy constraint Eq. (6.10), we consider the line element Eq. (6.6) with $m = m(r)$. We assume a constant mass value for the black hole exterior, such that the energy constraint will be satisfied for $\tau = 0$. In the interior region, we choose the following form for the second radial derivative of the mass

$$m''(r) = \mu(1 - \cos(4\pi r/M)), \qquad (6.12)$$

where μ is a constant. Imposing matching conditions at the center and the throat,

$$r = 0: \qquad\qquad\qquad\qquad m = m'' = 0, \qquad (6.13)$$

$$r = \frac{M}{2}: \qquad\qquad m = M, \qquad m' = m'' = 0, \qquad (6.14)$$

one can calculate the integration constants and obtain $m(r)$.

Then the metric factor takes the form

$$\psi = 1 + \frac{4r - (8/M)(r^2/2 + (M/(4\pi))^2(\cos(4\pi r/M) - 1))}{2r}, \qquad (6.15)$$

and the Laplacian of ψ can be written as

$$\Delta\psi = \frac{1}{r^2}\partial_r(r^2\psi') = \frac{m''(r)}{2r}. \qquad (6.16)$$

On the other hand, from the energy constraint, where the scalar field energy density is $\tau = (\phi_t/\alpha)^2/2$ and $K = 0$ initially, one can write in the conformally flat case,

$$\Delta \psi = -2\pi\tau\psi^5. \qquad (6.17)$$

Using the two equalities for the metric factor, the initial data for the time derivative of the scalar field can be computed as

$$\phi_t = 2\alpha\sqrt{\frac{1 - \cos(4\pi r/M)}{\pi r M \psi^5}}. \qquad (6.18)$$

The initial data of F_ϕ is presented in Fig. (6.12).

We present also an alternative scalar field initial data, for later comparison of numerical results. The mass can be chosen as

$$m(r) = M\left[1 + \frac{21}{4}\left(\frac{2r}{M} - 1\right)^5 + \frac{49}{8}\left(\frac{2r}{M} - 1\right)^6 + \frac{15}{8}\left(\frac{2r}{M} - 1\right)^7\right], \qquad (6.19)$$

such that the matching conditions Eqs. (6.13), (6.14) are satisfied.

6.2.2 Black Hole Evolution

6.2.2.a Numerical Setting

We performed numerical simulations in an uniform grid, with resolutions $dx = 0.1$ and $dx = 0.05$, boundaries at $10M$ and $20M$ (no mesh refinement). We use the 4th and 6th order centered FD methods, in combination with the corresponding order adaptive dissipation algorithm (derived from our CFV method, Section 5.2.3). The time integration algorithm is a 3rd order Runge Kutta method (Appendix 9.4).

The position of the apparent horizon can be calculated using Eq. (6.4) written as

$$g^{pq}\partial_p\tilde{n}_q - 2\tilde{n}_l D_{kqp}g^{kq}g^{pl} + \tilde{n}_l D_{pqk}g^{pl}g^{qk} + K_{pq}g^{ip}g^{qj}\tilde{n}_i\tilde{n}_j - K = 0,$$

with

$$g^{pq}\partial_p\tilde{n}_q = \frac{g^{kk}}{\sqrt{n_p n_q g^{pq}}} - \frac{1}{n_p n_q g^{pq}} + \frac{D^{kij}n_k n_i n_j}{(n_p n_q g^{pq})^{3/2}}.$$

Considering just the x-axis, where the normal is defined as $\tilde{n}_x = (\frac{1}{\sqrt{g^{xx}}}, 0, 0)$ and $n_x = (x, 0, 0)$, one can write the equation in a simple way,

$$\frac{g^{yy} + g^{zz}}{|x|\sqrt{g^{xx}}} + \frac{D_{pql}g^{px}g^{qx}g^{lx}}{g^{xx}\sqrt{g^{xx}}} - 2\frac{D_{lpq}g^{lq}g^{px}}{\sqrt{g^{xx}}} + \frac{D_{plq}g^{px}g^{ql}}{\sqrt{g^{xx}}} + \frac{K_{pq}g^{px}g^{qx}}{g^{xx}} - K = 0.$$

This formula will be used to compute the apparent horizon location in our numerical simulations.

6.2.2.b   Numerical Results

The evolution of the black hole initial data presented in the previous section, can be viewed in an embedding diagram of a two-dimensional slice ($time = const., \theta = \pi/2$) of the Schwarzschild solution Fig. (6.9). The singularity at $r = 0$ is replaced with a regular solution. The matching of the scalar field initial data is done at the throat $R = 2M$. At later times, a cylinder with radius $R = 1.31241M$ is formed, following an evolution similar to the one described in Fig. (6.1). Even though there is a difference between the initial slices in Fig. (6.9), as we use different scalar fields, the evolution shows an identical behavior.

Our observations are in agreement with the study presented in [69], where the numerical evolution of '1+log' foliations of the Schwarzschild solution is discussed in the context of the puncture method. We conclude that the behavior of standard Schwarzschild data in the '1+log' gauge is generally described by Fig. (6.9), whether one chooses to deal with the singularity by employing the puncture technique or one appeals to any scalar field content.

This behavior is expected, as the initial profile of the scalar field is matched inside the apparent horizon and it remains confined in the interior black hole region during the evolution. This can be noticed in the energy density profiles in the right panel of Fig. (6.13). In the left panel of the same figure, one can observe the collapse front of the lapse and the apparent horizon. As the gauge speed is $\alpha\sqrt{f(\alpha)g^{xx}}$, with $f(\alpha) = 2/\alpha$, the upper part of the collapse front moves faster then the apparent horizon, which travels at the speed of light $\alpha\sqrt{g^{xx}}$.

The dynamics of the lapse function in a Schwarzschild black hole evolution with scalar field matching can be viewed in Fig. (6.14). We notice that higher order methods lead to steeper profiles and slower propagation of the collapse front. The differences in the front propagation speed clearly grow in time, although the plot at $t = 40M$ is affected by the dissipative effect of the boundaries. This effect of steeper profiles was present also in our simulations in spherical symmetry, and it does not create stability problems. We can perform long term simulations, until the collapse front gets out of the computational domain.

We present also a plot of the lapse function obtained in a simulation using the third order algorithm Fig. (6.14), with double resolution $dx = 0.05$ in a smaller computational domain of $10M$. The position and slope of the collapse front are similar to the ones obtained using the fifth order algorithm, with a resolution $dx = 0.1$. This means that the accuracy of the numerical simulation can be significantly improved by employing higher order spatial discretization schemes.

Note however that higher order algorithms are known to be less robust [71]. As the profiles get steeper, the risk of under-resolution at the collapse front increases, so the minimum resolution required by a higher order algorithm is more expensive than for the minimum resolution for lower order methods. In this case, the fifth order algorithm is a convenient choice for the $dx = 0.1M$ resolution in isotropic
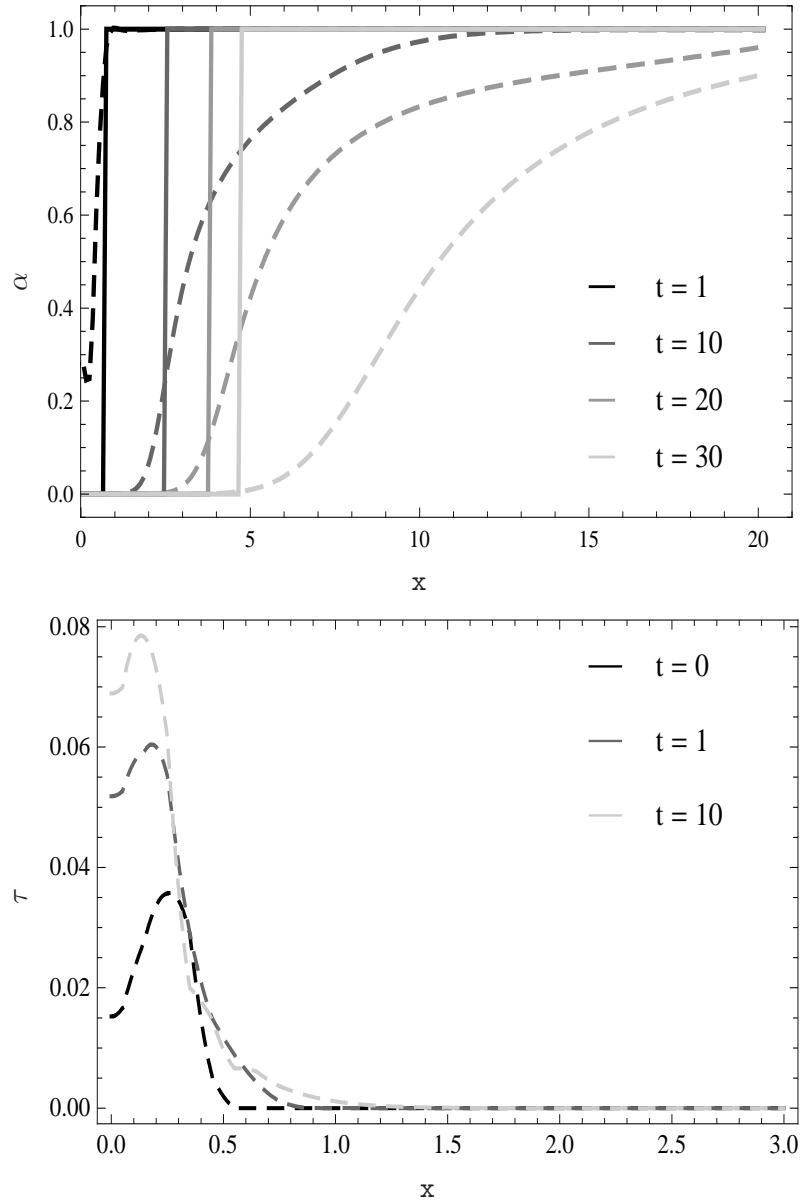
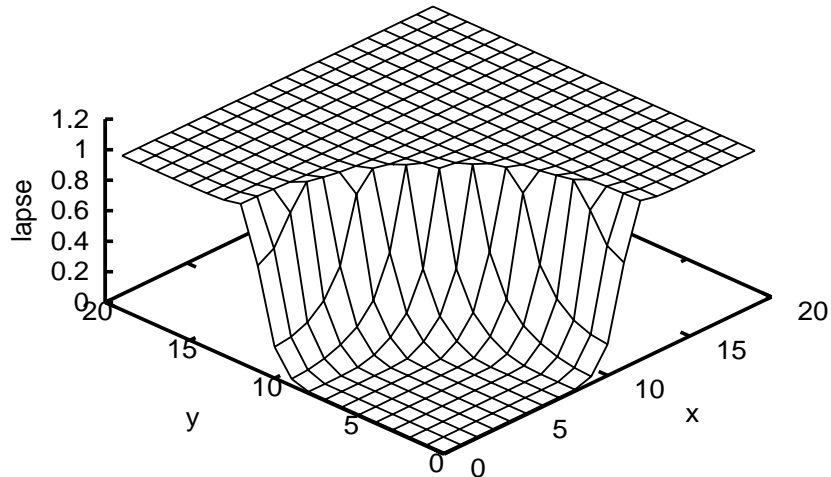**Figure 6.13**. Upper panel: Illustration of the Z4 lapse function on the x-axis, in a 3D Schwarzschild black hole evolution with scalar field stuffing. The dashed plots represent the collapse front of the lapse and the vertical lines the position of the apparent horizon, at $time = 1M$ (black plots), $time = 10M$ (dark-grey plots), $time = 20M$ (medium-grey plots), $time = 30M$ (light-grey plots). Lower panel: Illustration of Z4 energy density on the x-axis, in a 3D Schwarzschild black hole evolution with scalar field stuffing, at $time = 0$ (black plot), $time = 1M$ (dark-grey plot) and $time = 10M$ (light-grey plot).
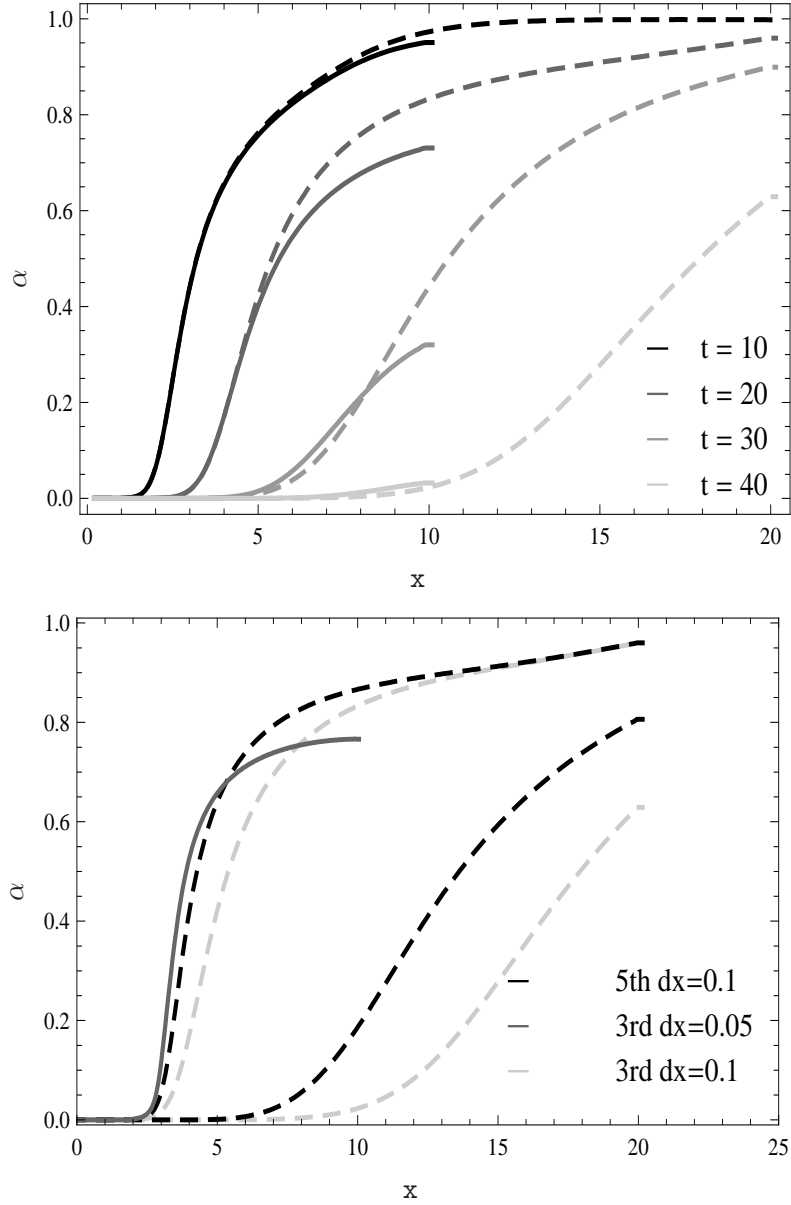
Figure 6.14. Illustration of the Z4 lapse function on the x-axis, in a 3D simulation of a Schwarzschild black hole with scalar field stuffing and '1+log' slicing. Upper panel: The collapse of the lapse function is presented from $time = 10M$ to $40M$ in intervals of $10M$, in a simulation with resolution $dx = 0.1$. The continuous plots correspond to a boundary set at $10M$ and the dashed plots, at $20M$. Lower panel: The collapse of the lapse function is presented at $time = 20M$ and $40M$, in a simulation with resolution $dx = 0.1$, using 3rd order (dashed grey plot) and 5th order (dashed black plot) methods. Notice that the higher order method leads to a slope steepening and a slower propagation of the collapse front. The same effect is visible when increasing the resolution to $dx = 0.05$ (continuous grey plot).

coordinates.

A similar evolution, using the puncture data, is presented in Fig. (6.15). One can notice that the two collapse fronts are almost identical, so the success of the simulations does not depend crucially on the treatment of the singularity. The key ingredients are most probably the numerical methods employed and the analytical properties of the system.
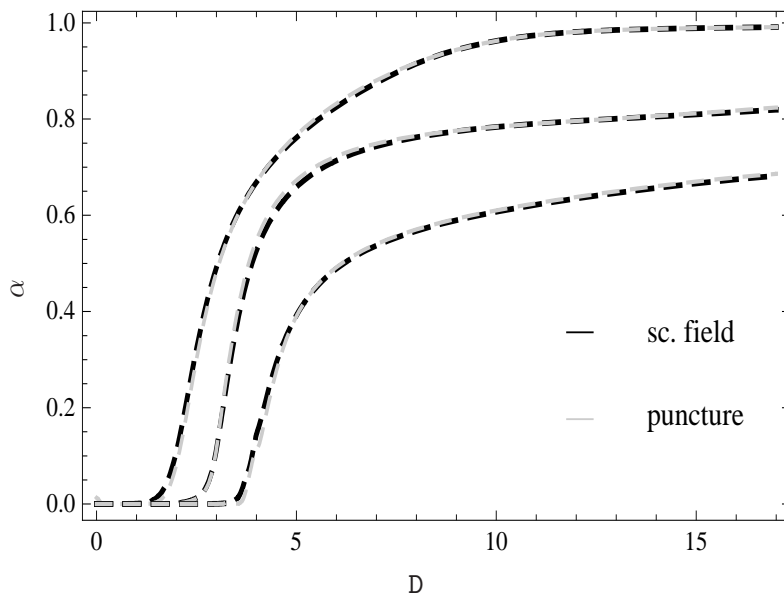
Figure 6.15. Illustration of the Z4 lapse function on the diagonal, in a 3D Schwarzschild black hole evolution, with resolution $dx = 0.05$. The collapse of the lapse is presented from $time = 10M$ to $30M$ in intervals of $10M$. The black plots correspond to an evolution with scalar field stuffing and the grey plots to a puncture evolution.

One can notice that our isotropic simulations are limited by the vicinity of the boundary. We appeal to the space coordinate freedom, switching to logarithmic coordinates, defined as

$$r = L \sinh(R/L),$$

where R is the new radial coordinate and L the length scale factor. We perform long-term numerical simulations with $L = 1.5M$, such that $R = 20M$ in these logarithmic coordinates corresponds to $r = 463000M$ in the original isotropic coordinates.

The collapse front is safely away from the boundary, even at late times Fig. (6.16). We stopped the simulation at $t = 1000M$ without any sign of instability. This provides a new benchmark for Numerical Relativity codes, namely a long-term simulation of a single black hole in normal coordinates, without excision. It

shows that a non-vanishing shift prescription is not a requisite for code stability in black hole simulations.

Figure 6.16. Illustration of the Z4 lapse function on the xy-plane, in a 3D Schwarzschild black hole evolution with scalar field stuffing. The collapse of the lapse is presented at $time = 1000M$, with resolution $dx = 0.1$. Only one of every ten points is shown along each direction.

6.2.3   Discussion

In this chapter, we presented the first long term simulation of a Schwarzschild black hole, with singularity avoiding '1+log' gauge in normal coordinates without excision. We developed a geometrical picture of the slicings approaching the stationary state, for situations where the treatment of the singularity involves both scalar field stuffing and the puncture technique.

Our system is based on a first order flux conservative version of the Z4 formalism (Section 3.1.1), that is adjusted for dealing with constraint violations. The implementation uses a family of robust, cost-efficient, finite difference adaptive dissipation algorithms (Section 5.2.3).

In a similar setting, the simulations performed with the BSSN system are reported to crash around $t = 40M$ [72]. The success of the BSSN in long term dynamical simulations of a single black hole without excision, relies completely on a specific combination of the '1+log' and 'Gamma-driver' gauge conditions. The choice of lapse is understandable, as dealing with the collapse singularity, without the use of excision, requires a singularity avoiding slicing. But this a property of

the time coordinate, which should be independent of the shift prescription. In the spirit of General Relativity, we expect a single black hole numerical code to work also in normal coordinates.

A further comparison with the old second order Bona-Masso formalism [73], shows that the steep profiles produced by slice stretching (radial expansion) could be evolved only by employing FV methods with slope limiters. Our numerical method is an efficient CFV algorithm, which does not require characteristic decomposition, it is easy to implement and not expensive in terms of computational costs. As the limiters are not required in the vacuum case, the method is comparable with a finite difference plus adaptive dissipation algorithm.

On an analytical level, both the BSSN and the Bona-Masso require a conformal decomposition of the spatial metric and trace-cleaning (the trace of the extrinsic curvature is set to zero). The numerical experience with the Bona-Masso system shows that spurious numerical trace modes arise in the trace-free part of the extrinsic curvature [73]. In our Z4 simulations, both the plain metric and extrinsic curvature can be used without any additional trace cleaning mechanisms.

The numerical results show that the Z4 implementation has a very good performance not only in the standard Numerical Relativity tests (Chapter 4), but also in black hole simulations [54], using both scalar field stuffing and the puncture technique. The code behaves well with different slicing conditions from the '1+log' family and is not especially tuned for normal coordinates, as we will present in Chapter 9 simulations with non-vanishing shift. However, our numerical simulations require further technical developments, like improving the boundary treatment and using mesh refinement techniques.

Chapter 7

Boson Stars

Dark matter and dark energy are believed to account for more than 90% of the mass in the universe. The existence of dark matter was postulated since 1933, by astronomers who observed that distant galaxies must be held together by a huge gravitational pull caused by some invisible form of matter. It gained the name "dark matter" because it is undetectable by its emitted radiation, but its presence can be inferred from gravitational effects on visible matter.

The observed phenomena which imply the presence of dark matter include the rotational speeds of galaxies, orbital velocities of galaxies in clusters, gravitational lensing of background objects by galaxy clusters and the temperature distribution of hot gas in galaxies and clusters of galaxies. Dark matter also plays a central role in structure formation and galaxy evolution, and has measurable effects on the anisotropy of the cosmic microwave background. One of the most convincing evidence comes from the observations of the rotational curves of galaxies. These usually exhibit a characteristic flat behavior at large distances [74].

Even though direct detection of dark matter has not been confirmed yet, there are promising detections which lead to the believe that dark matter is more then a theoretical concept. Recent observations [75] report an excess of galactic cosmic-ray electrons at high energies which could arise from (annihilation of) dark matter particles. A possible laboratory detection of dark matter particles hitting the Earth has been announced this year by the DAMA collaboration [76]. Even though scientists belive that this is not just a statistical fluke, the result should be confirmed by other research groups.

Determining the nature of the missing mass in the universe is one of the most important problems in modern cosmology and particle physics. A large number of different particles have been proposed as candidates for dark matter. We focus on scalar fields dark matter models, in which the particle is a massive spinless boson.

The boson particles can collapse into the same quantum state of the gravitational potential to form a Bose Einstein condensate. In these configurations, the quantum effects become apparent even on a macroscopic scale. One of these Bose

Einstein condensate is a compact gravitating object, named boson star. Boson stars are solutions of the Einstein equations that describe a family of self-gravitating scalar field configurations within General Relativity.

In this chapter we present boson stars evolutions performed with the Einstein-Klein-Gordon system, using as initial data several complex scalar fields, following the classical approximation. We show a brief description of how the initial data for the mixed states is constructed, and study these models in relativistic evolutions. The results are focused on two models. In the first one, we add a massless scalar field perturbation to a model of ground configuration and follow the evolution in order to see the effect of the perturbation on the stability of the configuration. In the second one, we study the evolution of Mixed State Boson Stars (MSBS) under perturbations, identify the unstable models and determine the final state of the configurations. We analyze the coupling phase and the growth rate of the unstable configurations, in order to find the separation between stable and unstable states.

7.1   Theoretical Aspects

Boson stars are self-gravitating scalar field objects, for which the gravity attraction balances the dispersive character of the scalar field. The treatment of boson stars follows two different approaches, the first settled by Kaup [77] and the latest by Ruffini and Bonazzola [32]. The one developed in [77] is a completely classical treatment with a massive complex scalar field which is minimally coupled to gravity. The second one [32], also known as semiclassical limit, adopts a real quantized scalar field though maintaining the geometry as a classical entity. It turns out that the two approaches lead to the same self-gravitating system. Until now, the only known stable boson stars are made of ground state scalar fields. The associated mass density profiles decay exponentially as $r \to \infty$, making it difficult to fit the flat rotational curves of most galaxies.

We use a generalization of boson stars which was previously pointed out in [32]. The idea is to consider a system of bosons which are not all in the ground state, but formed by particles which are coexisting in different states. In this view, the MSBS can be seen as a collection of complex scalar fields, one for each state, coupled only through gravity.

Our study is focused on the properties of these mixed (ground-excited) state configurations and their possibility to model dark matter in galaxy halos (see [33] for a recent review). For a single boson star without self-interaction, the only free parameters are the mass of the boson particle m and the central value of the scalar field $\phi(r = 0)$, which determines the compactness of the object (ie, ratio of total mass over radius) in adimensional units. There have been several attempts to fit these parameters, with different levels of success. By allowing more general MSBS, there are extra free parameters coming from the different fractions between

the ground and excited states. These parameters change not only the total mass, but also the compactness of the final object. The extra degrees of freedom may allow a better fit of the models to different galaxies.

An important point of our study is the stability of the models, which is a necessary condition in order to be considered models of galaxy halos. A single boson star in the ground state is stable against perturbations, if its mass is below a maximum allowed value M_{max}, result that has been shown both by analytical [78, 79] and numerical [31] studies. On the other hand, a single boson star in the excited state is unstable even for $M < M_{max}$, since small perturbations drive the star either to collapse to a black hole or to decay to the ground state. From these results one could expect that the MSBS states are unstable, since they contain at least one excited unstable state. However, our numerical results show that at least a subdomain of the solution space gives stable solutions. Roughly speaking, the ground state produces a deeper gravitational potential which can be enough to stabilize the excited state.

7.1.1   The Einstein-Klein-Gordon System

We consider a real massive scalar field with N different excited states, which is equivalent to considering a collection of N complex scalar fields, one for each state, coupled only through gravity.

In a curved spacetime, the dynamics of these MSBS can be described by the following Lagrangian density,

$$\mathcal{L} = -\frac{1}{16\pi}R + \sum_{n=1}^{N}\frac{1}{2}\left[g^{\mu\nu}\partial_\mu\bar{\phi}^{(n)}\partial_\nu\phi^{(n)} + V\left(\left|\phi^{(n)}\right|^2\right)\right], \qquad (7.1)$$

where $\phi^{(n)}$ are the scalar fields, $\bar{\phi}^{(n)}$ their complex conjugate, and $V(|\phi^{(n)}|^2)$ a potential depending only on $|\phi^{(n)}|^2$.

This Lagrangian gives rise to the equations determining the evolution of the metric (Einstein equations) and those governing the scalar field behavior (Klein-Gordon equations).

7.1.1.a   The Klein-Gordon Equations

The variation of the Lagrangian (7.1) with respect to each scalar field $\phi^{(n)}$ leads to a set of Klein-Gordon equations, which are coupled through gravity,

$$\Box\phi^{(n)} = \frac{dV}{d|\phi^{(n)}|^2}\phi^{(n)}. \qquad (7.2)$$

We restrict ourselves to the free field case where the potential takes the form

$$V(|\phi^{(n)}|^2) = m^2\,|\phi^{(n)}|^2\,, \qquad (7.3)$$

with m a parameter that can be identified with the bare mass of the field theory.

The complex scalar field can written as

$$
\begin{aligned}
\phi &= \phi^R - i\phi^I, \\
\bar{\phi} &= \phi^R + i\phi^I,
\end{aligned}
$$

where ϕ_R is the real part, ϕ_I provides the imaginary part and $\bar{\phi}$ is the complex conjugate. A reduction to first order can be performed by defining as evolution variables,

$$
\begin{aligned}
\phi_t^{(n)} &= \frac{\sqrt{h_{rr}}}{\alpha}\partial_t\phi^{(n)}, \\
\phi_r^{(n)} &= \partial_r\phi^{(n)}.
\end{aligned}
$$

Then the Klein-Gordon system can be written for each field $\phi \equiv \phi^{(n)}$ as

$$
\partial_t\phi^{R,I} = \alpha\sqrt{h^{rr}}\phi_t^{R,I}, \tag{7.4}
$$

$$
\partial_t\phi_r^{R,I} = \partial_r[\alpha\sqrt{h^{rr}}\phi_t^{R,I}], \tag{7.5}
$$

$$
\partial_t\phi_t^{R,I} = \partial_r[\alpha\sqrt{h^{rr}}\phi_r^{R,I}] + \alpha\sqrt{h^{rr}}[2(D_{r\theta}{}^{\theta} + 1/r)\phi_r^{R,I} +
$$

$$
+ 2\sqrt{h_{rr}}K_\theta{}^\theta\phi_t^{R,I} - m^2 h_{rr}\phi^{R,I}]. \tag{7.6}
$$

The matter Lagrangian is invariant under global U(1) transformations:

$$
\phi^{(n)} \rightarrow \phi^{(n)}e^{i\varphi^{(n)}}.
$$

This symmetry implies that there are a set of Noether currents, one for each field,

$$
J^\mu = \frac{i}{2}\sqrt{-g}g^{\mu\nu}[\bar{\phi}\,\partial_\nu\phi - \phi\,\partial_\nu\bar{\phi}],
$$

satisfying the conservation law

$$
\nabla_\mu J^\mu = \frac{1}{\sqrt{g}}\partial_\mu(\sqrt{g}J^\mu) = 0.
$$

This law ensures the conservation of the charge density $\tilde{N} = J^\mu n_\mu$, which can be computed as

$$
\tilde{N} = \alpha J^0 = \frac{1}{\sqrt{h_{rr}}}(\phi^I\phi_t^R - \phi^R\phi_t^I).
$$

As discussed in [32], the Noether charge

$$
N = \int \sqrt{h}\,\tilde{N}\,dx^3 = 4\pi\int r^2\tilde{N}\sqrt{h_{rr}}h_{\theta\theta}dr, \tag{7.7}
$$

can be associated with the number of bosonic particles.

7.1.1.b The Einstein Equations

The variation of the action associated with the Lagrangian (7.1), with respect to the metric g_{ab}, leads to the well-known Einstein equations

$$R_{\mu\nu} - \frac{R}{2} g_{\mu\nu} = 8\pi T_{\mu\nu}, \tag{7.8}$$

where $T_{\mu\nu}$ is given by the addition of the single stress-energy tensors for each scalar field, namely

$$T_{\mu\nu} = \sum_{n=1}^{N} T_{\mu\nu}^{(n)}, \tag{7.9}$$

$$
\begin{aligned}
T_{\mu\nu}^{(n)} &= \frac{1}{2}\left[\partial_\mu \bar{\phi}^{(n)} \partial_\nu \phi^{(n)} + \partial_\mu \phi^{(n)}\, \partial_\nu \bar{\phi}^{(n)}\right] \\
&\quad - \frac{1}{2} g_{\mu\nu}\left[\partial_\lambda \bar{\phi}^{(n)} \partial^\lambda \phi^{(n)} + V\left(|\phi^{(n)}|^2\right)\right].
\end{aligned} \tag{7.10}
$$

The explicit form of the matter terms can be found in the Appendix 9.6.2.

A useful quantity for the analysis of the system is the mass. The problem of finding a general definition for the total mass (or energy) of a system is a difficult challenge in General Relativity, mainly because the gravitational field energy is not part of the energy-momentum tensor. However, for spacetimes which are asymptotically flat, namely represent some isolated gravitating system in otherwise empty and gravity-free infinite space, the ADM mass can be well-defined,

$$M_{ADM} = \frac{1}{16\pi} \lim_{r \to \infty} \int g^{pq}[\partial_q g_{pk} - \partial_k g_{pq}]N^k dS,$$

where $N^r = \sqrt{h^{rr}}\delta_r{}^r$ is the unit outward normal to the sphere. In spherical symmetry, it can be translated into

$$M_{ADM} = -r^2 \sqrt{h^{rr}} D_{r\theta}{}^\theta. \tag{7.11}$$

The ADM mass gives valid results only in the regions where the spacetime asymptotically approaches Minkowski space.

We monitor also the Tolman mass, which can be written in the case of spherically symmetric systems with matter,

$$
\begin{aligned}
M_{Tol} &= \int (T_0{}^0 - T_i{}^i)\sqrt{-g}\; dx^3 = \\
&= -4\pi r^2 \alpha \sqrt{h_{rr}} h_{\theta\theta}(\tau + S_r{}^r + 2S_\theta{}^\theta).
\end{aligned} \tag{7.12}
$$

We write the Einstein equations (7.8) in the form of the Z3 strongly hyperbolic system in spherical symmetry (Appendix 9.6.1).

7.1.1.c   Regularization

We consider a generic spherically symmetric spacetime, where the line element takes the form,

$$ds^2 = -\alpha^2 dt^2 + \psi(r)^4(dr^2 + r^2 d\Omega^2),$$

with $\psi = \left(1 + \frac{M}{2r}\right)$. One can notice that $h_{\theta\theta} = r^2\psi^4$ is singular when $r \to 0$. Also $D_{r\theta}{}^\theta = \frac{h^{\theta\theta}}{2}\partial_r h_{\theta\theta}$ is proportional to $1/r$, which leads to a singular behavior at the origin. When dealing with black holes systems, this problem can be avoided by setting the inner boundary at the apparent horizon, far from the physical and coordinate singularity at $r = 0$ (Chapter 6). The problem is different when dealing with stars, since there is no way of cutting the solution before $r = 0$ without loosing physically relevant information. The coordinate singularity destroys stability and accuracy near the origin.

We use the approach proposed in [80] and remedy this problem using the extra Z^i quantities introduced in the Z3 formulation of the Einstein equations (Section 3.1.1). The first step consists in analytically extracting the geometrical factors from the equations, so that we only have to deal with the regular part. This can be done by writing the line element as

$$ds^2 = -\alpha^2 dt^2 + h_{rr}dr^2 + r^2 h_{\theta\theta}d\Omega^2,$$

which implies the following transformation of variables

$$
\begin{aligned}
\tilde{h}_{\theta\theta} &= r^2 h_{\theta\theta}, \\
\tilde{D}g_{r\theta}{}^\theta &= D_{r\theta}{}^\theta + \frac{1}{r},
\end{aligned}
$$

where the quantities marked with *tilde* are the old variables. The $h_{\theta\theta}$ and $D_{r\theta}{}^\theta$ are now regular at the center, but the stability of the implementation is still not insured. One has to deal with the factors $1/r$ in the fluxes and $1/r^2$ in the sources.

The second step consists in cross-cancellation between these terms, in order to obtain a regular system. One can take advantage of the way the momentum constraint was built into the system through the variable Z_r. A simple and convenient way to redefine the Z_r in order to obtain the desired cross-cancellation in the $n = 4/3$ case is

$$\tilde{Z}_r = Z_r + \frac{1}{4r}\left(1 - \frac{h_{rr}}{h_{\theta\theta}}\right).$$

We have eliminated this way the singularities from the evolution variables and the numerical error caused by the geometrical factors in the fluxes and sources. A detailed description of the evolution equations in given in the Appendix 9.6.2. One can notice that the sources contain terms like $1/r$ times other variables which

are radial derivatives of the metric coefficients. But these terms do not create problems as $r \to 0$, as the radial derivatives of any differentiable function vanish at the origin. However, due to finite differencing, we can not use a grid point at $r = 0$.

This way of performing the regularization of the Einstein equations in spherical symmetry allows us to evolve the whole grid, without any special techniques or different algorithms in the center. The system of equations is now intrinsically stable.

7.1.2 Boson Initial Data

The initial data for boson star configurations is computed in spherical symmetry with a one-dimensional code. We follow the technique proposed in [77, 81, 82], where the initial data is generated in maximal-isotropic coordinates, by first constructing the stars in polar-areal coordinates and then performing a coordinate transformation.

The line element in these coordinates takes the form,

$$ds^2 = -\alpha\left(r\right)^2 dt^2 + a\left(r\right)^2 dr^2 + r^2 d\Omega^2. \tag{7.13}$$

We adopt the following harmonic ansatz for each scalar field,

$$\phi^{(n)}(t,r) = \phi_n(r)\, e^{-i\omega_n t}. \tag{7.14}$$

With this assumption the source for the Einstein equations becomes time independent. Our goal is to find $\{\phi_n(r), \omega_n, a(r), \alpha\}$ such that the spacetime generated by this matter configuration is static. Then the extrinsic curvature tensor vanishes identically and the momentum constraint is automatically satisfied.

The Hamiltonian constraint and the Klein-Gordon equation lead to the following equilibrium equations:

$$\partial_r a = \frac{a}{2}\left\{-\frac{a^2-1}{r} + 4\pi r \sum_{n=1}^{N}\left[\left(\frac{\omega_n^2}{\alpha^2} + m^2\right)a^2\phi_n^2 + \Phi_n^2\right]\right\},$$

$$\partial_r \alpha = \frac{\alpha}{2}\left\{\frac{a^2-1}{r} + 4\pi r \sum_{n=1}^{N}\left[\left(\frac{\omega_n^2}{\alpha^2} - m^2\right)a^2\phi_n^2 + \Phi_n^2\right]\right\},$$

$$\partial_r \phi_n = \Phi_n,$$

$$\partial_r \Phi_n = -\left\{1 + a^2 - 4\pi r^2 a^2 m^2 \left(\sum_{s=1}^{N}\phi_s^2\right)\right\}\frac{\Phi_n}{r} - \left(\frac{\omega_n^2}{\alpha^2} - m^2\right)\phi_n a^2.$$

The conditions for regularity at the origin

$$a\left(0\right) = 1, \tag{7.15}$$

$$\Phi_n\left(0\right) = 0, \tag{7.16}$$

and for asymptotic flatness

$$\lim_{r \to \infty} \phi_n(r) \approx 0, \tag{7.17}$$

$$\lim_{r \to \infty} \alpha(r) = \frac{1}{a^2(r)}, \tag{7.18}$$

complete our system.

For given central values of the fields $\{\phi_{cn}\}$, using the conditions Eqs. (7.15, 7.16), one only needs to adjust the eigenvalues $\{\omega_n\}$ and the value $\alpha(0)$ in order to generate a solution with the appropriate asymptotic behavior Eqs. (7.17, 7.18). This is a 3-parameter shooting problem, that one solves by integrating from $r = 0$ outwards, using a second order shooting method for the parameters $\{\omega_n\}$ and $\alpha(0)$.

The outer boundary conditions for the scalar fields are imposed considering that localized solutions decrease asymptotically as

$$\phi_n \sim \exp\left(-\sqrt{m^2 - \omega_n^2}r\right)/r,$$

in a Scharzschild-type asymptotic background. These conditions are

$$\phi_n(r_{out})\left(\sqrt{m^2 - \omega_n^2} + \frac{1}{r_{out}^2}\right) + \Phi_n(r_{out}) = 0. \tag{7.19}$$

The shooting procedure is performed for different values of r_{out}. As r_{out} is increasing, the shooting parameters converge and we choose the solution as the one which satisfies the conditions Eq. (7.19), for some r_{out} within a prescribed tolerance. From this point on, we match to the scalar fields and the metric coefficients their asymptotic behavior. This is a necessary step in the construction of the initial data that we evolve in a numerical domain bigger than r_{out}.

A qualitative characteristic of the radial functions ϕ_n is their number of nodes, namely how many times do they cross zero, which determines the excited state of the boson star. If the radial function does not have any node, the boson star is in the ground state. If there is a node, the boson star is in the first excited state, and so on.

We have constructed initial configurations with two scalar fields, one in the ground state and the other in the first excited state. This is the easiest non-trivial state, since the MSBS with two scalar fields in the ground state can be reduced to one scalar field solution by redefining the scalar fields. This is a consequence of the indistinguishability of the boson particles in the same state.

Once the solution is computed in this coordinate system, a change of coordinates is performed to maximal isotropic ones,

$$ds^2 = \alpha^2(\tilde{r})\,dt^2 + \psi^4(\tilde{r})\left(d\tilde{r}^2 + \tilde{r}^2 d\Omega^2\right), \tag{7.20}$$

which is convenient for our numerical evolutions.

One obtains this way the initial data for the 4-metric components and the scalar field, which will be used in the following general relativistic simulations.

7.2 Numerical Results

Boson stars have equilibrium configurations corresponding to different levels of excitation of the scalar fields (different number of nodes). In this section, we present two classes of boson star models: single state (BS) and mixed states (MSBS) boson stars. From the first class, we choose a model of ground configuration and compare two cases: the unperturbed behavior and the evolution under the perturbation of a massless scalar field. In the second class, we focus on a model of mixed ground and excited configurations, and study the dynamical evolution of two cases (stable and unstable), which have different number of particles in the excited state.

We perform the BS analysis for two reasons. First, checking the validity of our numerical setting by comparison with previous results in the literature. Second, tuning the perturbation such that its effect would not change the dynamics of stable states. We are interested in applying the same perturbation to the stability study of MSBS configurations, for which previous results are not available. We note that numerical errors alone would also excite modes in the unstable configurations, but the timescale for which these would appear could be very large, depending on the resolution.

In order to facilitate the interpretation of the results, we remind the notation of the basic fields used in this section. The scalar field has the form

$$
\begin{aligned}
\phi^{(n)}(t,r) &= \phi_n(r)e^{-i\omega_n t} = \\
&= \phi_n(r)\cos(\omega_n t) - i\phi_n(r)\sin(\omega_n t),
\end{aligned}
$$

where by $\phi_n^R(t,r) = \phi_n(r)\cos(\omega_n t)$ we denote the real part, and $\phi_n^I(t,r) = \phi_n(r)\sin(\omega_n t)$ provides the imaginary part of the n scalar field. Each real and imaginary field can be viewed as a harmonic oscillator, with amplitude $\phi_n(r)$. At $t_0 = 0$, the real part of the scalar field is just the amplitude of the oscillator $\phi_n^R(r) = \phi_n(r)$. In the following, we will focus on the behavior of $\phi_n^R(t,r)$.

7.2.0.a Numerical Specifications

The numerical simulations are performed with Z3 system in spherical symmetry with regularization, as described in Section 7.1.1.c. In order to complete the system, we specify as gauge conditions a harmonic slicing and zero shift,

$$
\begin{aligned}
\partial_t \alpha &= -\alpha^2 (K_r{}^r + 2K_\theta{}^\theta), \\
\partial_t \beta^i &= 0.
\end{aligned}
$$

We need to perform long term evolutions, so it is important to diminish the amount of spurious reflections from the boundaries. We impose maximally dissipative boundary conditions, which suppress all incoming fields at the boundary.

This condition translates into:

$$\alpha K_\theta{}^\theta - \alpha\sqrt{h^{rr}}\frac{1}{3}(2Z_r - D_{r\theta}{}^\theta) \;\; = \;\; 0,$$

$$\alpha\,K - \alpha\sqrt{h^{rr}}A_r \;\; = \;\; 0,$$

$$\phi_t^{R,I} + \phi_r^{R,I} = 0.$$

The full characteristic decomposition of the system in presented in Appendix 9.6.2.

The numerical evolutions are performed using a third order centered finite volume algorithm for spatial discretization (Appendix 9.5.3), and a third order Runge Kutta method for time integration (Appendix 9.4).

The evolution domain extends to $r = 600M$, with resolution $dx = 0.02$. We use a Courant factor of 0.25. In most BS numerical simulations, an evolution up to $t = 5000M$ is sufficient in order to capture the relevant behavior. However, in the case of MSBS configurations we performed long term simulations, until $t = 15000M$ or more.

The Tolman and ADM masses Eqs. (7.12, 7.11), as well as the number of particles Eq. (7.7) are calculated at $r = 250M$.

7.2.1 Single State of Ground Configuration

In this subsection, we address the issue of stability for a single state boson star configuration. Stability refers to the ability of a star to settle into a new configuration from the same branch, when perturbed. Under radial finite perturbations, the ground state configurations of boson stars consist of a stable branch and an unstable branch. The transition point is at a critical mass of $M_{max} \approx 0.633 m_{pl}^2/m$, where m_{pl} is the Planck mass and m the mass of the boson star, corresponding to a central amplitude of the field $\phi(0) \approx 0.08$. The stars become more compact as $\phi(0)$ increases.

Numerical studies [31] show that the perturbed boson stars of the stable branch, will oscillate and settle into a new configuration, with less mass and larger radius than the initial configuration. Since the system is spherically symmetric (no gravitational waves can be emitted) and it satisfies the Klein-Gordon equation (with no viscous terms), the system can return to an equilibrium state only through radiation of scalar field. This mechanism seems to be crucial for the condensation and formation of boson stars. Heavier boson stars are unstable against small perturbations and they either collapse to a black hole or migrate and settle into the stable branch depending on the perturbation [31].

7.2.1.a Unperturbed case

We consider a boson star from the stable branch, namely a star with the central amplitude of the scalar field $\phi_1(0) = 0.0423$. The initial data is presented in Fig.
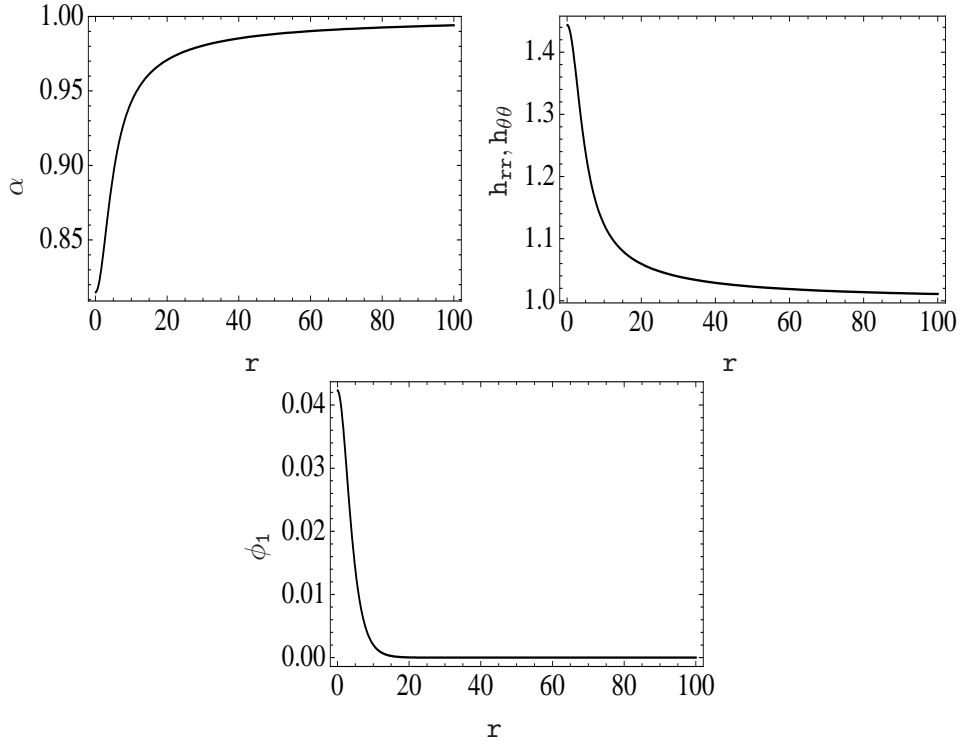
Figure 7.1. Illustration of initial data for an unperturbed boson star in the stable branch. The lapse function (upper left panel), the metric components (upper right panel) and the real component of scalar field (lower panel) are plotted as a function of the r isotropic coordinate.

(7.1). The Tolman mass gives the best agreement with the initial data, while the ADM mass tends as $r \to \infty$ to the expected value Fig. (7.2).

The configuration, evolved up to a time $t = 5000M$, presents a typical stable state BS dynamics. The central value of the scalar field $\phi_1^R(r_0)$ shows constant amplitude oscillations Fig. (7.4) . One can notice in its maximum $Max(\phi_1^R(r_0))$ Fig. (7.5), very small deviations from the initial value $\phi_1(r_0)$. There is a decrease in the number of particles, around 0.02% from the initial value, which is caused by numerical errors and the dissipative character of the outer boundary conditions. In Fig. (7.3) one can see that the mass remains constant. We compare different approaches in calculating the mass during the evolution and conclude that the Tolman mass provides very accurate results, while the ADM mass depends (as expected) on the radius of extraction.
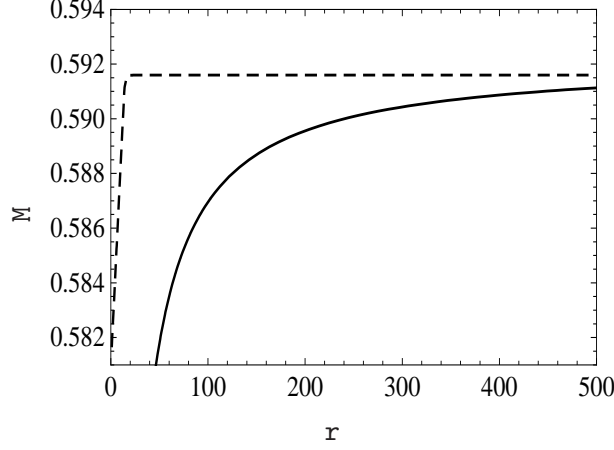
Figure 7.2. Illustration of the mass as a function of the r isotropic coordinate. Notice the values of the Tolman mass (dashed plot), which matches very well the expected value of $M = 0.5915$, and ADM mass (continuous plot), which approaches the expected value as $r \to \infty$.

7.2.1.b   Perturbed case

In order to study the stability of this model under perturbations, we send a spherical shell of "massless" scalar field into the boson star. The initial data for this field is a Gaussian of the form

$$\phi^{(3)}(t_0, r) = H \exp\left(-\frac{(r - r_c)^2}{\sigma^2}\right), \qquad (7.21)$$

where H, r_c, σ are adjustable parameters, accounting for the amplitude, position, and respectively width of the Gaussian.

For all the cases presented in this chapter, we set $H = 0.00007$, $r_c = 50$ and $\sigma = 2$. The position of the center ensures that the Gaussian field is well separated from the complex field of the boson star at the initial time. The width is chosen such that the Gaussian pulse is not too sharp and can be well resolved with a resolution $dx = 0.02$. The amplitude is very small, as we are only interested in a perturbation that accelerates the expected behavior. It was tuned such that the integral of the energy density associated with the Gaussian pulse is less than 0.01% from the energy of the boson star configuration.

The equations of evolution for the massless real scalar field are the Klein-Gordon Eqs. (7.4-7.6), with $m = 0$ and $\phi^I = 0$. The typical evolution of the perturbed initial data described above, proceeds as follows. The Gaussian perturbation splits into two pulses, traveling in opposite directions with the speed of light (gauge speed $\alpha\sqrt{h^{rr}}$, as we chose a harmonic slicing). One of the pulses is moving towards $r = 0$, while the boson star sits in its static state, centered in the
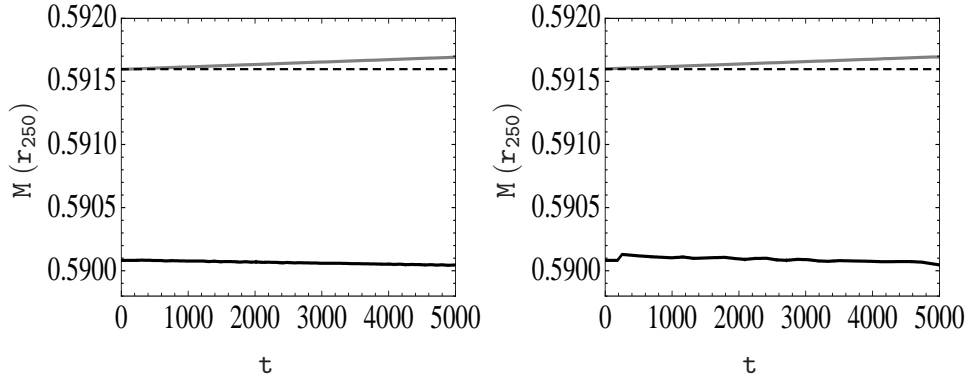
Figure 7.3. Illustration of the evolution of a boson star in the stable branch. The ADM (black plot) and Tolman (grey plot) masses are presented as a function of time, for the unperturbed (left panel) and perturbed (right panel) configurations. The dashed line marks the exact initial data value.
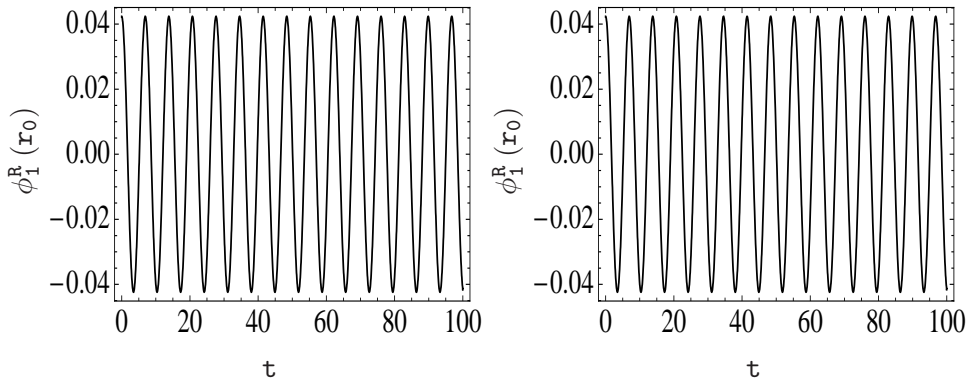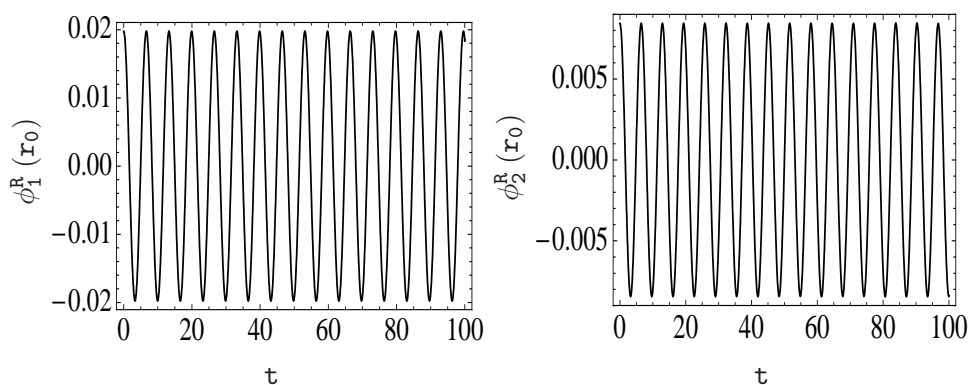

Figure 7.4. The amplitude of the central value of the scalar field is plotted as a function of time, for the unperturbed (left panel) and perturbed (right panel) configurations.
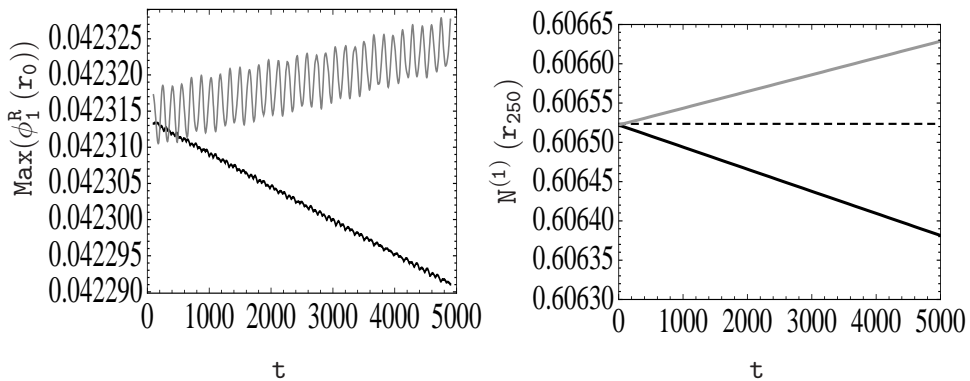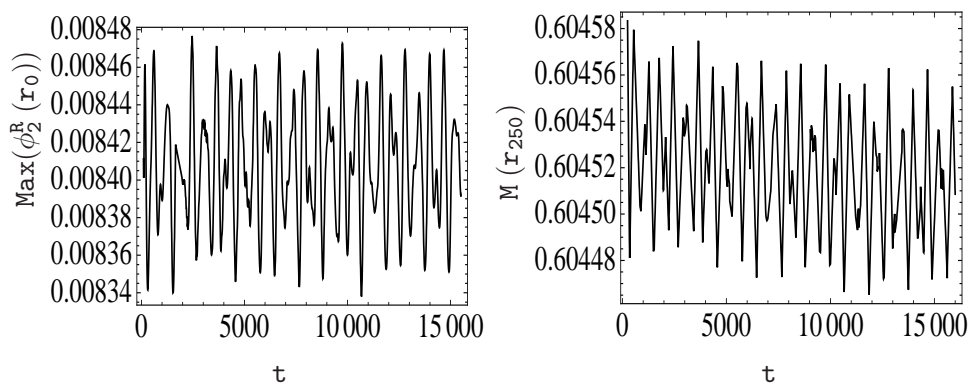

Figure 7.5. Left panel: The maximum value of the scalar field in the center is plotted as a function of time, for the unperturbed (black plot) and perturbed (grey plot) configurations. Right panel: The number of particles in the unperturbed (black plot) and perturbed (grey plot) configurations, are plotted as a function of time. The dashed line marks the exact initial data value.

origin. The massless field passes through the origin and then explodes outward, eventually propagating off the computational domain. As the perturbation is very small, the boson star remains in a stable state.

We compare the evolution of the two configurations, unperturbed and perturbed, in Fig. (7.3 - 7.5). Both configurations are stable in long term simulations, which shows that the perturbation has only a small effect on the constraint violations. It does not affect the dynamics of stable BS configurations, but it can be very useful in detecting unstable configurations. We will use this type of perturbation in the following study of MSBS configurations.

7.2.2   Mixed States of Ground and Excited Configurations

We consider the simplest non-trivial case, with only two scalar fields. The first one with $N^{(1)}$ particles in the ground state, and the second with $N^{(2)}$ particles in the first excited state. A useful way to define the initial data is by specifying the fraction between the number of particles in each state of the configuration

$$\eta = \frac{N^{(2)}}{N^{(1)}}.$$

In this case, the equilibrium equations for the initial data need to be completed with a differential expression for the number of particles in each state,

$$\partial_r N^{(n)} = 4\pi \frac{a}{\alpha} \omega_n \phi_n^2 r^2, \tag{7.22}$$

with boundary conditions $N^{(n)}(0) = 0$. If η is specified, one imposes as boundary conditions only one of the central values of the scalar fields, for instance ϕ_{c1}.

The new system of equations (7.19, 7.22) becomes a shooting problem for four parameters $\{\omega_1, \omega_2, \alpha(0), \phi_2(0)\}$. For a specific fraction η, it is necessary to adjust the four parameters such that Eq. (7.19) and the condition $N^{(2)}(r_{max}) = \eta N^{(1)}(r_{max})$ are satisfied. In this way, each configuration is fully determined by the fraction η and the amplitude of one of the scalar fields at the origin ϕ_{c1}.

We restrict our numerical analysis to only four different values of the central amplitude of the scalar field, namely $\phi_1(0) = \{0.007, 0.0113, 0.0197, 0.0423\}$. In the following, we will present the case $\phi_1(0) = 0.0197$, and focus on three subcases representative for the behavior of MSBS configurations: stable $\eta = 0.4$, and unstable $\eta = 1.6$ and $\eta = 3.0$.

7.2.2.a   *Fraction 0.4*

The initial data for the MSBS configuration, with an amplitude of the scalar field in the center $\phi_1 = 0.0197$ and fraction of the number of particles in the excited state $\eta = 0.4$, is presented in Fig. (7.6). The plots of the radial function ϕ_n
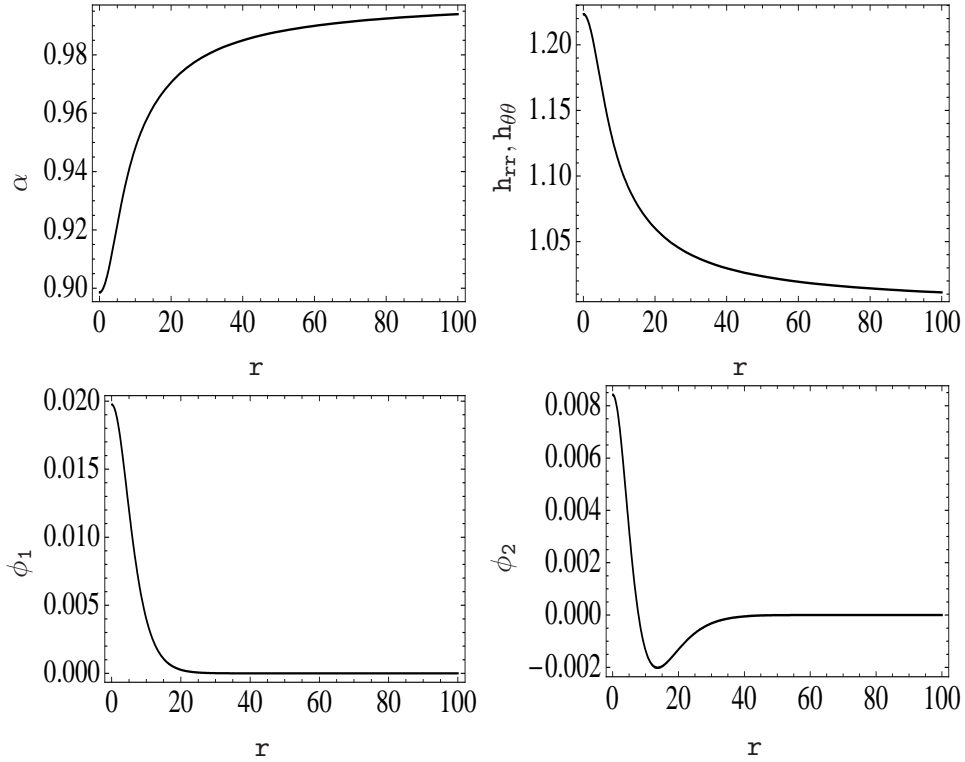
Figure 7.6. Illustration of initial data for a stable MSBS, with $\phi_1(0) = 0.0197$ and $\eta = 0.4$. The lapse function (upper left panel), the metric components (upper right panel), the real component of the zero nodes scalar field (lower left panel) and one node scalar field (lower right panel), are plotted as a function of the r isotropic coordinate.

correspond to the ground state configuration ϕ_1 (zero nodes), respectively excited state configuration ϕ_2 (one node).

We perturb the initial data with a massless scalar field Eq. (7.21), as described in Section 7.2.1.b and follow its evolution up to $t \approx 15000M$. One can not notice any growth in the central amplitudes of the two scalar fields $\phi_{1,2}^R(r_0)$ presented in Fig. (7.8). An analysis of the maximum amplitude $Max(\phi_2^R(r_0))$ reveals very small oscillations, Fig. (7.9). These deviations from the constant value are comparable with the case of a perturbed stable boson star, Fig. (7.3).

One can also notice an apparent decrease in the number of particles. However, this effect is very low, $0.002\% - 0.007\%$ of initial number of particles Fig. (7.7). The mass has very small amplitude oscillations around a constant value Fig. (7.9).

These results allow us to conclude that the $\eta = 0.4$ MSBS configuration is stable. We expect that any unstable growing modes would have been already excited by the perturbation within our time of observation.
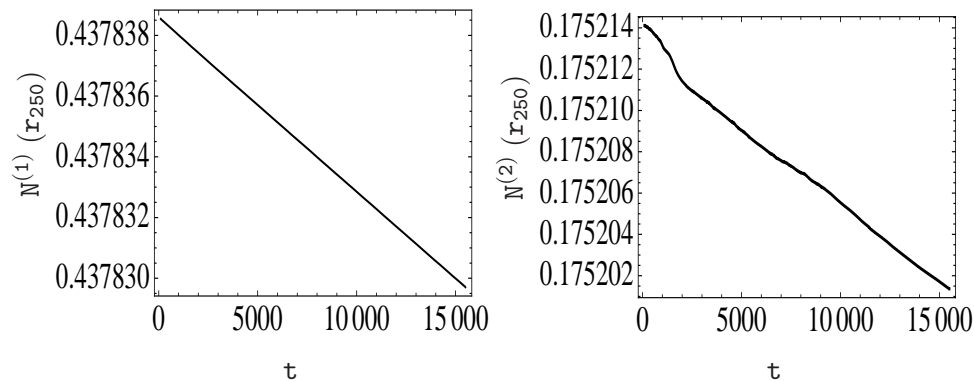
Figure 7.7. Illustration of the evolution of a stable MSBS configuration. The number of particles for the zero node (left panel) and one node (right panel) states, are plotted as a function of time.

Figure 7.8. The amplitude of the central value of the scalar field is plotted as a function of time, for the zero node (left panel) and one node (right panel) states.

Figure 7.9. Left panel: The maximum of the central value of the scalar field is plotted as a function of time, for the one node state. Right panel: The Tolman mass of the MSBS configuration is plotted as a function of time.

7.2.2.b   Fraction 1.6
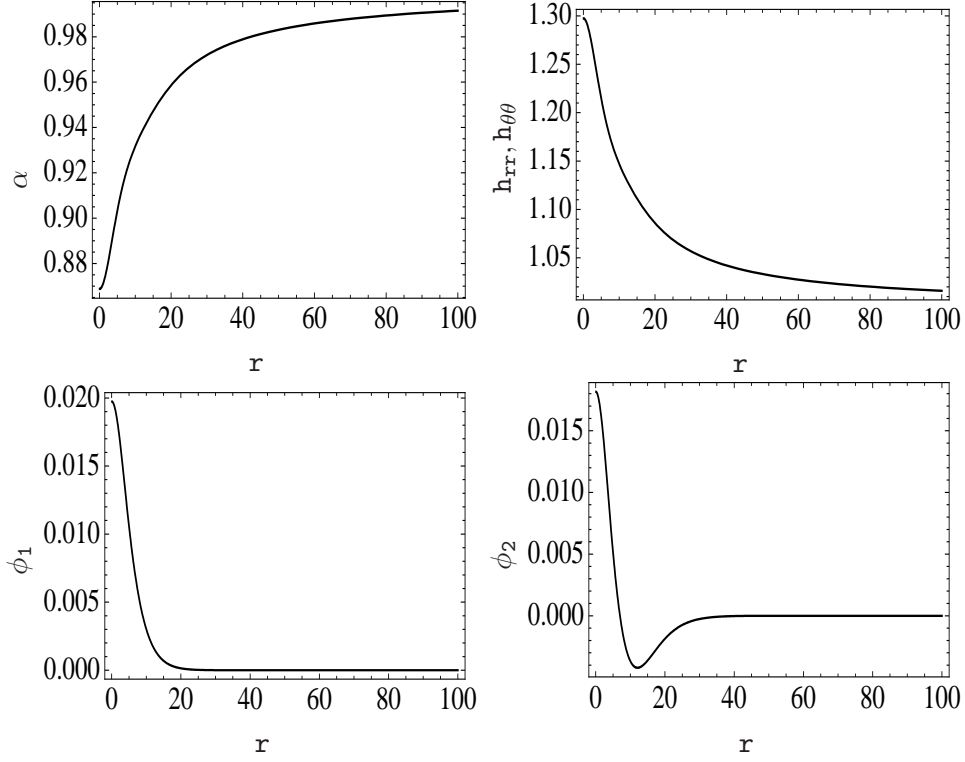
Figure 7.10.   Illustration of initial data for an unstable MSBS, with $\phi_1(0) = 0.0197$ and $\eta = 1.6$. The lapse function (upper left panel), the metric components (upper right panel), the real component of the zero nodes scalar field (lower left panel) and one node scalar field (lower right panel), are plotted as a function of the r isotropic coordinate.

The initial data for the unstable MSBS configuration, with an amplitude of the scalar field in the center $\phi_1 = 0.0197$, and fraction of the number of particles in the excited state $\eta = 1.6$, is presented in Fig. (7.10).

We follow the procedure described in Section 7.2.1.b and perturb the initial data with the same massless scalar field. The central amplitudes of the two scalar fields $\phi_{1,2}^R(r_0)$ show an exponential growth followed by oscillations Fig. (7.11). A detailed analysis of the function $Max(\phi_2^R(r_0))$ presented Fig. (7.13), reveals an exponentially growing behavior, which can be fitted by a function

$$\delta\phi^R = A \ \exp(-\sigma t) \ cos(\omega t + \varphi). \tag{7.23}$$

The growth rates of the unstable MSBS calculated in $\phi_1(0)$ and $\phi_2(0)$ show a very good agreement Fig. (7.16).
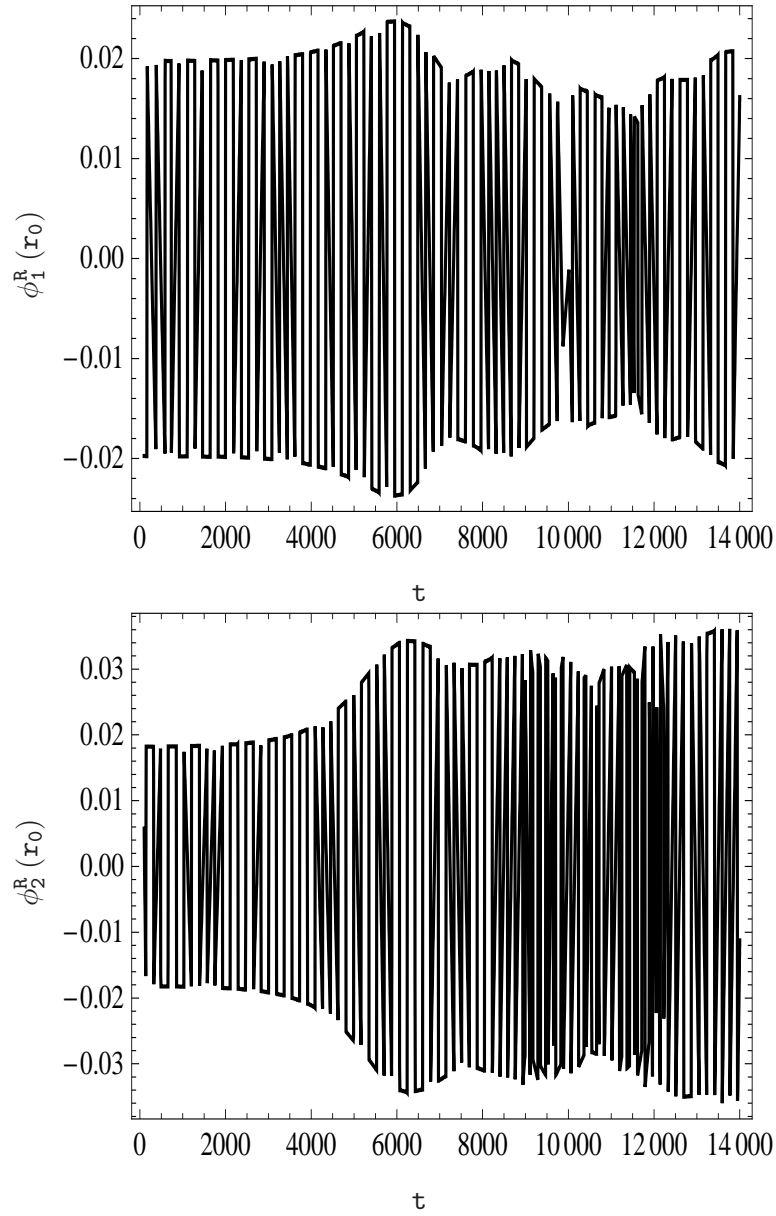
Figure 7.11. The amplitude of the central value of the scalar field is plotted as a function of time, for the zero node (upper panel) and one node (lower panel) states.
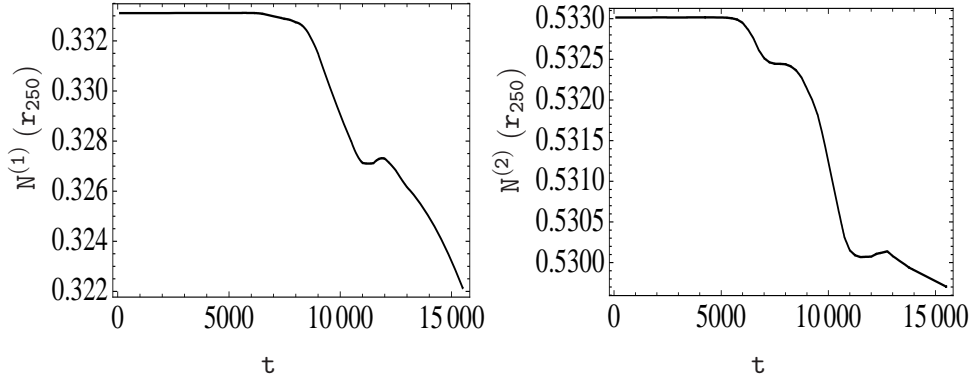
Figure 7.12. Illustration of the evolution of an unstable MSBS configuration. The number of particles for the zero node (left panel) and one node (right panel) states, are plotted as a function of time.
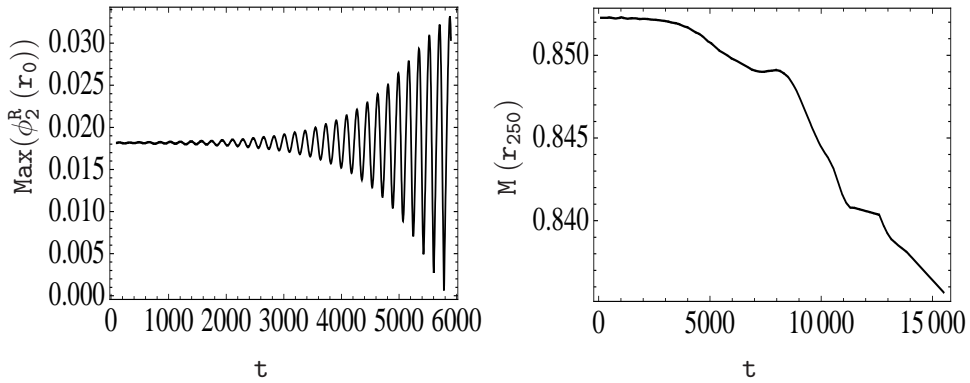
Figure 7.13. Left panel: The maximum of the central value of the scalar field is plotted as a function of time, for the one node state. Right panel: The Tolman mass of the MSBS configuration is plotted as a function of time.

One can also notice in Fig. (7.12 - 7.13) a clear decrease in the number of particles, $0.65\% - 3.3\%$ of initial value, and in the mass of the configuration (2%), which indicates that a part of the scalar field is radiated away. Indeed, a detailed analysis of the evolution shows that the unstable configuration is migrating into a stable configuration, through radiation of scalar field, as we will show in the following subsection.

7.2.2.c *Fraction 3*

In order to determine the final state of unstable MSBS configurations, we performed long term simulations, until $time = 30000M$ and beyond. In this section we present results obtained with an amplitude of the scalar field in the center

$\phi_1 = 0.0197$, and fraction of the number of particles in the excited state $\eta = 3$.
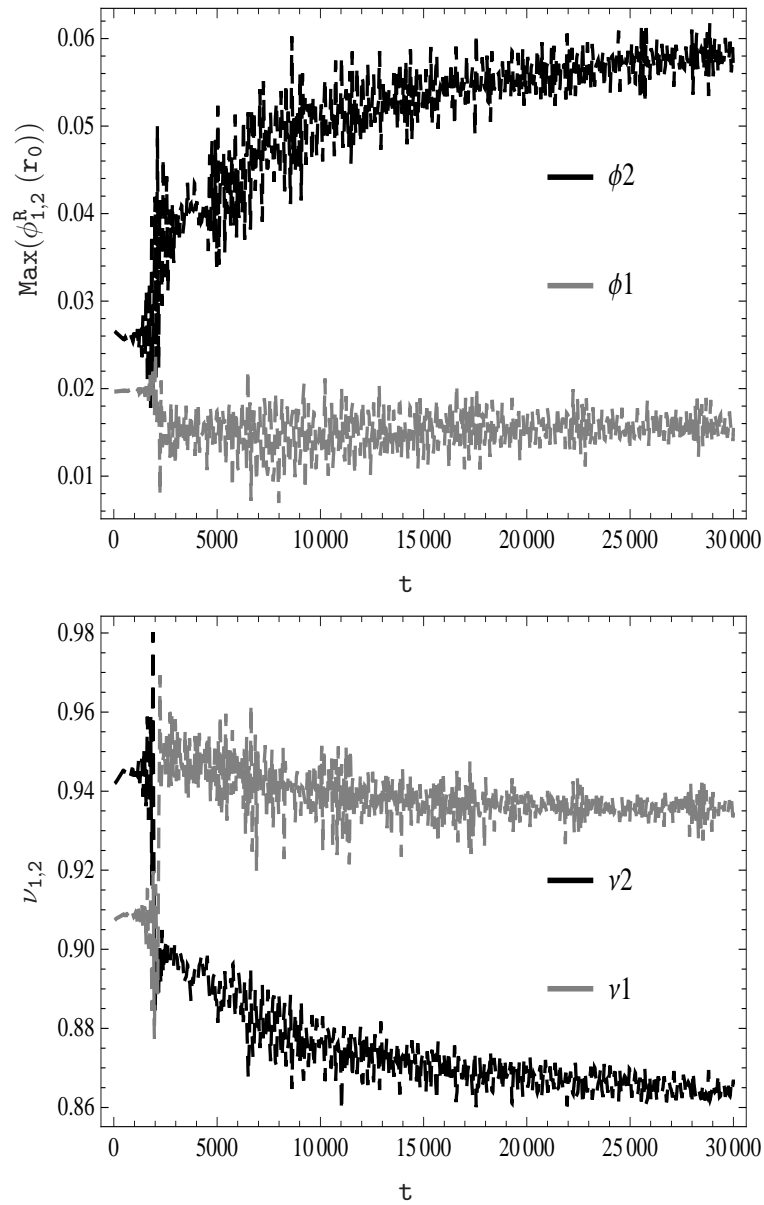
Figure 7.14. The maximums in the center (upper panel) and the frequencies of oscillation (lower panel) for the ϕ_1^R (grey plots) and ϕ_2^R (black plots) scalar fields are presented as a function of time, for an unstable MSBS configuration which settles into a stable configuration.

The evolution of the scalar fields maximums and their frequencies of oscilation are presented in Fig. (7.14). One can notice in the first $time = 2000M$ an expo-
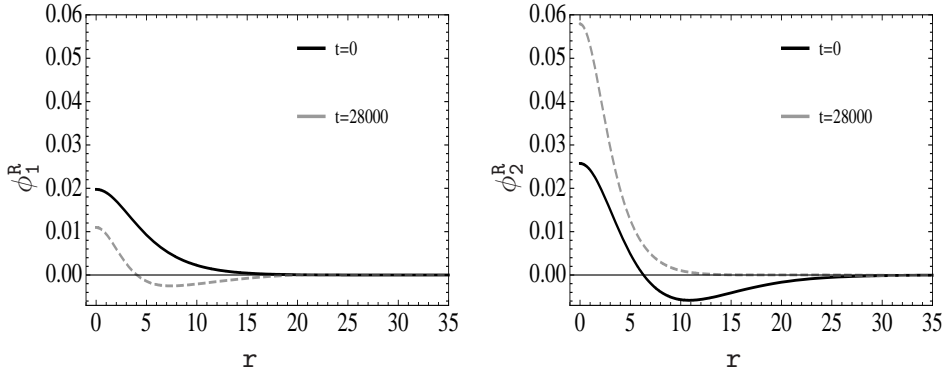
Figure 7.15. The scalar fields are presented as a function of radial coordinate r, at time=0 (dark continuous plots) and 28000M (grey dashed plots). The left panel corresponds to the initially ground state, which later becomes excited (one node), and the right panel to the initially one node state, which later transforms into a ground state (zero nodes).

nential growth similar to the one previously presented for the fraction $\eta = 1.6$. At the end of this strong couplig phase, there is a change between the two states of the configuration, namely the excited one node state collapses into a ground state, while the initially ground state becomes excited, Fig. (7.15). The behavior is reflected also in a change of the frequencies of oscilation for the two scalar fields, Fig. (7.14). Following the evolution, one can notice that the oscilations decrease in amplitude and the configuration settels into a stable state.

7.3   Discussion

MSBS configurations are an appealing model for dark matter. These configurations allow more freedom in matching the velocity rotational curves of galaxies with the observational data. However, the stability of the MSBS is a necessary condition in order to be considered as a model of galaxy halos. While the stability of a single boson star has been previously studied both analytically and numerically, the MSBS configurations require further investigation.

In this study, we focused on the numerical approach. The first step consisted in constructing initial data for MSBS, with different central amplitudes of the complex scalar field $\phi_1(0)$ and Noether fractions η. In order to study their stability, we added a real massless scalar field, which contains less than 0.01% of the energy of the configuration. This field acted only as a small perturbation, as we showed that its the effect on a single state ground configuration does not change the stability of the star.

The second step consisted in performing numerical evolutions with the Einstein-Klein-Gordon system and studying the dynamics of the perturbed MSBS. We
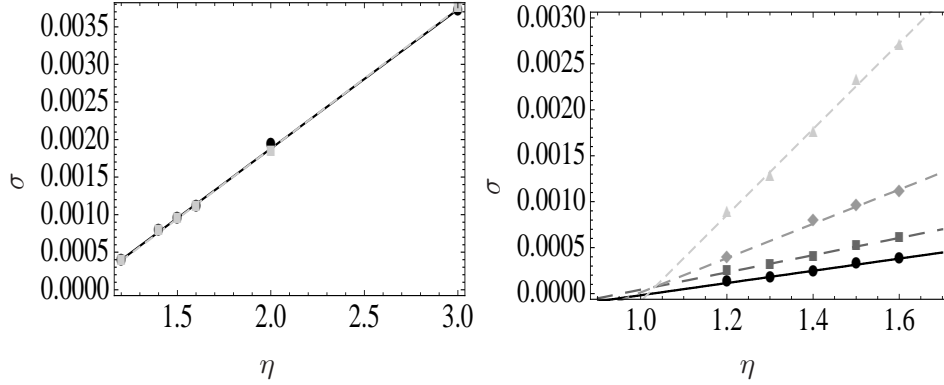
Figure 7.16. Illustration of the frequency fit for the exponentially growing modes in MSBS configurations, as a function of the fraction of the number of particles in the ground and excited states. Left panel: The frequency for $\phi^R(r_0) = 0.0197$ is calculated in $\text{Max}(\phi_1^R\ (r_0))$ (grey plot) and $\text{Max}(\phi_2^R\ (r_0))$ (black plot). Notice the agreement between the two frequencies. Right panel: The frequency is calculated in $\text{Max}(\phi_2^R\ (r_0))$, for $\phi(r_0) = 0.007$ (black plot), $\phi(r_0) = 0.0113$ (dark grey plot), $\phi(r_0) = 0.0197$ (medium grey plot) and $\phi(r_0) = 0.0423$ (light grey plot). The value of the fraction which separates the stable and unstable states is $\eta_\phi \approx 1$.

chose a small additional perturbation, as the unstable modes excited by numerical errors only, would require even larger timescale simulations.

Our numerical stability analysis is restricted to four different values of $\phi_1(0) = \{0.007, 0.0113, 0.0197, 0.0423\}$. In the simulations with $\eta \leq 1.2$, we did not find any unstable exponentially growing mode. We presented the typical behavior for $\eta = 0.4$ and $\eta = 1.6$ simulations, corresponding to a stable, respectively unstable MSBS.

Finally, we fitted the growth rate of the unstable MSBS for each $\phi_1(0)$, and extrapolated to find the maximum allowed Noether fraction η_{max} which separates the stable and unstable states. The results for the frequency of the exponentially growing modes are represented in Fig. (7.16), with the extrapolation to the η_{max} which in principle could be a function of $\phi_1(0)$. The four different family of solutions point to a value of $\eta_{max} \approx 1$.

An interesting result of this study is the final state of the unstable MSBS. Long term simulations show that even unstable MSBS settle into stable configurations through the scalar field radiation mechanism.

The results of our numerical studies, regarding the long term stability of MSBS configurations, suggest that they could be suitable candidates for dark matter models. The MSBS with $\eta < 1$ are intrinsically stable. The unstable ones with $1 < \eta < 3$, migrate into stable configurations, through radiation of scalar field.

Part IV

Gauge Conditions

Chapter 8

The behavior of the Lapse Function

The covariance of the Einstein theory implies that one can not determine a priori the spacetime coordinates. There is no preferred choice of coordinates, as the lapse function and the shift vector are not set by the field equations (Chapter 2). In order to complete the system of evolution equations, we have to choose the coordinates by providing some prescription for the gauge degrees of freedom.

The gauge choice played a crucial role in proving the well-possedness of the system of Einstein equations and finding exact solutions. Historically, the harmonic gauge was very important, as defining the spacetime coordinates by a set of four independent harmonic functions, it was possible to prove the well-possedness of the Cauchy problem for Einstein's equations.

Recently, the gauge has proven to be a very important ingredient in solving the binary black hole problem, which led to the recent impressive developments in the field of Numerical Relativity [83–85]. The problem of dealing with the black hole singularity was solved in two different ways. The codes based on generalized harmonic systems used the excision technique, which consists in cutting out a region inside the apparent horizon, in a consistent way. This approach was necessary, as these systems rely on the harmonic condition Eq. (2.25) which is just marginally singularity avoiding. Alternatively, the codes based on the BSSN system, worked with a global solution of the spacetime and could deal with the black hole interior through the puncture technique. The inner region is maintained sufficiently regular for numerical purposes, using a strong singularity avoiding slicing condition Eq. (2.28), in combination with a specific 'Gamma driver' shift Eq. (2.30), leading to the *moving puncture* approach [10, 84–86].

The so called *gold rush* towards new frontiers of Numerical Relativity left behind open questions. Some of them refer to gauge issues that need to be clarified, like the behavior of singularity avoidance slicing conditions and related instabili-

ties. We present in this chapter a study of these problems, applied on one of the most popular choices of hyperbolic gauge conditions currently used in BH simulations.

8.1   Singularity Avoiding Slicing Conditions

The lapse variable relates the proper time $d\tau$ with the coordinate time dt, namely $d\tau = \alpha(t, x, y, z)dt$. In numerical simulations, one can determine the lapse dynamically, through a general evolution equation of the type:

$$\partial_t \alpha = -\alpha^2 f(\alpha)K, \tag{8.1}$$

from which one can recover the particular cases of the geodesic ($f = 0$), maximal ($f = \infty$, $K = 0$), generalized harmonic ($f = n$) and generalized '1+log' ($f = n/\alpha$) foliations. Beside the numerical study of critical collapse phenomena, where maximal slicing is used, the preferred choice in black hole evolutions are singularity avoiding slicing conditions of the '1+log' type. These ensure that the lapse is dynamically adjusted in order to freeze the proper time of the observers near the singularity.

One could start the analysis of the singularity avoiding properties by considering first the harmonic condition for the time coordinate

$$\Box x^0 = 0, \tag{8.2}$$

which can be written in 3+1 language as

$$\partial_t \ln\left(\frac{\sqrt{h}}{\alpha}\right) = 0, \tag{8.3}$$

corresponding to a choice $f = 1$ in Eq. (8.1). One notices that the lapse can not be zero unless the space volume element $\sqrt{h}$ is zero, meaning that the time evolution will take us arbitrarily close to the singularity [87]. This implies a marginally singularity-avoidance behavior of the continuum equation for the lapse. The numerical errors accumulated during the evolution can spoil its singularity avoidance properties.

This situation is reflected in the class of harmonic codes based on the De Donder-Fock form of the Einstein field equations. The principal part of these systems can be generically written as a set of wave equation for the spacetime metric

$$\Box g_{\mu\nu} + \partial_\mu H_\nu + \partial_\nu H_\mu = ..., \tag{8.4}$$

where H_μ is given by the choice of coordinates

$$\Box x^\mu = -g^{\nu\tau}\Gamma^\mu{}_{\nu\tau} = H^\mu. \tag{8.5}$$

It is common to assume $H_\mu = 0$ (harmonic coordinates), or use the gauge sources approach by providing some kinematical prescription [88].

We present a brief comparison between the Generalized Harmonic and the Z4 system in order to study the singularity avoidance properties of the systems in the harmonic gauge. With the following parameterization

$$H^\mu = -g^{\nu\tau}\Gamma^\mu{}_{\nu\tau} - 2Z^\mu, \tag{8.6}$$

the system Eq. (8.4) can be viewed as an equivalent of the Z4, namely

$$R_{\mu\nu} + \nabla_\nu Z_\mu + \nabla_\mu Z_\nu = 8\pi(T_{\mu\nu} - \frac{T}{2}g_{\mu\nu}). \tag{8.7}$$

Then the time component of Eq. (8.6) reads in 3+1 language:

$$\alpha H^0 = \frac{1}{\alpha}\partial_t \ln \alpha + K - 2\alpha Z^0, \tag{8.8}$$

where $H_0 = 0$ in the harmonic gauge. This results into a singularity avoidance failure which is generic to harmonic codes. Long term numerical simulations are obtained only when the region close to the singularity is excised from the computational domain. The control of dynamical excision creates serious technical problems, as the collapse region grows and even moves across the computational grid.

An alternative to excision is the use of a foliation with singularity avoiding properties. One can use the slicing Eq. (8.1), in the generalized '1+log' variant. The choice $n = 2$ ($f = \frac{2}{\alpha}$) is known as the '1+log' condition, as it can be written in normal coordinates

$$\alpha = \alpha_0 + \ln(h/h_0), \tag{8.9}$$

where h is the determinant of the space metric. This condition implies that the coordinate time evolution stops before getting close to the singularity. The limit surface, namely the point where the lapse vanishes, is

$$\sqrt{h/h_0} = \exp(-\alpha_0/2). \tag{8.10}$$

As the initial lapse is usually close to one, the final volume element will be about 60% of the initial one.

We explored other slicing conditions, with the limit surface closer to the singularity [54]. We notice that the collapse front gets steeper than in the $f = 2/\alpha$ case Fig. (8.1), but we were able to perform long term stable evolutions. In our simulations, this specific choice is not mandatory, but it is the preferred choice for the current black hole simulations, not only due to its strong singularity avoidance properties, but also because it leads to smoother profiles in comparison with other gauge choices from the same class.
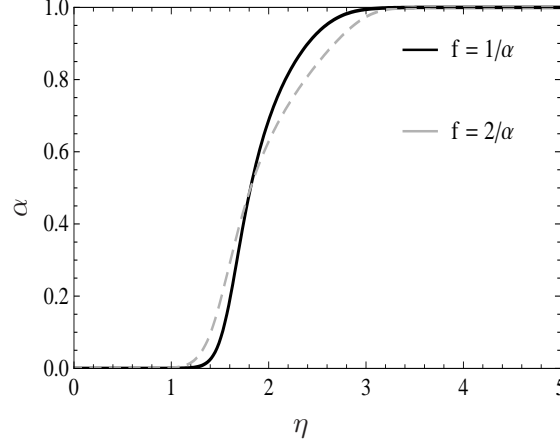
Figure 8.1. Illustration of the lapse as a function of η coordinate, at $time = 10M$ in a Schwarzschild black hole simulation. Notice how the collapse front gets steeper for a '1+log' slicing with $f = 1/\alpha$ (black continuous plot), in comparison with the $f = 2/\alpha$ case (grey dashed plot).

In the particular case of the Z4 system, hyperbolicity requires a generalization of the slicing condition Eq. (8.1) by adding a linear coupling with the θ variable,

$$\partial_t \alpha = -\alpha^2 f(\alpha)(K - m\theta).$$

This particular change of the slicing is more obvious if one writes the Z4 system as a harmonic formulation

$$\Box g_{\mu\nu} - \partial_\mu(\Gamma_\nu + 2Z_\nu) - \partial_\nu(\Gamma_\mu + 2Z_\mu) = ...,$$

with $\Gamma^\mu = g^{\nu\lambda}\Gamma^\mu{}_{\nu\lambda}$. In order to obtain a wave equation for the metric, one must ask

$$\Gamma^\mu = -2Z^\mu,$$

which is the equivalent of the harmonic condition for the standard Einstein equation ($Z^\mu = 0$). Then the harmonic slicing for the Z4 system must be modified with

$$\Gamma^0 = -2Z^0 = -2\frac{\theta}{\alpha}.$$

The Z4 system is strongly hyperbolic for any $f > 0$, with a value of $m = 2$ in the $f = 1$ harmonic case [89]. In the case of the '1+log' slicing, one can remove the coupling with the energy-constraint terms, but the numerical tests show that a choice $f = 2/\alpha$, $m = 2$ is the best option in black hole numerical simulations.

The use of the generalized '1+log' family of gauge condition in normal coordinates is known to lead to a distortion of the foliations, through the slice stretching

process, a problem that has been viewed as a final obstacle in the way of long term black hole evolutions. The increase along the radial direction produces a progressive loss of resolution, which leads to the appearance of high frequency noise. The problem can be delayed by increasing the grid refinement, but higher resolution produces steeper profiles for the dynamical fields, which can not be solved unless one employs special dissipation algorithms. We obtained the best numerical results (described in Chapter 6) using an adaptive algorithm, for which the dissipation parameter is tuned through the maximum gauge speed on the grid (for a detailed description see Chapter 5).

A possible problem related with hyperbolic slicing conditions typically used in numerical relativity is singularity formation due to gauge pathologies [90]. Recent studies based on a non-linear analysis of the system, show that these gauge instabilities arise due to the unbalance of the quadratic source terms. This modes grow only at a polynomial rate, so the evolution system is well-posed, but they will lead to code crash in long term simulations [91]. We are addressing this point in the next section, where we follow the behavior of '1+log' slicing in evolutions of Schwarzschild spacetime.

The numerical tests presented in the following section, were performed in normal coordinates (zero shift). In general, one would choose the shift to adapt the geometry to the physical system under study, by fixing it to some spacetime function or using it as a dynamical variable (Chapter 9). The choice of shift does not affect the behavior of the slices addressed in this study.

8.2   Numerical Study of Gauge Instabilities

The success of binary black hole numerical evolutions was based on two strategies of dealing with the singularity: excision and 'moving punctures'. The first approach is computationally challenging, as it requires tracking the two apparent horizons during the evolution, using one sided finite difference next to the excised region, and repopulating the grid via extrapolation. We are mainly interested in the second approach, which deals with a global solution of the spacetime and uses the gauge freedom in order to obtain a regular interior region, that can be evolved numerically. The key of this strategy are the punctures, artificial interior asymptotically flat regions, conformally compactified as a coordinate singularity. They are used to construct initial data with a given number of black holes. The numerical evolution of this BH initial data, with various gauges that allow a coordinate movement of the punctures, has proven to be a non-trivial task.

The geometric picture of the moving punctures evolutions has been only recently understood [11], in a study where 'trumpet data' time independent representations of black holes, play a crucial role. In the geometry of the stationary solution, corresponding to a foliation of Schwarzschild-Kruskal spacetime in maximal

slices, the slices were shown to asymptote to cylinders of constant areal radius. The result was extended to the hyperbolic slicing conditions commonly used in numerical relativity. Comparison with numerical results formed a simple picture of the gauge conditions used in the moving puncture recipe: they allow the interior of the black hole to approach the stationary representation. In particular the coordinate singularity associated with compactifying a cylindrically asymptotic end is milder than that associated with compactifying the Euclidean asymptotics of a standard puncture [11].

In these studies, numerical convergence to an analytical stationary solution can be observed at late times for an evolution of Schwarzschild-Kruskal spacetime, where the initial data is not adapted to the stationary solution. However, the analysis of standard hyperbolic gauge conditions [90–95], suggest the possibility of singularity formation and recently it has been argued to also spoil standard single and binary black hole evolutions [96].

We centered our study on the '1+log' slicing condition [97], which is the most popular singularity-avoiding slicing condition in binary puncture black hole simulations. Different pathologies which can result from this type of slicing condition have been discussed in the literature. Alcubierre identified mechanisms that lead to singularity formation in the slicing [90], which he calls "gauge shocks" to express the claim that they appear due to the crossing of characteristics associated with gauge propagation. Alcubierre has studied the formation of gauge shocks in a number of different simple models, and identifies scenarios where they can be avoided, and others where they can not be avoided. More recently it has been claimed that gauge shocks are indeed generic for evolved gauge conditions, as the slicing always shocks if α is different from 1 initially [96]. For a Schwarzschild black hole, these shocks can be triggered by propagating gauge perturbations ("gauge waves"), but in general situations they could be triggered by actual gravitational waves.

A different type of blowup behavior inherent to the '1+log' slicing, has been identified in [91]. This is a runaway phenomenon in the lapse triggered by a coupling to the mean extrinsic curvature K, in the case where K corresponds to expansion. Singularity avoidance works for positive K, but negative values of K trigger instead a blow-up in the lapse. This type of runaway solution are characterized by the growth of the lapse function without bound, at an accelerated rate, and can not be cured by using shock capturing algorithms.

In the following we will use numerical results to illustrate that gauge shocks in the form described by Alcubierre do not seem to be typical for '1+log' based evolutions of Schwarzschild spacetime that model the situation in a binary black hole simulation, since they seem to require rather contrived-looking perturbations of typical initial data. Singularities of the runaway type seem more typical, but can apparently be cured by a modification of the slicing equation.

For evolutions of manifestly spherically black hole spacetimes we use the Z3

system described in Chapter 3. The spatial discretization is performed with a standard fourth order centered finite difference scheme plus a third order accurate local dissipation term, which is automatically adapted to the requirements of either the interior or exterior black hole regions [24]. The time evolution algorithm is a third order strong stability preserving Runge Kutta method (time step $\Delta t = 0.01$, Courant factor $C = 0.5$). The condition for high resolution $\Delta r = M/50$, claimed in [96], necessary in order to reveal shock formation, is satisfied.

In addition to manifestly spherically symmetric simulations (1D), we also performed full 3D simulations with the Z4 system [98]. The treatment of the singularity in the 3D implementation of the Z4 system uses the "stuffed black hole" approach [70], assuming a regular interior solution with a suitable scalar field content as described in Chapter 6.

8.2.1   Gauge Initial Data

We consider the geometrical setup for Schwarzschild black hole evolutions in spherical symmetry as presented in Section 6.1, with the line element

$$ds^2 = -\tanh^2 \eta \, dt^2 + 4M^2(\cosh \eta/2)^4 \left(d\eta^2 + d\Omega^2\right). \tag{8.11}$$

For 3D stuffed black hole evolutions, discussed in detail in Section 6.2, the initial data is set in isotropic coordinates

$$ds^2 = -\left(\frac{1 - M/(2r)}{1 + M/(2r)}\right)^2 dt^2 + \left(1 + \frac{M}{2r}\right)^4 \left(dr^2 + r^2 d\Omega^2\right).$$

The isotropic radial coordinate r is related to the Schwarzschild radial coordinate (area radius) by $R = \sqrt{g_{\theta\theta}}$. We will use the notation $\ell = \int \sqrt{g_{rr}} \, dr$ for the proper distance along the slice.

We adopt two strategies to perturb the initial data for Schwarzschild with respect to the coordinate gauge. In the first approach, we just vary the initial lapse with respect to the metric Eq. (8.11), using a Gaussian in the η-coordinate,

$$\alpha = 1 + H \exp\left(-\frac{(\eta - \eta_c)^2}{\sigma^2}\right). \tag{8.12}$$

The initial values for the shift vector and the components of the extrinsic curvature are set to zero.

In the second approach we adopt the perturbations proposed in [90]. One considers an initial slice given in terms of Schwarzschild Killing time coordinate Eq. (8.11) in the following way:

$$t_w = \phi(t, \eta) = t + h(\eta). \tag{8.13}$$

The new line element will have the form

$$ds^2 = -\alpha_w^2 dt^2 - 2\alpha_w^2 h' dt d\eta + (\Psi - (\alpha_w h')^2)d\eta^2 + \Psi d\Omega^2,$$

with

$$\Psi = 4M^2(\cosh \eta/2)^4,$$

where α_w is the Schwarzschild Killing lapse (8.11) and we denote by *prime* the derivative with respect to η.

We can calculate the new lapse function as

$$\alpha = \alpha_w \sqrt{\frac{\Psi}{g_{\eta\eta}}},$$

and the shift vector

$$\beta^\eta = -\frac{\alpha_w^2 h'}{g_{\eta\eta}}.$$

The components of the extrinsic curvature for this slice take the form,

$$K_{\eta\eta} = \frac{[\alpha_w' h'(\alpha_w h')^2 - \Psi(\alpha_w h'' + 2\alpha_w' h') + \frac{\alpha_w h' \Psi'}{2}]}{\sqrt{\Psi g_{\eta\eta}}},$$

$$K_{\theta\theta} = -\frac{\alpha_w h' \Psi'}{2\sqrt{\Psi g_{\eta\eta}}}.$$

The initial values of the variables $D_{\eta\eta}{}^\eta = g^{\eta\eta}g_{\eta\eta}'/2$, $D_{\eta\theta}{}^\theta = g^{\theta\theta}g_{\theta\theta}'/2$ can be calculated according to their definitions in terms of the metric. The initial lapse is set to unity everywhere, so the component $A_\eta = \alpha'/\alpha$ is initially zero.

The functions $h(\eta)$ are chosen as a 3-parameter family of Gaussians,

$$h(\eta) = H \exp\left(-\frac{(\eta - \eta_c)^2}{\sigma^2}\right), \tag{8.14}$$

with amplitude H, width σ and center η_c.

8.2.2 Flat Space

We consider a non-trivial initial slice [90], given in terms of Minkowski coordinates as $t_M = h(r_M)$. Assuming that the radial coordinate r coincides initially with the Minkowski radial coordinate r_M, one can write the metric and the extrinsic curvature components as:

$$g_{rr} = 1 - h'^2,$$
$$g_{\theta\theta} = r^2,$$
$$K_{rr} = -h''/\sqrt{g_{rr}},$$
$$K_{\theta\theta} = -rh'/\sqrt{g_{rr}}.$$
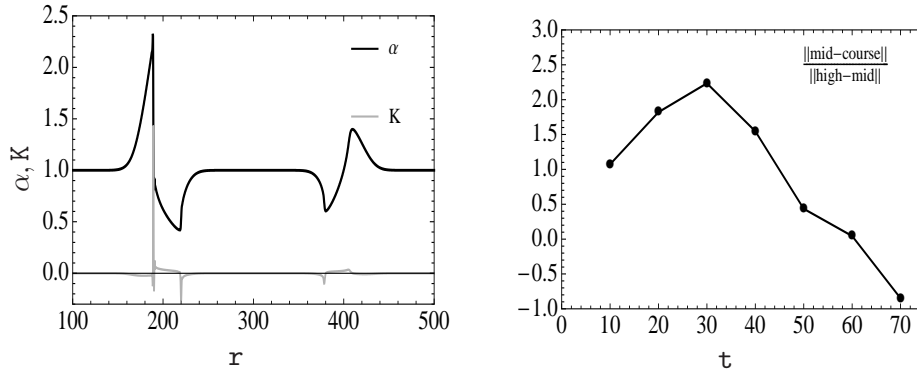
Figure 8.2. Illustration of the MFS model in a Z3 simulation with the '1+log' slicing condition. Left panel: The lapse and K as functions of the radial coordinate r, are represented by the black, respectively grey plots at $time = 70$M. Notice the presence of instabilities. Right panel: The plot represents the convergence factor in the L_2-norm of K, as a function of time. The factor is computed from $time = 0$ to 100M in intervals of 10M. Convergence is lost due to the presence of gauge instabilities.

The function $h(r)$ has a Gaussian profile,

$$h(r) = H \exp\left(-\frac{(r - r_c)^2}{\sigma^2}\right). \tag{8.15}$$

We chose the values of the perturbation parameters such that they match [90], namely amplitude $H = 15$, center $r_c = 300$, width $\sigma = 20$, and refer to this setting as "Model Flat Space" (MFS). Our numerical results confirm the ones presented by Alcubierre. The initial perturbation separates into two pulses traveling in opposite directions. The pulses moving in the in-going, respectively out-going directions are not symmetric, since the directions are not equivalent.

The numerical tests were performed using the '1+log' slicing. During the evolution, instabilities develop in both in- and out-going pulses and convergence is completely lost Fig. (8.2). As K has values in the negative domain because of the initial perturbation, these instabilities could be associated with runaway solutions.

8.3   Gauge Choice and Gauge Pathologies

8.3.1   Gauge Instabilities

The problem of finding a good coordinate system, that shows no pathologies for a generic spacetime, is very difficult. Even in very simple cases, a given prescription of the lapse and shift may not exist globally. An example are the geodesic or Gauss

coordinates ($\alpha = 1, \beta^i = 0$), where the coordinate lines typically cross over after some finite time, even when one starts from a curved slice in flat spacetime. This obvious gauge choice, which significantly simplifies the Einstein equations, is not a viable choice for numerical relativity.

Instead, the most popular form of specifying gauge conditions in numerical relativity is via hyperbolic evolution equations. I will focus on the family of Bona-Masso slicing conditions [97], which also include the family of harmonic slicings. The existence of discontinuous solutions to the Bona-Masso slicing conditions that arise from smooth initial data has been studied by Alcubierre [90, 92, 93, 95], who termed these instabilities "gauge shocks"or "coordinate shocks". These solutions are not physical discontinuities, but regions where the coordinate system breaks down. In this context, the term "shock" was used in a restricted sense of crossing of the characteristic lines. We prefer to use in the following the term "gauge instabilities" in order to denote any form of unbounded growth of the lapse or its first derivatives, related with the gauge behavior.

Alcubierre discusses in particular two types of instabilities within the Bona-Masso family of gauge conditions. In [90], performing an analysis of the characteristic speeds, he concludes that one type of instabilities affects just the gauge degrees of freedom with characteristic speed $\pm\alpha\sqrt{fh^{ii}}$, while the second one affects even the spatial metric degrees of freedom, with characteristic speed equal to the speed of light.

Alcubierre finds that the first class of instabilities can be avoided by ensuring that the evolution of the eigenvalues is independent of the corresponding eigenfields (condition for indirect linear degeneracy). This can be achieved by choosing $f(\alpha) = 1 + k/\alpha^2$, with k arbitrary constant, that leads to the following slicing

$$\partial_t\alpha = -(\alpha^2 + k)K. \tag{8.16}$$

However, this result is pointed out to be impractical in numerical simulations, since for small values of the lapse and positive K, there is nothing that prevents the lapse from becoming negative.

The analysis of the second class of instabilities leads to a very restrictive condition, that is impossible to satisfy with a diagonal metric. No practical cure was proposed for this class of instabilities, which were predicted even for the $f = 1$ case of harmonic slicing. Note that these instabilities are only characterized by the behavior of the $t = const.$ hypersurfaces and therefore do not depend on the choice of shift vector. Alcubierre showed that his analysis was in fact independent of the field equations in [99]. This class of instabilities have not been encountered in numerical simulations.

An analysis of the non-linear coupling between the K and the lapse function has been presented in [91], and suggests that this coupling can lead to runaway solutions, that grow without bound at an increasing rate. We consider, for exemplification, the Z3 system with $n = 4/3$. Taking a second time derivative of the

evolution equation for the lapse, one can write in the vacuum case,

$$\frac{1}{\alpha^2 f}\partial_{tt}\alpha - \Delta\alpha = \alpha[-K_{ij}K^{ij} + (2f + \alpha f')K^2] \qquad (8.17)$$

where $f' = \partial f/\partial\alpha$. This equation can be interpreted as a generalized wave equation for the lapse function, with the characteristic speeds $\pm\alpha\sqrt{f}$. The conclusion of the analysis was that gauge instabilities can be interpreted as the effect of the non-linear source terms in the evolution equations.

According to our numerical observations, the contribution coming from the non-linear right-hand-side terms does play a crucial role in the evolution of the lapse, as we will show that a modification of the slicing of the form

$$\partial_t\alpha = -f\alpha^2(K + K_0), \qquad (8.18)$$

with K_0 a small positive offset, can cure the runaway instabilities. This modified slicing condition amounts to

$$\frac{1}{\alpha^2 f}\partial_{tt}\alpha - \triangle\alpha = \alpha[-K_{ij}K^{ij} + (2f + \alpha f')(K + K_0)^2]. \qquad (8.19)$$

In a study of different types of blow-ups that can occur in systems of hyperbolic evolution equations of the type found in general relativity [94], Reimann investigates the existence of an ODE-mechanism that leads to blow-ups within finite time. Using as example a wave equation with sources and dynamic wave speed, a comparison is performed between the "geometric blow-up" (suggested by Alcubierre) and this "ODE-mechanism". In order to avoid instabilities a *source criteria* is proposed, which demands that the source terms should be free of quadratic terms in the eigenfields. The conclusion was that in most cases indirect linear degeneracy and the source criteria led to the same conditions for avoiding instabilities. In the cases where they don't, the source criteria proved to be more important. This result supports the idea that gauge instabilities are mainly the result of an ODE mechanism triggered by the source terms.

In the Sections 6.1 and 6.2, we presented foliations for a Schwarzschild black hole that do not show gauge instabilities. In the present study, we use two different families of data which do lead to the formation of gauge instabilities in Schwarzschild-Kruskal spacetime. The first consists in perturbing the initial slice, which has been used by Alcubierre [90]. The second family varies the initial lapse function. Since this family is simpler to implement, we use it to compare 1D and 3D evolutions. As "unperturbed" situation, we will consider an initial lapse $\alpha = 1$ and the 1+log slicing condition. As a first step in our analysis we will show that this case does not show any pathologies.

8.4 Numerical Results

8.4.1 Unperturbed Initial Data
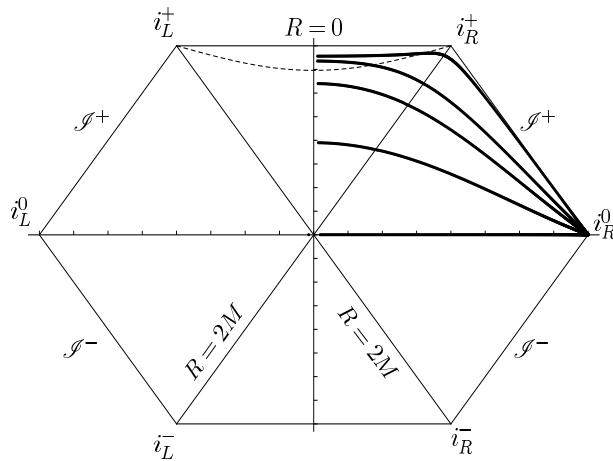
Figure 8.3. Penrose diagram of the slices at early times $t = \{1, 2, 3, 8M\}$, in an evolution of the unperturbed model of a Schwarzschild black hole, using the '1+log' slicing condition with $n = 2$. Our coordinates stop at the throat. As we use zero shift, the numerical slices penetrate R_0 and are not able to retreat to R_0 at later times.
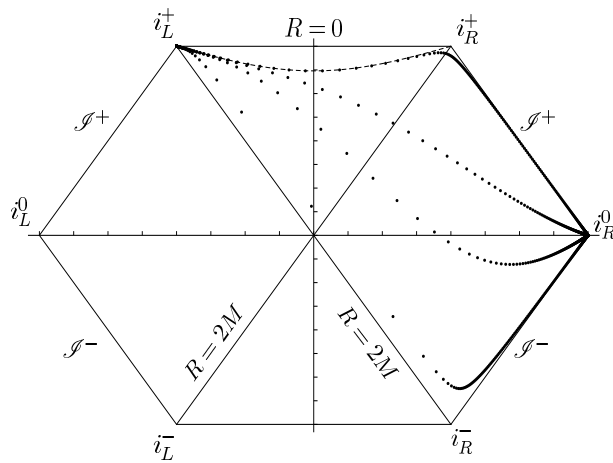
Figure 8.4. Penrose diagram of the slices at later times $t = \{30, 37, 40, 50M\}$, in an evolution of the unperturbed model of a Schwarzschild black hole. The picture is similar to Fig. 8.3, only that the slices are shifted along the Killing vector $R_0 \approx 1.31M$ in order to allow a better view of the exterior region. Every slice approaches i_L^+ along the curve R_0. This is the typical behavior of the slices defined by the stationary solution of the '1+log' condition with $n = 2$.
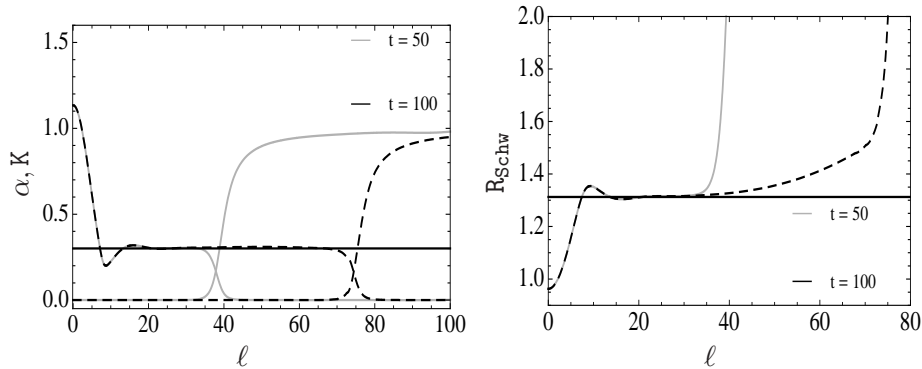
Figure 8.5. Illustration of the unperturbed model of a Schwarzschild black hole, using the '1+log' slicing condition. Left panel: The lapse α and K are plotted as functions of proper distance at $t = 50M$ (grey plots) and at $t = 100M$ (black dashed plots). Notice the agreement of the plateau value of K with the theoretically predicted value $K = 0.300934$, marked by the continuous black line. Right panel: The Schwarzschild radial coordinate R is presented as a function of proper distance at $t = 50M$ (grey plot) and at $t = 100M$ (black dashed plot). The result is in agreement with the theoretically predicted value $R_0 = 1.31241M$ marked by the continuous black line.

We consider first the "unperturbed" case, where the initial data is set according to Eq. (8.11). We evolve using the 1+log slicing condition, with $\alpha = 1$ initially. During evolution, the grid points situated at the throat are pushed to spatial infinity in accordance with the development of an asymptotically cylindrical region and the approach to the stationary solution as described in [69]. The values of the Schwarzschild radial coordinate $R = 1.31241M$ corresponding to the asymptotic cylinder, and the trace of the extrinsic curvature $K = 0.300934$ at the cylinder Fig. (8.5), are in agreement with the analytical and numerical solutions presented in [69].

The numerical results obtained, show the expected convergence factor of 3, as we use 3rd order accurate methods for both space discretization and time integration. In Fig. (8.6) we plot the convergence factor of the L_2-norm of K as a function of time. One can notice that the results of the simulation can be trusted up to a time $t \approx 60M$. Afterwards the convergence drops due to large numerical errors (see Section 6.1.4 for details). An estimate of the error in the mass aspect function Eq. (6.3) shows that at a time of $50 - 60M$ the deviations from the exact value are about $1.8 - 3.8\%$, while at $t = 100M$ the errors are around 23%. Independently of the choice of initial data, convergence is lost at late times due to the large errors which develop at the steep wall of the collapse front [23].

The second "unperturbed" case corresponds to a 3D stuffed Schwarzschild black hole, as described in Section 6.2. We consider the same slicing and initial data value for the lapse function as described above. The evolution is comparable

with the spherically symmetric case Fig. (8.6).
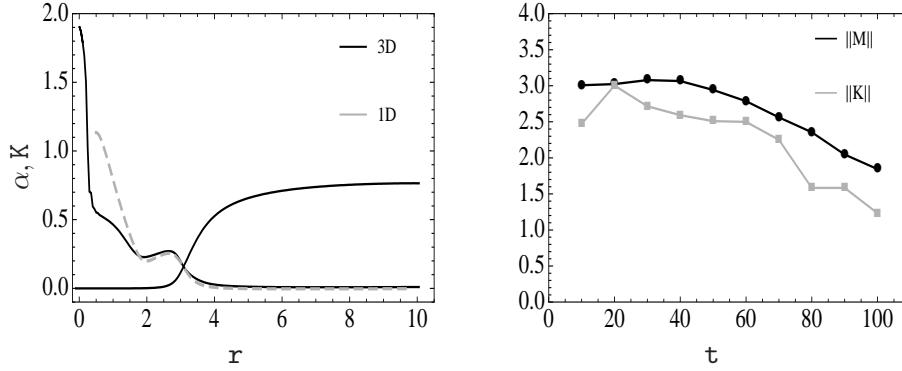
Figure 8.6. Illustration of the unperturbed model of a Schwarzschild black hole, using the '1+log' slicing condition. Left panel: The lapse α and K are presented as functions of the isotropic coordinate r at $t = 20M$, in a 3D simulation (black plots) and K is shown also in a 1D simulation in spherical symmetry (grey plot). There is a good agreement in the outer region between K in the 1D and 3D cases. The behavior in the inner region differs because of the treatment of the singularity. Right panel: The plots represent the convergence factor in the L_2-norm of the mass (black plot) and K (grey plot) as a function of time. The expected third order convergence is obtained up to $t \approx 60M$, afterwards the convergence is lost due to large numerical errors at the steep collapse front of the lapse.

8.4.2   Perturbing the Initial Lapse

We consider initial data induced at $t = 0$ by the metric Eq. (8.11), with a Gaussian perturbation in the lapse Eq. (8.14). We will refer to these data as "Model Perturbed Lapse" (MPL). The initial profile of the lapse produces perturbations in all other evolution variables. The evolution proceeds as follows. The initial Gaussian profile gives rise to two pulses traveling in opposite directions, with speeds $\pm \alpha \sqrt{f}$. The out-going pulse will eventually leave the domain, while the in-going pulse will collide with the collapse front of the lapse Fig. (8.7).

We illustrate the results obtained with two data sets, MPLw1 and MPLw2, both with center in $\eta_c = 5.0$, and widdhs $\sigma = 0.1$ (model MPLw1) and $\sigma = 1.0$ (model MPLw2). We consider this model with two amplitudes, one positive $H = 0.5$ (MPLw1P, MPLw2P) and the other negative $H = -0.5$ (MPLw1N, MPLw2N). For the sharper pulse (MPLw1), the in-coming wave gets steeper and produces instabilities Fig. (8.8). The smoother pulse (MPLw2) gets swept over by the collapse front and no problems occur Fig. (8.9).

One can compare the behavior of the slices for the MPLw2 model Fig. (8.11), with the unperturbed case in Fig. (8.4). The MPLw2 shows a small distortion of the slices, but they do not become pathological. Even though the unperturbed and
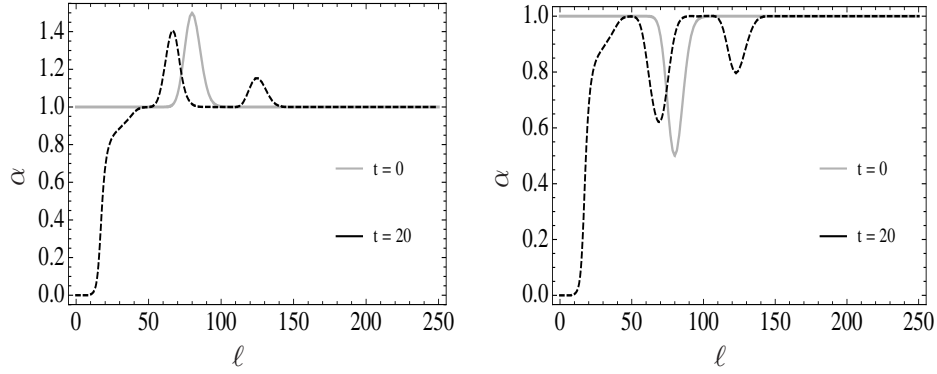
Figure 8.7. The lapse is presented as a function of proper distance for MPLw1P (left panel) and MPLw1N (right panel). The grey plots correspond to the initial profile, when the lapse was perturbed with a Gaussian profile. The black plots show the split perturbation at $time = 20M$, when the left and the right moving pulses can be clearly identified.
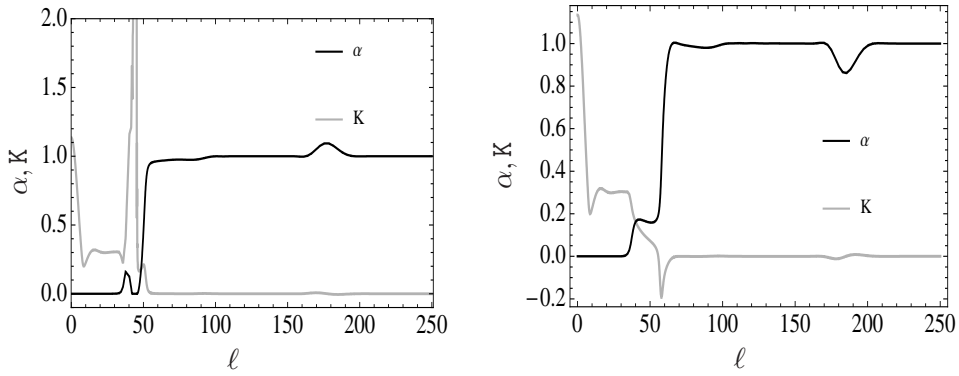
Figure 8.8. The plots correspond to MPLw1P (left panel) and MPLw1N (right panel), at $time = 50M$. The lapse and K as functions of proper distance, are represented by the black, respectively grey plots. One can notice the instabilities in the lapse function and K.
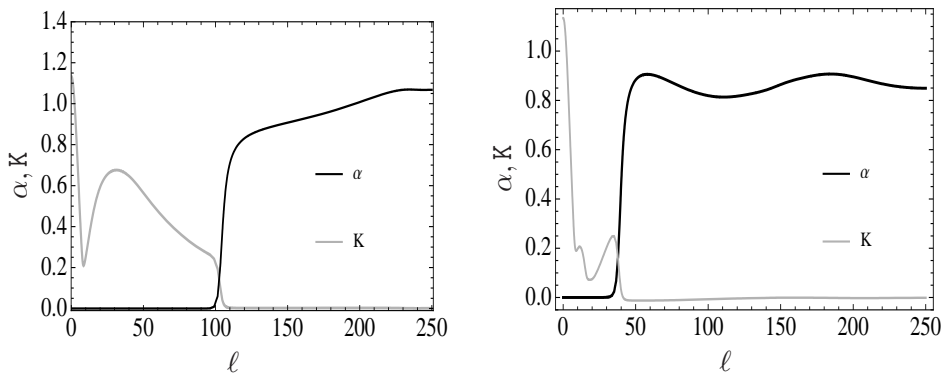
Figure 8.9. The plots correspond to MPLw2P (left panel) and MPLw2N (right panel), at $time = 100M$. The lapse and K as functions of proper distance, are represented by the black, respectively grey lines. The evolution proceeds without instabilities.
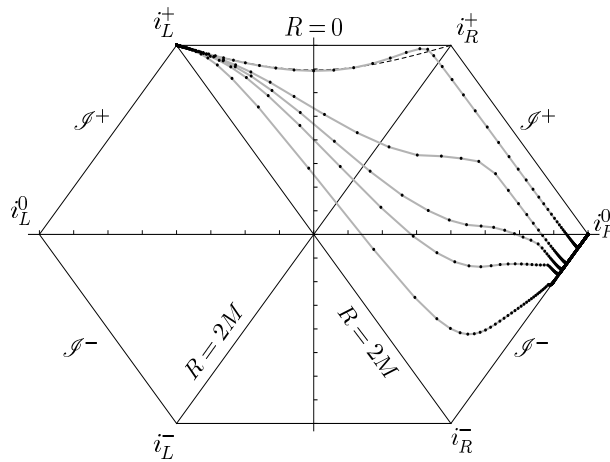
Figure 8.10. Penrose diagram of the slices at times $t = \{46, 46.8, 47.2, 50M\}$, in an evolution of the MPLw1 model of a Schwarzschild black hole, using the '1+log' slicing condition with $n = 2$. Notice how the slices are distorted with respect to the unperturbed model Fig. (8.4).
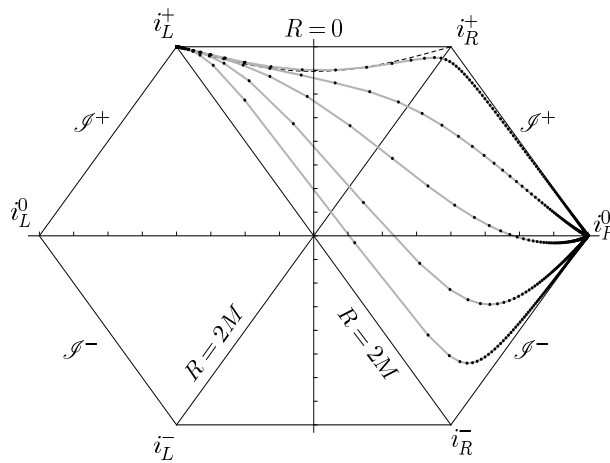
Figure 8.11. Penrose diagram of the slices at times $t = \{44, 46, 48, 50M\}$, in an evolution of the MPLw2 model of a Schwarzschild black hole, using the '1+log' slicing condition with $n = 2$. Notice how the slices reach the stationary state, as in the unperturbed model Fig. (8.4).
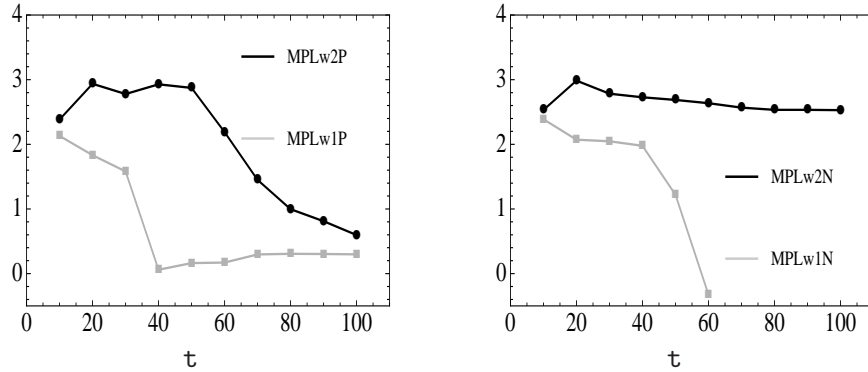
Figure 8.12. The plots represent the convergence factor in the L_2-norm of K, as a function of time. The factor is computed from $time = 0$ to $100M$ in intervals of $10M$. The grey plots correspond to MPLw1P and MPLw1N, for which convergence is completely lost. The black plots, marking the expected third order convergence, are obtained with MPLw2P and MPLw2N.

MPLw2 models start with different values of the lapse, they both reach the stationary state. This is not the case for the MPLw1 model, which develops instabilities and shows a strong distortion of the slices Fig. (8.10).

Our results prove that for this class of perturbed initial data one can find parameters which lead to long evolutions, free of instabilities. We check for blow-ups by performing a convergence test in the L_2-norm of K. A third order convergence factor is obtained for the MPLw2 case, while the MPLw1 case manifests a complete loss of convergence Fig. (8.12).

8.4.3   Perturbing the Initial Slice

We now consider an initial slice of the type Eq. (8.13), where the perturbation is a Gaussian in the height function, which depends on 3 parameters Eq. (8.14). We performed several tests in which we varied the values of one parameter, while keeping the other two fixed. The results show that instabilities develop only for some specific combinations of the parameters, so they are not generic. Moreover, these instabilities are identified as runaway solutions triggered by the trace of the extrinsic curvature becoming negative in some points of the domain. This leads to small rebounds of the lapse function in these points, while collapsing in the neighboring points. The resulting stretching determines increasingly large gradients, which trigger high frequency noise. This behavior has been reported before in [91]. The conclusion is that singularity avoiding conditions are fragile in the negative K domain, as they can produce runaway solutions.

One can picture this behavior in the following examples. We perform two numerical tests, choosing the initial data for the height function from the 3-parameter
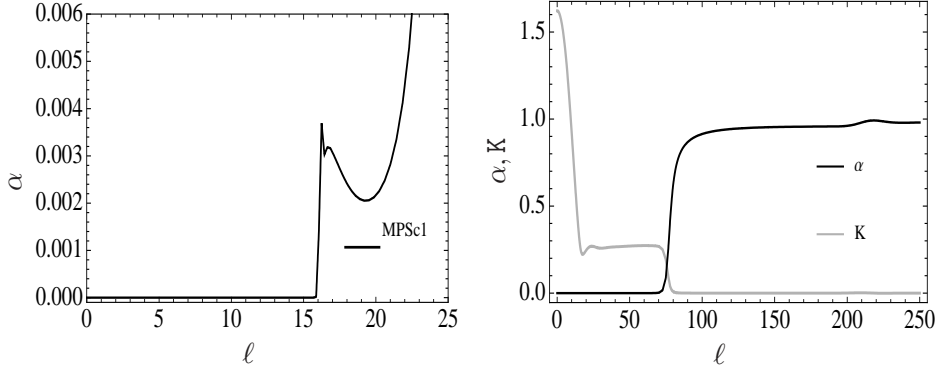
Figure 8.13. Left panel: The lapse is presented as a function of proper distance, at $time = 30M$, for MPSc1. The instability produced by K becoming negative (the grey plot in Fig. 8.15), determines at the same location a spike in the lapse function. Right panel: The plot corresponds to MPSc2, at $time = 100M$. The lapse and K as functions of proper distance are represented by the black, respectively grey lines. The evolution proceeds without instabilities.

family Eq. (8.14), which we will denote by 'Model Perturbed Slice' (MPS). The amplitude corresponding to this model is $H = 5.0$, and the width $\sigma = 2.3$. We chose different values for the center of the initial perturbation, namely $\eta_c = 3.0$ (model MPSc1) and $\eta_c = 4.6$ (model MPSc2). The second choice corresponds exactly to the initial data parameters chosen in [90], namely $H = 5.0$, $\sigma = 5.0$, $r_c = 50$ in isotropic coordinates. Both simulations are carried out in a similar way. One can notice that at the throat of the wormhole the lapse collapses, as expected for a black hole spacetime. In the outer wave zone, the initial perturbation separates into two pulses traveling in opposite directions with gauge speed.

In the plots corresponding to the MPSc1, we can notice the instabilities developing in K, located at the same points as the oscillations in the lapse, Fig. (8.13). This behavior in K appeared because of the negative values produced by the oscillations of the points where the in-going pulse met the out-going collapse front. By moving the center of the initial perturbation more in the wave zone (MPSc2), the in-going pulse gets swept over by the collapse front and K keeps positive values all over the domain. The behavior is shown in Fig. (8.15), where we compare K for the two simulations at times $20M$ and $30M$. The simulation in which K got negative values at $20M$, develops instabilities at $30M$, while the other one runs smoothly.

A way of avoiding the appearance of runaway solutions is preventing the values of K from entering in the negative domain. This can be achieved by adding a small offset in the lapse evolution equation, of the form

$$(\partial_t - \beta^i \partial_i)\alpha = -f(\alpha)\alpha^2(K + K_0), \qquad (8.20)$$
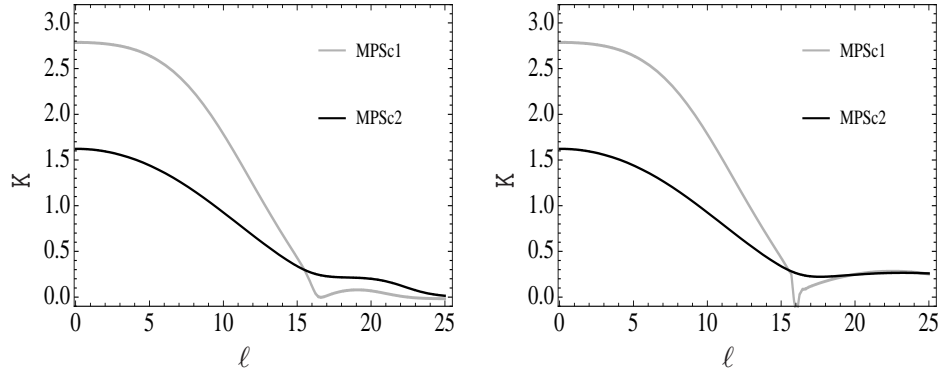
Figure 8.14. The plots correspond to K as a function of proper distance, for MPSc1 (grey plot) and MPSc2 (black plot). Left panel: K at $time = 20M$. Notice how a small change in the location of the center of the perturbation leads to a different behavior of K. This feature will get accentuated during the evolution. Right panel: K at $time = 30M$. One can notice an instability developing in K for MPSc1, due to K entering in the negative domain, which leads to runaway solutions. The MPSc2 continues with a smooth evolution (Fig. 8.13).
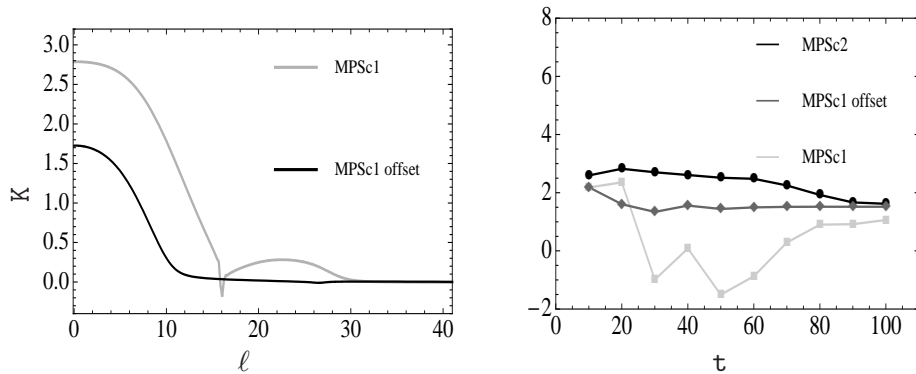
Figure 8.15. Left panel: The plots correspond to K as a function of proper distance, in the MPSc1 with and without offset, at $time = 30M$. The grey line corresponds to the slicing without offset, which leads to instabilities. The black line represents a smooth evolution, using the slicing with offset. Right panel: The plots represent the convergence factor in the L_2-norm of K, as a function of time. The factor is computed from $time = 0$ to 100M in intervals of 10M. The light grey plot corresponds to MPSc1, where convergence is completely lost. The dark grey plot presents the convergence factor for MPSc1, in an evolution which uses the slicing with a small offset $K_0 = 0.1$. The convergence factor drops between first and second order. The black plot, marking the expected third order convergence, is obtained with MPSc2.

where K_0 is a positive constant. In the example presented above, adding a $K_0 = 0.1$ is sufficient for a long smooth evolution Fig. (8.14). The disadvantage of using this type of slicing comes from the fact that the lapse collapses very fast and soon all the computational domain enters inside the black hole region.

We showed that not all initial data of this type produces instabilities, as for some range of parameters (MPSc2) we can obtain long term smooth simulations Fig. (8.13). In order to show that no blow-ups are hidden and propagated in this case, we analyze the convergence properties of the computational simulation. A convergence test in the L_2-norm of K is performed ($\Delta x = 0.04, 0.02, 0.01$). Fig. (8.14) shows the expected third order convergence for the MPSc2 case and a complete loss of convergence for the MPSc1 case. The second order convergence for the MPSc1 case with K_0 correction can be explained by the fact that all the computational region is soon contained inside the apparent horizon.

8.4.4 Comparison between the 1D and the 3D cases
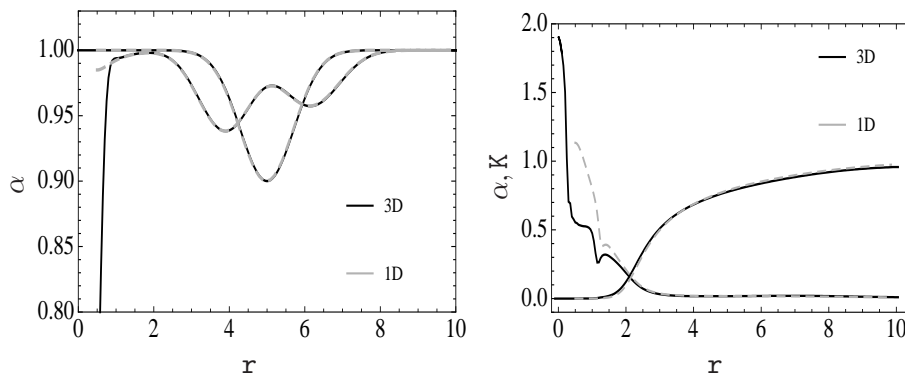
Figure 8.16. Illustration of MPL13. Left panel: The black plots correspond to the lapse in the 3D case, and the grey plots in the 1D case, at $time = 0$ and $1M$. The 1D plots start at $r = 0.5$, as a result of our choice of coordinates, which stop at the throat. The 3D plots cover the entire domain and the interior is regular by scalar field matching. In both cases the singularity is absent from our computational domain. Right panel: The black plots correspond to the lapse and K, as a function of the r isotropic coordinate in the 3D case and the grey plots in the 1D case, at $time = 10M$. The two cases show very good agreement in the outer regions, despite the difference in resolution (for an explanation of the difference in the inner region see in the main text the unperturbed case). The evolutions proceed without instabilities.

We perform a comparison between a black hole collapse in 1D spherical symmetry and in full 3D. The initial data settings correspond to a MPL13 model with the following parameters: amplitude $H = -0.1$, width $\sigma = 0.1$ and center $\eta_c = 2.3$, respectively $r_c = 5.0$, for the Gaussian perturbation in the initial lapse profile.

We have chosen a negative initial pulse. The behavior is the same as in the previous cases, namely the perturbation splits into a left going and a right going pulse. The pulse traveling right will loose amplitude and eventually leave the computational domain, while the left pulse will interact with the collapse front. One can notice in Fig. (8.16) that the lapse and K profiles manifest the same behavior for the 1D (radial direction) and the 3D (x direction, cut at $y = 0, z = 0$) cases.

8.5   Discussion

We study two classes of initial data with various perturbation models and conclude that instabilities appear only for a restricted set of initial perturbation parameters. Most instabilities are related with the K entering the negative domain, because of numerical errors or just initial data perturbations. In case $K < 0$ locally, according to the slicing condition $\partial_t \alpha = -\alpha^2 f(\alpha) K$ the lapse will have local rebound points, which contrast with the general collapse behavior dictated by the source terms. We associate this instabilities with runaway solutions, in agreement with [91].

Our study satisfies the criteria of high resolution proposed in [96]. We search for instabilities in the models using the standard criteria of proposed in the literature, namely convergence tests. Furthermore, we present Penrose diagrams in order to picture the dynamics of the slicings. This chapter contains only a restricted collection of relevant results. The full study extends to various choices of the parameters in the MPL and MPS models.

Based on our numerical results, we will argue that these instabilities are not generic for evolved gauge conditions as claimed by [96]. We support the conclusion that instabilities can appear, but whether they do or not depends strongly on the form of the initial data. The slicing with $\alpha = 1$ initially never creates instabilities, which is in agreement with the current numerical observations.

Chapter 9

Symmetry Seeking Shift Conditions

In the 3+1 formalism of General Relativity, the evolution equations and the slicing condition determine the history of the geometry. The lapse specifies the distance between the spatial slices, while the shift dictates how the spatial coordinates are carried between the slices. In practice, in computational simulations, the shift determines how the distribution of points is carried from one spatial slice to the next.

There have been many attempts of finding good coordinates adapted to specific problems in Numerical Relativity (like critical collapse or binary systems). We presented in the Chapter 8 several possibilities for adopting time coordinate conditions. In this chapter, we will concentrate on the choice of space coordinate conditions, with focus on a particular case well suited for black hole evolutions.

It is worth reminding the fact that Numerical Relativity is based on Einstein's theory of gravitation, which does not assume a preferred set of coordinates. So the success of the black hole codes should not depend on a specific space coordinate system, as long as the slicing condition is appropriately chosen in order to avoid singularities.

We consider as a convenient slicing condition for black hole spacetimes, one that has a suitable behavior near the singularity and ensures singularity avoidance (Chapter 8). Regarding the choice of shift conditions, ideally one wishes to decouple the true physical behavior of the spacetime from the coordinate effects, by constructing 3-covariant shift gauge conditions, such that the behavior would be independent of coordinate changes within a given hypersurface. For spacetimes that have a Killing vector, it is useful to use coordinates adapted to the symmetry, while for spacetimes with an approximate Killing vector, one would wish to minimize the rate of change of the metric with time.

We present in this chapter a generalization of the harmonic almost-Killing

equation (HAKE) [100], derived from considerations of approximative symmetries in the spacetime. The numerical simulations performed with the Z3 and Z4 systems, show that the generalized almost-Killing equation (AKE) [20] provides a space coordinate condition that satisfies these requirements.

9.1 The Almost-Killing Equation

9.1.1 Harmonic Almost-Killing Equations

Killing vectors are solutions of the equation:

$$\mathcal{L}_\xi(g_{\mu\nu}) = \nabla_\mu \xi_\nu + \nabla_\nu \xi_\mu = 0. \tag{9.1}$$

An intuitive example is choosing the time lines to be the integral curves of ξ and the time coordinate to be the affine parameter on these curves,

$$\xi = \partial_t.$$

Then the Killing equation written as

$$\partial_t g_{\mu\nu} = 0, \tag{9.2}$$

tells us that the metric is stationary, so the spacetime geometry is preserved along the integral curves of ξ.

The AKE address the problem of finding 'quasi-stationary' coordinates (as stationary as possible) in a generic spacetime [100]. It is based on the idea of finding 'almost-Killing' vectors fields ξ^μ, using the standard variational principle,

$$\delta S = 0, \qquad S = \int L \sqrt{g} \, d^4 x. \tag{9.3}$$

We consider for the Lagrangian density L a general quadratic form, which can be written as a linear combination of the two scalars formed with the tensor Eq. (9.1),

$$L = \nabla_{(\mu} \xi_{\nu)} \nabla^{(\mu} \xi^{\nu)} - \frac{k}{2} (\nabla_\sigma \xi^\sigma)^2.$$

The resulting Euler-Lagrange equations take the following form

$$\nabla_\nu [\nabla^\nu \xi^\mu + \nabla^\mu \xi^\nu - k(\nabla_\sigma \xi^\sigma) g^{\mu\nu}] = 0, \tag{9.4}$$

or equivalently written as a wave equation,

$$\Box \xi_\mu + R_{\mu\nu} \xi^\nu + (1-k) \partial_\mu (\nabla_\nu \xi^\nu) = 0, \tag{9.5}$$

which admits as solutions Killing vectors and 'almost-Killing' vectors, for any value of the k parameter. This AKE condition can be viewed from a generalization of Eq. (9.1).

An intuitive example of a vector satisfying the AKE, is the Z vector of the Z4 formalism. The Z4 can be written in the vacuum case as

$$R_{\mu\nu} + \nabla_\nu Z_\mu + \nabla_\mu Z_\nu = 0.$$

Its subsidiary system is given by the contracted Bianchi identities

$$\Box Z^\mu + R^\mu{}_\nu Z^\nu = 0. \tag{9.6}$$

Then the AKE case $k = 1$ is a special choice, as Eq. (9.5) becomes the condition Eq. (9.6) for the Z vector. One finds that the combination $(\nabla_\mu Z_\nu + \nabla_\nu Z_\mu)$ in the Z4 system is minimized for this particular value of k, such that one gets as close as possible to the original Einstein system.

We consider the integral curves of ξ to be the time lines of our coordinate system. Then the Euler-Lagrange equations (9.4) in these adapted coordinates read:

$$g^{\mu\nu}\partial_t\Gamma^\sigma{}_{\mu\nu} + (1-k)g^{\sigma\mu}\partial_t\Gamma^\nu{}_{\nu\mu} = 0. \tag{9.7}$$

The choice $k = 1$ becomes a generalization of the harmonic coordinate condition,

$$g^{\nu\tau}\partial_t\Gamma^\mu{}_{\nu\tau} = 0.$$

The relationship between the harmonic and the 3+1 formalism is more transparent if we decompose the contracted Christoffel symbols $\Gamma^\mu \equiv g^{\nu\tau}\Gamma^\mu{}_{\nu\tau}$ as

$$\begin{aligned}
n_\mu\Gamma^\mu &= \alpha\Gamma^0 = -\frac{1}{\alpha^2}(\partial_t - \beta^p\partial_p)\alpha - K, \\
\alpha\Gamma_i &= -\frac{h_{ij}}{\alpha}(\partial_t - \beta^p\partial_p)\beta^j - \partial_i\alpha + \frac{\beta^p}{\alpha}A_p + \alpha{}^{(3)}\Gamma_i.
\end{aligned} \tag{9.8}$$

The value of Γ^0 will provide an evolution equation for the lapse, namely the time slicing, and the value of Γ_i amounts to an evolution equation for the shift, which determines the time lines for a given slicing. The main difference is that the Γ^μ are constraints in the harmonic formalism, while the corresponding 3+1 conditions are part of the evolution system.

In the case of the Z4 system, $k = 1$ is the only choice that ensures strong hyperbolicity for the full system of evolution equations plus gauge conditions. This choice leads to the HAKE equation [100],

$$g^{\mu\nu}\partial_t\Gamma^\sigma{}_{\mu\nu} + ... = 0, \tag{9.9}$$

with extra Z terms included in order to obtain a well posed problem. However, this leads to a slicing condition which is not well suited for black hole simulations, as the principal part exhibits a close resemblance with the harmonic coordinates

$$g^{\mu\nu}\Gamma^{\sigma}{}_{\mu\nu} = 0, \qquad (9.10)$$

so it presents the same singularity avoidance problem as the harmonic lapse (Section 8.1).

9.1.2   Almost-Killing Shift

The idea of the AKE shift is still very appealing, as this coordinate condition is not only well adapted to the stationary spacetimes, but it also minimizes the deviation from the stationary regime. The problem consists in making the quasi-stationary conditions derived from the variation principle Eq. (9.3) compatible with the singularity avoidance requirement for black hole evolutions.

A solution would be to split the slicing from the time lines condition. One can notice that by enforcing $\xi = \partial_t$ we demand two things, namely that the time lines are the integral curves of the almost Killing vector ξ, and that the time coordinate is chosen to be the preferred affine parameter associated with these lines. While the first requirement fits the idea of obtaining a quasi-stationary gauge condition, the second one does not have a clear physical motivation. As we wish to enforce singularity avoidance in black hole simulations, the second requirement is not well suited.

A better strategy is to choose a priori the time coordinate. The spacetime slicing

$$\phi(x^{\mu}) = constant,$$

can be chosen such that it ensures singularity avoidance. Then one can use this time coordinate as a parameter along the integral lines of the almost-Killing vector ξ, by requiring

$$\xi^{\mu}\partial_{\mu}\phi = 1. \qquad (9.11)$$

One constrains this way the vector ξ to fulfill Eq. (9.11) in the minimization process.

The new Lagrangian can be written as

$$L' = L + \lambda(\xi^{\mu}\partial_{\mu}\phi - 1). \qquad (9.12)$$

The Euler-Lagrange equations include now the constraint Eq. (9.11) and the system

$$\nabla_{\nu}[\nabla^{\nu}\xi^{\mu} + \nabla^{\mu}\xi^{\nu} - k(\nabla_{\sigma}\xi^{\sigma})g^{\mu\nu}] = \lambda\partial^{\mu}\phi, \qquad (9.13)$$

which is a generalization of the almost-Killing equation (9.4). In adapted coordinates,

$$\phi = t, \quad \xi = \partial_t,$$

the generalized AKE takes the form

$$g^{\mu\nu}\partial_t\Gamma^\sigma{}_{\mu\nu} + (1-k)g^{\sigma\mu}\partial_t\Gamma^\nu{}_{\nu\mu} = \lambda\partial^\sigma\phi. \tag{9.14}$$

We split the system into 3+1 components and use only the space coordinate conditions, as the time slicing was chosen a priori. One obtains a second order evolution equation for the shift

$$g_{\sigma\tau}g^{\mu\nu}\partial_t\Gamma^\sigma{}_{\mu\nu} + (1-k)\partial_t\Gamma^\nu{}_{\nu\tau} = 0. \tag{9.15}$$

This way, the AKE gauge conditions are completely separated and the generalized AKE shift equation is compatible with any a priori chosen time slicing.

One can observe that the shift condition is independent of the value of the Lagrangian. This means that we could obtain the same condition from the original unconstraint Lagrangian. We can conclude that the slicing constraint does not affect the minimization process in the shift sector. The generalized AKE shift Eq. (9.15) contains a free parameter, for which one can choose now even the harmonic value $k = 1$, as the requirement of singularity avoidance can be enforced separately.

9.1.3 Gauge Evolution Equations

In the 3+1 form of the Z3 and Z4 systems, the gauge evolution is provided by the following equations for the lapse and shift,

$$\partial_t\alpha = -\alpha^2 Q, \tag{9.16}$$

$$\partial_t\beta^i = -\alpha Q^i, \tag{9.17}$$

where Q and Q^i can be either a combination of other dynamical fields, or independent quantities with their own evolution equation.

In the numerical evolution of harmonic spacetimes, as we are not interested in singularity avoidance, it is convenient to use the full AKE conditions Eq. (9.7) which have a form close to the harmonic gauge. Their decomposition provides the following evolution equations for the shorthands Q and Q^i:

$$\partial_t P + 2\alpha^2(K_{ab}Q^{ab} - Q\,K) + 2\alpha Q^p(A_p + Z_p) = 0, \tag{9.18}$$

$$\begin{aligned}\partial_t P^i &- 2\alpha Q^p(\alpha K_p{}^i - B_p{}^i) - 2\alpha^3 h^{in}(Q^{pq} - h^{pq}Q)(D_{pqn} + D_{qpn} - \\ &- D_{npq}) - 4\alpha^3(Q^{ip} - h^{ip}Q)Z_p + \alpha Q^i(\alpha(Q - K) + \beta^p A_p) - \\ &- 2\alpha^3(1-k)(Q^{ip} - h^{ip}Q)(A_p + D_{pq}{}^q) = 0,\end{aligned} \tag{9.19}$$

where P and P^i stand for the following combinations

$$P = \alpha(Q - K + 2\theta) + \beta^p A_p, \tag{9.20}$$

$$P^i = \alpha Q^i + \beta^p B_p{}^i + 2\alpha^2 (D_p{}^{pi} + Z^i) - k\alpha^2 (D^{ip}{}_p + A^i). \qquad (9.21)$$

We use damping terms of the form $\sigma\alpha^2 Q$ in Eq. (9.18) and $\sigma\alpha Q^i$ in Eq. (9.19), in order to ensure the stability of the solutions.

The standard harmonic lapse and shift gauge conditions can be recovered from the AKE Eqs. (9.20 - 9.21), by setting the P and P^i evolution variables to zero and choosing a value of $k = 1$ for the gauge parameter. In this way, the shorthands Q and Q^i can be directly calculated as

$$Q = K - 2\theta - \frac{\beta^p}{\alpha} A_p, \qquad (9.22)$$

$$Q^i = \alpha(A^i + D^{ip}{}_p) - 2\alpha(Z^i + D_p{}^{pi}) - \frac{\beta^p}{\alpha} B_p{}^i. \qquad (9.23)$$

In the black hole evolutions presented in Chapter 6, we chose algebraic gauge conditions, namely a singularity avoiding slicing of the '1+log' type and zero shift, translated into

$$Q = \frac{2}{\alpha} K, \qquad (9.24)$$

$$Q^i = 0.$$

Even though a vanishing shift works well, the black hole horizon grows rapidly in coordinate space, such that soon all the computational domain is inside the black hole. For long term evolutions, we would like to have an outward pointing shift vector, that will prevent the time lines from falling into the black hole.

The generalized AKE shift Eq. (9.15) offers us the possibility of applying a shift condition which is well adapted to stationary spacetimes. Even in cases where there is only an approximate symmetry, the coordinates are expected to adapt in order to minimize the rate of change of the metric. For the black holes evolutions presented in the following section, we considered a combination of the singularity avoiding slicing Eq. (9.24), with the quasi-stationary AKE shift Eq. (9.19).

9.2   Numerical Analysis

9.2.1   Harmonic Spacetimes

In order to test the properties of the AKE gauge conditions, we choose first a simple numerical setting, one of the standard ApplesWithApples proposals. As described in Chapter 4, the Gauge Waves test provides initial data of flat space in non-trivial coordinates. It was designed for testing the ability of different formulations to handle gauge dynamics.

The test considers flat Minkowski space in a slicing where the 3-metric is time dependent

$$ds^2 = (1 - H)(-dt^2 + dx^2) + dy^2 + dz^2,$$
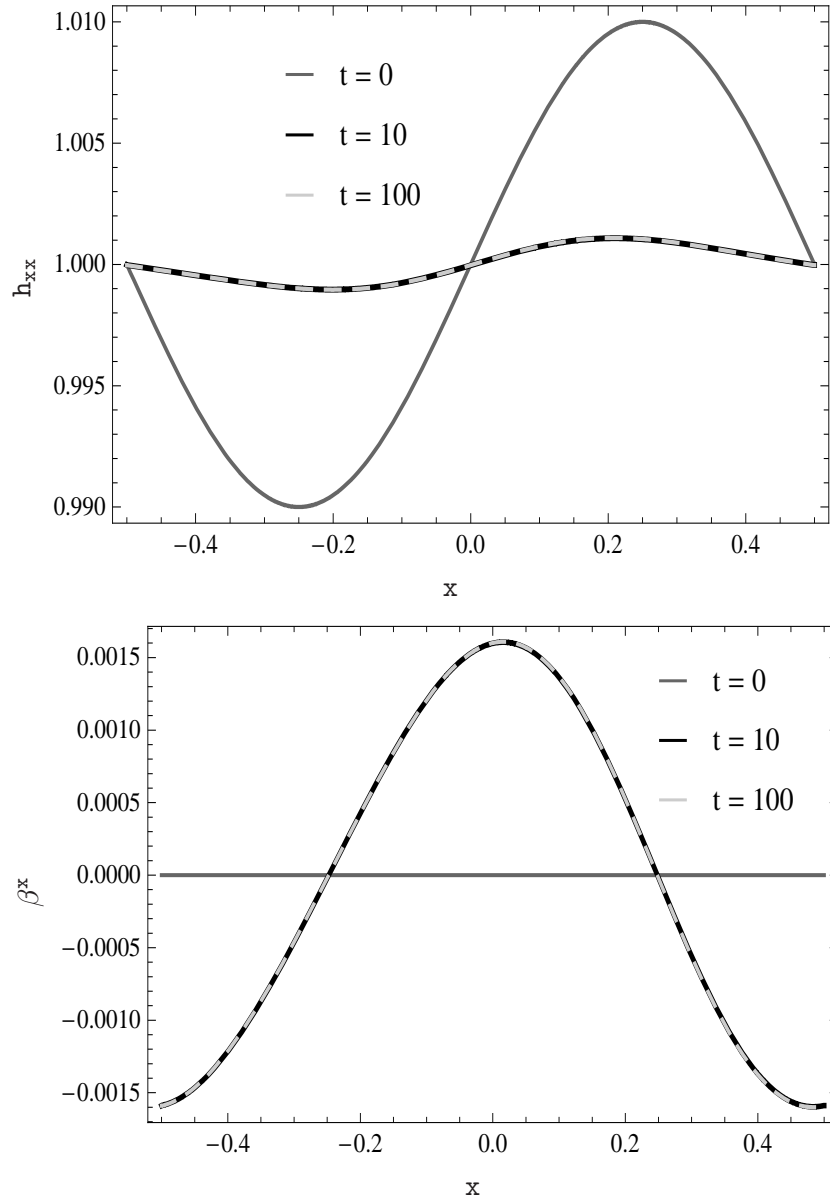
Figure 9.1. Illustration of the Z4 metric components on the x-axis, in a Gauge Wave test ($H = 0.01$) with the AKE conditions ($k = 1$, $\sigma = 2$), resolution $dx = 0.005$ and 3rd order CFV method. The plots correspond to the h_{xx} component of the metric (upper panel) and the β^x component of the shift (lower panel), at $time = 0$ (continuous dark-grey plot), $time = 10\mathrm{CT}$ (dashed light-grey plot) and $time = 100\mathrm{CT}$ (black plot).
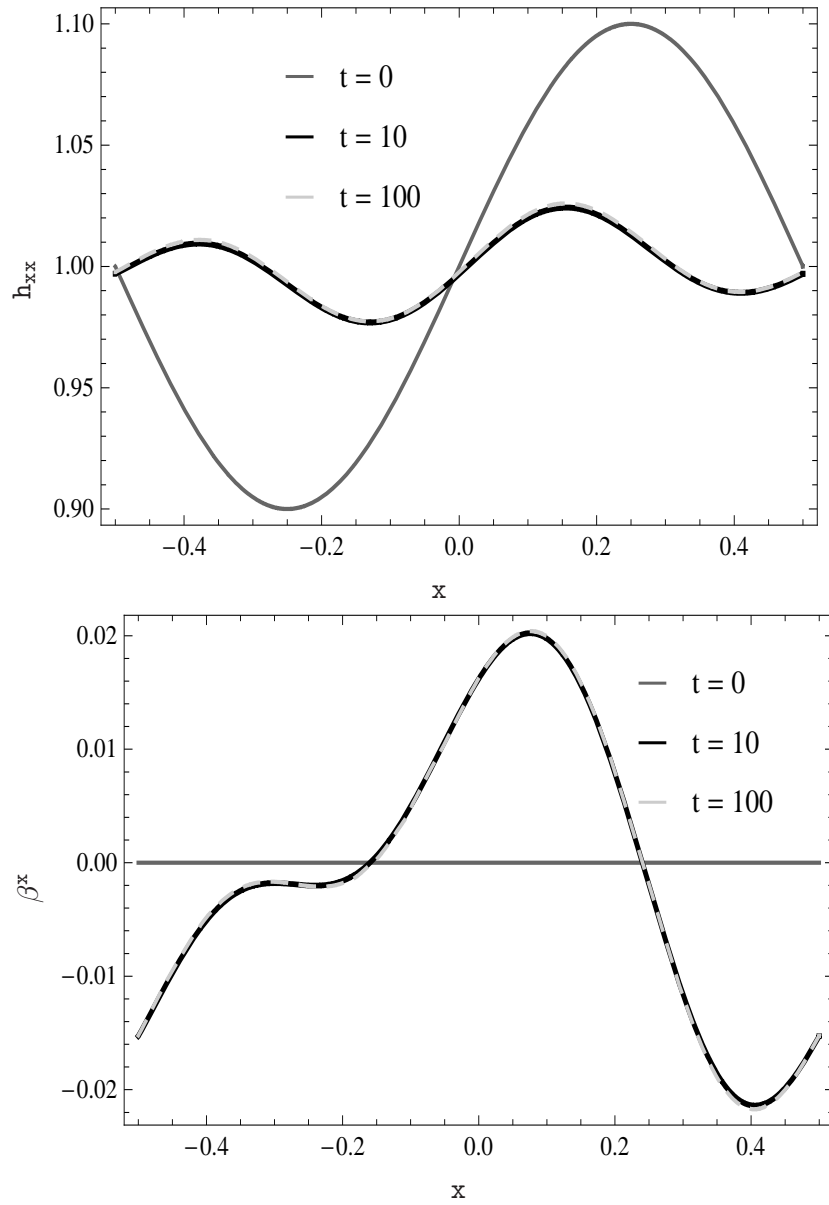
Figure 9.2. Illustration of the Z4 metric components on the x-axis, in a Gauge Wave test ($H = 0.1$) with the AKE conditions ($k = 1$, $\sigma = 2$), resolution $dx = 0.005$ and 3rd order CFV method. The plots correspond to the h_{xx} component of the metric (upper panel) and the β^x component of the shift (lower panel), at $time = 0$ (continuous dark-grey plot), $time = 10$ CT (dashed light plot) and $time = 100$ CT (black plot).

and $H = A \sin\left(\frac{2\pi(x-t)}{d}\right)$ is a propagating sine wave in the x direction. We run the test with amplitudes $H = 0.001$ and $H = 0.01$, on a computational domain $d = 1$, with periodic boundary conditions. As the relevant dynamics is along the x-axis, we consider a chanel with higher resolution in the one direction ($dx = 0.005$), while for the y and z axis we assign a minimum number of points. The numerical methods employed are a third order Centered Finite Volume algorithm for the spatial discretization (Appendix 9.5) and a third order Runge Kutta time integration method (Appendix 9.4).

We perform the evolution with the Z4 system using the AKE conditions, with a parameter $k = 1$ and damping $\sigma = 2$. Notice the form of the damping terms in the AKE Eqs. (9.18 - 9.19), which are constructed from the right-hand-sides of the evolutions equations for the lapse and shift Eqs. (9.16 - 9.17). This damping is responsible for the 'freezing' behavior of the wave, presented in Fig. (9.1) for low amplitude and Fig. (9.2) for medium amplitude.

One can see for comparison in Chapter 4 the results obtained with the harmonic gauge for a medium amplitude wave. The profiles follow very closely the exact solution Fig. (4.3). Only a small amount of dissipation is visible, as we are using a third order method in order to get rid of the dispersion error.

The behavior of the quasi-stationary AKE in the same setting, shows that the amplitude is quickly decreasing, such that we get very close to the stationary Minkowski value $g_{xx} = 1$ after only 10 crossing-times (CT). Although a small residual profile remains even after 100 CT, the change in the initial amplitude is significantly reduced. Additionally, the shift vector grows and stabilizes at a non-zero value, while the lapse approaches a value of $\alpha = 1$.

The same behavior has been reported in [20], where a similar test was performed with the Z3 system, for a value of the AKE parameter $k = 0.5$ and damping $\sigma = 2$.

9.2.2   Black Hole Spacetimes

9.2.2.a   Black Hole in Spherical Symmetry

We present the evolution of a Schwarzschild black hole in spherical symmetry as described in Section 6.1, in this case with non-vanishing shift. The line element takes the form

$$ds^2 = -(\tanh \eta)^2 dt^2 + 4M^2(\cosh \eta/2)^4(d\eta^2 + d\Omega^2), \qquad (9.25)$$

where we performed a coordinate transformation of the type $r = \frac{M}{2}\exp(\eta)$ to the Schwarzschild line element in isotropic coordinates Eq. (6.1). Our evolution domain extends to $\eta = 10M$ ($r \approx 11000M$).

The tests are performed with the Z3 system (Appendix 9.6.1), where the free parameter that couples the energy constraint in the evolution equation for the ex-
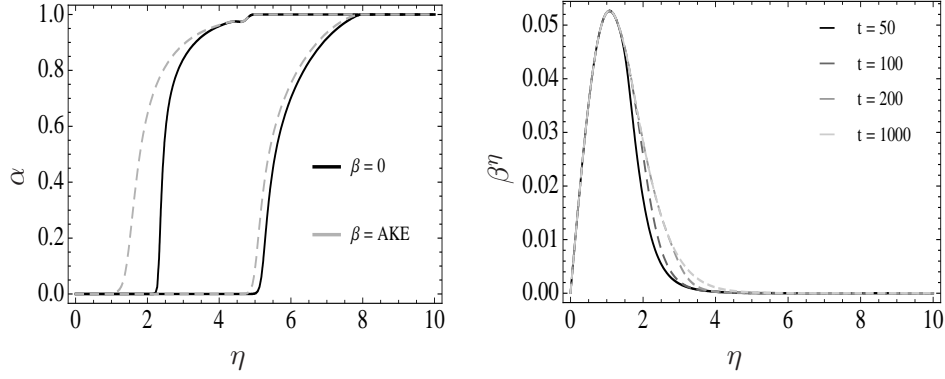
Figure 9.3. Illustration of the Z3 metric components as a function of the logarithmic η coordinate, in a Schwarzschild black hole simulation in spherical symmetry, using the '1+log' lapse and AKE shift ($k = 0.5$, $\sigma = 2$) conditions. We use a 3rd order CFV method, with resolution $dx = 0.05$. Left panel: The collapse of the lapse function is presented at $time = 50M$ and $time = 1000M$, in a simulation with zero shift (continuous black plot) and the AKE shift (dashed grey plot). Right panel: The evolution of the AKE shift is presented at $time = 50M$ (continuous black plot), $time = 100M$ (dashed dark-grey plot), $time = 200M$ (dashed medium-grey plot) and $time = 1000M$ (dashed light-grey plot).

trinsic curvature is $n = 4/3$. This choice leads to a system equivalent to a first order in space variant of the BSSN, without the conformal decomposition. We combine the '1+log' singularity avoiding lapse condition Eqs. (9.16), (9.24), and the quasi-stationary AKE shift Eqs. (9.17), (9.19), (9.21), with a value of $k = 0.5$ for the gauge parameter and $\sigma = 2$ for the gauge damping.

One can see in Fig. (9.3) a comparison with the simulation in normal coordinates, as presented in Section 6.1. The lapse shows a singularity avoiding behavior in both cases. The effect of the shift is adding some outgoing speed to the grid nodes, so that the advance of the collapse front across the grid is delayed. One can also notice a smoothing in the profile of the lapse, so that it can be better solved numerically. The logarithmic character of the grid makes the difference between the two simulations less obvious at later times, when the collapse front is at situated at larger values of the η coordinate.

9.2.2.b   Black Hole in 3D

We present the evolution of a Schwarzschild black hole in 3D as described in Section 6.2, in this case with non-vanishing shift. The initial data is provided by the metric in isotropic coordinates, where the line element takes the form

$$ds^2 = -\alpha^2 dt^2 + \left(1 + \frac{M}{2r}\right)^4 \left(dr^2 + r^2 d\Omega^2\right), \qquad (9.26)$$
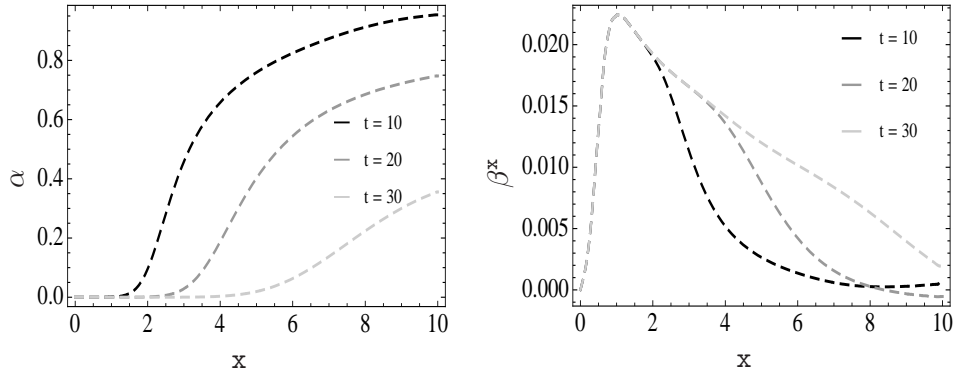
Figure 9.4. Illustration of the Z4 metric components on the x-axis, in a 3D Schwarzschild black hole simulation, with '1+log' lapse and AKE shift ($k = 1$, $\sigma = 10$). We use a 3rd order CFV method, with resolution $dx = 0.1$. Left panel: The collapse of the lapse function is presented at $time = 10M$ (black plot), $time = 20M$ (dark-grey plot) and $time = 30M$ (light-grey plot). Right panel: The evolution of the AKE shift is presented at $time = 10M$ (black plot), $time = 20M$ (dark-grey plot) and $time = 30M$ (light-grey plot).

and $d\Omega^2 = d\theta^2 + (\sin\theta)^2 d\phi^2$. We follow the *stuffed black hole* approach and match a scalar field such that the metric becomes regular inside the horizon Eq. (6.15).

The test is performed with the Z4 system (Appendix 9.7). The gauge conditions are provided by '1+log' singularity avoiding lapse condition Eqs. (9.16), (9.24), in combination with the AKE shift Eqs. (9.17), (9.19), (9.21), with $k = 1$ for the gauge parameter and $\sigma = 2$ for the gauge damping.

One can notice in Fig. (9.4) that the lapse function shows almost the same rate of collapse in the simulation where the AKE shift is active, compared with the vanishing shift simulation in Chapter 6, Fig. (6.14). We find only a small decrease in the K variable, which controls time variation of the metric coefficients. The shift is not successful in slowing the dynamics and one does obtain the behavior associated with the 'Gamma driver' condition Eq. (2.30).

9.3   Discussion

From a numerical point of view, the desired coordinates should be free of artificial (coordinate) singularities, they should take advantage of the symmetry of the problem, namely in stationary spacetimes they should lead to explicitly time independent metric components, and in the absence of symmetries they should minimize the rate of change of the metric.

The 'Gamma driver' shift condition currently used in combination with the BSSN system in the moving puncture approach, manages to evolve the binary

black hole data to a stationary state. In the case of an inspiral binary system, one can consider an approximative Killing vector and one defines a (non-unique) corotating coordinate system. The coordinate system on the spacetime is obtained by Lie-dragging the slice and its coordinates along the Killing vector. However this shift choice does not have the expected behavior when used in combination with other 3+1 Einstein systems.

We developed the AKE shift condition as an alternative to the 'Gamma driver' shift condition. The AKE gauge shows very good results in the Gauge Wave Test, as the metric gets very close to the stationary Minkowski value. In the case of a black hole in spherical symmetry, the results are also satisfactory. We have shown both analytically and numerically, that one can combine the '1+log' slicing with the generalized AKE shift, without loosing the quasi-stationary properties of the AKE condition and the singularity avoidance of the slicing. The effect of the shift is a delay in the advance of the collapse front across the grid, such that the computational domain is prevented from falling into the black hole. However, the generalization to full 3D black hole evolutions requires further investigation.

We have added standard damping terms to the AKE condition, in order to control the growth of the lapse and shift values. We found that the results depend crucially on the particular value of the gauge parameter k and on the damping. Furthermore, the preferred values of k changes for different evolution systems, namely we found $k = 0.5$ for the Z3, and $k = 1$ for the Z4. These particular values are in fact special, as $k = 1$ is a generalization of the harmonic coordinate condition, while for $k = 0.5$ the minimum principle leads to a minimization of the conformal-Killing equation, namely a quasi-conformal shift condition. This opens an interesting perspective for future work.

Concluding Remarks

In this thesis, we studied several analytical and numerical problems related with simulations of general relativistic black holes and boson stars. The principal new results are as follows.

We developed a new centered finite volume (CFV) method based on the flux splitting approach (Chapter 5). This algorithm is the first one in the class of finite volume methods which allows third order accuracy by only piece-wise linear reconstruction. Used in combination with positive-coefficients Runge Kutta methods, it ensures that the monotonicity properties of the basic evolution step will be preserved by the resulting strong stability preserving algorithm. This CFV method can also be used in the form of an adaptive dissipation algorithm, which can be combined with the standard finite difference methods. As long as one does not require the use of limiters, the two approaches are equivalent and can be applied even to systems implemented in a non flux-conservative form.

A comparison between different techniques currently used in Numerical Relativity, is performed in the context of a Schwarzschild black hole simulation in spherical symmetry (Chapter 6). The study shows that our CFV method allows longer and more accurate evolutions, even at low resolutions. The method is efficient especially in dealing with the steep gradients which arise in black hole evolutions with vanishing shift.

We performed the first long term simulation of a Schwarzschild black hole in normal coordinates without excision (Chapter 6). Our success does not rely on a specific choice of gauge conditions or treatment of the singularity. We consider two approaches for dealing with the BH singularity, namely the puncture technique and scalar field stuffing, and provide numerical evidence that they have a similar approach to the stationary state, in the context of normal coordinates and '1+log' slicing.

The crucial ingredients in our 3D Schwarzschild black hole simulations are the Z4 system and the efficiency of our CFV method. We devised an improved version of the Z4 system, with constraint adjustments and damping terms (Chapter 3). In addition, we use a flux conservative implementation, which proved to be important in standard Numerical Relativity tests (Chapter 4).

We present the first general relativistic study of Mixed State Boson Stars

(MSBS) configurations (Chapter 7). Performing numerical evolutions with the Einstein-Klein-Gordon system in spherical symmetry, we follow the evolution of MSBS under massless scalar field perturbations. We fit the growth rate of the unstable configurations and extrapolate to find the maximum allowed Noether fraction which separates the stable and unstable models. Our simulations show that even unstable MSBS settle into stable configurations through the scalar field radiation. The results of this numerical study, regarding the long term stability of MSBS configurations, suggest that they can be suitable candidates for dark matter models.

We performed a detailed study of gauge instabilities related with the '1+log' family of singularity avoiding slicing conditions (Chapter 8). We study two classes of Schwarschild initial data, by perturbing the initial lapse and perturbing the initial slice. Our numerical results based on evolutions with various perturbation models, show that instabilities appear only for a restricted set of initial perturbation parameters. Most instabilities are associated with runaway solutions. The slicing with lapse equal to one initially, never creates instabilities, which is in agreement with the current numerical observations. We argue that these instabilities are not generic for evolved gauge conditions.

We developed a generalized Almost Killing Equation (AKE), which is expected to adapt the coordinates to the symmetry of the problem under study (Chapter 9). The resulting 3-covariant AKE space coordinate condition can be used in combination with any slicing, without loosing its quasi-stationary properties. The behavior of the AKE shift in numerical evolutions of harmonic spacetimes (Gauge Wave Test), manages to bring the metric close to the stationary value. In the case of a black hole in spherical symmetry, the effect of the shift is a delay in the advance of the collapse front across the grid, such that the computational domain is prevented from falling into the black hole. However, the generalization to full 3D black hole evolutions requires further investigation.

Appendix: Numerical Methods

9.4 Time Integration Methods

9.4.1 Crank Nicholson

The iterative Crank Nicholson integrator is defined as:

$$
\begin{aligned}
k_1 &= kf(t_n, u^n), \\
k_2 &= kf(t_n + k/2, u^n + k_1/2), \\
k_3 &= kf(t_n + k/2, u^n + k_2/2), \\
u^{n+1} &= u^n + k_3.
\end{aligned}
$$

9.4.2 Runge Kutta

Most of our numerical results are based on a 3rd order accurate RK time integration method:

$$
\begin{aligned}
u^* &= f(u^n, \Delta t), \\
u^{**} &= \frac{3}{4}u^n + \frac{1}{4}f(u^*, \Delta t), \\
u^{n+1} &= \frac{1}{3}u^n + \frac{2}{3}f(u^{**}, \Delta t).
\end{aligned}
$$

9.5 Spatial Discretization

9.5.1 Finite Differencing

The spatial discretization is based on a centered finite difference method, 2nd order accurate,

$$
\partial_i \to D_{0i}, \qquad \partial_i\partial_j \to
\begin{cases}
D_{0i}D_{0j} & \text{if } i \neq j \\
D_{+i}D_{-i} & \text{if } i = j
\end{cases},
$$

or 4th order accurate,

$$\partial_i \to D_i^{(4)} = D_{0i}(1 - \frac{\Delta x^2}{6} D_{+i} D_{-i}),$$

$$\partial_i \partial_j \to \quad \begin{cases} D_i^{(4)} D_j^{(4)} & \text{if } i \neq j \\ D_{+i} D_{-i} (1 - \frac{\Delta x^2}{12} D_{+i} D_{-i}) & \text{if } i = j \end{cases} \quad ,$$

where

$$\begin{aligned} D_+ v_j &:= \frac{v_{j+1} - v_j}{\Delta x}, \\ D_- v_j &:= \frac{v_j - v_{j-1}}{\Delta x}, \\ D_0 v_j &:= \frac{v_{j+1} - v_{j-1}}{2\Delta x}, \\ D_+ D_- v_j &:= \frac{v_{j+1} - 2v_j + v_{j-1}}{\Delta x^2}. \end{aligned}$$

For a summary of definitions and results for standard finite difference discretizations one can see [40], where some results concerning the evolution systems that we considered in this thesis are derived.

9.5.2 Kreiss-Oliger Dissipation

It is common practice to add third order accurate Kreiss–Oliger dissipation [101] to all the right-hand-sides of the time evolution equations as

$$\partial_t \mathbf{u} \to \partial_t \mathbf{u} + Q \mathbf{u}.$$

We use the following general form of the Kreiss–Oliger dissipation operator Q of order $2r$,

$$Q = \sigma(-1)^{(r-1)} (\Delta x)^{2r-1} (D_+)^r (D_-)^r / 2^{2r},$$

for a $(2r - 2)$ accurate scheme, where the parameter σ regulates the strength of the dissipation.

9.5.3 Finite Volumes

The explicit steps that one needs to follow when applying our Centered Finite Volume (CFV) method are:

- The algorithm for the i grid point:

- Calculate the left and right predictions for the fluxes:

$$FL_i = F_i + \lambda_i u_i, \qquad (9.27)$$

$$FR_i = F_i - \lambda_i u_i. \qquad (9.28)$$

- Calculate the left and right slopes of the left flux in the cell i, by using the left fluxes in the neighboring points:

$$DL_i = (FL_i - FL_{i-1}),$$

$$DR_i = (FL_{i+1} - FL_i).$$

- Calculate the slope of the left flux in the cell i, by averaging the above computed slopes:

$$SL_i = aDL_i + bDR_i. \qquad (9.29)$$

- Calculate the left and right slopes of the right flux in the cell i, by using the right fluxes in the neighboring points:

$$DL_i = (FR_i - FR_{i-1}),$$

$$DR_i = (FR_{i+1} - FR_i).$$

- Calculate the slope of the right flux in the cell i, by averaging the above computed slopes:

$$SR_i = bDL_i + aDR_i. \qquad (9.30)$$

- Repeat the algorithm for the $(i + 1)$ grid point.
- Compute the left and right flux at the interface $(i + \frac{1}{2})$:

$$L_{i+\frac{1}{2}} = FL_i + \frac{1}{2}SL_i, \qquad (9.31)$$

$$R_{i+\frac{1}{2}} = FR_{i+1} - \frac{1}{2}SR_{i+1}, \qquad (9.32)$$

and average them in order to obtain the final flux at the interface:

$$F_{i+\frac{1}{2}} = \frac{1}{2}(L_{i+\frac{1}{2}} + R_{i+\frac{1}{2}}).$$

- Repeat the scheme for the flux at the interface $(i - \frac{1}{2})$.
- Obtain the value of the flux in the grid point i as:

$$F_i = \frac{1}{dx}(F_{i+\frac{1}{2}} - F_{i-\frac{1}{2}}).$$

A comparison between our CFV method with the dissipation (λ terms) suppressed, and the standard 4th order finite difference scheme, allows us to uniquely determine the slope coefficients Eqs. (9.29), (9.30).

An equivalence between the CFV method with $\lambda = 0$ and the standard FD algorithms can be obtained in the following way:

- The second order finite difference algorithm can be recovered from the previously described CFV method by setting the numerical speeds $\lambda = 0$ in Eqs. (9.27), (9.28) and the slopes $SL = SR = 0$ in Eqs. (9.31), (9.32). After performing the replacements, one obtains:

$$
\begin{aligned}
F_{i+\frac{1}{2}} &= \frac{1}{2dx}(F_i + F_{i+1}), \\
F_{i-\frac{1}{2}} &= \frac{1}{2dx}(F_{i-1} + F_i), \\
F_i &= \frac{F_{i+1} - F_{i-1}}{2dx}.
\end{aligned}
$$

- The fourth order finite difference algorithm can be recovered from the previously described CFV method, by setting the numerical speeds $\lambda = 0$ in Eqs. (9.27), (9.28). A simple calculation leads to:

$$
\begin{aligned}
F_{i+\frac{1}{2}} &= \frac{1}{2dx}[F_i + \frac{1}{2}((a-b)F_i - aF_{i-1} + bF_{i+1}) + \\
&+ F_{i+1} - \frac{1}{2}((b-a)F_{i+1} + aF_{i+2} - bF_i)], \\
F_{i-\frac{1}{2}} &= \frac{1}{2dx}[F_{i-1} + \frac{1}{2}((a-b)F_{i-1} - aF_{i-2} + bF_i) + \\
&+ F_i - \frac{1}{2}((b-a)F_i + aF_{i+1} - bF_{i-1})], \\
F_i &= \frac{(-aF_{i+2} + 8aF_{i+1} - 8aF_{i-1} + aF_{i-2})}{4dx},
\end{aligned}
$$

Comparing with the standard 4th order FD algorithm, one obtains $a = \frac{1}{3}$. The value of $b = \frac{2}{3}$ is obtained taking into account the constraint $(a+b) = 1$.

Appendix: Einstein Systems

9.6 The Z3 system

9.6.1 The Z3 system in spherical symmetry and normal coordinates

Consider a Schwarzschild line element written as

$$ds^2 = -(\tanh r)^2 dt^2 + 4M^2(\cosh r/2)^4 (dr^2 + d\Omega^2), \qquad (9.33)$$

corresponding to

$$ds^2 = -\alpha^2 dt^2 + h_{rr} dr^2 + h_{\theta\theta} d\Omega^2.$$

Then the evolution equations of the Z3 system used to evolve a Schwarzschild black hole in spherical symmetry can be translated into:

$$
\begin{aligned}
\partial_t h_{rr} &= -2\alpha h_{rr} K_r{}^r, \\
\partial_t h_{\theta\theta} &= -2\alpha h_{\theta\theta} K_\theta{}^\theta, \\
\partial_t A_r &+ \partial_r[\alpha f K] = 0, \\
\partial_t D_{rr}{}^r &+ \partial_r[\alpha K_r{}^r] = 0, \\
\partial_t D_{r\theta}{}^\theta &+ \partial_r[\alpha K_\theta{}^\theta] = 0, \\
\partial_t Z_r &+ \partial_r[2\alpha K_\theta{}^\theta] = \\
&= 2\alpha[D_{r\theta}{}^\theta(K_r{}^r - K_\theta{}^\theta) + A_r K_\theta{}^\theta - K_r{}^r Z_r],
\end{aligned}
$$

$$\partial_t K_r{}^r \;+\; \partial_r[\alpha h^{rr}(A_r + (2-n)D_{r\theta}{}^\theta - (2-\tfrac{n}{2})Z_r)] =$$

$$= \; \alpha[K_r{}^r K_r{}^r + (2-n)K_r{}^r K_\theta{}^\theta - \tfrac{n}{2}K_\theta{}^\theta K_\theta{}^\theta -$$

$$-\; h^{rr}D_{rr}{}^r(A_r + (2-n)D_{r\theta}{}^\theta + (\tfrac{n}{2}-2)Z_r) +$$

$$+\; h^{rr}D_{r\theta}{}^\theta((2-n)A_r - (2-\tfrac{3n}{2})D_{r\theta}{}^\theta - nZ_r) -$$

$$-\; h^{rr}(2-n)A_r Z_r - \tfrac{n}{2}h^{\theta\theta}],$$

$$\partial_t K_\theta{}^\theta \;+\; \partial_r[\alpha h^{rr}((1-n)D_{r\theta}{}^\theta + \tfrac{n}{2}Z_r)] =$$

$$= \; \alpha[(1-n)K_r{}^r K_\theta{}^\theta + (2-\tfrac{n}{2})K_\theta{}^\theta K_\theta{}^\theta -$$

$$-\; h^{rr}D_{rr}{}^r((1-n)D_{r\theta}{}^\theta + \tfrac{n}{2}Z_r) +$$

$$+\; h^{rr}D_{r\theta}{}^\theta((2-n)Z_r - (2-\tfrac{3n}{2})D_{r\theta}{}^\theta) -$$

$$-\; nh^{rr}A_r(D_{r\theta}{}^\theta - Z_r) + (1-\tfrac{n}{2})h^{\theta\theta}].$$

9.6.2 The Z3 system in spherical symmetry, normal coordinates and regularization

Consider a Schwarzschild line element written as

$$ds^2 = -\alpha^2 dt^2 + \left(1 + \frac{M}{2r}\right)^4 (dr^2 + r^2 d\Omega^2),$$

corresponding to

$$ds^2 = -\alpha^2 dt^2 + h_{rr}dr^2 + h_{\theta\theta}r^2 d\Omega^2.$$

Then the evolution equations of the Z3 system used to evolve a boson star configuration can be translated into:

$$\partial_t h_{rr} \;=\; -2\alpha h_{rr}K_r{}^r,$$

$$\partial_t h_{\theta\theta} \;=\; -2\alpha h_{\theta\theta}K_\theta{}^\theta,$$

$$\partial_t A_r \;+\; \partial_r[\alpha f K] = 0,$$

$$\partial_t D_{rr}{}^r \;+\; \partial_r[\alpha K_r{}^r] = 0,$$

$$\partial_t D_{r\theta}{}^\theta \;+\; \partial_r[\alpha K_\theta{}^\theta] = 0,$$

$$\partial_t Z_r \;+\; \partial_r[2\alpha K_\theta{}^\theta] =$$

$$= \; 2\alpha \left\{ \frac{1}{4r}\frac{h_{rr}}{h_{\theta\theta}}(K_\theta{}^\theta - K_r{}^r) - K_r{}^r \left[Z_r + \frac{1}{4r}\left(1 - \frac{h_{rr}}{h_{\theta\theta}}\right) \right] + \right.$$

$$\left. + \; \left(D_{r\theta}{}^\theta + \frac{1}{r}\right)(K_r{}^r - K_\theta{}^\theta) + A_r K_\theta{}^\theta - 4\pi\tau \right\},$$

$$\partial_t K_r{}^r \;+\; \partial_r\left[\alpha h^{rr}\left(A_r + \frac{2}{3}D_{r\theta}{}^\theta - \frac{4}{3}Z_r\right)\right] =$$

$$= \; \alpha \left\{ (K_r{}^r)^2 + \frac{2}{3}K_\theta{}^\theta(K_r{}^r - K_\theta{}^\theta) - h^{rr}D_{rr}{}^r A_r + \right.$$

$$+ \; \frac{1}{3r}[h^{rr}(D_{rr}{}^r - A_r - 4Z_r) + h^{\theta\theta}(D_{r\theta}{}^\theta - A_r)] +$$

$$+ \; \frac{2}{3}h^{rr}\left[Z_r + \frac{1}{4r}\left(1 - \frac{h_{rr}}{h_{\theta\theta}}\right)\right](2D_{rr}{}^r - 2D_{r\theta}{}^\theta - A_r) -$$

$$\left. - \; \frac{2}{3}h^{rr}\left(D_{r\theta}{}^\theta + \frac{1}{r}\right)(D_{rr}{}^r - A_r) + 8\pi\left(\frac{\tau}{6} - \frac{S_r{}^r}{2} + S_\theta{}^\theta\right) \right\},$$

$$\partial_t K_\theta{}^\theta \;+\; \partial_r\left[\alpha h^{rr}\left(-\frac{1}{3}D_{r\theta}{}^\theta + \frac{2}{3}Z_r\right)\right] =$$

$$= \; \alpha \left\{ \frac{1}{3}K_\theta{}^\theta(-K_r{}^r + 4K_\theta{}^\theta) + \right.$$

$$+ \; \frac{1}{6r}[h^{rr}(A_r - 2D_{rr}{}^r - 4Z_r) + h^{\theta\theta}(A_r - 2D_{r\theta}{}^\theta)] -$$

$$- \; \frac{2}{3}h^{rr}\left[Z_r + \frac{1}{4r}\left(1 - \frac{h_{rr}}{h_{\theta\theta}}\right)\right](D_{rr}{}^r - D_{r\theta}{}^\theta - 2A_r) +$$

$$\left. + \; \frac{1}{3}h^{rr}\left(D_{r\theta}{}^\theta + \frac{1}{r}\right)(D_{rr}{}^r - 4A_r) + 8\pi\left(\frac{\tau}{6} - \frac{S_r{}^r}{2} + S_\theta{}^\theta\right) \right\}.$$

9.6.2.a The Matter Terms

The matter terms introduced by a complex scalar field $\phi = \phi^R - i\phi^I$, can be explicitly written as:

$$\tau \;=\; \frac{1}{2}\{h^{rr}[(\phi_t^I)^2 + (\phi_t^R)^2] + h^{rr}[(\phi_r^I)^2 + (\phi_r^R)^2] + m^2[(\phi^I)^2 + (\phi^R)^2]\},$$

$$S_r \;=\; \sqrt{h^{rr}}(\phi_t^I\phi_r^I + \phi_t^R\phi_r^R),$$

$$S_r{}^r \;=\; \frac{1}{2}\{h^{rr}[(\phi_t^I)^2 + (\phi_t^R)^2] + h^{rr}[(\phi_r^I)^2 + (\phi_r^R)^2] - m^2[(\phi^I)^2 + (\phi^R)^2]\},$$

$$S_\theta{}^\theta \;=\; \frac{1}{2}\{h^{rr}[(\phi_t^I)^2 + (\phi_t^R)^2] - h^{rr}[(\phi_r^I)^2 + (\phi_r^R)^2] - m^2[(\phi^I)^2 + (\phi^R)^2]\},$$

where the radial and temporal derivatives are denoted by

$$\phi_t = \frac{\sqrt{h_{rr}}}{\alpha}\partial_t\phi,$$
$$\phi_r = \partial_r\phi,$$

and the evolution of $\phi_{t,r}$ is given by the Klein-Gordon equations.

9.6.2.b Characteristic Decomposition

The characteristic decomposition of the system, along any given space direction, is given by the following fields which propagate

- along the time lines (with zero speed):

$$\alpha, h_{rr}, h_{\theta\theta}, \phi, A_r, (A_r - f\ trD), (2D_{r\theta}{}^\theta - Z_r);$$

- along the light cones, with speeds $\pm\alpha\sqrt{h^{rr}}$:

$$\alpha K_\theta{}^\theta \pm \alpha\sqrt{h^{rr}}\frac{1}{3}(2Z_r - D_{r\theta}{}^\theta),$$

$$\phi_r \pm \phi_t;$$

- with gauge speed $\pm\alpha\sqrt{f}$:

$$\alpha\sqrt{f}\ K \pm \alpha\sqrt{h^{rr}}A_r,$$

where $f = 1$ for our gauge choice of harmonic slicing.

9.6.3 The full Z3 system

The Z3 system has the form:

$$\partial_t h_{ij} = -2\alpha[K_{ij} - \frac{1}{2\alpha}(B_{ij} + B_{ji}) - \frac{1}{\alpha}D_{pij}\beta^p],$$
$$\partial_t Z_i + \partial_p[-\beta^p Z_i + \alpha(-K_i{}^p + \delta_i{}^p K) + \mu(B_i{}^p - \delta_i{}^p B_q{}^q)] = S(Z_i),$$
$$\partial_t K_{ij} + \partial_p[-\beta^p K_{ij} + \alpha\{\lambda^p{}_{ij} - \frac{n}{2}h_{ij}(D^p - E^p - Z^p)\}] = S(K_{ij}),$$

where the ξ parameter comes from the definition of the Ricci tensor, μ corresponds to the ordering choice and n tunes the coupling with the energy constraint, allowing us to obtain different forms of the Z3 system (Section 3.1.1). The shorthands can be translated as $D_i = D_{ip}{}^p$ and $E_i = D^p{}_{pi}$.

The $\lambda^p{}_{ij}$ in principal part of the extrinsic curvature equation can be written explicitly as

$$\lambda^p{}_{ij} = D^p{}_{ij} - \frac{1}{2}(1 + \xi)(D_{ij}{}^p + D_{ji}{}^p) +$$

$$+ \frac{1}{2}\delta_j{}^p(A_i + D_i - (1 - \xi)E_i - 2Z_i) +$$

$$+ \frac{1}{2}\delta_i{}^p(A_j + D_j - (1 - \xi)E_j - 2Z_j).$$

The Z3 source terms are given by

$$S(K_{ij}) = S_{Z4}(K_{ij}) - \frac{n}{2}h_{ij}S_{Z4}(\theta) - \frac{n}{2}\alpha(D^p - E^p - Z^p)(2D_{pij} + A_p h_{ij}),$$

$$S(Z_i) = \alpha[A_i K - A_p K^p{}_i - D_i{}^{pq}K_{pq} + D^p K_{pi} - 2K^p{}_i Z_p] - Z_i trB -$$

$$-8\pi\alpha S_i.$$

9.7 The Z4 system

The Z4 system has the form:

$$\partial_t h_{ij} = -2\alpha[K_{ij} - \frac{1}{2\alpha}(B_{ij} + B_{ji}) - \frac{1}{\alpha}D_{pij}\beta^p],$$

$$\partial_t Z_i + \partial_p[-\beta^p Z_i + \alpha\{-K_i{}^p + \delta_i{}^p(K - \theta)\} + \mu(B_i{}^p - \delta_i{}^p trB)] = S(Z_i),$$

$$\partial_t K_{ij} + \partial_p[-\beta^p K_{ij} + \alpha\lambda^p{}_{ij}] = S(K_{ij}),$$

$$\partial_t \theta + \partial_p[-\beta^p \theta + \alpha(D^p - E^p - Z^p)] = S(\theta).$$

The Z4 source terms are given by

$$S(K_{ij}) = -K_{ij}trB + K_{pi}B_j{}^p + K_{pj}B_i{}^p +$$

$$+\alpha\{D^p(D_{ijp} + D_{jip} - D_{pij}) +$$

$$+\frac{1}{2}(1 - \xi 1)[(A_p - 2E_p)(D_{ij}{}^p + D_{ji}{}^p) - (A_j E_i + A_i E_j) +$$

$$+2(D_{pqi}D_j{}^{pq} + D_{pqj}D_i{}^{pq})] + \frac{1}{2}(A_j D_i + A_i D_j) +$$

$$+2(D_{pqj}D^{pq}{}_i - D_{pqj}D^{qp}{}_i - \frac{1}{2}D_{ipq}D_j{}^{pq}) +$$

$$-2Z^p(D_{ipj} + D_{jpi} - D_{pij}) - (A_j Z_i + A_i Z_j) -$$

$$-2K^q{}_j K_{qi} + K_{ij}(K - 2\Theta)\} - 8\pi\alpha[S_{ij} - \frac{h_{ij}}{2}(trS - \tau)],$$

$$
\begin{aligned}
S(Z_i) &= \alpha[A_i(K - 2\theta) - A_p K^p{}_i - D_i{}^{pq} K_{pq} + D^p K_{pi} - 2K^p{}_i Z_p] - \\
&\quad - Z_i trB + Z_p B_i{}^p - 8\pi\alpha S_i, \\
S(\theta) &= \frac{\alpha}{2}[2A_p(D^p - E^p - 2Z^p) + D_p{}^{rq}(2D_{rq}{}^p - D^p{}_{rq}) - \\
&\quad - D^p(D_p - 2Z_p) - K^p{}_q K^q{}_p + K(K - 2\theta)] - \theta trB - 8\pi\alpha\tau.
\end{aligned}
$$

9.8 The Friedrich-Nagy system

9.8.0.a The constraint equations for Γ

$$
\begin{aligned}
(e_1)^p \partial_p \Gamma_{232} &- (e_2)^p \partial_p \Gamma_{231} - E_{31} + \\
&+ \chi_{23}\chi_{21} + \chi_{22}\chi_{13} - 2\chi_{23}\chi_{12} + \\
+ \Gamma_{232}\Gamma_{221} &- \Gamma_{221}\Gamma_{131} + 2\Gamma_{231}\Gamma_{121} = 0,
\end{aligned}
\tag{9.34}
$$

$$
\begin{aligned}
(e_2)^p \partial_p \Gamma_{131} &- (e_1)^p \partial_p \Gamma_{231} - E_{32} + \\
&+ \chi_{23}\chi_{11} + \chi_{12}\chi_{13} - 2\chi_{21}\chi_{13} + \\
+ \Gamma_{232}\Gamma_{121} &- \Gamma_{121}\Gamma_{131} - 2\Gamma_{231}\Gamma_{221} = 0,
\end{aligned}
\tag{9.35}
$$

$$
\begin{aligned}
(e_3)^p \partial_p \Gamma_{131} &- (e_1)^p \partial_p \Gamma_{331} + E_{22} + \\
&+ \chi_{33}\chi_{11} + \chi_{13}\chi_{13} - 2\chi_{31}\chi_{13} + \\
+ \Gamma_{332}\Gamma_{121} &- \Gamma_{131}\Gamma_{131} - \Gamma_{331}\Gamma_{331} - \\
&- \Gamma_{231}\Gamma_{231} - 2\Gamma_{321}\Gamma_{231} = 0,
\end{aligned}
\tag{9.36}
$$

$$
\begin{aligned}
(e_3)^p \partial_p \Gamma_{232} &- (e_2)^p \partial_p \Gamma_{332} + E_{11} + \\
&+ \chi_{33}\chi_{22} + \chi_{23}\chi_{23} - 2\chi_{32}\chi_{23} - \\
&- \Gamma_{331}\Gamma_{221} - \Gamma_{232}\Gamma_{232} - \Gamma_{332}\Gamma_{332} - \\
&- \Gamma_{231}\Gamma_{231} + 2\Gamma_{321}\Gamma_{231} = 0,
\end{aligned}
\tag{9.37}
$$

$$
\begin{aligned}
(e_3)^p \partial_p \Gamma_{231} &- (e_1)^p \partial_p \Gamma_{332} - E_{21} + \\
+ \chi_{33}\chi_{12} + \chi_{23}\chi_{13} &- \chi_{32}\chi_{13} - \chi_{31}\chi_{23} - \\
&- \Gamma_{331}\Gamma_{121} - \Gamma_{232}\Gamma_{231} - \Gamma_{332}\Gamma_{331} - \\
&- \Gamma_{231}\Gamma_{131} - \Gamma_{321}\Gamma_{232} + \Gamma_{321}\Gamma_{131} = 0,
\end{aligned}
\tag{9.38}
$$

$$
\begin{aligned}
(e_3)^p \partial_p \Gamma_{231} &- (e_2)^p \partial_p \Gamma_{331} - E_{21} + \\
+ \chi_{33}\chi_{21} + \chi_{23}\chi_{13} &- \chi_{32}\chi_{13} - \chi_{31}\chi_{23} - \\
&- \Gamma_{331}\Gamma_{332} - \Gamma_{232}\Gamma_{321} + \Gamma_{332}\Gamma_{221} - \\
&- \Gamma_{231}\Gamma_{131} - \Gamma_{232}\Gamma_{231} + \Gamma_{321}\Gamma_{131} = 0,
\end{aligned}
\tag{9.39}
$$

$$
\begin{aligned}
(e_1)^p \partial_p \Gamma_{321} &- (e_3)^p \partial_p \Gamma_{121} + E_{32} - \\
&- \chi_{32}\chi_{11} + \chi_{31}\chi_{12} + \\
&+ \Gamma_{331}\Gamma_{321} + \Gamma_{221}\Gamma_{321} + \Gamma_{332}\Gamma_{131} + \\
&+ \Gamma_{121}\Gamma_{131} - \Gamma_{331}\Gamma_{231} + \Gamma_{231}\Gamma_{221} = 0,
\end{aligned}
\tag{9.40}
$$

$$(e_2)^p\partial_p\Gamma_{321} - (e_3)^p\partial_p\Gamma_{221} - E_{31} -$$
$$-\chi_{32}\chi_{21} + \chi_{31}\chi_{22} -$$
$$-\Gamma_{331}\Gamma_{232} + \Gamma_{221}\Gamma_{232} + \Gamma_{332}\Gamma_{231} -$$
$$-\Gamma_{121}\Gamma_{321} + \Gamma_{121}\Gamma_{231} + \Gamma_{332}\Gamma_{321} = 0, \tag{9.41}$$

$$(e_2)^p\partial_p\Gamma_{121} - (e_1)^p\partial_p\Gamma_{221} - E_{11} -$$
$$-E_{22} - \chi_{12}\chi_{21} + \chi_{11}\chi_{22} -$$
$$-\Gamma_{221}\Gamma_{221} - \Gamma_{121}\Gamma_{121} + \Gamma_{231}\Gamma_{231} -$$
$$-\Gamma_{232}\Gamma_{131} = 0. \tag{9.42}$$

9.8.0.b The constraint equations for χ

$$(e_2)^p\partial_p\chi_{11} - (e_1)^p\partial_p\chi_{21} - B_{31} - \chi_{21}F_1 + \chi_{12}F_1 -$$
$$-\chi_{13}\Gamma_{231} - \chi_{21}\Gamma_{221} - \chi_{12}\Gamma_{221} +$$
$$+\chi_{23}\Gamma_{131} + \chi_{22}\Gamma_{121} - \chi_{11}\Gamma_{121} = 0, \tag{9.43}$$

$$(e_2)^p\partial_p\chi_{12} - (e_1)^p\partial_p\chi_{22} - B_{32} - \chi_{21}F_2 + \chi_{12}F_2 -$$
$$-\chi_{13}\Gamma_{232} + \chi_{23}\Gamma_{231} - \chi_{22}\Gamma_{221} +$$
$$+\chi_{11}\Gamma_{221} - \chi_{21}\Gamma_{121} - \chi_{12}\Gamma_{121} = 0, \tag{9.44}$$

$$(e_3)^p\partial_p\chi_{21} - (e_2)^p\partial_p\chi_{31} - B_{11} - \chi_{32}F_1 + \chi_{23}F_1 -$$
$$-\chi_{31}\Gamma_{332} - \chi_{23}\Gamma_{331} - \chi_{22}\Gamma_{321} + \chi_{11}\Gamma_{321} -$$
$$-\chi_{21}\Gamma_{232} + \chi_{33}\Gamma_{231} - \chi_{11}\Gamma_{231} + \chi_{32}\Gamma_{221} = 0, \tag{9.45}$$

$$(e_3)^p\partial_p\chi_{12} - (e_1)^p\partial_p\chi_{32} + B_{22} - \chi_{31}F_2 + \chi_{13}F_2 -$$
$$-\chi_{13}\Gamma_{332} - \chi_{32}\Gamma_{331} - \chi_{22}\Gamma_{321} + \chi_{11}\Gamma_{321} +$$
$$+\chi_{33}\Gamma_{231} - \chi_{22}\Gamma_{231} - \chi_{12}\Gamma_{131} - \chi_{31}\Gamma_{121} = 0, \tag{9.46}$$

$$(e_3)^p\partial_p\chi_{11} - (e_1)^p\partial_p\chi_{31} + B_{21} - \chi_{31}F_1 + \chi_{13}F_1 -$$
$$-\chi_{31}\Gamma_{331} - \chi_{13}\Gamma_{331} - \chi_{21}\Gamma_{321} - \chi_{12}\Gamma_{321} -$$
$$-\chi_{21}\Gamma_{231} + \chi_{33}\Gamma_{131} - \chi_{11}\Gamma_{131} + \chi_{32}\Gamma_{121} = 0, \tag{9.47}$$

$$(e_3)^p\partial_p\chi_{22} - (e_2)^p\partial_p\chi_{32} - B_{21} - \chi_{32}F_2 + \chi_{23}F_2 -$$
$$-\chi_{32}\Gamma_{332} - \chi_{23}\Gamma_{332} + \chi_{21}\Gamma_{321} + \chi_{12}\Gamma_{321} +$$
$$+\chi_{33}\Gamma_{232} - \chi_{22}\Gamma_{232} - \chi_{12}\Gamma_{231} - \chi_{31}\Gamma_{221} = 0, \tag{9.48}$$

$$(e_1)^p\partial_p\chi_{23} - (e_2)^p\partial_p\chi_{13} + f\chi_{21} - f\chi_{12} - B_{22} - B_{11} +$$
$$+\chi_{21}\Gamma_{232} - 2\chi_{12}\Gamma_{232} + \chi_{22}\Gamma_{231} - \chi_{11}\Gamma_{231} +$$
$$+\chi_{23}\Gamma_{221} + 2\chi_{21}\Gamma_{131} - \chi_{12}\Gamma_{131} + \chi_{13}\Gamma_{121} = 0, \tag{9.49}$$

$$(e_3)^p\partial_p\chi_{13} - (e_1)^p\partial_p\chi_{33} - f\chi_{31} + f\chi_{13} + B_{32} +$$
$$+\chi_{12}\Gamma_{332} - \chi_{33}\Gamma_{331} + \chi_{11}\Gamma_{331} - \chi_{23}\Gamma_{321} - \chi_{31}\Gamma_{232} +$$
$$+\chi_{13}\Gamma_{232} - \chi_{32}\Gamma_{231} - \chi_{23}\Gamma_{231} - 2\chi_{31}\Gamma_{131} = 0, \tag{9.50}$$

$$(e_3)^p\partial_p\chi_{23} - (e_2)^p\partial_p\chi_{33} - f\chi_{32} + f\chi_{23} - B_{31} -$$
$$-\chi_{33}\Gamma_{332} + \chi_{22}\Gamma_{332} + \chi_{21}\Gamma_{331} + \chi_{13}\Gamma_{321} - 2\chi_{32}\Gamma_{232} -$$
$$-\chi_{31}\Gamma_{231} - \chi_{13}\Gamma_{231} - \chi_{32}\Gamma_{131} + \chi_{23}\Gamma_{131} = 0. \tag{9.51}$$

9.8.0.c The evolution equations for Γ

$$(e_0)^p \partial_p \Gamma_{121} + B_{31} + \chi_{11} F_2 - \chi_{12} F_1 +$$
$$+ \chi_{11} \Gamma_{121} - \chi_{23} \Gamma_{131} + \chi_{12} \Gamma_{221} + \chi_{13} \Gamma_{231} = 0, \tag{9.52}$$

$$(e_0)^p \partial_p \Gamma_{221} + B_{32} + \chi_{21} F_2 - \chi_{22} F_1 +$$
$$+ \chi_{13} \Gamma_{232} - \chi_{23} \Gamma_{231} + \chi_{22} \Gamma_{221} + \chi_{21} \Gamma_{121} = 0, \tag{9.53}$$

$$(e_0)^p \partial_p \Gamma_{321} - B_{22} - B_{11} + \chi_{31} F_2 - \chi_{32} F_1 +$$
$$+ \chi_{13} \Gamma_{332} - \chi_{23} \Gamma_{331} + \chi_{33} \Gamma_{321} + \chi_{32} \Gamma_{221} +$$
$$+ \chi_{23} \Gamma_{221} + \chi_{31} \Gamma_{121} + \chi_{13} \Gamma_{121} = 0, \tag{9.54}$$

$$2(e_0)^p \partial_p \Gamma_{231} - (e_2)^p \partial_p \chi_{13} - (e_1)^p \partial_p \chi_{23} +$$
$$+ f \chi_{21} + f \chi_{12} - B_{22} + B_{11} - 2\chi_{13} F_2 - 2\chi_{23} F_1 +$$
$$+ \chi_{21} \Gamma_{232} + 2\chi_{12} \Gamma_{232} + \chi_{22} \Gamma_{231} + \chi_{11} \Gamma_{231} +$$
$$+ \chi_{23} \Gamma_{221} + 2\chi_{21} \Gamma_{131} + \chi_{12} \Gamma_{131} - \chi_{13} \Gamma_{121} = 0. \tag{9.55}$$

$$(e_0)^p \partial_p \Gamma_{331} - (e_1)^p \partial_p \chi_{33} - \chi_{33} F_1 + \chi_{12} \Gamma_{332} + \chi_{11} \Gamma_{331} = 0, \tag{9.56}$$

$$(e_0)^p \partial_p \Gamma_{332} - (e_2)^p \partial_p \chi_{33} - \chi_{33} F_2 + \chi_{22} \Gamma_{332} + \chi_{21} \Gamma_{331} = 0, \tag{9.57}$$

$$(e_0)^p \partial_p \Gamma_{131} - (e_1)^p \partial_p \chi_{13} + f \chi_{11} - B_{21} -$$
$$- 2\chi_{13} F_1 + \chi_{11} \Gamma_{232} + \chi_{12} \Gamma_{231} + 2\chi_{11} \Gamma_{131} + \chi_{23} \Gamma_{121} = 0, \tag{9.58}$$

$$(e_0)^p \partial_p \Gamma_{232} - (e_2)^p \partial_p \chi_{23} + f \chi_{22} + B_{21} -$$
$$- 2\chi_{23} F_2 + 2\chi_{22} \Gamma_{232} + \chi_{21} \Gamma_{231} - \chi_{13} \Gamma_{221} + \chi_{22} \Gamma_{131} = 0, \tag{9.59}$$

9.8.0.d The evolution equations for χ

$$(e_0)^p \partial_p \chi_{12} - (e_1)^p \partial_p F_2 + E_{21} -$$
$$- \chi_{23} \chi_{13} + \chi_{22} \chi_{12} + \chi_{12} \chi_{11} -$$
$$- F_2 F_1 + f \Gamma_{231} - F_1 \Gamma_{121} + \Gamma_{232} \Gamma_{231} + \Gamma_{231} \Gamma_{131} = 0, \tag{9.60}$$

$$(e_0)^p \partial_p \chi_{21} - (e_2)^p \partial_p F_1 + E_{21} -$$
$$- \chi_{23} \chi_{13} + \chi_{22} \chi_{21} + \chi_{21} \chi_{11} -$$
$$- F_2 F_1 + f \Gamma_{231} + F_2 \Gamma_{221} + \Gamma_{232} \Gamma_{231} + \Gamma_{231} \Gamma_{131} = 0, \tag{9.61}$$

$$(e_0)^p \partial_p \chi_{11} - (e_1)^p \partial_p F_1 + E_{11} -$$
$$- \chi_{13} \chi_{13} + \chi_{12} \chi_{21} + \chi_{11} \chi_{11} -$$
$$- F_1 F_1 + f \Gamma_{131} + F_2 \Gamma_{121} + \Gamma_{232} \Gamma_{131} + \Gamma_{131} \Gamma_{131} = 0, \tag{9.62}$$

$$(e_0)^p \partial_p \chi_{22} - (e_2)^p \partial_p F_2 + E_{22} -$$
$$- \chi_{23} \chi_{23} + \chi_{12} \chi_{21} + \chi_{22} \chi_{22} -$$
$$- F_2 F_2 + f \Gamma_{232} - F_1 \Gamma_{221} + \Gamma_{232} \Gamma_{232} + \Gamma_{232} \Gamma_{131} = 0, \tag{9.63}$$

$$(e_0)^p \partial_p \chi_{13} - (e_1)^p \partial_p f - (e_2)^p \partial_p \Gamma_{231} - (e_1)^p \partial_p \Gamma_{131} +$$
$$+ \chi_{23} \chi_{21} + \chi_{22} \chi_{13} + 2\chi_{13} \chi_{11} -$$
$$- f F_1 - F_1 \Gamma_{232} - F_2 \Gamma_{231} - 2F_1 \Gamma_{131} +$$
$$+ 2\Gamma_{231} \Gamma_{121} - \Gamma_{221} \Gamma_{131} + \Gamma_{221} \Gamma_{232} = 0, \tag{9.64}$$

$$(e_0)^p\partial_p\chi_{23} - (e_2)^p\partial_p f - (e_2)^p\partial_p\Gamma_{232} - (e_1)^p\partial_p\Gamma_{231}+$$
$$+\chi_{23}\chi_{11} + \chi_{12}\chi_{13} + 2\chi_{23}\chi_{22}-$$
$$-fF_2 - F_1\Gamma_{231} - F_2\Gamma_{131} - 2F_2\Gamma_{232}-$$
$$-2\Gamma_{221}\Gamma_{231} + \Gamma_{232}\Gamma_{121} - \Gamma_{131}\Gamma_{121} = 0, \tag{9.65}$$

$$(e_0)^p\partial_p\chi_{31} - (e_3)^p\partial_p F_1 + E_{31}+$$
$$+\chi_{31}\chi_{11} + \chi_{13}\chi_{11} - \chi_{33}\chi_{13} + \chi_{23}\chi_{21} + \chi_{32}\chi_{21} + \chi_{33}\chi_{31}+$$
$$-fF_1 + f\Gamma_{331} - F_1\Gamma_{232} - F_1\Gamma_{131} + F_2\Gamma_{321}+$$
$$+\Gamma_{331}\Gamma_{232} + \Gamma_{331}\Gamma_{131} = 0, \tag{9.66}$$

$$(e_0)^p\partial_p\chi_{32} - (e_3)^p\partial_p F_2 + E_{32}+$$
$$+\chi_{31}\chi_{12} + \chi_{13}\chi_{12} + \chi_{33}\chi_{32} + \chi_{23}\chi_{22} + \chi_{32}\chi_{22} - \chi_{33}\chi_{23}+$$
$$-fF_2 + f\Gamma_{332} - F_1\Gamma_{321} - F_2\Gamma_{232} - F_2\Gamma_{131}+$$
$$+\Gamma_{131}\Gamma_{332} + \Gamma_{332}\Gamma_{232} = 0, \tag{9.67}$$

$$(e_0)^p\partial_p\chi_{33} - (e_3)^p\partial_p f - (e_2)^p\partial_p\Gamma_{332} - (e_1)^p\partial_p\Gamma_{331}+$$
$$+\chi_{33}\chi_{33} + \chi_{33}\chi_{11} + \chi_{33}\chi_{22} + 2\chi_{23}\chi_{23} + 2\chi_{13}\chi_{13}-$$
$$-f^2 - 2f\Gamma_{131} - 2f\Gamma_{232} - F_1\Gamma_{331} - F_2\Gamma_{332}-$$
$$-\Gamma_{332}\Gamma_{332} - \Gamma_{331}\Gamma_{331} + \Gamma_{332}\Gamma_{121} - \Gamma_{331}\Gamma_{221}-$$
$$-2\Gamma_{232}\Gamma_{232} - 2\Gamma_{231}\Gamma_{231} - 2\Gamma_{232}\Gamma_{131} - 2\Gamma_{131}\Gamma_{131} = 0, \tag{9.68}$$

where the following constraints for Γ were added to the evolution equations for χ: Eq. (9.34) to Eq. (9.64); Eq. (9.35) to Eq. (9.65); Eqs. (9.36), (9.37) to Eq. (9.68), and the constraints for χ to the evolution equations for Γ: Eq. (9.50) to Eq. (9.56); Eq. (9.51) to Eq. (9.57), in order to obtain a symmetric hyperbolic system.

The Gauss equation with respect to the hypersurface T_c ($R_{0i'''j'''k'''}$) corresponds to R_{0121} Eq. (9.52), R_{0221} Eq. (9.53), R_{0120} Eq. (9.60), R_{0210} Eq. (9.61), R_{0110} Eq. (9.62), R_{0220} Eq. (9.63). The Codazzi equation with respect to T_c ($R_{i'''j'''3k'''}$) can be written as R_{0131} Eq. (9.58), R_{0232} Eq. (9.59), $R_{0132} + R_{0231}$ Eq. (9.55), $R_{0130} + R_{1232}$ Eq. (9.64), $R_{0230} + R_{2131}$ Eq. (9.65).

9.8.0.e   *The evolution equations for the frame*

In the following, we will consider a specific gauge, for which $(e_1)^4 = (e_2)^4 = 0$ and $F_1 = F_2 = 0$.

$$\partial_0(e_1)^0 - F_1 + \chi_{12}(e_2)^0 + \chi_{11}(e_1)^0 = 0, \tag{9.69}$$

$$\partial_0(e_1)^1 + \chi_{12}(e_2)^1 + \chi_{11}(e_1)^1 = 0, \tag{9.70}$$

$$\partial_0(e_1)^2 + \chi_{12}(e_2)^2 + \chi_{11}(e_1)^2 = 0, \tag{9.71}$$

$$\partial_0(e_2)^0 - F_2 + \chi_{22}(e_2)^0 + \chi_{21}(e_1)^0 = 0, \tag{9.72}$$

$$\partial_0(e_2)^1 + \chi_{22}(e_2)^1 + \chi_{21}(e_1)^1 = 0, \tag{9.73}$$

$$\partial_0(e_2)^2 + \chi_{22}(e_2)^2 + \chi_{21}(e_1)^2 = 0, \tag{9.74}$$

$$\partial_0(e_3)^1 + \chi_{33}(e_3)^1 + \chi_{32}(e_2)^1 + \chi_{23}(e_2)^1 + \chi_{31}(e_1)^1 + \chi_{13}(e_1)^1 = 0, \quad (9.75)$$

$$\partial_0(e_3)^2 + \chi_{33}(e_3)^2 + \chi_{32}(e_2)^2 + \chi_{23}(e_2)^2 + \chi_{31}(e_1)^2 + \chi_{13}(e_1)^2 = 0, \quad (9.76)$$

$$\partial_0(e_3)^3 + \chi_{33}(e_3)^3 = 0. \quad (9.77)$$

$$\partial_0(e_3)^0 + \chi_{33}(e_3)^0 + \chi_{32}(e_2)^0 + \chi_{23}(e_2)^0 + \chi_{31}(e_1)^0 + \chi_{13}(e_1)^0 - f - $$
$$-\Gamma_{232} - \Gamma_{131} = 0, \quad (9.78)$$

9.8.0.f The constraint equations for E

$$(e_3)^p\partial_p E_{31} + (e_2)^p\partial_p E_{21} + (e_1)^p\partial_p E_{11} -$$
$$-B_{32}\chi_{33} - B_{22}\chi_{32} - 2B_{11}\chi_{32} + B_{21}\chi_{31} - B_{22}\chi_{23} +$$
$$+B_{11}\chi_{23} + B_{32}\chi_{22} - B_{31}\chi_{21} - 2B_{21}\chi_{13} + 2B_{31}\chi_{12} +$$
$$+E_{21}\Gamma_{332} + E_{22}\Gamma_{331} + 2E_{11}\Gamma_{331} - E_{32}\Gamma_{321} - E_{31}\Gamma_{232} -$$
$$-E_{32}\Gamma_{231} - E_{22}\Gamma_{221} + E_{11}\Gamma_{221} - 2E_{31}\Gamma_{131} - 2E_{21}\Gamma_{121} = 0, \quad (9.79)$$

$$(e_3)^p\partial_p E_{32} + (e_2)^p\partial_p E_{22} + (e_1)^p\partial_p E_{21} +$$
$$+B_{31}\chi_{33} - B_{21}\chi_{32} + 2B_{22}\chi_{31} + B_{11}\chi_{31} + 2B_{21}\chi_{23} -$$
$$-2B_{32}\chi_{21} - B_{22}\chi_{13} + B_{11}\chi_{13} + B_{32}\chi_{12} - B_{31}\chi_{11} +$$
$$+2E_{22}\Gamma_{332} + E_{11}\Gamma_{332} + E_{21}\Gamma_{331} + E_{31}\Gamma_{321} - 2E_{32}\Gamma_{232} -$$
$$-E_{31}\Gamma_{231} + 2E_{21}\Gamma_{221} - E_{32}\Gamma_{131} - E_{22}\Gamma_{121} + E_{11}\Gamma_{121} = 0, \quad (9.80)$$

$$(e_1)^p\partial_p E_{31} - (e_3)^p\partial_p E_{22} - (e_3)^p\partial_p E_{11} -$$
$$-2B_{31}\chi_{32} + 2B_{32}\chi_{31} + B_{31}\chi_{23} - B_{21}\chi_{22} + 2B_{22}\chi_{21} +$$
$$+B_{11}\chi_{21} - B_{32}\chi_{13} - B_{22}\chi_{12} - 2B_{11}\chi_{12} + B_{21}\chi_{11} +$$
$$+2E_{32}\Gamma_{332} + 2E_{31}\Gamma_{331} + 2E_{22}\Gamma_{232} + 2E_{11}\Gamma_{131} + 2E_{21}\Gamma_{231} +$$
$$+E_{31}\Gamma_{221} + E_{22}\Gamma_{131} + E_{11}\Gamma_{232} - E_{32}\Gamma_{121} = 0. \quad (9.81)$$

9.8.0.g The constraint equations for B

$$(e_3)^p\partial_p B_{31} + (e_2)^p\partial_p B_{21} + (e_1)^p\partial_p B_{11} +$$
$$+\chi_{33}E_{32} - \chi_{22}E_{32} + \chi_{21}E_{31} - 2\chi_{12}E_{31} + \chi_{32}E_{22} +$$
$$+\chi_{23}E_{22} - \chi_{31}E_{21} + 2\chi_{13}E_{21} + 2\chi_{32}E_{11} - \chi_{23}E_{11} +$$
$$+B_{21}\Gamma_{332} + B_{22}\Gamma_{331} + 2B_{11}\Gamma_{331} - B_{32}\Gamma_{321} - B_{31}\Gamma_{232} -$$
$$-B_{32}\Gamma_{231} - B_{22}\Gamma_{221} + B_{11}\Gamma_{221} - 2B_{31}\Gamma_{131} - 2B_{21}\Gamma_{121} = 0, \quad (9.82)$$

$$(e_3)^p\partial_p B_{32} + (e_2)^p\partial_p B_{22} + (e_1)^p\partial_p B_{21} +$$
$$+2\chi_{21}E_{32} - \chi_{12}E_{32} - \chi_{33}E_{31} + \chi_{11}E_{31} - 2\chi_{31}E_{22} +$$
$$+\chi_{13}E_{22} + \chi_{32}E_{21} - 2\chi_{23}E_{21} - \chi_{31}E_{11} - \chi_{13}E_{11} +$$
$$+2B_{22}\Gamma_{332} + B_{11}\Gamma_{332} + B_{21}\Gamma_{331} + B_{31}\Gamma_{321} - 2B_{32}\Gamma_{232} -$$
$$-B_{31}\Gamma_{231} + 2B_{21}\Gamma_{221} - B_{32}\Gamma_{131} - B_{22}\Gamma_{121} + B_{11}\Gamma_{121} = 0, \quad (9.83)$$

$$(e_3)^p \partial_p B_{22} + (e_3)^p \partial_p B_{11} - (e_2)^p \partial_p B_{32} - (e_1)^p \partial_p B_{31} +$$
$$+ 2\chi_{31} E_{32} - \chi_{13} E_{32} - 2\chi_{32} E_{31} + \chi_{23} E_{31} + 2\chi_{21} E_{22} -$$
$$- \chi_{12} E_{22} - \chi_{22} E_{21} + \chi_{11} E_{21} + \chi_{21} E_{11} - 2\chi_{12} E_{11} -$$
$$- 2B_{32}\Gamma_{332} - 2B_{31}\Gamma_{331} - 2B_{22}\Gamma_{232} - 2B_{11}\Gamma_{131} - 2B_{21}\Gamma_{231} -$$
$$- B_{31}\Gamma_{221} - B_{22}\Gamma_{131} - B_{11}\Gamma_{232} - B_{32}\Gamma_{121} = 0.$$

(9.84)

9.8.0.h   *The evolution equations for E*

$$(e_0)^p \partial_p E_{11} + (e_2)^p \partial_p B_{31} - (e_3)^p \partial_p B_{21} -$$
$$- E_{22}\chi_{33} + E_{11}\chi_{33} + E_{32}\chi_{32} - E_{31}\chi_{31} + E_{32}\chi_{23} +$$
$$+ E_{22}\chi_{22} + 2E_{11}\chi_{22} - E_{21}\chi_{21} - 2E_{31}\chi_{13} - 2fB_{21} +$$
$$+ 2B_{31}F_2 + B_{31}\Gamma_{332} + B_{32}\Gamma_{331} + B_{22}\Gamma_{321} - B_{11}\Gamma_{321} -$$
$$- B_{21}\Gamma_{232} + B_{22}\Gamma_{231} + 2B_{11}\Gamma_{231} - B_{32}\Gamma_{221} - 2B_{21}\Gamma_{131} = 0,$$

(9.85)

$$(e_0)^p \partial_p E_{22} - (e_1)^p \partial_p B_{32} + (e_3)^p \partial_p B_{21} +$$
$$+ E_{22}\chi_{33} - E_{11}\chi_{33} - E_{32}\chi_{32} + E_{31}\chi_{31} - 2E_{32}\chi_{23} +$$
$$+ E_{31}\chi_{13} - E_{21}\chi_{12} + 2E_{22}\chi_{11} + E_{11}\chi_{11} + 2fB_{21} -$$
$$- 2B_{32}F_1 - B_{31}\Gamma_{332} - B_{32}\Gamma_{331} - B_{22}\Gamma_{321} + B_{11}\Gamma_{321} +$$
$$+ 2B_{21}\Gamma_{232} - 2B_{22}\Gamma_{231} - B_{11}\Gamma_{231} - B_{31}\Gamma_{121} + B_{21}\Gamma_{131} = 0,$$

(9.86)

$$2(e_0)^p \partial_p E_{31} + 2(e_1)^p \partial_p B_{21} - 2(e_2)^p \partial_p B_{11} +$$
$$+ E_{31}\chi_{33} - E_{21}\chi_{32} + 2E_{22}\chi_{31} + E_{11}\chi_{31} + 4E_{31}\chi_{22} -$$
$$- 2E_{32}\chi_{21} + 3E_{22}\chi_{13} + 3E_{11}\chi_{13} - E_{32}\chi_{12} + E_{31}\chi_{11} -$$
$$- E_{31}\chi_{33} + E_{21}\chi_{32} - 2E_{22}\chi_{31} - E_{11}\chi_{31} - 2E_{21}\chi_{23} +$$
$$+ 2E_{32}\chi_{21} + E_{22}\chi_{13} - E_{11}\chi_{13} - E_{32}\chi_{12} + E_{31}\chi_{11} -$$
$$- 2B_{32}f - 2B_{22}F_2 - 4B_{11}F_2 + 2B_{21}F_1 -$$
$$- 2B_{32}\Gamma_{232} + 2B_{31}\Gamma_{231} + 4B_{21}\Gamma_{221} -$$
$$- 4B_{32}\Gamma_{131} - 2B_{22}\Gamma_{121} + 2B_{11}\Gamma_{121} = 0,$$

(9.87)

$$2(e_0)^p \partial_p E_{32} + 2(e_1)^p \partial_p B_{22} - 2(e_2)^p \partial_p B_{21} +$$
$$+ E_{32}\chi_{33} - E_{21}\chi_{31} + E_{22}\chi_{32} + 2E_{11}\chi_{32} + 4E_{32}\chi_{11} +$$
$$+ E_{32}\chi_{22} + 3E_{22}\chi_{23} + 3E_{11}\chi_{23} - E_{31}\chi_{21} - 2E_{31}\chi_{12} -$$
$$- E_{32}\chi_{33} - E_{22}\chi_{32} - 2E_{11}\chi_{32} + E_{21}\chi_{31} - E_{22}\chi_{23} +$$
$$+ E_{11}\chi_{23} + E_{32}\chi_{22} - E_{31}\chi_{21} - 2E_{21}\chi_{13} + 2E_{31}\chi_{12} +$$
$$+ 2B_{31}f - 2B_{21}F_2 + 4B_{22}F_1 + 2B_{11}F_1 +$$
$$+ 4B_{31}\Gamma_{232} - 2B_{32}\Gamma_{231} + 2B_{22}\Gamma_{221} -$$
$$- 2B_{11}\Gamma_{221} + 2B_{31}\Gamma_{131} + 4B_{21}\Gamma_{121} = 0.$$

(9.88)

$$2(e_0)^p \partial_p E_{21} + (e_2)^p \partial_p B_{32} - (e_1)^p \partial_p B_{31} - (e_3)^p \partial_p B_{22} + (e_3)^p \partial_p B_{11} +$$
$$+ 4E_{21}\chi_{33} - 2E_{31}\chi_{32} - 2E_{32}\chi_{31} - 3E_{31}\chi_{23} + E_{21}\chi_{22} - 2E_{22}\chi_{21} -$$
$$- E_{11}\chi_{21} - 3E_{32}\chi_{13} - E_{22}\chi_{12} - 2E_{11}\chi_{12} + E_{21}\chi_{11} -$$
$$- 2fB_{22} + 2fB_{11} + 2B_{32}F_2 - 2B_{31}F_1 +$$
$$+ 2B_{32}\Gamma_{332} - 2B_{31}\Gamma_{331} - 4B_{21}\Gamma_{321} + 3B_{11}\Gamma_{232} +$$
$$+ B_{31}\Gamma_{221} - 3B_{22}\Gamma_{131} + B_{32}\Gamma_{121} = 0,$$

(9.89)

9.8.0.i   The evolution equations for B

$$(e_0)^p\partial_p B_{11} - (e_2)^p\partial_p E_{31} + (e_3)^p\partial_p E_{21} -$$
$$-B_{22}\chi_{33} + B_{11}\chi_{33} + B_{32}\chi_{32} - B_{31}\chi_{31} + B_{32}\chi_{23} +$$
$$+B_{22}\chi_{22} + 2B_{11}\chi_{22} - B_{21}\chi_{21} - 2B_{31}\chi_{13} + 2fE_{21} -$$
$$-2E_{31}F_2 - E_{31}\Gamma_{332} - E_{32}\Gamma_{331} - E_{22}\Gamma_{321} + E_{11}\Gamma_{321} +$$
$$+E_{21}\Gamma_{232} - E_{22}\Gamma_{231} - 2E_{11}\Gamma_{231} + E_{32}\Gamma_{221} + 2E_{21}\Gamma_{131} = 0, \tag{9.90}$$

$$-(e_0)^p\partial_p B_{22} - (e_1)^p\partial_p E_{32} + (e_3)^p\partial_p E_{21} -$$
$$-B_{22}\chi_{33} + B_{11}\chi_{33} + B_{32}\chi_{32} - B_{31}\chi_{31} + 2B_{32}\chi_{23} -$$
$$-B_{31}\chi_{13} + B_{21}\chi_{12} - 2B_{22}\chi_{11} - B_{11}\chi_{11} + 2fE_{21} -$$
$$-2E_{32}F_1 - E_{31}\Gamma_{332} - E_{32}\Gamma_{331} - E_{22}\Gamma_{321} + E_{11}\Gamma_{321} +$$
$$+2E_{21}\Gamma_{232} - 2E_{22}\Gamma_{231} - E_{11}\Gamma_{231} - E_{31}\Gamma_{121} + E_{21}\Gamma_{131} = 0, \tag{9.91}$$

$$2(e_0)^p\partial_p B_{31} - 2(e_1)^p\partial_p E_{21} + 2(e_2)^p\partial_p E_{11} +$$
$$+B_{31}\chi_{33} - B_{21}\chi_{32} + 2B_{22}\chi_{31} + B_{11}\chi_{31} + 4B_{31}\chi_{22} -$$
$$-2B_{32}\chi_{21} + 3B_{22}\chi_{13} + 3B_{11}\chi_{13} - B_{32}\chi_{12} + B_{31}\chi_{11} -$$
$$-B_{31}\chi_{33} + B_{21}\chi_{32} - 2B_{22}\chi_{31} - B_{11}\chi_{31} - 2B_{21}\chi_{23} +$$
$$+2B_{32}\chi_{21} + B_{22}\chi_{13} - B_{11}\chi_{13} - B_{32}\chi_{12} + B_{31}\chi_{11} +$$
$$+2E_{32}f + 2E_{22}F_2 + 4E_{11}F_2 - 2E_{21}F_1 +$$
$$+2E_{32}\Gamma_{232} - 2E_{31}\Gamma_{231} - 4E_{21}\Gamma_{221} +$$
$$+4E_{32}\Gamma_{131} + 2E_{22}\Gamma_{121} - 2E_{11}\Gamma_{121} = 0, \tag{9.92}$$

$$2(e_0)^p\partial_p B_{32} - 2(e_1)^p\partial_p E_{22} + 2(e_2)^p\partial_p E_{21} +$$
$$+B_{32}\chi_{33} - B_{21}\chi_{31} + B_{22}\chi_{32} + 2B_{11}\chi_{32} + 4B_{32}\chi_{11} +$$
$$+B_{32}\chi_{22} + 3B_{22}\chi_{23} + 3B_{11}\chi_{23} - B_{31}\chi_{21} - 2B_{31}\chi_{12} -$$
$$-B_{32}\chi_{33} - B_{22}\chi_{32} - 2B_{11}\chi_{32} + B_{21}\chi_{31} - B_{22}\chi_{23} +$$
$$+B_{11}\chi_{23} + B_{32}\chi_{22} - B_{31}\chi_{21} - 2B_{21}\chi_{13} + 2B_{31}\chi_{12} -$$
$$-2E_{31}f + 2E_{21}F_2 - 4E_{22}F_1 - 2E_{11}F_1 -$$
$$-4E_{31}\Gamma_{232} + 2E_{32}\Gamma_{231} - 2E_{22}\Gamma_{221} +$$
$$+2E_{11}\Gamma_{221} - 2E_{31}\Gamma_{131} - 4E_{21}\Gamma_{121} = 0, \tag{9.93}$$

$$2(e_0)^p\partial_p B_{21} - (e_2)^p\partial_p E_{32} + (e_1)^p\partial_p E_{31} + (e_3)^p\partial_p E_{22} - (e_3)^p E_{11} +$$
$$+4B_{21}\chi_{33} - 2B_{31}\chi_{32} - 2B_{32}\chi_{31} - 3B_{31}\chi_{23} + B_{21}\chi_{22} - 2B_{22}\chi_{21} -$$
$$-B_{11}\chi_{21} - 3B_{32}\chi_{13} - B_{22}\chi_{12} - 2B_{11}\chi_{12} + B_{21}\chi_{11} +$$
$$+2fE_{22} - 2fE_{11} - 2E_{32}F_2 - 2E_{31}F_1 -$$
$$-2E_{32}\Gamma_{332} + 2E_{31}\Gamma_{331} + 4E_{21}\Gamma_{321} - 3E_{11}\Gamma_{232} -$$
$$-E_{31}\Gamma_{221} + 3E_{22}\Gamma_{131} - E_{32}\Gamma_{121} = 0, \tag{9.94}$$

where the constraints for E, Eq. (9.79), respectively Eq. (9.80), were added to the evolutions for B, Eq. (9.93), respectively Eq. (9.92), and the constraints for B, Eq. (9.82), respectively Eq. (9.83) to the evolutions for B, Eq. (9.88), respectively Eq. (9.87), in order to obtain a symmetric hyperbolic system.

Bibliography

[1] Carsten Gundlach, Jose M. Martin-Garcia, G. Calabrese, and I. Hinder. Constraint damping in the Z4 formulation and harmonic gauge. *Class. Quantum Grav.*, 22:3767–3774, 2005.

[2] Maria C. Babiuc, Béla Szilágyi, and Jeffrey Winicour. Testing numerical relativity with the shifted gauge wave. *Class. Quantum Grav.*, 23:S319–S342, 2006.

[3] Helmut Friedrich and Alan D. Rendall. The Cauchy problem for the Einstein equations. *Lect. Notes Phys.*, 540:127–224, 2000.

[4] F. Pretorius. Numerical relativity using a generalized harmonic decomposition. *Class. Quantum Grav.*, 22:425–451, 2005. gr-qc/0407110.

[5] Lee Lindblom, Mark A. Scheel, Lawrence E. Kidder, Robert Owen, and Oliver Rinne. A new generalized harmonic evolution system. *Class. Quantum Grav.*, 23:S447–S462, 2006.

[6] Bela Szilágyi, Denis Pollney, Luciano Rezzolla, Jonathan Thornburg, and Jeffrey Winicour. An explicit harmonic code for black-hole evolution using excision. 2006. gr-qc/0612150.

[7] M. Shibata and T. Nakamura. Evolution of three-dimensional gravitational waves: Harmonic slicing case. *Phys. Rev. D*, 52:5428–5444, 1995.

[8] Thomas W. Baumgarte and Stuart L. Shapiro. On the numerical integration of Einstein's field equations. *Phys. Rev. D*, 59:024007, 1998.

[9] F. Pretorius. Evolution of Binary Black-Hole Spacetimes. *Phys. Rev. Lett.*, 95:121101, 2005. gr-qc/0507014.

[10] Bernd Brügmann, José A. González, Mark Hannam, Sascha Husa, Ulrich Sperhake, and Wolfgang Tichy. Calibration of moving puncture simulations. *Phys. Rev. D*, 77:024027, 2008. gr-qc/0610128.

[11] Mark Hannam, Sascha Husa, Denis Pollney, Bernd Brügmann, and Niall Ó Murchadha. Geometry and regularity of moving punctures. *Phys. Rev. Lett.*, 99:241102, 2007. gr-qc/0606099.

[12] Luca Baiotti and Luciano Rezzolla. Challenging the paradigm of singularity excision in gravitational collapse. *Phys. Rev. Lett.*, 97:141101, 2006.

[13] T. Goodale, G. Allen, G. Lanfermann, J. Massó, T. Radke, E. Seidel, and J. Shalf. The Cactus framework and toolkit: Design and applications. In *Vector and Parallel Processing – VECPAR'2002, 5th International Conference, Lecture Notes in Computer Science*, Berlin, 2003. Springer.

[14] Erik Schnetter, Scott H. Hawley, and Ian Hawke. Evolutions in 3d numerical relativity using fixed mesh refinement. 2003. gr-qc/0310042.

[15] Matthew Anderson, Eric Hirschmann, Steven L. Liebling, and David Neilsen. Relativistic MHD with Adaptive Mesh Refinement. *Class. Quantum Grav.*, 23:6503–6524, 2006.

[16] M. Campanelli, C. O. Lousto, P. Marronetti, and Y. Zlochower. Accurate Evolutions of Orbiting Black-Hole Binaries without Excision. *Phys. Rev. Lett.*, 96:111101, 2006. gr-qc/0511048.

[17] J. G. Baker, J. Centrella, D.-I. Choi, M. Koppitz, and J. van Meter. Gravitational-Wave Extraction from an inspiraling Configuration of Merging Black Holes. *Phys. Rev. Lett.*, 96:111102, 2006. gr-qc/0511103.

[18] Benjamin Aylott et al. Testing gravitational-wave searches with numerical relativity waveforms: Results from the first Numerical INJection Analysis (NINJA) project. 2009. gr-qc/0901.4399.

[19] Benjamin Aylott et al. Status of NINJA: the Numerical INJection Analysis project. *Class. Quant. Grav.*, 26:114008, 2009.

[20] C. Bona and D. Alic. Gauge and constraint degrees of freedom: from analytical to numerical approximations in general relativity. In *Proceedings of ERE2007 (Spanish Relativity Meeting 2007) "Relativistic Astrophysics and Cosmology", Tenerife, Spain, September 10-14, 2007*, volume 30. EDP Sciences, 2008.

[21] Lee Lindblom and Bela Szilagyi. An Improved Gauge Driver for the GH Einstein System. 2009. gr-qc/0904.4873.

[22] M. A. Aloy, J. A. Pons, and J. M. Ibanez. An Efficient Implementation of Flux Formulae in Multidimensional Relativistic Hydrodynamical Codes. *Comput. Phys. Commun.*, 120:115–121, 1999.

[23] Daniela Alic, Carles Bona, Carles Bona-Casas, and Joan Masso. Efficient implementation of finite volume methods in Numerical Relativity. *Phys. Rev. D*, 76:104007, 2007.

[24] Daniela Alic, Carles Bona, and Carles Bona-Casas. A new dissipation term for finite-difference simulations in relativity. In *Proceedings of ERE2007 (Spanish Relativity Meeting 2007) "Relativistic Astrophysics and Cosmology", Tenerife, Spain, September 10-14, 2007*, volume 30. EDP Sciences, 2008.

[25] Luca Baiotti, Bruno Giacomazzo, and Luciano Rezzolla. Accurate evolutions of inspiralling neutron-star binaries: assessment of the truncation error. *Class. Quant. Grav.*, 26:114005, 2009.

[26] Matthew Anderson et al. Magnetized Neutron Star Mergers and Gravitational Wave Signals. *Phys. Rev. Lett.*, 100:191101, 2008.

[27] Kenta Kiuchi, Yuichiro Sekiguchi, Masaru Shibata, and Keisuke Taniguchi. Longterm general relativistic simulation of binary neutron stars collapsing to a black hole. 2009. gr-qc/0904.4551.

[28] Luca Baiotti, Bruno Giacomazzo, and Luciano Rezzolla. Accurate evolutions of inspiralling neutron-star binaries: prompt and delayed collapse to black hole. *Phys. Rev. D*, 78:084033, 2008.

[29] Carlos Palenzuela, Luis Lehner, Oscar Reula, and Luciano Rezzolla. Beyond ideal MHD: towards a more realistic modeling of relativistic astrophysical plasmas. 2008. astro-ph/0810.1838.

[30] Michael Dumbser and Olindo Zanotti. Very High Order PNM Schemes on Unstructured Meshes for the Resistive Relativistic MHD Equations. 2009. gr-qc/0903.4832.

[31] E. Seidel and W.-M. Suen. The dynamical evolution of boson stars: Perturbing the ground state. *Phys. Rev. D*, 42:384, 1990.

[32] Remo Ruffini and Silvano Bonazzola. Systems of selfgravitating particles in general relativity and the concept of an equation of state. *Phys. Rev.*, 187:1767–1783, 1969.

[33] E. W. Mielke, B. Fuchs, and F. Schunck. Dark matter halos as Bose-Einstein condensates. Prepared for 10th Marcel Grossmann Meeting on Recent Developments in Theoretical and Experimental General Relativity, Gravitation and Relativistic Field Theories (MG X MMIII), Rio de Janeiro, Brazil, 20-26 Jul 2003.

[34] H. F. M. Goenner. On the history of unified field theories. *Living Rev. Rel.*, 7:2, 2004.

[35] Robert M. Wald. *General Relativity*. University of Chicago Press, Chicago, 1984.

[36] Miguel Alcubierre, Bernd Brügmann, Peter Diener, Michael Koppitz, Denis Pollney, Edward Seidel, and Ryoji Takahashi. Gauge conditions for long-term numerical black hole evolutions without excision. *Phys. Rev. D*, 67:084023, 2003.

[37] Carsten Gundlach and Jose M. Martin-Garcia. Well-posedness of formulations of the Einstein equations with dynamical lapse and shift conditions. *Phys. Rev. D*, 74:024016, 2006.

[38] James R. van Meter, John G. Baker, Michael Koppitz, and Dae-Il Choi. How to move a black hole without excision: gauge conditions for the numerical evolution of a moving puncture. *Phys. Rev. D*, 73:124011, 2006.

[39] Bertil Gustafsson, Heinz-Otto Kreiss, and Joseph Oliger. *Time dependent problems and difference methods*. Wiley, New York, 1995.

[40] Gioel Calabrese, Ian Hinder, and Sascha Husa. Numerical stability for finite difference approximations of Einstein's equations. *J. Comp. Phys.*, 218:607–634, 2005.

[41] Oscar Reula. Hyperbolic methods for Einstein's equations. *Living Rev. Relativity*, 1:3, 1998.

[42] John Baker, Bernd Brügmann, Manuela Campanelli, and Carlos O. Lousto. Gravitational waves from black hole collisions via an eclectic approach. *Class. Quantum Grav.*, 17:L149–L156, 2000.

[43] J. Baker, M. Campanelli, and C. O. Lousto. The Lazarus project: A pragmatic approach to binary black hole evolutions. *Phys. Rev. D*, 65:044001, 2002. gr-qc/0104063.

[44] P. D. Lax and R. S. Phillips. Local boundary conditions for dissipative symmetric linear differential operators. *Commun. Pure Appl. Math.*, 13:427–455, 1960.

[45] J. Rauch. Symmetric positive systems with boundary characteristics of constant multiplicity. *Trans. Am. Math. Soc.*, 291:167, 1985.

[46] Paolo Secchi. Well-posedness of characteristic symmetric hyperbolic systems. *Arch. Rat. Mech. Anal.*, 134:155–197, 1996.

[47] Helmut Friedrich and Gabriel Nagy. The initial boundary value problem for Einstein's vacuum field equations. *Commun. Math. Phys.*, 201:619–655, 1999.

[48] B. Szilágyi and Jeffrey Winicour. Well-posed initial-boundary evolution in general relativity. *Phys. Rev. D*, 68:041501, 2003.

[49] B. Szilágyi, Roberto Gomez, N. T. Bishop, and Jeffrey Winicour. Cauchy boundaries in linearized gravitational theory. *Phys. Rev. D*, 62:104006, 2000.

[50] G. Calabrese, L. Lehner, and M. Tiglio. Constraint-preserving boundary conditions in numerical relativity. *Phys. Rev. D*, 65:104031, 2002.

[51] Richard Arnowitt, Stanley Deser, and Charles W. Misner. The dynamics of general relativity. In L. Witten, editor, *Gravitation: An introduction to current research*, pages 227–265. John Wiley, New York, 1962.

[52] Carles Bona and Carlos Palenzuela-Luque. *Elements of Numerical Relativity*. Springer-Verlag, Berlin, 2005.

[53] C. Bona, T. Ledvinka, C. Palenzuela, and M. Zacek. A symmetry-breaking mechanism for the Z4 general-covariant evolution system. *Phys. Rev.*, D69:064036, 2004.

[54] Daniela Alic, Carles Bona, and Carles Bona-Casas. Towards a gauge-polyvalent Numerical Relativity code. *Phys. Rev. D*, 79:044026, 2009.

[55] M. C. Babiuc et al. Implementation of standard testbeds for numerical relativity. *Class. Quant. Grav.*, 25:125012, 2008.

[56] D. Alic. Toward the numerical implementation of well-posed, constraint preserving evolution systems for general relativity. Master's thesis, West University of Timisoara, Romania, 2005.

[57] Miguel Alcubierre, Gabrielle Allen, Thomas W. Baumgarte, Carles Bona, David Fiske, Tom Goodale, Francisco Siddhartha Guzmán, Ian Hawke, Scott Hawley, Sascha Husa, Michael Koppitz, Christiane Lechner, Lee Lindblom, Denis Pollney, David Rideout, Marcelo Salgado, Erik Schnetter, Edward Seidel, Hisa aki Shinkai, Deirdre Shoemaker, Béla Szilágyi, Ryoji Takahashi, and Jeffrey Winicour. Towards standard testbeds for numerical relativity. *Class. Quantum Grav.*, 21(2):589–613, 2004.

[58] G. Nagy, O. E. Ortiz, and O. A. Reula. Strongly hyperbolic second order Einstein's evolution equations. *Phys. Rev. D*, 70:044012, 2004.

[59] L. E. Kidder, Mark A. Scheel, and Saul A. Teukolsky. Extending the lifetime of 3D black hole computations with a new hyperbolic system of evolution equations. *Phys. Rev. D*, 64:064017, 2001.

[60] Manuel Tiglio, Luis Lehner, and David Neilsen. 3d simulations of Einstein's equations: symmetric hyperbolicity, live gauges and dynamic control of the constraints. *Phys. Rev. D*, 70:104018, 2004.

[61] Jorg Frauendiener and Tilman Vogel. Algebraic stability analysis of constraint propagation. *Class. Quantum Grav.*, 22:1769–1793, 2005.

[62] Sascha Husa, Carsten Schneemann, Tilman Vogel, and Anil Zenginoglu. Hyperboloidal data and evolution. *AIP Conf. Proc.*, 841:306–313, 2006.

[63] Sascha Husa, Ian Hinder, and Christiane Lechner. Kranc: a Mathematica application to generate numerical codes for tensorial evolution equations. *Comput. Phys. Comm.*, 174:983–1004, 2006.

[64] Christiane Lechner, Dana Alic, and Sascha Husa. From tensor equations to numerical code – computer algebra tools for numerical relativity. In *SYNASC 2004 – 6th International Symposium on Symbolic and Numeric Algorithms for Scientific Computing, Timisoara, Romania, September 26-30, 2004*, volume XLII. Editura Mirton, 2004.

[65] Mark Hannam et al. The Samurai Project: verifying the consistency of black-hole-binary waveforms for gravitational-wave detection. 2009. gr-qc/0901.2437.

[66] L. F. Richardson. The approximate arithmetic solution by finite differences of physical problems involving differential equations, with applications to the stresses in a masonry dam. *Phil. Trans. Roy. Soc.*, 210:307–357, 1910.

[67] C. Bona and J. Massó. Hyperbolic evolution system for numerical relativity. *Phys. Rev. Lett.*, 68:1097, 1992.

[68] R. J. Leveque. In Steiner O. and Gautschy A., editors, *Computational Methods for Astrophysical Fluid Flow*. Springer-Verlag, 1998.

[69] Mark Hannam, Sascha Husa, Frank Ohme, Bernd Bruegmann, and Niall O'Murchadha. Wormholes and trumpets: the Schwarzschild spacetime for the moving-puncture generation. 2008. gr-qc/0804.0628.

[70] A. Arbona, C. Bona, J. Carot, L. Mas, Joan Massó, and J. Stela. Stuffed black holes. *Phys. Rev. D*, 57:2397, 1998.

[71] C. Bona, C. Bona-Casas, and J. Terradas. Linear high-resolution schemes for hyperbolic conservation laws: TVB numerical evidence. *J. Comput. Phys.*, 228:2266–2281, 2009.

[72] M. Alcubierre, B. Brügmann, P. Diener, M. Koppitz, D. Pollney, E. Seidel, and R. Takahashi. Gauge conditions for long-term numerical black hole evolutions without excision. *Phys. Rev. D*, 67:084023, 2003. gr-qc/0206072.

[73] A. Arbona, C. Bona, J. Massó, and J. Stela. Robust evolution system for numerical relativity. *Phys. Rev. D*, 60:104014, 1999. gr-qc/9902053.

[74] Stacy S. McGaugh, Vera C. Rubin, and W. J. G. de Blok. High-resolution rotation curves of low surface brightness galaxies: Data. *Astron. J.*, 122:2381–2395, 2001.

[75] J. Chang et al. An excess of cosmic ray electrons at energies of 300.800 GeV. *Nature*, 456:362–365, 2008.

[76] R. Bernabei et al. Direct detection of dark-matter particles. *Nuovo Cim.*, 123B:928–931, 2008.

[77] David J. Kaup. Klein-Gordon Geon. *Phys. Rev.*, 172:1331–1342, 1968.

[78] Marcelo Gleiser. Stability of Boson Stars. *Phys. Rev.*, D38:2376, 1988.

[79] Marcelo Gleiser and Richard Watkins. Gravitational stability of scalar matter. *Nucl. Phys.*, B319:733, 1989.

[80] A. Arbona and Carles Bona. Dealing with the center and boundary problems in 1D Numerical Relativity. *Comput. Phys. Commun.*, 118:229–235, 1999.

[81] S. H. Hawley and M. W. Choptuik. Boson stars driven to the brink of black hole

formation. *Phys. Rev. D*, 62:104024, 2000.

[82] C. W. Lai. *A numerical study of boson stars*. PhD thesis, The University of British Columbia, Canada, 2005.

[83] Frans Pretorius. Evolution of binary black hole spacetimes. *Phys. Rev. Lett.*, 95:121101, 2005.

[84] Manuela Campanelli, Carlos O. Lousto, Pedro Marronetti, and Yosef Zlochower. Accurate evolutions of orbiting black-hole binaries without excision. *Phys. Rev. Lett.*, 96:111101, 2006.

[85] John G. Baker, Joan Centrella, Dae-Il Choi, Michael Koppitz, and James van Meter. Gravitational wave extraction from an inspiraling configuration of merging black holes. *Phys. Rev. Lett.*, 96:111102, 2006.

[86] James van Meter, John G. Baker, Michael Koppitz, and Dae-Il Choi. How to move a black hole without excision: gauge conditions for the numerical evolution of a moving puncture. 2006. gr-qc/0605030.

[87] C. Bona and J. Masso. Harmonic Synchronizations of Spacetime. *Phys. Rev. D*, 38:2419–2422, 1988.

[88] H. Friedrich. Hyperbolic reductions for Einstein's equations. *Class. Quantum Grav.*, 13:1451–1469, 1996.

[89] C. Bona, J. Massó, E. Seidel, and J. Stela. New Formalism for Numerical Relativity. *Phys. Rev. Lett.*, 75:600–603, 1995.

[90] Miguel Alcubierre. The appearance of coordinate shocks in hyperbolic formalisms of General Relativity. *Phys. Rev. D*, 55:5981–5991, 1997.

[91] C. Bona, T. Ledvinka, C. Palenzuela-Luque, J. A. Pons, and M. Žáček. Gauge pathologies in singularity-avoidant spacetime foliations. gr-qc/0410079, 2004.

[92] Miguel Alcubierre and Joan Masso. Pathologies of hyperbolic gauges in general relativity and other field theories. *Phys. Rev. D*, 57:4511–4515, 1998.

[93] Miguel Alcubierre. Hyperbolic slicings of spacetime: singularity avoidance and gauge shocks. *Class. Quant. Grav.*, 20:607–624, 2003.

[94] Bernd Reimann, Miguel Alcubierre, José A. González, and Darío Núñez. Constraint and gauge shocks in one-dimensional numerical relativity. *Phys. Rev. D*, 71:064021, 2005.

[95] Miguel Alcubierre. Are gauge shocks really shocks? *Class. Quantum Grav.*, 22:4071–4082, 2005.

[96] David Garfinkle, Carsten Gundlach, and David Hilditch. Comments on bona-masso type slicing conditions in long-term black hole evolutions. 2007. gr-qc/0707.0726.

[97] C. Bona, J. Massó, E. Seidel, and J. Stela. A New Formalism for Numerical Relativity. *Phys. Rev. Lett.*, 75:600–603, 1995. gr-qc/9412071.

[98] C. Bona, T. Ledvinka, C. Palenzuela, and M. Zacek. General-covariant evolution formalism for numerical relativity. *Phys. Rev. D*, 67:104005, 2003.

[99] Miguel Alcubierre. Hyperbolic slicings of spacetime: singularity avoidance and gauge shocks. *Class. Quantum Grav.*, 20(4):607–624, 2003.

[100] C. Bona, L. Lehner, and C. Palenzuela-Luque. Geometrically motivated hyperbolic

coordinate conditions for numerical relativity: Analysis, issues and implementations. gr-qc/0509092, 2005.

[101] Heinz Otto Kreiss and Joseph Oliger. *Methods for the approximate solution of time dependent problems*. GARP publication series No. 10, Geneva, 1973.

List of Figures

195

CURRICULUM VITAE

Daniela Delia Alic

Personal Data

First names:	Daniela Delia
Surname:	Alic
Date of birth:	May 29 1981
Place of birth:	Hunedoara
Nationality:	Romanian
Civil Status:	Single
Affiliation:	University of the Balearic Islands, Department of Physics
Address:	Cra.Valldemossa km 7.5, E-07122 Palma de Mallorca, Baleares, Spain
Office Phone:	+34 971 17 3207
Fax:	+34 971 17 3426
E-mail:	alicdana@gmail.com

Academic Degrees

Degree:	*Diploma in Physics*
Year:	2003
Center:	West University of Timisoara (Romania)
Advisor:	Prof. Dr. Dumitru Vulcanov

Degree:	*Master in Theoretical and Computational Physics*
Year:	2005
Center:	West University of Timisoara (Romania)
Advisors:	Prof. Dr. Dumitru Vulcanov, Dr. Sascha Husa, Dr. Christiane Lechner

Degree:	*Diploma of Advanced Studies in Theoretical Physics*
Year:	2007
Center:	University of the Balearic Islands (Spain)
Advisors:	Prof. Dr. Carles Bona

Awarded Fellowships

Oct. 2001 - July 2002   Scholarship for undergraduate studies supported by the *Socrates-Erasmus* program, at the Vienna University of Technology (Austria).
Coordinator: Prof. Dr. Maria Ebel

Oct. 2003 - March 2004   Scholarship for graduate studies supported by the *European Physical Society*, at the Free University of Berlin (Germany).
Coordinator: Prof. Dr. Bodo Hamprecht

April 2004 - Aug. 2004   Research scholarship supported by the *Max Planck Society*, at the Albert Einstein Institute (Germany).
Coordinator: Prof. Dr. Helmut Friedrich

Sept. 2005 - Sept. 2009   Scholarship for PhD studies supported by the *Spanish Ministry of Science and Innovation*, at the University of the Balearic Islands (Spain).
Coordinator: Prof. Dr. Carles Bona

Education

1995-1999   Secondary school in Hunedoara, final examination *Bacalaureat* (Physics, Mathematics, German Language, History, Romanian Language and Literature)

Oct. 1999 - Sept. 2001   Undergraduate study of physics at the West University of Timisoara (Romania)

Oct. 2001 - Sept. 2002   Undergraduate study of physics at Vienna University of Technology (Austria)

Oct. 2002 - June 2003   Undergraduate study of physics at the West University of Timisoara (Romania)

June 2003   Graduation in physics, with the diploma thesis titled *The Post-Newtonian Approximation with applications in Numerical Relativity*, advisor: Prof. Dr. Dumitru Vulcanov

Oct. 2003 - Sept. 2004	Graduate study of physics at the Free University of Berlin (Germany) and research work for master thesis at the Albert Einstein Institute (Germany)
Oct. 2004 - June 2005	Graduate study of physics at the West University of Timisoara (Romania)
June 2005	Graduation of master in physics, with the thesis titled *Toward the Numerical Implementation of Well-Posed Constraint Preserving Evolution Systems for General Relativity*, advisors: Prof. Dr. Dumitru Vulcanov, Dr. Sascha Husa, Dr. Christiane Lechner
Sept. 2005 -	PhD study at the University of the Balearic Islands (Spain), with the thesis titled *Theoretical issues in Numerical Relativity simulations*, advisor: Prof. Dr. Carles Bona
Sept. 2007	Graduation of advanced studies in physics, with the thesis titled *Robust Numerical Relativity Codes and Black Hole Simulations*, advisor: Prof. Dr. Carles Bona

Schools and Conferences

March 01 - 05 2004	*Mathematical Relativity: New Ideas and Developments Conference*, Bad Honnef
Sept. 26 - 30 2004	*6th International Symposium on Symbolic and Numeric Algorithms for Scientific Computing*, Timisoara
Oct. 24 - 25 2005	*2nd Annual ILIAS-GW Meeting*, Palma de Mallorca
July 17 - 21 2006	*New Frontiers in Numerical Relativity Conference*, Potsdam
July 23 - 29 2006	*11th Marcel Grossmann Meeting*, Berlin
Sept. 04 - 08 2006	*XXIX Spanish Relativity Meeting*, Palma de Mallorca

Aug. 20 - 24 2007   *International Summer School on Theoretical Gravitational Wave Astronomy*, Bad Honnef

Sept. 10 - 14 2007   *XXX Spanish Relativity Meeting*, with oral presentation: "Efficient implementation of finite volume methods in Numerical Relativity", Tenerife

June 11 - 14 2008   *Post Newtonian 2008 International Workshop* , Jena

Sept. 08 - 12 2008   *Numerical modelling of astrophysical sources of gravitational radiation*, Valencia (Spain)

Sept. 15 - 19 2008   *XXXI Spanish Relativity Meeting*, with oral presentation: "Slicing the throat of a black hole", Salamanca (Spain)

Publications in Refereed Journals

- *Efficient implementation of finite volume methods in Numerical Relativity*,

  D. Alic, C. Bona, C. Bona Casas, J. Masso, Phys. Rev. D 76, 104007 (2007).

- *Implementation of standard testbeds for numerical relativity*,

  M.C. Babiuc, S. Husa, D. Alic, I. Hinder, C. Lechner, E. Schnetter, B. Szilagyi, Y. Zlochower, N. Dorband, D. Pollney, J. Winicour, Class. Quant. Grav. 25, 125012 (2008).

- *Towards a gauge-polyvalent Numerical Relativity code*,

  D. Alic, C. Bona, C. Bona-Casas, Phys. Rev. D 79, 044026 (2009).

- *Slicing the throat of a black hole*,

  D. Alic, M. Hannam, S. Husa, F. Ohme, C. Bona, in preparation, to be submitted at Class. Quant. Grav.

Conference Proceedings

- *Gauge and constraint degrees of freedom: from analytical to numerical approximations in General Relativity*,

  D. Alic, C. Bona, published in Proceedings of Spanish Relativity Meeting - Encuentros Relativistas Espanoles ERE2007, "Relativistic Astrophysics and Cosmology", EAS Publications Series 30 (2008); arXiv: gr-qc/0710.4425.

- *A new dissipation term for finite difference simulations in Relativity*,

  D. Alic, C. Bona, C. Bona Casas, published in Proceedings of Spanish Relativity Meeting - Encuentros Relativistas Espanoles ERE2007, "Relativistic Astrophysics and Cosmology", EAS Publications Series 30 (2008); arXiv: gr-qc/0711.4685.

- *From Tensor Equations to Numerical Code – Computer Algebra Tools for Numerical Relativity*,

  C. Lechner, D. Alic, S. Husa, published in Proceedings of the 6th International Symposium on Symbolic and Numeric Algorithms for Scientific Computing SYNASC04, Editura Mirton, ISBN 973-661-441-7; arXiv: cs/0411063.

Research Visits

01 Nov. - 13 Nov. 2004	Max Planck Institute for Gravitational Physics, *Albert Einstein Institute* (AEI), Geometric Analysis and Gravitation Division, Potsdam (Germany).
26 Feb. - 13 March 2005	Max Planck Institute for Gravitational Physics, *Albert Einstein Institute* (AEI), Geometric Analysis and Gravitation Division, Potsdam (Germany).
31 Jan. - 03 Apr. 2007	*Louisiana State University* (LSU), Physics and Astronomy Department, Baton Rouge (USA).
22 Oct. - 15 Dec. 2007	Max Planck Institute for Gravitational Physics, *Albert Einstein Institute* (AEI), Astrophysical Relativity Division, Potsdam (Germany).
28 Apr. - 27 June 2008	Max Planck Institute for Gravitational Physics, *Albert Einstein Institute* (AEI), Astrophysical Relativity Division, Potsdam (Germany).
02 March - 02 May 2009	Max Planck Institute for Gravitational Physics, *Albert Einstein Institute* (AEI), Astrophysical Relativity Division, Potsdam (Germany).

Seminars

12 Dec. 2007	*Efficient implementation of finite volume methods in Numerical Relativity*, Albert Einstein Institute, Astrophysical Relativity Division, Numerical Relativity Group, Potsdam (Germany).
22 Feb. 2008	*Finite Volume Methods and Dissipation in Numerical Relativity Black Hole Simulations*, University of the Balearic Islands, Department of Theoretical Physics, Relativity and Gravitation Group, Palma de Mallorca (Spain).

Teaching experience

Oct. 2004 - June 2005	Teaching assistantship for Statistical Physics (seminars, exercises) at the West University of Timisoara (Romania).

Computer skills

Programming: C, C++, Fortran, Mathematica.
Operating systems: UNIX, Windows.

Languages

English (fluent), German (advanced), Spanish (advanced), Romanian (native).